

Adolphe Merkle Institute
University of Fribourg (Switzerland)

**Physiologically Responsive Mechanically Adaptive Polymeric Materials
for Biomedical Applications**

THESIS

Presented to the Faculty of Science of the University of Fribourg (Switzerland)
in fulfillment of the requirements for the academic grade of *Doctor of Science*
Doctor rerum naturalium, Dr. rer. nat.

by

Mehdi Jorfi

Thesis No: 1829
University of Fribourg
2014

Accepted by the Faculty of Science of the University of Fribourg (Switzerland) upon the recommendation of

- Prof. Dr. Christoph Weder, Adolphe Merkle Institute, University of Fribourg, Switzerland (Thesis Supervisor)
- Dr. E. Johan Foster, Adolphe Merkle Institute, University of Fribourg, Switzerland (Internal Co-Examiner)
- Prof. Jeffrey R. Capadona, Department of Biomedical Engineering, Case Western Reserve University, USA (External Co-Examiner)
- Prof. Nico Bruns, Adolphe Merkle Institute, University of Fribourg, Switzerland (President of Jury)

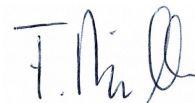
Fribourg, 25/03/2014

Thesis Supervisor



Prof. Dr. Christoph Weder

Dean



Prof. Dr. Fritz Müller

Dedication

This dissertation is dedicated to my mother, who through her invaluable actions has taught me that anything is possible as long as you work hard. This dissertation also dedicated to my family. Their support and encouragement have sustained me throughout my life.

Acknowledgements

This was made possible by the assistance and contributions of many others. Most notably, my supervisor, Prof. Christoph Weder, who has been an extraordinary mentor and helped me to guide this work through many twists and turns. I learned tremendously from him in many ways. The robustness and thoroughness of his work is something I will always try to apply in my own work. His technical insights and contributions were important, and so his broader knowledge about science and career development. I have often admired his excellence in writing which have shaped this work into something much better than what I could have done myself. Chris has a great ability to guide his students, while retaining the patience to allow students to develop their own interests and become capable independent researchers. I am forever grateful for the privilege of working with him.

I would like to thank my group leader, Dr. Johan Foster, for many things. Among them: his scientific creativity and fearlessness to tackle any challenge, his infectious enthusiasm towards science, and his dedication to support his students to be even better than they think they could be. I am also thankful for his personal attention, suggestions, endless encouragement and full support during last years of my Ph.D. research. I am fortunate to have been part of his group during its amazing growth.

My other committee member, Prof. Jeffrey Capadona, has provided valuable comments and has shown a great deal of patience and support as my project developed over time. I appreciate his time out of busy schedules to provide helpful criticisms, comments, and feedback regarding my thesis projects.

This interdisciplinary research would not have been possible without the help of many brilliant colleagues and collaborators. In particular, Dr. Jeff Capadona has been a valuable collaborator on several of my cortical implant projects. I would like to gratefully acknowledge all the members of the Capadona Lab for their contributions, helpful discussions, and their kind host during my trip to Cleveland. In particular, I am grateful to

Kyle Householder, Jessica Nguyen, and Kelsey Potter who worked closely with me throughout my drug-releasing materials' project.

AMI has been a great place to grow and develop as a scientist. I want to thank all the members of the Chris Lab with whom I had a pleasure to discuss science and collaborate with. Many researchers of Chris Lab have directly or indirectly contributed to my research at AMI. I would like to thank especially Pratheep Annamalai, Mahesh Biyani, Matt Roberts, Janak Sapkota, Apiradee Nicharat and Tobias Kuhnt for all the fruitful collaborative works we have done together. I also owe special thanks to all Polymer Chemistry and Materials' group members, especially Soo, Christian, Silvana, Sonja, Sandeep, Sandra and Souleymane for good times, support and friendship. I would like to extend my thanks to Katharina Gries for translating my thesis abstract into German language and Rebecca Parkhurst who helped me proofread the present dissertation's conclusions and outlook. Also, I would like to express my gratitude to all AMI colleagues for maintaining friendly atmosphere throughout my work.

Lastly, I would like to thank my family for inspiration and support received throughout these years. I believe this achievement is theirs as much as it is mine. Most importantly, my mother, for her decades of love and support, for her smiles and tears throughout my studies and the several years that I have been away from home. My mother has always supported my ambitions and it is because of her work and sacrifices that I am in this position today. Finally, my deepest appreciation goes to my lovely wife, Sarminaz, for providing constant support and encouragement, for her admiration, and her ever-positive attitude.

Physiologically Responsive Mechanically Adaptive Polymeric Materials for Biomedical Applications

Mehdi Jorfi

University of Fribourg, 2014

Supervisor: Professor Christoph Weder

Abstract

Artificial neural interfaces can connect the central nervous system with the outside world and hold great potential for rehabilitating patients that suffer from paralysis, other forms of motor dysfunction, or limb loss. Several types of brain neural interfaces, with varying levels of invasiveness and abilities to acquire neural signals, have been developed. For example, non-penetrating recording electrodes placed externally on the scalp or subdurally on the brain surface can gain functional information. However, many researchers believe that recording and stimulating devices that penetrate into specific regions of the brain (i.e. intracortical microelectrodes) will likely provide the most useful signals for neural interfacing. Despite the potential that intracortical microelectrodes have shown, widespread clinical implementation is impeded by the fact that it is difficult to consistently record high quality neural signals over clinically relevant time frames. This is in large part due to neuro-inflammation, which involves both neuron degeneration and foreign body encapsulation. Several factors have been implicated to contribute to neuro-inflammation following device implantation, including the mechanical mismatch between the often highly rigid implant and the much softer brain tissue, and the oxidative stress state that forms around the implant as a result of inflammation. To enable long-term consistent neural recordings, new materials are needed for the next generation of intracortical microelectrodes, with an increased emphasis on reducing the neuro-inflammatory response.

This dissertation pursued the development of new physiologically responsive, mechanically adaptive polymeric materials for neural interfacing applications and the study of the structure-property relationships of these materials. Expanding a previously established design principle for chemo-responsive mechanically adaptive materials inspired by the architecture of the sea cucumber dermis, several families of nanocomposites were designed, prepared and studied. These materials consist of a matrix polymer that is reinforced with rigid cellulose nanocrystals (CNCs) and the interactions between the CNCs, and therewith the overall mechanical properties, can be influenced by exposure to water. The adaptive nature of these materials makes them useful as a basis for penetrating cortical microelectrodes that are sufficiently stiff to be easily implanted into the cortex, but upon exposure to physiological conditions soften to better match the stiffness of the brain. Several new rationally designed materials systems were investigated.

Thus, nanocomposites based on poly(vinyl alcohol) and CNCs derived from tunicates and cotton were studied to explore how aspect ratio, surface charge density, and filler content influence the mechanical properties. The new materials offer an initial stiffness that is significantly higher than that of previous generations of such responsive materials, presumably on account of polymer-CNC interactions. It was also shown that the aqueous swelling characteristics of the nanocomposites could be controlled via the processing conditions. Using this tool, the switching “contrast” of the nanocomposites upon exposure to (emulated) physiological conditions could be varied.

Physiologically responsive mechanically adaptive materials based on poly(vinyl alcohol) or poly(vinyl acetate) and CNCs isolated from tunicate or cotton were further bestowed with the capability to also locally administer the anti-oxidant drugs curcumin, resveratrol or superoxide dismutase mimetic with burst or sustained release profiles. These materials represent the first examples of materials for intracortical implants which combine two independently effective mechanisms – mechanical morphing and localized anti-oxidant release. They permit, for the first time, to explore if the combination leads to synergistic effects and will permit investigations of how the release kinetics of anti-oxidant therapies

at the intracortical implant-tissue interface influence neural integration. A first *in vivo* study of PVA/CNC/curcumin nanocomposites in rats revealed that over the first four weeks of the implantation, curcumin-releasing, mechanically adaptive implants were associated with higher neuron survival and a more stable blood-brain barrier at the implant-tissue interface than the neat poly(vinyl alcohol) controls.

Finally, the ability to mechanically morph upon exposure to physiological conditions was imparted to optical fibers for optogenetics. This recently developed neural interfacing platform relies on the activation or muting of neurons using light and one must expect that mechanical mismatch of conventional optical fibers and the cortical tissue also contribute to the chronic neuroinflammatory response. Thus mechanically adaptive optical fibers made of PVA were developed, which may mitigate this problem. Produced by a one-step wet-spinning process, the fibers display an initial stiffness that is slightly higher than that of commercial optical fibers and permits facile insertion of small-diameter implants into the cortex. Upon exposure to (emulated) physiological conditions, the fibers swell slightly with water and their stiffness is reduced significantly, while the concomitant changes to the fiber's optical properties are small. The PVA optical fibers permit to deliver light of a range of wavelengths that is sufficiently intense to stimulate neurons in the brain and meet the optical demands of optogenetic applications.

This dissertation derived fundamental insights into the structure-property relationships by governing the adaptive nature of these materials through composition (i.e. different polymer matrices, types and amount of nanofiller, and therapeutic agents) and also processing conditions. While *in vivo* studies using the new materials presented here have only begun, it is already clear that the materials made and studied in this dissertation will be useful to advance the understanding of how stimuli-responsive polymeric materials can help to decrease the neuroinflammation effects associated with intracortical implants.

Physiologisch Responsive Mechanisch Adaptive Polymere für Biomedizinische Anwendungen

Mehdi Jorfi

Universität Freiburg, 2014

Betreuer: Professor Christoph Weder

Zusammenfassung

Künstliche neurale Schnittstellen können verwendet werden, um das zentrale Nervensystem mit der äusseren Welt zu verbinden. Sie bieten deshalb grosses Potential für die Rehabilitierung von Patienten, die unter Lähmung, anderen Formen von motorischer Dysfunktion oder Amputationen leiden. Es wurden verschiedene Arten neuraler Gehirnschnittstellen entwickelt, mit unterschiedlichen Invasivitätsgraden sowie der Fähigkeit, neurale Signale aufzunehmen. Beispielsweise können nicht-eindringende aufzeichnende Elektroden, welche extern auf der Kopfhaut oder subdural auf der Hirnoberfläche angebracht werden, funktionale Informationen gewinnen. Allerdings ist unter Forschern die Annahme verbreitet, dass Aufzeichnungs- und Stimulationsgeräte, die in spezifische Regionen des Gehirns eindringen (z. B. intrakortikale Mikroelektroden), wahrscheinlich die nützlichsten Signale einer neuralen Schnittstelle liefern werden. Trotz des Potentials, welches intrakortikale Mikroelektroden gezeigt haben, ist die breite klinische Implementation durch die Tatsache behindert, dass es schwierig ist, beständig qualitativ hochwertige neurale Signale über einen klinisch relevanten Zeitrahmen aufzuzeichnen. Dies wird hauptsächlich durch Neuroinflammation verursacht, was sowohl Neuronendegeneration als auch Fremdkörperverkapselung beinhaltet. Viele Faktoren werden in Zusammenhang gebracht, einen Beitrag zur Entzündung der Gehirnareale in Folge von Geräteimplantationen zu leisten, darunter die mechanische Diskrepanz zwischen dem häufig sehr steifen Implantat und dem deutlich weicheren Hirngewebe, sowie dem oxidativen Stresszustand, der um das Implantat als

Resultat der Entzündung entsteht. Um langzeit-beständige neurale Aufzeichnungen zu ermöglichen, werden neue Materialien für die nächste Generation intrakortikaler Mikroelektroden benötigt, mit grösserer Betonung auf einer Reduktion der neuroinflammatorischen Antwort benötigt.

Die vorliegende Dissertation verfolgt die Entwicklung physiologisch responsiver, mechanisch adaptiver Polymere für neurale Schnittstellenapplikationen sowie eine Studie zur Struktur-Eigenschaftsbeziehung dieser Materialien. Ausgehend von einem zuvor etablierten Designprinzip für chemisch-responsive mechanisch adaptive Materialien, inspiriert durch die Architektur der Dermis von Seegurken, wurden verschiedene Familien von Nanokompositen entworfen, präpariert und untersucht. Diese Materialien beinhalten ein Matrixpolymer, welches durch steife Cellulose Nanokristalle (*cellulose nanocrystals*, CNCs) und die Wechselwirkungen zwischen den CNCs verstärkt wird, so dass auch die gesamten mechanischen Eigenschaften durch Kontakt mit Wasser beeinflusst werden können. Die adaptive Natur dieses Materials lässt es nützlich erscheinen als Basis für eindringende kortikale Mikroelektroden, die ausreichend steif sind, um einfach in den Kortex implantiert werden zu können, aber unter physiologischen Bedingungen erweichen und besser zur Steifigkeit des Gehirns passen. Mehrere neue, rational entworfene Materialien wurden untersucht.

Nanokomposite basierend auf Polyvinylalkohol (PVA) und CNCs, gewonnen aus Manteltieren und Baumwolle, wurden hinsichtlich des Einflusses von Aspektverhältnis, Oberflächenladungsdichte und Füllstoffkonzentration auf die mechanischen Eigenschaften untersucht. Die neuen Materialien bieten eine anfängliche Steifigkeit, welche signifikant höher ist als bei vorangegangenen Generationen solcher responsiver Materialien, vermutlich wegen der Wechselwirkungen zwischen Polymer und CNCs. Ferner wurde gezeigt, dass die Quellcharakteristika der Nanokomposite im wässrigen Medium durch die Verarbeitungsbedingungen kontrolliert werden konnten. Unter Verwendung dieses Instruments konnte der „Schaltkontrast“ der Nanokomposite durch Kontakt mit (emulierten) physiologischen Bedingungen variiert werden.

Physiologisch responsive mechanisch adaptive Materialien basierend auf Polyvinylalkohol oder Polyvinylacetat und CNCs, die aus Manteltieren oder Baumwolle gewonnen wurden, wurden so konzipiert, auch lokal die antioxidativen Wirkstoffe Curcumin, Resveratrol oder Superoxiddismutase mimetisch mit plötzlichen („burst“) oder nachhaltigen Freisetzungsprofilen zu regulieren. Diese Materialien repräsentieren die ersten Beispiele für interkortikale Implantate, welche zwei voneinander unabhängig effektive Mechanismen kombinieren – mechanische Verformbarkeit und lokale Freisetzung von Antioxidantien. Sie erlauben erstmals Untersuchungen darüber, wie die Freisetzungskinetik bei Antioxidantherapie an der intrakortikalen Implantat-Gewebe Grenzfläche die neurale Integration beeinflusst. Eine erste *in-vivo* Studie mit PVA/CNC/Curcumin Nanokompositen an Ratten zeigte, dass über die ersten vier Wochen der Implantation Curcumin-freisetzende, mechanisch adaptive Implantate mit einer höheren Neuronenüberlebensrate und einer stabileren Blut-Hirn-Schranke an der Grenzfläche zwischen Implantat und Gewebe assoziiert wurden als die reinen Polyvinylalkohol Kontrollproben.

Abschliessend wurde die Fähigkeit der mechanischen Verformung durch Einfluss physiologischer Bedingungen für optische Fasern für die Optogenetik verwendet. Diese kürzlich entwickelte Plattform für neurale Schnittstellen beruht auf der Aktivierung oder Stummschaltung von Neuronen, die Licht verwenden. Es wird erwartet, dass die mechanische Diskrepanz zwischen konventionellen optischen Fasern und kortikalem Gewebe auch zur chronischen neuroinflammatorischen Antwort beiträgt. Daher wurden mechanisch adaptive optische Fasern aus PVA entwickelt, welche dieses Problem lindern könnten. Die Fasern wurden in einem einstufigen „dry-jet“ Nassspinnprozess produziert und sie zeigen eine anfängliche Steifigkeit, die geringfügig höher ist als die kommerziell erhältlicher optischer Fasern, und die müheloses Einführen von Implantaten mit geringem Durchmesser in den Kortex ermöglicht. Unter (emulierten) physiologischen Bedingungen quellen die Fasern mit Wasser geringfügig auf und ihre Steifigkeit wird signifikant reduziert, während die begleitenden Veränderungen der optischen Eigenschaften der Faser gering sind. Die optischen Fasern aus PVA erlauben es, Licht in einem

Wellenlängenbereich zu transportieren, der hinreichend intensiv ist, Neuronen im Gehirn zu stimulieren und optischen Anforderungen für optogenetische Anwendungen gerecht zu werden.

Die vorliegende Dissertation leitet fundamentale Einblicke in Struktur-Eigenschaftsbeziehungen her, indem sie die adaptive Natur dieser Materialien durch Zusammensetzung (z.B. unterschiedliche Polymermatrices, Art und Menge der Nanofüller und therapeutischer Substanzen) sowie die Verarbeitungsbedingungen vertieft. Während *in-vivo* Studien zum hier vorliegenden neuen Material gerade erst begonnen haben, ist es schon heute ersichtlich, dass die im Rahmen dieser Dissertation hergestellten und untersuchten Materialien zum Fortschritt des Verständnisses nützlich sind, wie stimuli-responsive Polymere helfen können, neuroinflammatorische Effekte in Zusammenhang mit Intrakortikalimplantaten zu verringern.

Table of Contents

List of Tables	xix
List of Figures	xx
List of Abbreviations	xxix
Chapter 1 – Introduction to Biocompatible Materials for Intracortical Microelectrodes	1
1.1. TRADITIONAL INTRACORTICAL MICROELECTRODES FOR BRAIN MACHINE INTERFACING	2
1.2. CHALLENGES TO OBTAINING CONSISTENT, HIGH-QUALITY NEURAL RECORDINGS	4
1.2.1. The Neuro-Inflammatory Response	5
1.3. MATERIAL STRATEGIES FOR IMPROVING MICROELECTRODE BIOCOMPATIBILITY AND RECORDING PERFORMANCE	5
1.3.1. Mechanically Compliant Intracortical Microelectrodes	7
1.3.1.1. Introduction to Microelectrodes Mechanics	8
1.3.1.2. Compliant Polymeric Materials for Intracortical Microelectrodes	10
1.3.1.3. Insertion Aides and Biodegradable Materials	16
1.3.1.4. In Situ Softening Materials	19
1.3.2. Incorporating Bioactive Materials	30
1.3.3. Conducting Polymers	37
1.3.4. Nanomaterials	46
1.4. REFERENCES	57
Chapter 2 – Scope and Objectives	67
Chapter 3 – Physiologically Responsive Mechanically Adaptive Bio-Nanocomposites for Biomedical Applications	69
3.1. ABSTRACT	69
3.2. INTRODUCTION	70
3.3. EXPERIMENTAL SECTION	72

3.4. RESULTS AND DISCUSSION	77
3.4.1. Isolation and Physical Properties of Cellulose Nanocrystals	77
3.4.2. Nanocomposite Processing	78
3.4.3. Thermal Properties	79
3.4.4. Mechanical Properties of Dry PVA/CNC Nanocomposites	79
3.4.5. Analysis of Mechanical Data in the Framework of the Percolation Model	85
3.4.6. Swelling Behavior	88
3.4.7. Mechanical Properties of ACSF-Swollen Nanocomposites	90
3.5. CONCLUSIONS	93
3.6. REFERENCES	95
3.7. APPENDIX	98

Chapter 4 – Curcumin-Releasing Mechanically Adaptive Intracortical Implants Improve Proximal Neuronal Density and Blood-Brain Barrier Stability	105
4.1. ABSTRACT	105
4.2. INTRODUCTION	106
4.3. EXPERIMENTAL SECTION	108
4.4. RESULTS	117
4.4.1. Characterization of Curcumin-Loaded Materials	117
4.4.2. Mechanically Adaptive Properties of Materials	118
4.4.3. Curcumin Release Profiles	120
4.4.4. Anti-oxidative Activity of Curcumin-Loaded Materials	121
4.4.5. <i>In vivo</i> Studies	121
4.4.6. Neuronal Nuclei Density (NeuN)	121
4.4.7. Blood Brain Barrier Permeability (IgG)	125
4.4.8. Astrocytic Scar Formation: Astrogliosis (GFAP)	127
4.4.9. Microglia and Macrophage Density	129
4.4.10. Wound Healing (HMGB-1)	131
4.5. DISCUSSION	133
4.6. CONCLUSIONS	140

4.7. REFERENCES	142
4.8. APPENDIX.....	146
Chapter 5 – Physiologically Responsive Mechanically Adaptive Antioxidant-Releasing Nanocomposites for Cortical Implants with Improved Neural Integration	154
5.1. ABSTRACT	154
5.2. INTRODUCTION	155
5.3. EXPERIMENTAL SECTION	156
5.4. RESULTS AND DISCUSSION	161
5.4.1. Processing and Characterization of Materials.....	161
5.4.2. Mechanically Adaptive Properties of Antioxidant-Loaded Materials	165
5.4.3. Drug Release Studies	168
5.4.4. Antioxidative Activity of Drug-Loaded Nanocomposites	171
5.5. CONCLUSIONS	175
5.6. REFERENCES	176
5.7. APPENDIX.....	177
Chapter 6 – Physiologically Responsive Mechanically Adaptive Polymer Optical Fibers for Optogenetics	178
6.1. ABSTRACT	178
6.2. INTRODUCTION	179
6.3. EXPERIMENTAL SECTION	180
6.4. RESULTS AND DISCUSSION	182
6.5. CONCLUSIONS	189
6.6. REFERENCES	190
Chapter 7 – Conclusions and Outlook	192
7.1. CONCLUSIONS	192
7.2. OUTLOOK	195
<i>Curriculum Vitae</i>	<i>199</i>

List of Tables

Table 1-1. Non-Exhaustive List of Bioactive Surface Treatments for Intracortical Microelectrodes.....	31
Table 3-1. Thermal properties of neat PVA and PVA/CNC nanocomposites as a function of CNC type and content.....	80
Table 3-2. Tensile storage moduli of dry and ACSF-swollen films of neat PVA and PVA/CNC nanocomposites determined by DMA.	81
Table 3-3. Comparison of tensile storage moduli of current materials with previous mechanically-adaptive nanocomposites.....	85
Table 3-4. Swelling data of neat PVA and PVA/t-CNC nanocomposites at 37 °C in ACSF as a function of t-CNC content.	90
Table 4-1. Swelling properties of neat PVA and curcumin-loaded films.	118
Table A4-1. Thermal properties of materials studied.	153
Table A4-2. Tensile storage moduli of dry and ACSF-swollen films determined by dynamic mechanical analyzer	153
Table 5-1. Storage moduli of dry and ACSF-swollen PVAc/CNC nanocomposites determined by DMA. Data represent averages and are shown for the neat PVAc/CNC reference nanocomposite as well as for curcumin (Cur) and resveratrol (Res) releasing nanocomposites loaded with different contents of these antioxidants.....	165
Table 5-2. Cumulative release (%) data of curcumin (Cur)-loaded PVAc/CNC nanocomposites and resveratrol (Res)-loaded PVAc/CNC nanocomposites in ACSF at 37 °C determined by UV-vis..	168

List of Figures

Figure 1-1. Electrical circuit model of intracortical microelectrode in the brain.	4
Figure 1-2. Forces acting on the intracortical microelectrodes upon penetration.....	9
Figure 1-3. Chemical structures of compliant polymeric materials and monomers commonly used for neural interfaces.	11
Figure 1-4. SEM pictures of microelectrode tips of SU-8-based electrodes..	15
Figure 1-5. Top: Pictures of a sea cucumber, in the threatened (stiff) and relaxed (soft) and state. Bottom: Simplified schematic representation of the switching mechanism found in the sea cucumber dermis and used in physiologically responsive mechanically-adaptive nanocomposites	20
Figure 1-6. Plot showing the log of the Young's modulus of mechanically adaptive PVAc/CNC nanocomposites as function of exposure time to ACSF or implantation time in the rat cortex.	22
Figure 1-7. Photograph of a 2-electrode contact intracortical probe.	24
Figure 1-8. PVAc/CNC nanocomposite implants (NC) reduce chronic neuroinflammation.	25
Figure 1-9. Schematic and light micrographs of a prototype SMP neuronal probe.....	26
Figure 1-10. Picture (left) and optical microscope image (right) of a mechanically adaptive cortical probe with 8 recording channels fabricated from a shape- memory polymer by transfer-by- polymerization process	27
Figure 1-11. (A) SEM images of uncoated and silk-coated stainless steel microwires	29

Figure 1-12. (a, b) Representative images of NeuN+ cells (green) around the NM (unmodified) and L1 (L1-peptide grafted) probes after 8 weeks of implantation in rat cortex. (c, d) Representative images of neuronal filament (green) stained tissue after 8 weeks of implantation in rat cortex35

Figure 1-13. Chemical structures of poly(pyrrole) (PPy) and poly-(3,4-ethylene dioxothiophene) (PEDOT), examples of conducting polymers explored in neural interfaces.38

Figure 1-14. Chemical structures of monomers used to fabricate PEDOT and PEDOT-MeOH.41

Figure 1-15. (a) Schematic of the electrochemical deposition cell and the neural cell monolayer cultured on the surface of the metal electrode prior to polymerization. (b) PEDOT polymerized around living cells.42

Figure 1-16. (a–d) Schematic representation of the fabrication of microtherad electrodes, and (e) SEM images of a fully assembled, functional electrode.....44

Figure 1-17. GFAP immunostaining for the Pt implant control (A) and PPy/SWCNT coated Pt implant (C) after 6 weeks post-implantation. (E) Quantitative comparison of GFAP immunoreactivity between the control and coated electrodes as a function of distance from the electrode. The survival of neurons around the implanted electrode for the control (B) and coated implant (D) at 6 weeks post-implantation. (F) Quantification comparison of neuron survival between the control and coated electrodes as a function of distance from the electrode.49

Figure 1-18. Scanning electron microscopy images of (a) An as-grown CNF array. (b) An as-grown CNF array after being soaked in water and then dried in the air. (c, d) an as-grown CNF arrays after electrodepositing a 40-nm-thick conformal polypyrrole film.....	51
Figure 1-19. Schematic represents fabrication of multifunctional biomaterial-based microelectrode. (A) Uncoated microelectrode. (B) Electrospining of drug-loaded nanofibers. (C) Hydrogel coating. (D) Electrochemical polymerization of a conducting polymer.	53
Figure 1-20. Schematic illustration of conducting polymer (PEDOT) nanotube fabrication on neural microelectrodes.....	54
Figure 1-21. Scanning electron microscopy images of conducting polymers after CV measurements on a neural electrode.	55
Figure 3-1. AFM amplitude images for (a) lyophilized t-CNCs, and (b) spray-dried c-CNCs.....	78
Figure 3-2. Dynamic mechanical analysis (DMA) data of dry PVA and dry PVA/CNC nanocomposites as a function of temperature and CNC content	83
Figure 3-3. (a) Tensile storage moduli of neat PVA and PVA/t-CNC nanocomposites as a function of CNC content in the dry state at 100 °C (□), re-dried after swelling with ACSF for 1 week (□), ACSF-swollen after immersion in ACSF at 37 °C for 1 week (□) and 1 month (Δ). (b) Tensile storage moduli of neat PVA and PVA/c-CNC nanocomposites as a function of CNC content in the dry state at 100 °C (□), and ACSF-swollen after immersion in ACSF at 37 °C for 1 week (□).....	88

Figure 3-4. Swelling of PVA/t-CNC nanocomposites compression-molded at 150 °C (■), PVA/c-CNC nanocomposites compression-molded at 120 °C (●), a PVA/t-CNC nanocomposite compression-molded at 120 °C (○), and a PVA/c-CNC nanocomposite compression-molded at 150 °C (□) as a function of CNC content, after the samples were immersed in ACSF at 37 °C for 1 day.	89
Figure 3-5. Dynamic mechanical analysis (DMA) data of ACSF-swollen films of (a) neat PVA and PVA/t-CNC nanocomposites and (b) PVA/c-CNC nanocomposites as a function of temperature and CNC content after immersion in ACSF at 37 °C for 1 week.	92
Figure A3-1. Conductometric titration curves of CNCs. (a) Lyophilized t-CNCs, (b) spray-dried c-CNCs, (c) lyophilized c-CNCs, and (d) a blank titration without CNCs.	99
Figure A3-2. Representative transition electron microscopy (TEM) images of CNCs. (a) lyophilized t-CNCs, and (b) spray-dried c-CNCs.....	99
Figure A3-3. Transition electron microscopy (TEM) images lyophilized c-CNCs.....	100
Figure A3-4. Three-dimensional AFM topographic (height) images for (a) lyophilized t-CNCs, and (b) spray-dried c-CNCs.	100
Figure A3-5. Photographs of solution-cast and compression-molded PVA/c-CNC nanocomposite films (16% v/v c-CNCs) processed at 120 (left) and 150 °C (right), respectively.	101
Figure A3-6. DSC thermograms (second heating) of (a) PVA/t-CNC and (b) PVA/c-CNC nanocomposites and neat PVA films compression-molded at (a) 150 °C and (b) 120 °C, respectively.	102
Figure A3-7. Chart showing the stress-strain curves of neat PVA and PVA/CNC nanocomposites as a function of CNC content.	102

Figure A3-8. DMA data of ACSF-swollen films of neat PVA and PVA/t-CNC nanocomposites after immersion in ACSF at 37 °C for 1 month.	103
Figure A3-9. DMA data of ACSF-swollen films of 16% v/v PVA/t-CNC nanocomposites after immersion in ACSF at 37 °C for 1 day.....	103
Figure A3-10. DMA data of ACSF-swollen films of 16% v/v PVA/c-CNC nanocomposites after immersion in ACSF at 37 °C for 1 day.....	104
Figure 4-1. Chemical structure of poly(vinyl alcohol) (PVA) and curcumin.....	108
Figure 4-2. Representative dynamic mechanical analysis (DMA) traces showing the tensile storage moduli of (A) dry and (B) ACSF-swollen curcumin-loaded poly(vinyl alcohol) (PVA) samples as a function of temperature and curcumin content (1 or 3% w/w).	119
Figure 4-3. Cumulative <i>in vitro</i> release profile of curcumin-loaded polymers in ACSF at 37 °C.	120
Figure 4-4. (A) Plot showing the absorbance at 516 nm of a methanolic solution of DPPH (100 µM) as a function of time, and of the same solution in the presence of films consisting of neat PVA, or PVA with 1 or 3% w/w curcumin, respectively, incubated at 37 °C in the dark for up to 48 hours. (B) DPPH scavenging activity calculated from the results shown in (A)...	122
Figure 4-5. Neuronal nuclei populations surrounding neat PVA control and curcumin- releasing PVA implants. Neuronal (NeuN) density was investigated at 2, 4 and 12 weeks after polymer implantation up to 600 µm from the implant interface.....	125
Figure 4-6. Infiltration of immunoglobulin-g (IgG) around neat PVA controls and curcumin-releasing PVA implants	127

Figure 4-7. Astrogliosis surrounding neat PVA control and curcumin-loaded PVA implants in the cortex.....	128
Figure 4-8. Total microglia and macrophage accumulation (IBA-1 ⁺ cells) around neat PVA controls and curcumin-releasing polymer implants.....	130
Figure 4-9. Accumulation of activated microglia and macrophages (CD68 ⁺) around neat PVA controls and curcumin-releasing implants.	131
Figure 4-10. Expression of High Mobility Group Box-1 (HMGB-1) around neat PVA controls and curcumin-releasing PVA implants.	132
Figure A4-1. (Left) AFM height image of CNCs derived from tunicates.	147
Figure A4-2. Conductometric titration curve of lyophilized CNCs.....	147
Figure A4-3. Representative dynamic mechanical analysis (DMA) traces showing the tensile storage moduli of (A) dry and (B) wet curcumin-loaded PVA/CNCs polymers as a function of temperature.....	148
Figure A4-4. Cumulative <i>in vitro</i> release profile of curcumin-loaded materials in ACSF at 37 °C.	149
Figure A4-5. (Top) Chemical structure of DPPH and its reaction with an anti-oxidant (AO-H). (Bottom) Representative photographs of solutions of DPPH in methanol (100 μM, 3 mL) at 0, 9, 24 and 48 hours and after placing a film of the neat PVA control, or the curcumin-loaded PVA films into the DPPH solution.....	150
Figure A4-6. Representative photographs of solutions of DPPH in methanol.	151

Figure A4-7. (A) Plot showing the absorbance at 516 nm of a methanolic solution of DPPH (100 μ M) as a function of time, and of the same solution in the presence of films consisting of the neat PVA/CNC nanocomposite, or the PVA/CNC nanocomposites with 1 or 3% w/w curcumin, respectively, incubated at 37 °C in the dark for up to 48 hours. (B) DPPH scavenging activity calculated from the results shown in (A).	152
Figure 5-1. Chemical structures of materials used in this study.	157
Figure 5-2. Atomic force microscopy (AFM) image of lyophilized CNCs isolated from tunicates. The CNCs were deposited from aqueous dispersions (0.01 mg/mL) onto freshly cleaved mica surfaces.	162
Figure 5-3. Photographs of solution-cast PVAc/CNC nanocomposite films (15% w/w CNCs) with either 0.005% or 0.01% w/w resveratrol (Res, A and B) or curcumin (Cur, C and D).	162
Figure 5-4. Swelling behavior of PVAc/CNC nanocomposites (15% w/w CNCs) with different amounts of antioxidants after the films were immersed in ACSF at 37 °C for 1 week.	163
Figure 5-6. Representative dynamic mechanical analysis (DMA) traces showing the storage moduli E' of (A) dry Cur/PVAc/CNC, (B) dry Res/PVAc/CNC, (C) ACSF-swollen Cur/PVAc/CNC, and (D) ACSF-swollen Res/PVAc/CNC nanocomposites as a function of temperature and drug content.	167
Figure 5-8. Representative photographs of solutions of DPPH in methanol.	172

Figure 5-9. (A, B) Plots showing the absorbance at 516 nm of a methanolic solution of DPPH (100 μ M) as function of time, and of the same solution in the presence of nanocomposite films consisting of the neat PVAc/CNC reference nanocomposite, or PVAc/CNC nanocomposites with different content of curcumin (Cur, A) or resveratrol (Res, B), respectively. (C, D) DPPH scavenging activity of curcumin-loaded (C) or resveratrol-loaded nanocomposites (D) calculated from the data shown in (A) and (B) according to equation 3.....	174
Figure A5-1. Representative transition electron microscopy (TEM) image of CNCs isolated from tunicates.....	177
Figure A5-2. Atomic force microscopy (AFM) images of a PVAc/CNC nanocomposite film showing the dispersion of cellulose nanocrystals within the polymer matrix as made surface.....	177
Figure 6-1. Schematic representation of the various processing steps used to fabricate physiologically-responsive, mechanically adaptive optical fibers based on PVA.	183
Figure 6-2. Optical microscopic images of a PVA optical fiber.....	184
Figure 6-3. Tensile storage modulus (E') of an adaptive PVA fiber and a commercial single mode (SM) optical fiber as a function of immersion time in water at 37 $^{\circ}$ C..	185
Figure 6-4. Optical losses of PVA optical fibers in the dry and wet state as function of fiber length. Data are shown for 470 (dry, \square ; wet, \square) and 590 nm (dry, \square ; wet, \square) incident light.	186

Figure 6-5. (a) Schematic representation of the cell used to operate optical fibers in the dry and water-swollen state. (b, c) Photographs of a 5 cm long PVA fiber transmitting 470 nm light in the dry state (b) and after adding water of a temperature of 25 °C (c).186

Figure 6-6. Changes of transmitted power (\square) and power density (\square) over time as a 10 cm long PVA fiber transporting 470 nm light from a 10.1 mW fiber-coupled high-power LED is switched from the dry, rigid state to the water-swollen soft state (room temperature) and back.....188

List of Abbreviations

a.u.	Arbitrary unit
ACSF	Artificial cerebrospinal fluid
AFM	Atomic Force Microscopy
ATRP	Atom transfer radical polymerization
BBB	Blood-brain barrier
BCB	Benzocyclobutene
BDNF	Brain-derived neurotrophic factor
BMI	Brain Machine Interface
CD68	Cluster of differentiation 68
CF	Clamping force
CH	Chitosan
CNFs	Carbon nanofibers
CNTs	Carbon nanotubes
CNCs	Cellulose Nanocrystals
c-CNCs	Cotton cellulose nanocrystals
CS	Chondroitin sulphate
Cur	Curcumin
CVD	Chemical vapor deposition
DARPA	Defense Advanced Research Projects Agency
DEX	Dexamethasone
DMF	N,N-dimethylformamide
DMSO	Dimethylsulphoxide
DPPH	2,2-diphenyl-1-picrylhydrazyl
DSC	Differential scanning calorimetry
E'	Tensile storage modulus
ECM	Extracellular matrix

EDOT	3,4-ethylenedioxythiophene
EDOT-MeOH	Hydroxymethyl 3,4-ethylenedioxythiophene
EIS	Electrochemical impedance spectrum
EO-EPI	Ethylene oxide-epichlorohydrin copolymer
FDA	Food and drug administration
FF	Friction force
FN	Fibronectin
GFAP	Glial fibrillary acidic protein
GPa	Gigapascal
GO	Graphene oxide
HMGB1	High mobility group box 1
IBA1	Ionized calcium-binding adapter molecule 1
IgG	Immunoglobulin G
IHC	Immunohistochemistry
LBL	Layer-by-layer
LFPs	Local field potential
LN	Laminin
MPa	Megapascal
MWCNTs	Multi-walled carbon nanotubes
NaDBS	Sodium dodecylbenzenesulfonate
NeuN	Neuronal nuclei
NGF	Nerve Growth Factor
PDDA	Poly(diallyldimethylammoniumchloride)
PBS	Phosphate buffered saline
PECVD	Plasma enhanced chemical vapor deposition
PEDOT	Poly(ethylene dioxythiophene)
PEGMA	Poly(ethylene glycol) methacrylate
PEG	Poly(ethylene glycol)
PEI	Poly(ethyleneimine)

PLGA	Poly(lactic- <i>co</i> -glycolic acid)
PSS	Poly(styrene sulfonate)
Ppy	Poly(pyrrole)
Res	Resveratrol
SEM	Scanning electron microscopy
Si	Silicon
SiC	Silicon carbid
SMP	Shape memory polymer
SNR	Signal-to-noise
SOD	Superoxide Dismutase
T_m	Melting temperature
T_g	Glass transition temperature
TEM	Transmission electron microscopy
t-CNCs	Tunicate cellulose nanocrystals
TGA	Thermogravimetric analysis
UV-Vis	Ultraviolet-visible

Chapter 1 – Introduction to Biocompatible Materials for Intracortical Microelectrodes¹

Neural interfaces bridge the central nervous system to the outside world. Originally, neural interfaces were developed as a basic science tool, and as such, have been used extensively to develop an understanding of how the nervous system works.¹⁻³ Additionally, neural interfaces hold great potential for rehabilitating persons with paralysis, other forms of motor dysfunction, or limb loss. Such rehabilitative applications require signal transducing systems that are commonly referred to as brain machine (or brain computer) interfaces.⁴ In brain machine interface (BMI) applications, a recording device is used to extract volitional intent in the form of consciously modulated neuronal signals from the nervous system. Using a variety of signal processing algorithms, extracted neural signals can then be used to drive external devices such as limb prostheses or computers.⁵⁻¹¹

A number of types of recording devices which rely on varying levels of invasiveness and access different forms of neural information have been developed. For example, non-penetrating recording electrodes placed externally on the scalp or sub-durally on the brain surface can gain functional information.^{10, 11} However, many researchers believe that recording devices that penetrate into specific regions of the brain will likely provide the most useful control signals for brain machine interfacing.¹² Despite the potential that penetrating intracortical microelectrodes have shown, widespread clinical implementation is impeded by the inability to consistently record high quality neural signals over clinically relevant time frames.¹³⁻¹⁶ As such, this thesis focuses on intracortical microelectrodes implanted within the cerebral cortex, which record from single or small populations of nearby neurons.

¹This chapter is adapted from Jorfi, M.; Skousen, J.L.; Weder, C.; Capadona, J.R. *Journal of Neural Engineering*, **2015**, 12, 011001. DOI:10.1088/1741-2560/12/1/011001

In this introduction the evolution of traditional intracortical microelectrode systems is discussed from a materials science perspective. Particular emphasis is given to key material developments that have facilitated the longest and highest quality *in vivo* recordings. In addition, a number of primary failure modes are discussed that must be overcome to achieve the full potential of intracortical microelectrodes for *in vivo* recording applications. Lastly, the impressive progress that has been made in recent years to develop the next generation of materials for intracortical microelectrodes is reviewed. By framing recent advancements within the context of current successes, the most promising strategies are highlighted and the most critical challenges for improving intracortical electrode-based neural interfaces are discussed.

1.1. TRADITIONAL INTRACORTICAL MICROELECTRODES FOR BRAIN MACHINE INTERFACING

A number of intracortical microelectrodes have been designed to interface with cortical neurons, including insulated metal microwires and semiconductor-based devices such as the Michigan and Utah electrode arrays, which are discussed in more detail below. Regardless of the specific design or manufacturer, a similar compound circuit can be used to describe how microelectrodes extract electrical signals generated from single target neurons. Extensive descriptions of each of the primary portions of the compound circuit are available elsewhere,^{17, 18} and therefore only a brief description will be included here.

The first portion of the circuit involves the complex set of presynaptic inputs that interact with the target neuron being recorded from. These inputs can be both excitatory and inhibitory. If a sufficient excitatory postsynaptic potential is created within the target neuron then a compound action potential is generated through depolarization of the axon hillock. The ion-based signal generated at the axon hillock then travels through the extracellular space to the electrode-recording site. As transport is primarily diffusion based, the strength of the ionic signal that reaches the recording site is governed by the overall distance traveled and the impedance of the extracellular space.

At the recording site, intracortical electrodes measure microvolt changes in neural activity (or action potentials), which reflect the above described changes in the flow of ions across the neuronal membrane.¹⁹ The electric potential produced by this ion-based neural activity is recorded by the electrode arrays as voltage change. Signals can be amplified and converted into an electrical current, which can be processed by signal acquisition and processing techniques.²⁰ Signal processing can be classified into three stages: 1) pre-processing, 2) feature extraction, and 3) detection and classification. First, the signals will be processed to remove the unwanted components (i.e. noise) and extract specific signal features by filtering or source separation. Then, once the signals are classified, an algorithm can be applied to translate the signal into device commands/orders that carry out the user's intent.²⁰⁻²² The output device can vary from application to application and have ranged from overt command or control functions such as moving a cursor on a computer screen, to a facilitating a robot to walk on a treadmill, driving a wheelchair, or controlling a robotic arm.²³

Figure 1-1 shows a commonly used equivalent circuit model (Robinson Model) of metal microelectrode recording in the brain.¹⁷ In particular, signals at the tip of the microelectrode (V_{sig}) generate currents (I) that flow to ground through the microelectrode and effective amplifier circuit, creating the potential (V_{in}) at the input of the amplifier before being recorded (V_{rec}); R_s is the resistance of the electrolyte; R_e is the leakage resistance which models the flow of the charge carriers crossing the electric double layer; C_e is the capacitance of the microelectrode-electrolyte interface; R_m is the resistance of the microelectrode; C_s is all the shunt capacitance to ground; and Z_a is the input impedance of the amplifier. Thus, the effective impedance of the microelectrode is comprised of the resistance of the electrolyte (R_s), the resistance and capacitance of the double layer interface of the electrolyte (R_e and C_e) and the (negligible) resistance of the microelectrode (R_m). The impedance of the microelectrode is frequency dependent. At low frequencies, the impedance is dominated by the series combination of R_s and R_e , whereas at high frequencies C_e bypasses the effect of R_e so that the impedance is now close to R_s . Thus, by measuring the impedance of an electrode at high and low

frequencies, it is possible to determine the component values for the equivalent circuit. It is worth noting that several physical properties of electrodes effect the electrical characteristics and thereby the electrode impedance.^{17, 18, 24}

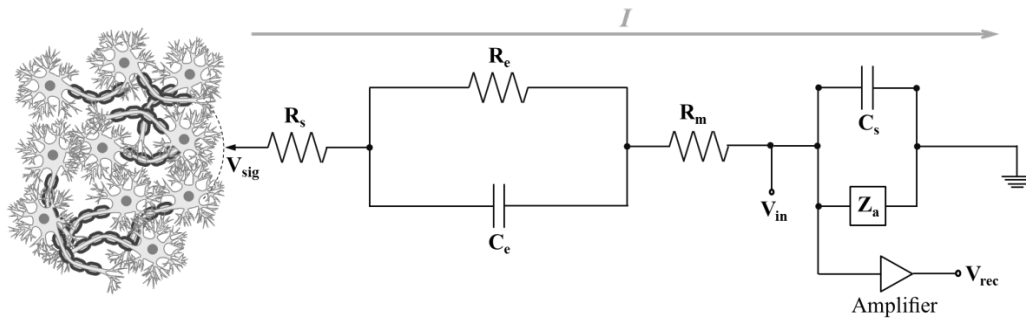


Figure 1-1. Electrical circuit model of intracortical microelectrode in the brain.

1.2. CHALLENGES TO OBTAINING CONSISTENT, HIGH-QUALITY NEURAL RECORDINGS

Despite substantial success that has been achieved using intracortical microelectrode in neural interface applications, many studies have shown chronic cortical recording to be inconsistent in a variety of species and with multiple electrode types. As early as 1974, Burns *et al.* showed a progressive decline in unit recordings in cat cerebral cortex after implantation, with only 8% of the electrodes functioning after 5 months.²⁵ Forty years later, recording instability is still a commonly documented problem. For example, Liu *et al.* reported that implanted electrodes have low recording stability during acute tissue remodeling, and thereafter experience a continual decrease in recording ability over the ensuing months.^{15, 16} Additionally, Ludwig *et al.* and Freire *et al.* have both described fluctuations in recording stability that agree well with previous findings.^{26, 27}

A number of failure modes likely influence chronic recording stability and quality including: 1) direct mechanical damage of the electrode; 2) corrosion of electrical contacts; 3) degradation of passivation layers and insulating coatings; and 4) the neuro-inflammatory response that the brain mounts against chronically implanted devices.^{13, 28}

Traditionally, microelectrode failure modes have largely been studied independently from one another. However, as recently suggested by Sanchez,²⁹ there is likely considerable interplay among the various failure modes making it difficult isolate a single mechanism of failure.

1.2.1. The Neuro-Inflammatory Response

There is increasing consensus that the neuro-inflammatory response to intracortical microelectrodes is a primary hurdle preventing applications in brain machine interface from reaching their full potential. Therefore, improving the understanding of the neuro-inflammatory response that develops following microelectrode implantation in the brain, and developing strategies to reduce its impact is critical to achieving the promise of brain machine interfaces and enable longer durations for basic science experiments.

Over 100 studies have described stereotypic features of the brain's response to microelectrodes that occur irrespective of the type of implant, method of sterilization, species studied, or implantation method. From this rich body of literature, it has become increasingly clear that the brain's response consists of an interconnected web of molecular and cellular components. The ultimate result of this interplay is the continuous perpetuation of response, and the prevention of microelectrode integration into the surrounding tissue. With respect to the molecular and cellular components, several theories have been presented that explain how individual components of the response might adversely impact recording quality. However, it is highly likely that multiple aspects of the response are at play simultaneously. Thus, further study into the details of the neuro-inflammatory response and the development of more comprehensive mitigation strategies are indicated.

1.3. MATERIAL STRATEGIES FOR IMPROVING MICROELECTRODE BIOCOMPATIBILITY AND RECORDING PERFORMANCE

In the last decade, various materials-based strategies have been investigated with the objective of minimizing the neuro-inflammatory response and enabling long-lasting

neural interfaces with high fidelity recording performance. In all cases, developers have sought to address one, or a set of limitations, of traditional intracortical microelectrodes. Throughout the following sections we will review the primary approaches to develop the next generation of intracortical microelectrodes including:

- Minimizing motion-induced trauma using compliant microelectrode substrates
- Limiting surgical trauma and/or inflammatory cell accumulation by manipulating microelectrode architecture
- Preventing protein and inflammatory cell adhesion through non-fouling surface coatings
- Manipulating inflammatory cell phenotype through use of surface topography
- Directing wound healing and tissue integration at the microelectrode-tissue interface using bioactive materials
- Reducing the concentration or impact of inflammatory soluble factors through the use of passive and active antagonists
- Improving the chronic performance of intracortical microelectrodes using conducting polymers or nanomaterials

The following sections discuss the progression of each of the primary materials-based approaches to improve intracortical microelectrode performance. Each subsection is concluded with our interpretation on the strengths/limitations and questions that must be addressed to enable consistent, high-quality long-term neural recordings.

There are a number of important facts to consider when comparing and analyzing the impact of material-based approaches for improving microelectrode function. First, isolating the impact of a given strategy to one variable that could influence the neuro-inflammatory response is difficult at best. For example, as will be discussed in Section 1.3.1, a major strategy in the field for reducing the neuro-inflammatory response is the creation of compliant, polymer-based microelectrodes that better match the mechanical properties of the surrounding tissue. It is believed that the improved mechanical matching between the implant and the surrounding tissue will limit repetitive, micromotion-induced damage at the biotic/abiotic interface. However, many of the polymers used to

create compliant microelectrodes absorb a significant degree of water and are likely permeable to small molecules, adding the possibility that the findings in these studies have been influenced by improved clearance of macrophage secreted factors. Conversely, as will be discussed in Section 1.3.2, strategies that aim to reduce the neuro-inflammatory response by manipulating microelectrode architecture also unavoidably alter underlying mechanical properties such as microelectrode compliance. Therefore, further studies should be conducted to isolate the impact of individual design variables as well as possible interactions or emergent phenomena to elucidate the overall design space available for microelectrode designers.

Equally as important when analyzing findings from studies that have examined new strategies for reducing the neuro-inflammatory response, one must critically assess the role that tissue processing and other employed techniques may have on reported results. For example, in almost all cases the implanted microelectrodes are removed from tissue prior to analysis. Microelectrode removal may disrupt the tissue interface by removing adherent tissue and may influence data interpretation,³⁰⁻³³ especially for coatings that improve cell attachment. Different groups also use a variety of markers to describe the same cellular and molecular features of the neuro-inflammatory response. An example of this is the use of pan-macrophage markers such as OX-42 and IBA-1 vs. markers for macrophage activation such as CD-68. There are also large to subtle differences in the methods used to image and quantify tissue that can lead to differences in interpretation. Common differences include the use of confocal vs. traditional microscopy as well as a large variety of boutique software packages. Therefore, efforts to improve consistency across studies and groups could be quite useful for improving comparisons between studies.

1.3.1. Mechanically Compliant Intracortical Microelectrodes

As discussed above, traditionally, microelectrodes have been composed of metals, silicon and/or ceramics. These materials have high stiffness (high modulus) relative to brain tissue. While the high stiffness has enabled current microelectrode geometries the ease of

implantation into the cortical tissue,³⁴ the Young's modulus difference between brain tissue (3-13 kPa)³⁵ and typical electrode materials (~200 GPa) is believed to result in strain on the surrounding brain tissue.^{36, 37} Therefore, mechanically-compliant intracortical microelectrodes, which have a mechanical behaviour that more closely matches that of the brain tissue, offer exciting alternatives for intracortical microelectrode technology over the traditional stiffer devices. This is perhaps most readily accomplished with polymeric materials which permit access to a Young's modulus range that stretches from ones of kPa (in the case of hydrogels) to the tens of GPa (in the case of naturally oriented fibers) regime. Initial approaches to relieve microelectrode-associated tissue strain relied on the implementation of “softer” materials in the development of mechanically compliant microelectrode. As discussed below, the selection of “off-the-shelf” polymers with a reduced modulus allowed researchers to begin to investigate the role of tissue strain in microelectrode performance. However, the use of “softer” materials introduced additional hurdles, and interesting potential solutions. One important challenge of compliant materials is associated with the required physical characteristics. In particular, sufficient mechanical strength and toughness are needed for handling and each of the devices. “Softer” penetrating microelectrode must also be sufficiently strong and stiff to enable insertion into the brain without buckling,^{38, 39} and to permit eventual removal. Therefore, it is important to understand the basic mechanic characteristics of the neural interfacing devices and the neural tissue. A comprehensive discussion of the governing equations which drive microelectrodes mechanics is out of the scope of this review. However, the following section provides the essential aspects of the mechanical requirements for intracortical microelectrodes.

1.3.1.1. Introduction to Microelectrodes Mechanics

Intracortical microelectrodes experience different forces during penetration through the brain tissue. The three relevant forces acting on the electrode shank (see Figure 1-2) are: 1) the tip force (*TF*), i.e., the reaction acting on the tip in the axial direction during penetration, whose value depends on the shape and dimension of the tip; 2) the friction

force (FF), which is exerted on the side walls of the electrode in the axial direction and can be determined by the normal force acting on the surface and the coefficient of friction; and 3) the clamping force (CF), which is exerted by the compressed tissue on the electrode's walls – CF increases as the electrode penetrates deeper due to the continual increase in contact area.⁴⁰

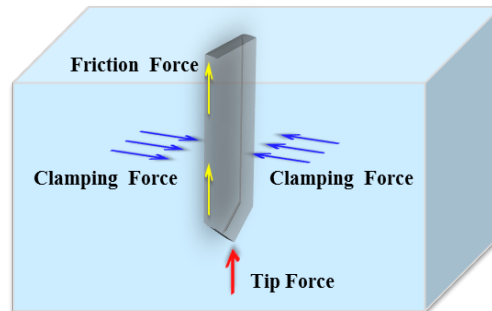


Figure 1-2. Forces acting on the intracortical microelectrodes upon penetration.

The microelectrode insertion force (IF) is equal to the total axial force acting on the probe during penetration ($IF = TF + FF + CF$). The maximum IF during microelectrode insertion for a rigid metal electrode into the rat brain was reported to be 500-1000 μN , depending on the electrode shapes, tip angle and dimensions.^{41, 42} In order to allow intracortical microelectrode insertion into the brain tissue without buckling of the implant, the IF must be lower than the critical loading force for a given electrode. Therefore, this range of insertion forces can serve as a reference for the buckling forces any new microelectrode design must overcome for successful insertion. Given similar dimensions as a planar silicon or microwire microelectrode, “softer” polymer-derived microelectrodes should exceed a force of 1000 μN for successful insertion into cortical brain tissue.⁴³⁻⁴⁶

In order to quantitatively determine the strength of intracortical probes, at least two parameters have to be measured: the maximum load (force) required to buckle the probe shank, which determines the stiffness of the probe, and the maximum fracture stress, which determines the strength of the shank after it buckles. These two parameters can be

calculated from the following two equations:

$$F_{Cr} = \frac{2EI\pi^2}{L^2} \quad (1 - 1)$$

$$\sigma_{max} = \frac{6Ehu}{L^2} \quad (1 - 2)$$

Equation (1-1) express the buckling load, F_{Cr} , and is derived using mechanical Euler theory of columns. The Euler theory defines E as the Young's modulus, I as the area moment of inertia, and L as the length of the column.⁴⁷ Equation (1-2) defines the fracture stress of the shank, where h is the shank thickness, u is the maximum amount of lateral deflection of the buckled shank, and both E and L are consistent with the Euler's equation.

Several studies have characterized both the properties of the brain tissue surrounding an implanted microelectrode, and the forces required to insert or extract the devices.⁴⁸ The known mechanical interactions between the microelectrode and the brain tissue have been used to identify and quantify the primary mechanical requirements for microelectrodes insertion.⁴⁹ Future studies may also utilize this information to evaluate the efficacy of design strategies intended to modify the material properties or geometry of novel microelectrodes. Effective microelectrode design must be concerned with a trade-off between the conflicting requirements of proper materials to minimize the tissue damage and chronic strain on the tissue, as well as potential buckling and damage to the microelectrode itself.

1.3.1.2. Compliant Polymeric Materials for Intracortical Microelectrodes

Several research groups have attempted to investigate the effects of mechanical mismatch between the microelectrodes and the cortical tissue. Many groups have developed microelectrode substrates and substrate coatings from materials such as poly(imides), benzocyclobutene (BCB), SU-8, polydimethylsiloxane (PDMS), and Parylene-C (Figure

1-3) that are more compliant than materials traditionally used to create electrodes.⁵⁰⁻⁵⁷ For example, Rousche *et al.* reported the fabrication of poly(imide)-based multichannel implantable intracortical electrodes and recorded the neural activity from the cortex of rat's brain.⁵⁸ Polyimide presents several attractive features such as inherent flexibility, and manufacturability using existing microfabrication technology. However, due to its low stiffness (in comparison to metal- or silicon-based microelectrodes), polyimide-based electrodes of typical dimensions cannot penetrate through the tissue during surgery (i.e., $IF > F_{Cr}$), resulting in device buckling. Another problem in the use of polyimide for neuroprosthetic devices is the high moisture uptake (4-6% w/w), which can lead to a rapid decrease of the electrode impedance after implantation.

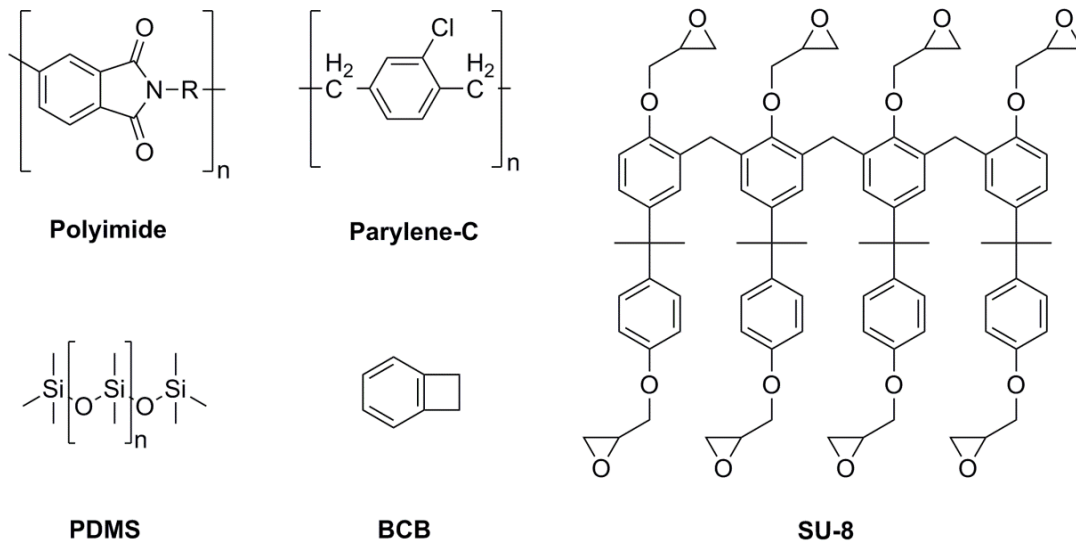


Figure 1-3. Chemical structures of compliant polymeric materials and monomers commonly used for neural interfaces.

To address some of the challenges associated with the use of polyimides, Lee *et al.* reported a new design for polyimide-based intracortical microelectrodes, which provide adequate stiffness for insertion into neural tissue.^{59, 60} In their design, a 5-10 μm thick silicon layer was applied to the polymer to increase the composite stiffness to prevent buckling during insertion. The Young's modulus of these electrodes increased

significantly from 2.8 GPa (neat polyimide without silicon backbone) to 31 GPa and 58 GPa with 5 and 10 μm thick silicon layers, respectively. A penetration test into rat brains showed that the electrodes with silicon backbone layers could penetrate the rat pia without buckling. *In vitro* biocompatibility tests revealed no cytotoxic effects on cultured cells and supported cell adhesion and growth over the polyimide electrode surface. However, one of the initial goals for the design of polyimide-based microelectrodes was to facilitate a “softer” implant after insertion. The intent was to minimize strain field generations within the surrounding “soft” brain tissue. The use of a “stiff” silicon backing to increase the polyimide devices from 2.8 GPa to 31 or 58 GPa (defined above) prevents buckling failure during insertion, yet appears counterproductive towards minimizing chronic *in vivo* tissue strain.

Alternative work on flexible polymer-based intracortical electrodes included the use of benzocyclobutene (BCB)-based polymers as a template for chronic neural applications.⁶¹⁻⁶³ BCB polymers offer a lower moisture uptake (0.2% w/w) than polyimide (4-6% w/w), good chemical resistance, and also a low dielectric constant (~ 2.6). BCB polymers display a stiffness which is comparable to that of polyimides, and therefore buckling during insertion is also an issue for this type of polymer. Thus, reinforcing strategies have been developed to increase the stiffness of BCB-based neural interfaces to enable insertion into neural tissue. For example, Lee *et al.* micro-machined a thin layer of silicon backing (5-10 μm) onto the electrode.^{63, 64} Clement *et al.*⁶² succeeded in recording neural signals in a rat cortex using BCB-based electrodes without the problem of water uptake that occurs with polyimide-based electrodes as mentioned above. However, the silicon-backed BCB microelectrode possesses similar concerns for increase tissue strain described above for polyimide-based devices. Either tissue strain does not directly impact recording quality, or the reported study was not carried out long enough to realize the strain-induced detriments to the neuroinflammatory response. To this end, an alternative approach is the use of dissolvable materials such as glucose or sugar.⁶⁵ Therefore, BCB-based electrodes may have the potential for further development of long-term compliant neural implants.

Parylene-C is another compliant polymer with low water absorption and low dielectric constant. While both polyimide and parylene have comparable elastic moduli, Parylene-C has several advantages such as easy fabrication, and lower water absorption than polyimide. However, it has a low tensile strength, and is also suffering from buckling during insertion.⁴⁶ Nevertheless, several studies have reported the development of Parylene-C based microelectrodes that can be inserted into the brain tissue without assistive aids. For example, the LaPlaca lab fabricated flexible Parylene-C based electrodes using photolithography techniques that were inserted into the rat barrel cortex.⁴⁶ LaPlaca was interested in determining the extent and duration that a controlled cortical impact and device micromotion effects on both the integrity of the microelectrode, and the ability to obtain neural recordings. To facilitate insertion of the “flexible” Parylene-C devices, implants were designed larger, at 100 μm wide and 25 μm thick. LaPlaca and colleagues demonstrated that the “flexible” devices withstood the trauma and associated micromotion, and remained capable of obtaining neural recordings minutes after impact, suggesting future applicability of such devices. While promising, the histological effects of the larger implant size may negatively affect chronic recording abilities. In an attempt to better understand how modifications to traditional microelectrode geometries could facilitate insertion of flexible polymer microelectrodes, Egert *et al.* engineered parylene-based microelectrodes with a variety of shank footprints.⁴⁴ In their brief conference proceedings, the team reported on the application of the addition of vertical stiffeners, alternative geometries, and insertion guides designed to remain attached throughout the life of the implant or be removed either directly after implantation or slowly through bio-degradation. Each of the novel devices tested remained electrically active after 3 months of a soak test. Unfortunately, design strategies that facilitate insertion and were capable of integration into array technology required permanent features that either increased the stiffness or footprint, both which have been linked to increased neuroinflammatory responses. Therefore, while Parylene-C microelectrodes have been developed for acute *in vivo* and chronic cell-free recording, long-term reliability of “flexible” non-reinforced devices has to our knowledge yet to be

achieved. The cross-linked epoxy resin SU-8 is another flexible polymer that has been investigated widely as alternative substrate to silicon-based microelectrodes. In comparison to polyimide, BCB-based substrates and Parylene-C, SU-8 offers several advantages. The most prominent advantages of SU-8 include: 1) the possibility of easily adjusting the probe thickness to overcome the buckling issues associated with flexible polymers, 2) high aspect-ratio lithography capability, 3) suitable dielectric properties, 4) thermochemical stability, 5) low-cost photolithographic processability, and 6) suitable for microfluidic applications.^{66, 67} Fully cross-linked SU-8 has a glass transition temperature of around ~200 °C, a degradation temperature of ~380 °C and a Young's modulus of ~4-5 GPa.⁶⁶ In a series of contributions, Fernández and colleagues developed different SU-8-based microelectrodes for neural applications using photolithography techniques (see Figure 1-4).⁶⁷⁻⁷¹ Impedance spectroscopy studies showed that the electric behavior of these SU-8-based microelectrodes was very similar to that of silicon (Si) and silicon carbide (SiC)-based microelectrodes.⁶⁹ Altuna *et al.* fabricated SU-8-based multisite microelectrodes with multiple fluidic channels (Figure 1-4c) and studied their electrical recording and drug delivery ability in the brain.⁷¹ Drug delivery was achieved in quantities in the range of tens of nanoliters to a few microliters at the CA1 cellular layer in order to stimulate neuronal firing. *In vivo* rat studies showed that the SU-8-based microelectrodes were able to record from identifiable isolated neurons together with multi-unit firing and local field potentials similar to conventional silicon-based microelectrodes.

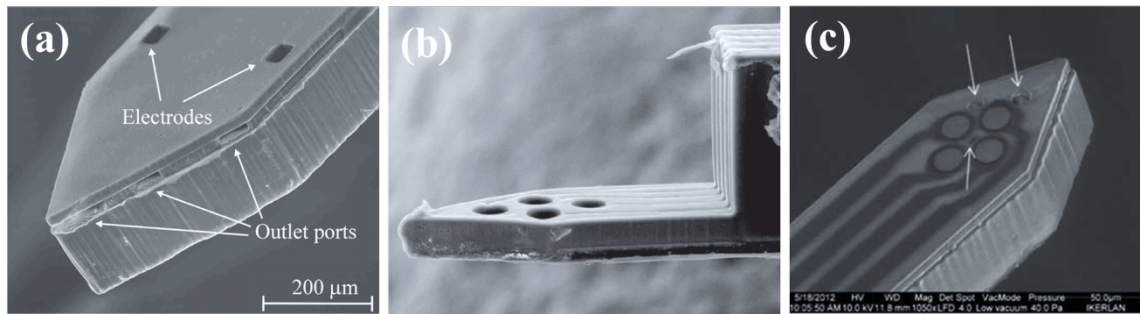


Figure 1-4. SEM pictures of microelectrode tips of SU-8-based electrodes. Figure (a) reprinted with permission from Ref. ⁶⁸, copyright © 2009 IOPScience, Figure (b) reprinted with permission from Ref. ⁷⁰, copyright © 2010 IOPScience, and Figure (c) reprinted with permission from Ref. ⁷¹, copyright © 2013 Royal Society of Chemistry.

Despite the advantages of SU-8, the toxicity of this polymer limits its use in neural applications. The first characterization of SU-8 cytotoxicity to neuronal culture was reported by Vernekar *et al.* in 2008.⁷² Vernekar showed that thick untreated SU-8 substrates are not compatible with primary neuronal culture.⁷² It was found that less than 10% of primary neurons survived when cultured to or on top of a SU-8 substrate. The authors suggested that the poor cytocompatibility of SU-8 is due to leaching of toxic components such as residual solvents and (fragments of) the photo acid generator used for the polymer, as well as poorly sustained neural adhesion. Additionally, it was found that post-processing strategies play a key role on the cytocompatibility of SU-8 *in vitro* cell culture. For example, Vernekar *et al.* improved the neuronal cell viability to 45.8% and 86.4% following 3-day heat treatment (150 °C) under vacuum, and sonication (in isopropanol) of the SU-8 substrates, respectively. Since neuronal loss is well documented following the inflammatory response to implanted microelectrodes that do not demonstrate poor cytocompatibility, the benefits associated with SU-8 device fabrication may not outweigh the cytotoxic handicaps associated with current SU-8 derived microelectrodes. Due to the biocompatibility of poly(dimethylsiloxane) PDMS for many device applications, several groups have also explored the suitability of PDMS as flexible material for intracortical interfacing applications. For example, in an *in silico* model, Subbaroyan and Kipke examined the strain effect induced by an intracortical

microelectrode using a flexible PDMS interconnect.⁵¹ A PDMS interconnect ($E' = 6$ MPa) resulted in two orders of magnitude smaller strain compare to commercial silicon ($E' = 200$ GPa). The results suggest that reducing interconnect stiffness could reduce interfacial strain and eventually may reduce the shear induce damages around the implant. However, quantitative immunohistochemistry showed significant neuronal loss up to 60 μm from the implant interface. In another study, Guo and DeWeerth used multilayer wiring interconnect technology to implement PDMS-based conformable microelectrode arrays.⁷³ In our own experience (unpublished), PDMS can also suffer from poor cytotoxicity, presumably due to leaching components. Similar results have been noted offline, and have dampened some of the initial enthusiasm for penetrating PDMS-based microelectrode devices. Despite the mixed results for the applicability of PDMS-based microelectrode technologies, if the difficulties associated with implanting “softer” microelectrodes are overcome, the breadth of knowledge in both microfabrication and the neuroinflammatory response to peripheral nervous system neural interfaces may propel PDMS to the forefront of materials selections for compliant intracortical microelectrodes.

In summary, intracortical microelectrodes derived from polymeric substrates with a Young’s modulus of less than 3-5 GPa have had limited success in attenuating glial scar formation or improving neural recordings. One drawback of most of these materials is that their Young’s modulus is still 6 orders of magnitude larger than that of the brain.^{52, 53, 64, 74, 75} Additionally, the slight decrease in the stiffness of these polymeric devices results in a critical buckling load that is smaller than the insertion forces, presenting difficulties in implanting the microelectrodes.^{52, 76-78} While insertion aides and shuttles have been explored, none have been identified that facilitates insertion without increasing the device footprint or stiffness.

1.3.1.3. Insertion Aides and Biodegradable Materials

As mentioned above, a key limitation of compliant polymer-based intracortical microelectrodes is their limited stiffness. It is important to note that a high-level of

compliance that is well suited for *in vivo* applications can also be fabricated from a thinner film of stiff materials or lattice structures.⁷⁹⁻⁸¹ Nanomaterials and open architecture structures fall into this category, and will be addressed separately below in sections 4.8. In the case compliant polymeric microelectrodes, low material stiffness yields a low buckling force. Without increasing the cross-sectional area, it can become difficult to insert compliant polymer-based intracortical microelectrodes into the brain without damaging excess tissue or the microelectrode.³⁸ Thus, methods and strategies have been developed to facilitate the implantation of “compliant” intracortical microelectrodes. Such methods include coating the microelectrode with biodegradable polymers,⁸²⁻⁸⁵ hydrogels,⁸⁶⁻⁸⁸ and gelatine,⁸⁹ using a removable insertion shuttle to carry the polymer microelectrode into the cerebral cortex,⁹⁰ or stiffening the microelectrode by incorporating a thin silicon backing.^{59, 60, 63, 64, 91, 92} In this section a few of the many examples of insertion aides for complaint microelectrodes based on “soft” polymers are discussed.

As an alternative to the silicon-backed compliant polymer systems discussed above, Takeuchi *et al.* incorporated a microfluidic channel into a compliant Parylene-C based microelectrode.⁵² Takeuchi filled the channel with a reinforcing material designed to dissolve after implantation. In a first proof of concept study, the channel was filled with biocompatible poly(ethylene glycol) (PEG) to stiffen the compliant microelectrode for insertion into the rat’s brain. PEG is solid at room temperature, but dissolves when in contact with tissue. The authors were able to successfully record neural signals from the rat’s brain through the microelectrodes. In this early work, Takeuchi *et al.* developed a clever alternative to silicon-back reinforcements that only temporarily increased the device stiffness, yet permanently increased the device footprint.

More recently, and perhaps inspired by Takeuchi’s dissolvable system, several groups began investigating the use of biodegradable polymers as a shuttle for compliant devices.^{243, 251, 252} Rapidly degrading polymers could be used as templates for neural electrodes if their incorporation increases the bucking force beyond the required insertion force, yet the stiffer degradable material quickly decomposes upon insertion, leaving

behind a small compliant device. The appropriate biodegradable polymer should have the following criteria: (i) sufficient stiffness for insertion, (ii) faster degradation rate than the time frame of chronic inflammation, and degradation and formation of non-toxic products.⁹³

Perhaps one of the most promising examples of neural interfaces with degradable polymers has been explored by Shain and Kohn. In a series of investigations, Kohn and colleagues studied several different tyrosine-based polycarbonates as biodegradable carriers for intracortical microelectrodes with the objective to identify a material with the most suitable property.^{84, 93, 95} The tyrosine-derived polymers have attracted great interest in the context of soft neural interfaces due to their biocompatibility, biodegradability, and neutral pH of the hydrolysis products. A set of tyrosine-derived terpolymers was reported, in which the composition of the monomer constituents was varied (ethylene oxide; desaminotyrosyl-tyrosine; desaminotyrosyl-tyrosine alkyl ethyl ester), with the objective to tune the mechanical and thermal properties, as well as the degradation rate. Polymers with appropriate composition had a sufficient stiffness (Young's modulus of ~393 MPa) in the dry state to facilitate implant insertion. Despite the relatively low modulus, Kohn's materials possess an intrinsic strength of ~ 4 MPa (critical strength for insertion into cortical tissue is reported to be 0.3-1.3 MPa depending on the size and insertion speed of the microelectrode). Tyrosine-derived terpolymers become soft (modulus of ~85 MPa) within 30 minutes when immersed in artificial cerebrospinal fluid (ACSF).⁹³ Interestingly, uncoated Kapton film is too flexible to implant into cortical brain tissue, while the tyrosine-coated Kapton film is able to penetrate the rat cortex. Additionally, by altering the degradation rates of the same tyrosine-based polymer, Lewitus *et al.*⁸⁴ found that a rapid degrading and resorbing tyrosine-derived polymer significantly reduced the glial response at the implant site, while the slow resorbing implant resulted in continuous glia activation. The *in vivo* tissue response to the new tyrosine-based implants was compared to that of poly(lactic-*co*-glycolic acid) (PLGA)-made implants as a commercially available and commonly used rapidly degrading polymer. It was found that the fate of surrounding neural tissue depended on the rate of

microelectrode resorption, more so than the rate of degradation. For example, at one and four weeks post implantation the fast resorbing and degrading tyrosine-derived terpolymers displayed the most rapid and efficient tissue recovery. Alternatively, the ultrafast degrading but slow resorbing did not show any difference in tissue response compared to the slow degrading and slow resorbing polymer (i.e. PLGA) Additionally, immunohistochemistry evaluation of tyrosine-derived polymers showed minimal cytotoxicity and tissue inflammation over the course of 12 week test period in a rabbit calvaria model.⁹⁴ Therefore, the authors of the study concluded that this class of biodegradable polymers offers a high potential for future design of long-term neural interfacing devices.

In summary, several innovative approaches have been investigated to achieve temporary stiffening of soft polymer-based microelectrodes. Although, some of these approaches have been shown to be useful for insertion of single-shank electrodes, challenges still exist if they are to be applied to multi-shank electrodes. Therefore, current strategies must be refined, or new ones must be continually pursued. Parallel to the idea that it is difficult to determine one absolute mechanism for microelectrode failure, it is also unlikely that one device will serve the needs of the entire community. Therefore, insertion aided implants may provide promise to individual laboratories.

1.3.1.4. In Situ Softening Materials

An alternative approach to insertion aides and biodegradable materials is the use of *in situ* softening materials. Materials that can respond to external stimuli – referred as “stimuli-responsive” or “smart” materials – are being considered for a broad range of biomedical applications, including the delivery of therapeutic molecules, as actuators, in tissue engineering and in the context of regenerative medicine.⁹⁶⁻¹⁰¹ Recently, the idea to utilize physiologically responsive mechanically adaptive materials as substrates for intracortical microelectrodes has been proposed, with the objective to improve microelectrode biocompatibility by minimizing the microelectrode-induced mechanical strain on the surrounding tissue.^{102, 103} “Smart” softening neural interfaces are defined as sufficiently

stiff to be easily implanted into the brain, yet soft *in vivo* to better match the stiffness of the cortical tissue.

The first realization of “smart” intracortical microelectrode materials was reported by Weder, Rowan, Capadona *et al.* in 2008.¹⁰⁴ The team utilized the architecture of the sea cucumber dermis as their initial blueprint to develop a new class of biologically-inspired, stimuli-responsive, mechanically adaptive polymer nanocomposites whose mechanical properties can be switched between stiff and soft states (Figure 1-5).¹⁰⁴

NATURAL MODEL: SEA CUCUMBER DERMIS



BIOMIMETIC DESIGN: ADAPTIVE NANOCOMPOSITES

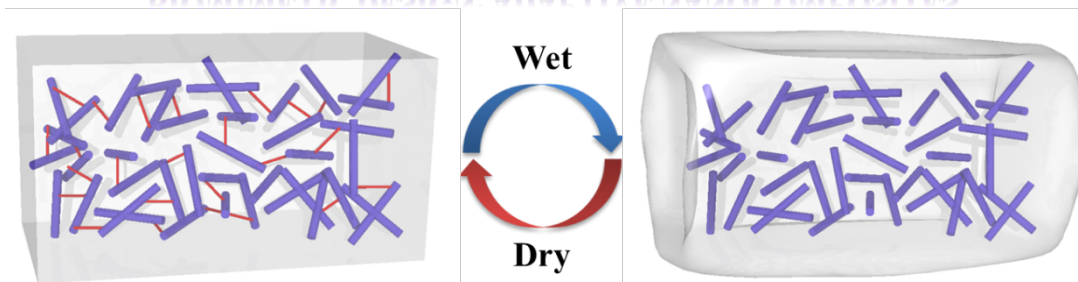


Figure 1-5. Top: Pictures of a sea cucumber, in the threatened (stiff) and relaxed (soft) state. Bottom: Simplified schematic representation of the switching mechanism found in the sea cucumber dermis and used in physiologically responsive mechanically adaptive nanocomposites. A soft matrix is reinforced with rigid particles, whose interactions in are moderated by a chemical agent.

The generation of mechanically adaptive nanocomposites currently under evaluation for intracortical microelectrodes was designed based on glassy poly(vinyl acetate) (PVAc) matrix and rigid cellulose nanocrystals (CNCs) isolated from tunicates as reinforcing

filler.^{105, 106} These mechanically adaptive nanocomposites display a dual responsive behaviour. When dry, these nanocomposites are in the rigid state, because the matrix is glassy and the CNCs have a percolating rigid network, in which stress is effectively transferred. Attractive interactions among the CNCs are likely dominated by hydrogen bonds among the abundant hydroxyl groups of the CNC surface, but van der Waals' interactions may also contribute. Upon exposure to physiological conditions, the materials swell with the aqueous fluid and undergo a phase transition, water plasticized the matrix and lowers the glass transition temperature; in addition, the CNC network is disassembled on account of comprehensive hydrogen bonding with water molecules. PVAc nanocomposites with 16.5% v/v CNCs exhibited a mechanical contrast of three orders of magnitude upon exposure to physiological conditions and upon implantation into cortical tissue ($E' = 5.1$ GPa for a dry/pre-insertion and 12 MPa for artificial cerebrospinal fluid (ACSF)-swollen nanocomposite).^{38, 104, 105} It was shown that dry implants of this nanocomposite can readily be inserted through the *pia mater* into the cerebral cortex of a rat without the need for assistive devices. The insertion of the chronically compliant materials was a significant feat as reference implants consisting of the neat matrix polymer (PVAc) buckled under lower loads before they could be inserted into the cortical tissue.³⁸ *Ex vivo* studies confirmed that the initially stiff microscale nanocomposites rapidly softened when implanted into the rodent brain. Figure 1-6 shows the stiffness of a 12.2% v/v PVAc/CNC nanocomposite upon introduction into ACSF at 22 °C (Young's modulus ~3400 MPa), and reveals that the softening occurs over the period of 15 min to reach a Young's modulus of ~33 MPa. A comparison between the Young's modulus of microprobes that had either been implanted in a living rat cortex showed no statistical difference immersed for 15 min in ACSF (Figure 1-6).^{38, 49}

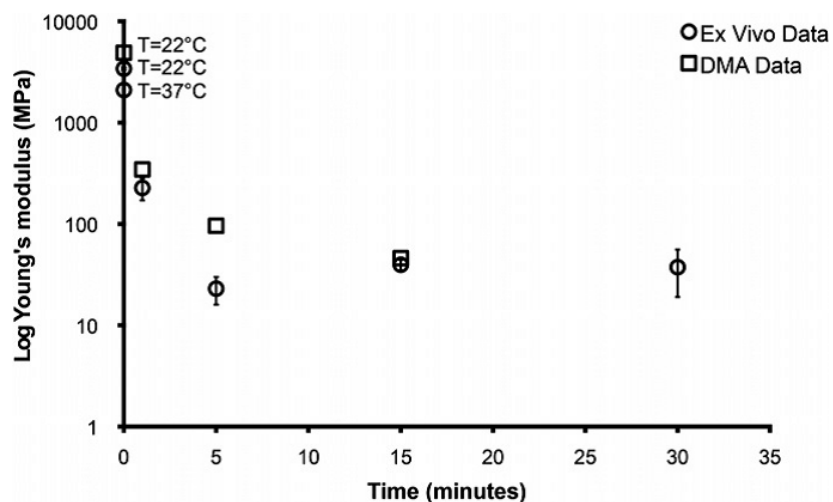


Figure 1-6. Plot showing the log of the Young's modulus of mechanically adaptive PVAc/CNC nanocomposites as function of exposure time to ACSF or implantation time in the rat cortex. Data were acquired by either a dynamic mechanical analysis (DMA Data, open squares; bulk materials) using a submersion clamp and exposing the sample to ACSF preheated to 37 °C or mechanical tests of microprobes that had been implanted into the rat cortex for the time indicated and which were explanted for microtensile testing (*Ex vivo* Data, open circles). The x-axis indicates the time of exposure to either ACSF or implanted in the rat cortex, respectively. Reprinted with permission from Ref. ³⁸. Copyright © 2011 IOP Publishing.

In preliminary investigations, Hess *et al.*^{107, 108} showed that laser micromachining followed by deposition of Parylene-C insulating layer, sputtering and patterning Ti/Au electrodes, and deposition and of Parylene-C layer is a suitable process for fabricate micro-scale multi-layered structure electrodes from the biologically-inspired nanocomposites. When patterned with titanium/gold, the nanocomposite-derived microelectrodes exhibited an impedance ($95.0 \pm 4.8 \text{ k}\Omega$) that is comparable to that of Au electrodes (130 k Ω) on conventional substrates. Since the electrodes and insulation layers were thin in comparison to the nanocomposites substrate, the electrodes retained the dynamic mechanical properties. Swelling of the devices was highly anisotropic and much more pronounced in the direction orthogonal to the device, so that delamination did not pose a problem, at least in the laboratory conditions. While the significant swelling of the initially employed materials (70-90 % w/w for PVAc reinforced with 10.5% v/v CNCs

isolated from tunicates), this effect could be substantially lowered (~28% w/w swelling) by substitution the filler with CNCs isolated from cotton, which are less hydrophilic (Figure 1-7).¹⁰⁹

The first *in vivo* evaluation of the neuro-inflammatory response to mechanically adaptable PVAc/CNC nanocomposites as substrate for penetrating microelectrodes was reported by Harris *et al.*³⁹ Initial histological evaluations of these materials demonstrated that at four weeks post-implantation, compliant implants more rapidly stabilize neural cell populations within 200 μm of the implant than rigid, non-dynamic systems.³⁹ However, no significant difference between the mechanically-dynamic and the much stiffer control implants with respect to local neuron density was observed at 8 weeks. Thus, the results of Harris's initial studies can be interpreted that, despite acute benefits after 4 weeks, the mechanical mismatch between microelectrodes and cortical tissue has appears to have little effect on the chronic neuro-inflammatory response. However, recent findings by Potter *et al.* demonstrate that the neuro-inflammatory response to intracortical microelectrodes is multi-phasic, and that a drop in neuronal density is observed at 16 weeks with stiff electrodes.¹¹⁰ Therefore, it will be important to also study the response to the mechanically-dynamic, compliant materials after at least 16 weeks of implantation.

More recently, Nguyen *et al.* have completed a more comprehensive histological evaluation of the neuroinflammatory response to PVAc/CNC nanocomposites implants. At 16 weeks post-implantation, Nguyen demonstrated the near complete attenuation of microglia activation and the absence of any appreciable neuron loss surrounding PVAc/CNC nanocomposites implants, compared to chemically-matched PVAc-coated Michigan-type microelectrodes (Figure 1-8).¹¹¹

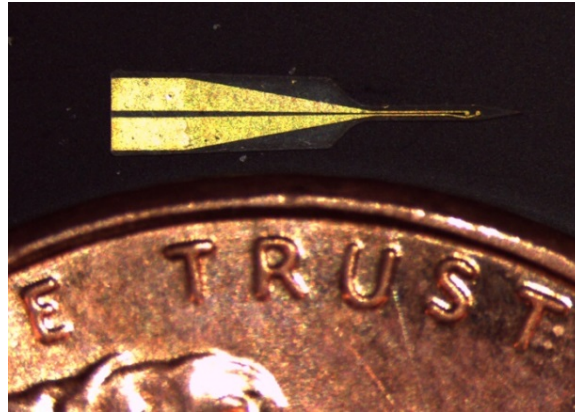


Figure 1-7. Photograph of a 2-electrode contact intracortical probe. The connection contact pads are at the larger end on the left, and the electrode contacts are near the tip of the shank on the right. Only the shank is intended to be inserted into tissue, as the connector end is only for making electrical connection to external electronics. For size comparison, the probe is sitting next to a United States penny. By layer, the structure of the probe is a 50 μm -thick PVAc/CNC film on the bottom (substrate layer), then a 1 μm -thick Parylene C layer to insulate the electrodes from moisture absorbed by the PVAc, then a 250 nm-thick sputtered gold conducting film on a 50 nm-thick titanium adhesion layer, and finally a second 1 μm -thick Parylene C film to insulate the gold traces from the biological environment. The shank is 2 mm long and 230 μm -wide. Each electrode contact is 30 μm in diameter. Copyright: Allison Hess, Case Western Reserve University, United States.

Interestingly, at earlier time points, few statistically significant differences we visualized between chemically-match compliant and stiff PVAc implants. Nguyen's results demonstrate that the mechanical strain placed on cortical tissue by stiffer implants played a lesser role early after implantation than at more chronic time points. Our interpretation of these results is that subtle changes in the maturation of the glia cell populations around compliant versus stiff implants are initially dominated by wound healing. However, once the scar matures, it is more likely that differences in scar mechanics translates to differences in neuronal survival. Experiments to test this hypothesis are currently underway in collaboration between the Capadona and Muthswamy Laboratories.

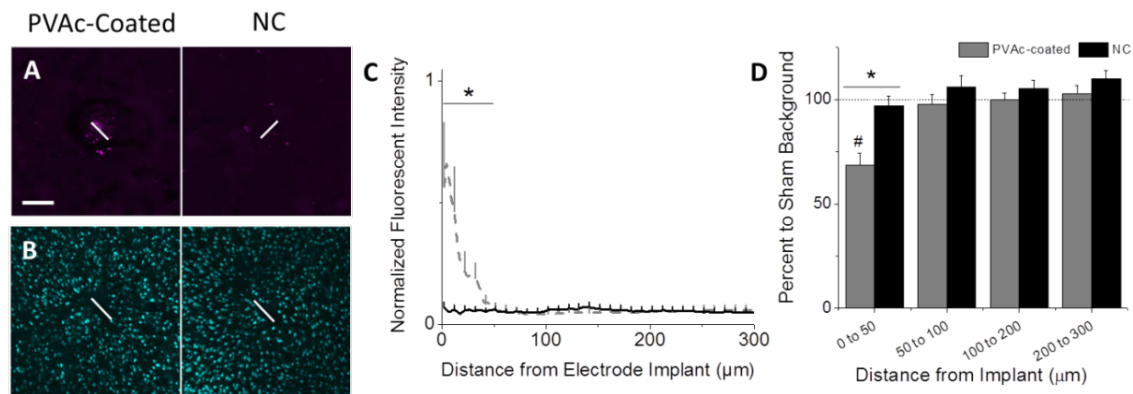


Figure 1-8. PVAc/CNC nanocomposite implants (NC) reduce chronic neuroinflammation. IHC staining of CD68 for activated microglia showed increased expression surrounding PVAc-coated silicon control implants (PVAc-coated) compared to NC (A, C). Accordingly, staining of neuronal nuclei (NeuN) (B) and quantification of neuron counts indicated significant improvement in neuronal populations surrounding the NC implants from 0 to 50 μm as well (D). Scale bar = 100 μm . * $p < 0.05$ Reprinted from Ref. ¹¹¹.

Softening intracortical implants have also been made from shape memory polymers (SMPs).^{92, 112} Shape memory polymers can both change their mechanical properties and also have the ability to recover from a programmed temporary shape. The original shape is regained upon application of external stimulus, such as temperature, humidity, light or a combination of these stimuli.^{113, 114} Sharp *et al.*⁹² developed SMP-based microelectrodes in an attempt to decrease initial tissue damage resulting from electrode implantation and enhance long-term biocompatibility. A micro-casting method was used to fabricate intracortical microelectrodes from an epoxy-based shape memory polymer (Figure 1-9). Pre-deformation was achieved by stretching the SMP horizontally on a hot/cold stage. Sharp *et al.* concluded that it is feasible to fabricate SMP electrodes that would self-implant at controlled rate, although this was not yet demonstrated. Histological analysis of implants that were inserted in the cortex of rats only investigated the role of reactive astrocytes, at one week post-implantations. Therefore, conclusions on the effects of implantation rate on initial damage or long-term biocompatibility will require additional time points and histological markers.

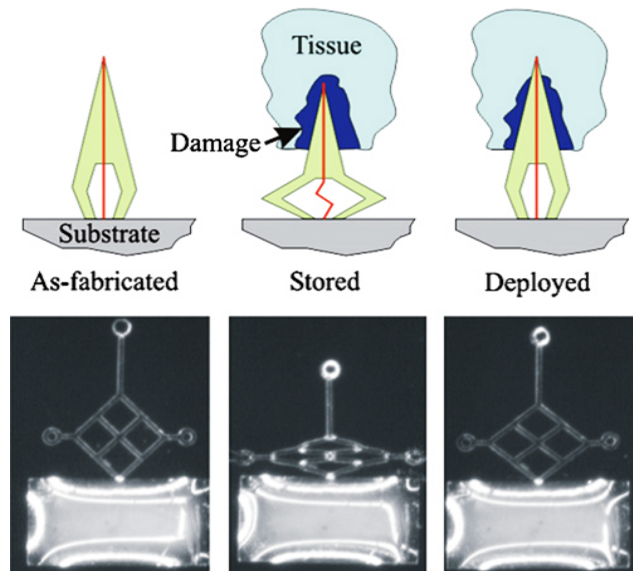


Figure 1-9. Schematic (top) and light micrographs of a prototype SMP neuronal probe. The first panel shows the as-fabricated probe. The middle panel shows the deformed probe after stretching horizontally. The final panel shows the recovered shape of the probe after deployment at 37 °C. Reprinted with permission from ref. ⁹² Copyright © 2006 IOP Publishing.

More recently, Ware *et al.*¹¹² developed a thermally and water-responsive SMP system based on commercially available acrylate monomers. The fabricated neural electrodes are stiff before swelling (storage modulus of ~700 MPa at 37 °C) and soften *in vivo* (storage modulus of ~300 MPa at 37 °C) within 24 h. The SMP used in this study is sensitive to many of photolithography processing requirements (i.e., organic solvents, water, heat, vacuum, bases, acids and adhesion). Thus, to overcome these challenges, a transfer-by-polymerization was used to fabricate reproducible and robust neural microelectrodes (Figure 1-10) with tunable moduli to improve biocompatibility of the microelectrodes with brain tissue. Acute *in vivo* studies demonstrated that acrylate-derived *in situ* softening SMP-based microelectrodes were capable of recording an excitatory neuron in a rat cortex.

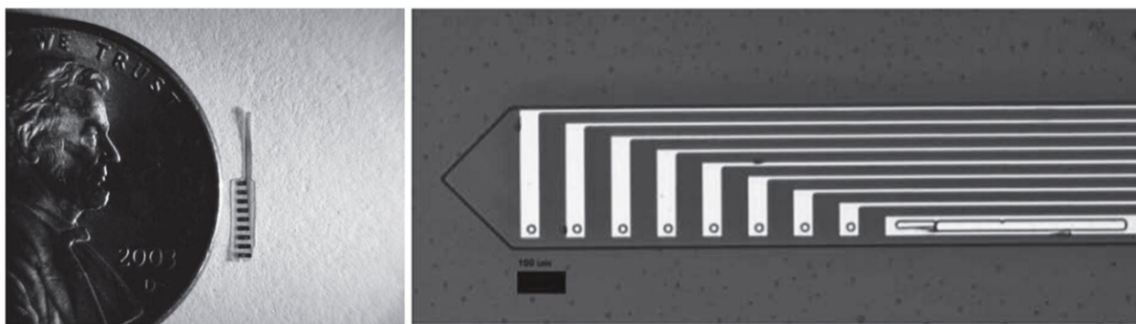


Figure 1-10. Picture (left) and optical microscope image (right) of a mechanically adaptive cortical probe with 8 recording channels fabricated from a shape-memory polymer by transfer-by-polymerization process. Reprinted with permission from Ref. ¹¹². Copyright © 2012 Wiley-VCH.

Ware and co-workers also utilized thiol-ene/acrylate-based polymers to create second generation physiologically responsive neural interfaces.^{115, 116} The thiol-ene/acrylate-based substrates soften from a Young's modulus of >1 GPa (dry state at room temperature) to 18 MPa upon exposure to physiological conditions, as a result of plasticization by small water uptake (less than 3%). Ware *et al.* demonstrated that the modulus of the thiol-ene/acrylate polymers could be controlled through variation of the diacrylate content as a result of variable glass transition temperature. Although, intracortical electrode arrays derived from the thiol-ene/acrylate-based polymers were capable of recording neural activity in rats over 1 month post-implantation., long-term chronic recording studies compare with silicon electrode arrays as control are required.¹¹⁶ Finally, immunohistochemical studies are required to quantify the potential benefits of these thiol-ene/acrylate-based polymers as basis for thermally-responsive neural interfaces, following chronic (≥ 16 week) implantation.

Tien *et al.* used silk fibroin to fabricate mechanically adaptive neural electrodes, which are also capable of releasing therapeutic agents.¹¹⁷ The elastic modulus of silk is reduced upon hydration from 1.8 GPa in the dry state to 20 MPa in the wet state. In addition to dynamic mechanical properties, the effect of silk fibroin coatings on reactive gliosis was studied using an *in vitro* glia scarring model around the electrode array. While *in vitro* immunohistochemical staining after one week showed that silk-coated stainless steel

wires stimulated less “scar index” for both the microglia marker ionized calcium binding adapter molecule 1 (IBA1) and chondroitin sulphate (CS) proteoglycan, no significant difference was observed in case of the astrocyte marker glial fibrillary acid protein (GFAP) “scar index”, relative to the uncoated stainless steel microwires (Figure 1-11). Finally, Tien *et al.* investigated the capacity for silk to encapsulate and release scar-inhibiting agents such as the enzyme chABC as a potential avenue to ameliorate axonal growth inhibition by CSs within the glial scar. . Reactive glia cells produce extracellular matrix molecules, such as CSs, that inhibit axonal growth, and prevent regeneration of damaged neurons near the electrode. It was found that the chABC releasing silk films exhibited an almost 50% reduction in CS staining in the glial scarring model over 1 week. In summary, the hypothesis that the mechanical mismatch between current metallic- or silicon-based intracortical microelectrodes and the brain tissue propagates neuroinflammatory events leading to microelectrode failure has led to the development of new class of *in situ* softening polymeric materials such as mechanically adaptive polymer nanocomposites and shape memory polymers for neural interfaces. While, initial histological studies of implants based on mechanically adaptive polymers suggest that adaptive materials can better stabilize neural cells populations at the neural tissue/electrode interface than rigid electrodes (up to eight weeks), there are still several challenges that need to be addressed. First, as stated above, Nguyen’s results demonstrate that the mechanical strain placed on cortical tissue by stiffer implants played a lesser role early after implantation than at more chronic time points. Therefore, histological studies for such adaptive materials must be conducted for long-term implantation times. Second, if such *in vivo* tissue response studies confirm that adaptive materials are indeed better than previously developed rigid electrodes, one must ask how soft do they need to be? Answers to these questions are important to the development of this field.

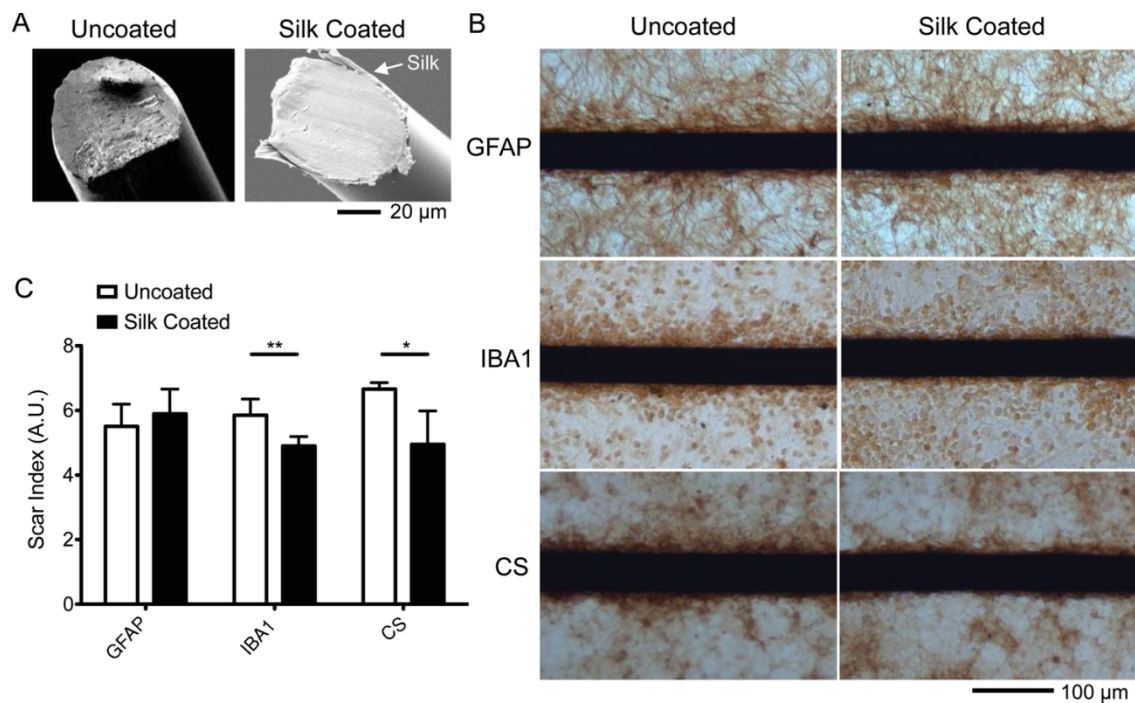


Figure 1-11. (A) SEM images of uncoated and silk-coated stainless steel microwires. (B) Representative images of brain sections labelled for GFAP, IBA1, and CS around uncoated and silk-coated microwires. (C) Quantification of staining for GFAP, IBA1, and CS around the microwires. Error bars show standard deviation. Horizontal bars denote a significant difference between staining around uncoated and silk-coated wires ($*p < 0.05$, $**p < 0.005$). Reprinted with permission from ref. ¹¹⁷. Copyright © 2013 Wiley-VCH.

Additionally, the work of the combined work of the laboratories presented within this section suggests the potential for synergistic effects of combinatorial approaches throughout the progressive inflammatory response. For example, one could envision the incorporation of bioactive molecules such as anti-inflammatory, anti-oxidant drugs and/or proteins on or within the mechanically-dynamic neural electrode devices to mitigate initial trauma, coupled with a chronically compliant device to dictate scar mechanics and mediate chronic tissue strain. Finally, it is important to note that since much of softening polymeric materials (e.g. shape-memory polymers) are synthesized in laboratories, leaking residues from any of these materials can be highly toxic and probably lead to cell death around the electrode (as described for SU-8 above). Therefore, development of

robust processes that allow repeatable control of properties (e.g. efficient polymerization reactions or non-solvent processes) is necessary.

1.3.2. Incorporating Bioactive Materials

Over the last decade, another promising approach to control cell phenotype at the biotic/abiotic interface has been developed, which involves the decoration of microelectrodes with bioactive surface coatings.¹¹⁸⁻¹²⁹ A broad-spectrum of bioactive materials has been immobilized on the implant surface to control the neuro-inflammatory response (Table 1-1). Bioactive materials have been shown to be at least temporarily successful in attenuating the neuro-inflammatory response to intracortical microelectrodes within the brain tissue. However, it is not clear if the temporary effect of most bioactive strategies is a result of biomolecule consumption (exhausted supply or degradation), or an evolution of redundant biology overcoming the initial effect of the surface modification.

Perhaps one of the simplest and most common biomaterials approaches is the passive adsorption or covalent immobilization of ECM components to promote “directed” cell attachment. As biomaterialists became interested in the device-mediated neuro-inflammatory limitations to intracortical microelectrodes, the attachment of ECM proteins and peptides onto the microelectrode surface were among the first methods reported. Extracellular matrix-based materials for neural interfacing applications have been recently reviewed by Chen and Allen.¹³⁰ Therefore, only select representative examples or new considerations will be discussed here.

Table 1-1. Non-Exhaustive List of Bioactive Surface Treatments for Intracortical Microelectrodes.

Bioactive Agent	Coating Material	Electrode Type	Reference
Dexamethasone (DEX)	Poly(pyrrole) (PPy)	Gold-coated coverslip	131
	PLGA nanoparticles embedded in alginate hydrogel	Silicon	132
	Nitrocellulose	Silicon	133
	PLGA nanofibers	Silicon	134
	Poly(propylene sulfide) nanoparticles embedded in poly(ethylene oxide)	Platinum	135
Laminin (LN)	Dextran	Silicon, gold and polyimide	136
	Poly(ethyleneimine) (PEI) or Chitosan (CH)	Silicon	126
	Poly(pyrrole) (PPy)	Gold-coated coverslip	137
	Poly(ethyleneimine) (PEI)	Silicon	138
L1	Poly(ethylene glycol) (PEG)	Silicon	139
	Silicon dioxide modified using silane chemistry	Silicon	121
	Parylene-C	Tungsten	140
α -MSH	Nitrocellulose	Silicon	129
	Silicon modified using silane chemistry	Silicon	120
Nerve Growth Factor (NGF)	Parylene-C	Silicon	82
	Poly(ethylene dioxythiophene) (PEDOT)	Platinum	141
	Poly(pyrrole) (PPy)	Polystyrene	142
Superoxide Dismutase (SOD)	Surface functionalization	Silicon	143

Among the most important ECM proteins for neural applications is laminin (LN), an adhesive protein that plays crucial roles in cell migration, differentiation, and axonal pathfinding.¹⁴⁴ The two main peptide sequences from LN that are often targeted for

biomaterial applications include Ile-Lys-Val-Ala-Val (IKVAV) and Tyr-Ile-Gly-Ser-Arg (YIGSR). In 1993, Massia and Hubble were among the first to report on receptor-specific cell spreading on surfaces covalently immobilized with YIGSR.¹⁴⁵ Twenty years later, Massia developed a surface grafting method that allows for the covalent immobilization of IKVAV on the surface of silicon, silicon oxide, gold and insulating polymers such as polyimide, all common components of intracortical microelectrodes.¹³⁶ This work highlights the specificity of LN peptides for supporting neuronal attachment, and reinvigorated the use of LN-derived strategies for intracortical microelectrode applications.

Likely based on Massia's work, the Bellamkonda group reported a series of publications utilizing LN-based coatings as surface modifications for intracortical microelectrodes applications.^{126, 138} First, a layer-by-layer (LBL) assembly was used to build up a deposition of poly(ethyleneimine) (PEI) and LN on silicon wafers with an oxide layer. It was found that the PEI-LN layer was stable for at least 7 days under simulated physiological conditions, and significantly improved neuron adhesion and differentiation *in vitro*.¹²⁶ The subsequent *in vivo* study revealed that PEI-LN coatings are able to reduce the counts of reactive microglia and astrocytic tissue response to Si-based electrodes after 4 weeks post-implantation.¹³⁸ However, LN coating elicited a more robust pro-inflammatory response at one day post-implantation than uncoated devices, as indicated by increased CD-68 positive microglia, GFAP astrocytes, and pro-inflammatory cytokine expression. Interestingly, neuron densities were statistically similar at all of the time points investigated, suggesting no advantage to the LN coating for recording applications. In parallel to the LN work in the Bellamkonda lab, several laboratories have investigated the ability of doping conductive polymers, with LN-based peptides in order to increase neuronal attachment. For example, Stauffer and Cui investigated two different LN fragments, YIGSR and RNIAEIIKDI, as dopants in an electropolymerized poly(pyrrole) (PPy). The goal of the initial *in vitro* study was to combine the critical electrical properties of conducting polymers with the ability to promote specific-cell attachment (YIGSR) and neurite outgrowth (RNIAEIIKDI).¹³⁷ Stauffer and Cui's results confirm the

cell-specific attachment and growth seen over the previous decades in many laboratories. The novelty of their work was that the combination of the two peptides on a conducting polymer scaffolding synergistically increased both neuronal attachment, and neurite outgrowth, while also demonstrating low impedance and increased charge capacity. Despite the promising *in vitro* results suggesting that LN-containing coatings may enhance the long-term recording stability of neural interfaces, the *in vivo* recording performance of these materials have not been reported to date.

In a second example of LN-derived peptide incorporation into conducting polymers, Green *et al.* doped PEDOT with DEDEDYFQRYLI and DCDPGYIGSR.¹⁴⁶ Interestingly, Green *et al.* demonstrated that large peptide dopants produced softer PEDOT films with a minimal decrease in electrochemical stability. However, despite the retained bioactivity of dopant peptides, the effects were largely dependent on initial cell attachment, and neither of the peptides investigated provided the bioactivity of the native LN protein. In a later study, Green *et al.* also examined the effect of entrapping nerve growth factor (NGF) within the PEDOT during electrodeposition.¹⁴⁷ The incorporation of NGF was shown to remain biologically active within the PEDOT. However, Green *et al.* also found that the use of both a LN peptide dopant and NGF in the PEDOT resulted in polymers with decreased mechanical and electrical properties compared with controls containing only NGF.¹⁴⁷

Despite retained biological activity of the incorporated peptides, the combination of biological molecules within conducting polymers has thus far failed to provide the synergistic benefits that the field has anticipated. In fact, the most recent reported studies from the Poole-Warren group provided an interesting report of the performance of conducting polymer electrodes, without the incorporation of biological molecules.¹⁴⁸ Since isolated peptide sequences typically demonstrate enhanced activity of targeted functions compared to full protein controls,¹⁴⁹ it is likely that the immobilization methods employed within conducting polymer requires further optimization, perhaps insulating spacer groups to isolate the biomolecules from the polymers.

While the use of LN surface modification alone has not successfully improved the biocompatibility or recording quality of microelectrodes, there is increasing evidence that the presentation of other specific ECM molecules or networks of ECM components that mimic the complexity of natural brain tissue may be useful. For example, the Cui group has demonstrated encouraging work with the cell adhesion molecule L1. L1 is a neuronal adhesion molecule that can specifically promote neurite outgrowth, neural migration, and neuronal survival. Azemi *et al.* demonstrated that neural electrode arrays coated with immobilized L1 showed enhanced levels of attachment of mouse cerebellum neurons *in vitro*.¹³⁹ Azemi *et al.* directly compared the efficacy of L1 with LN. The study showed that while the LN-functionalized surfaces greatly promoted the growth of astrocytes, the L1-functionalized surfaces showed significantly reduced astrocyte attachment compared to both LN-coated and uncoated control surfaces.¹³⁹ In a subsequent paper,¹²¹ Azemi *et al.* investigated the neuro-inflammatory response to L1-functionalized Michigan-type microelectrodes implanted in a rat cortex for up to 8 weeks. The study revealed that L1-functionalized microelectrodes show significant reduction in reactive tissue gliosis when compared with uncoated electrodes. The most promising aspect of the L1 approach is the ability to maintain normal neuronal populations at the microelectrode interface, and the significant increased density of neuronal filament at the interface (Figure 1-12). Interestingly, the Cui laboratory has more recently begun to explore the utility of L1-functionalized electrodes for peripheral nervous system applications. Unfortunately, to date, no description of the impact of L1 immobilization on recording quality for intracortical microelectrode applications has been reported, but deserves further attention due to the success of foundational studies.

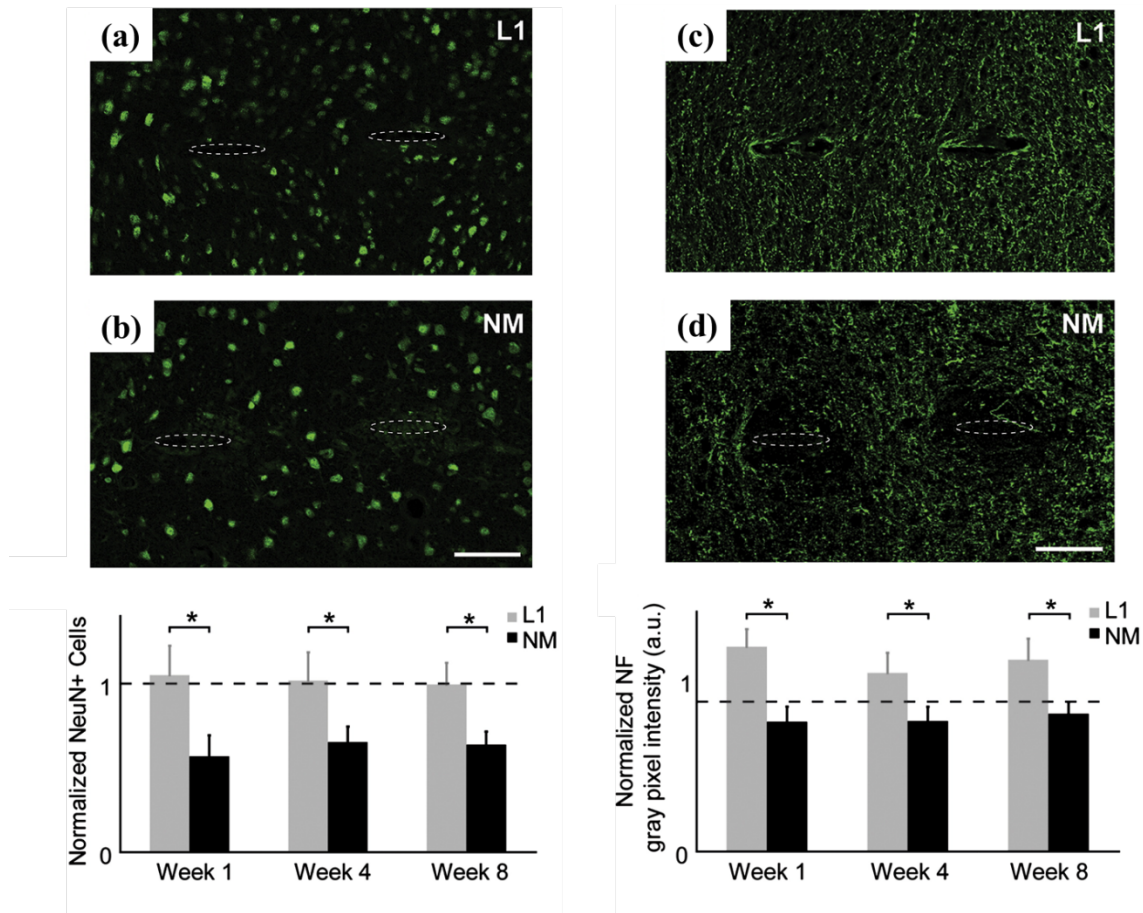


Figure 1-12. (a, b) Representative images of NeuN+ cells (green) around the NM (unmodified) and L1 (L1-peptide grafted) probes after 8 weeks of implantation in rat cortex. Below the set off images, the corresponding normalized cell count differences between L1 and NM probes for the 0–100 μm region away from the interface ($*p < 0.05$). (c, d) Representative images of neuronal filament (green) stained tissue after 8 weeks of implantation in rat cortex. Below the set off images, the corresponding normalized neuronal filament intensity level differences between L1 and NM probes for the 0–100 μm region away from the interface ($*p < 0.05$). Scale bar = 100 μm. Reprinted with permission from Ref.¹²¹ Copyright © 2011 Elsevier.

While Azemi *et al.* showed the supremacy of L1 over LN,¹²¹ other studies have also shown that presentation of LN alone may not be sufficient to mitigate the neuro-inflammatory response. For example, Tanaka *et al.* showed that microglia cultured on fixed (dead) astrocyte monolayers, even in the presence of serum, display a resting phenotype. Tanaka's results indicate that cues presented by the astrocyte ECM are

sufficient to regulate microglia activation. Interestingly, the impact of fixed astrocyte ECM was significantly more effective at reducing microglial activation than individual ECM components such as LN or fibronectin (FN).

However, utilizing complete, tissue-specific ECM may provide additional benefits to single protein approaches. Although ECM throughout the body shares common protein and glycosaminoglycan building blocks, subtle differences indicate that the precise make-up of a tissue-specific ECM is vital in regenerative applications.¹⁵⁰ Several studies have shown that culturing cells on tissue-specific ECM improves infiltrating cell proliferation rates and increases the expression of desired phenotypic cell and tissue characteristics.¹⁵¹⁻¹⁵⁵ In contrast, implantation of non-tissue specific ECM induces the formation of undesired, phenotypically irregular tissue at the implantation site.^{156, 157}

While bioactive approaches, based primarily on ECM proteins and peptides, have shown promise in improving the neuro-inflammatory response to intracortical microelectrodes, one limitation of these strategies is their short-lived nature. For example, inflammatory cells that unavoidably become activated in response to the initial iatrogenic trauma are known to phagocytize and remove adherent and even covalently immobilized proteins over time. Therefore, bioactive coatings should primarily be thought of and used as one component of a combinatorial strategy for improving microelectrode function and biocompatibility. Specifically, bioactive materials may serve as a key component to direct initial wound healing events and tissue integration following implantation.

A further, and often overlooked, concern with protein-based coatings is their potential for immunogenicity. While the majority of proteins found in the ECM are well conserved between animals and humans, interspecies differences do exist. As a result the implantation of even decellularized, xenogenic ECM has been shown to elicit an adaptive immune response. Therefore the use of autologous or allogenic materials may prove key to maximizing the clinical success of ECM-based coatings.

1.3.3. Conducting Polymers

The inherent conductive properties of intrinsically conductive polymers make them a useful class of materials for a wide range of biomedical applications, such as biosensors, tissue engineering, neuroprosthetic electrodes, drug delivery, and actuators.^{158, 159} Conducting polymers are particularly attractive for intracortical microelectrode applications because they have mechanical properties that lie between those of conventional metallic microelectrodes and the brain tissue, can provide high surface area and therewith facilitate an efficient ion exchange between recording sites and the brain tissue, and can at least in principle, be processed into a broad range of geometries/structures/architectures. Charge transfer is improved through reduced impedance and greater selectivity for both recording and stimulating neural interfacing applications; although their intrinsic conductivity is lower than that of gold, platinum, or stainless steel electrodes.

The key feature of conducting polymers is conjugated double bonds along the backbone with a high degree of π -orbital overlap, results in electrically conductive materials. Conducting polymers with various morphologies can be directly deposited onto intracortical microelectrode surfaces. As a result, the conducting polymer coatings lower the impedance of the electrodes and can provide a mechanical buffer between the stiff intracortical microelectrode and the compliant brain tissue. Additionally, bioactive agents such as anti-inflammatory drugs and neurotrophic factors can be incorporated and delivered from these conducting polymer coatings. Several studies have shown that intracortical microelectrode functionality can be improved to some extent by coating the microelectrode surface with low-impedance conductive polymer with nanoscale roughness or porosity,^{85, 160, 161} or through addition of cell adhesion peptides,⁸⁵ proteins,^{126, 127, 162} or anti-inflammatory drugs.^{132, 163} Overall, *in vivo* studies have shown that these conducting coatings may enhance the chronic recording performance of intracortical microelectrodes.¹⁶⁰

Among the currently available conducting polymers, poly(pyrrole) (PPy) and poly-(3,4-ethylene dioxythiophene) (PEDOT) (Figure 1-13) are the most studied conducting

polymers for intracortical microelectrode applications. Such conducting polymers have been doped with various dopants such as poly(styrene sulfonate) (PSS),¹⁶¹ perchlorate (ClO_4^-),¹⁶⁴ *para*-toluene sulfonate (pTS),¹⁴⁸ or sulphate (SO_4)¹⁶⁵ to modify the surface of metallic intracortical microelectrodes.¹⁶⁶ In this section we discuss the development of conducting polymers used to modify the intracortical microelectrode surfaces with particular attention to the use of PPy and PEDOT.

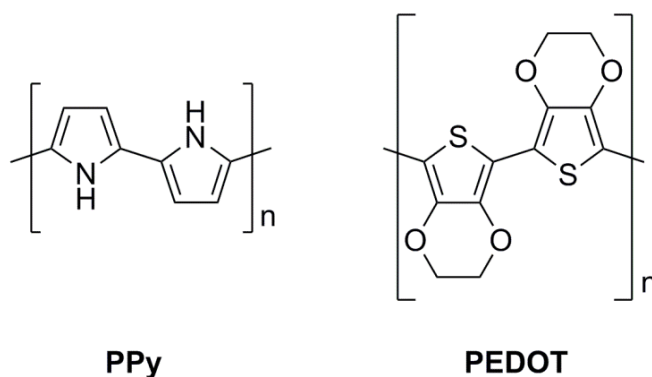


Figure 1-13. Chemical structures of poly(pyrrole) (PPy) and poly-(3,4-ethylene dioxythiophene) (PEDOT), examples of conducting polymers explored in neural interfaces.

Much of the initial research on conducting polymers for neural interfacing focused on PPy due to the ease of preparation, high conductivity, controllable surface properties, and the possibility to electropolymerize this polymer from water. In 2001, Martin and co-workers investigated the use of PPy as a surface coating for neural electrodes.⁸⁵ In his report, PPy was combined with a genetically engineered protein, designed to incorporate GAGAGS sequences of silk alternated with the cell-binding sequence RGD. The polymers were deposited electrochemically onto the silicon microelectrodes. The study showed that the PPy-coated Michigan-style microelectrodes had a higher surface area and charge density compared with uncoated electrodes, which facilitates charge transport, and more efficient neural communication.⁸⁵ In addition, it has been reported that a higher surface area significantly lowers the overall impedance of the intracortical microelectrodes.¹⁶⁷

PSS has been used commonly as a dopant material for PPy due to its stability and *in vitro* compatibility with mammalian neuronal cells.^{161, 168-170} Cui and Martin electrochemically deposited PPy doped with PSS on the neural electrodes, and found that the coated electrodes had an increased surface area, which resulted in a 30-fold decrease in impedance.¹⁶¹ In 2005, George *et al.* reported on the biocompatibility of PPy-based cortical implants that had been doped with PSS or sodium dodecylbenzenesulfonate (NaDBS).¹⁶⁹ Immunohistochemical studies showed that PPy-based intracortical implants doped either with PSS or NaDBS after 3 and 6 weeks implanted in a rat cerebral cortex had less gliosis than Teflon-coated microwire controls. However, the differences in gliosis at the 6-week time point had lessened compared to 3 weeks. George's study also showed that incorporating neurotrophic molecules such as nerve growth factor (NGF) and brain-derived neurotrophic factor (BDNF) into the PPy matrix promoted the ingrowth of neural tissue into the lumen of the PPy-based implants, compared to implants without growth factors. As noted in earlier sections, analysis at limited intermediate time points can lead to incomplete conclusions. Therefore, further works need to be done to demonstrate whether the bioactive molecules can enhance neuronal adhesion and interaction with conducting polymer-based intracortical implants.

The incorporation of conducting polymers within hydrogels that are used to coat conventional microelectrodes is another intriguing approach to better integrate intracortical microelectrodes with the neural tissue. Hydrogels are attractive due to their use in many biomedical device applications, their high water content which causes the mechanical properties to be similar to those of the brain tissue, and their porous network structure which can facilitate charge transport especially if conducting polymers are insulated. In one example, Michigan-style microelectrodes were first coated with cross-linked alginate and then PPy/PSS was subsequently electrochemically polymerized on the device surface.¹⁶⁸ PPy was observed to grow vertically from the electrode surface, and at the recording site recording site. It was found that the impedances of the porous hydrogel modified with conducting polymer films are around three orders of magnitude less than the impedance of the metal microelectrodes. The authors also found that the PPy/PSS-

alginate-coated recording sites were capable to transporting charges as efficiently as conventional electrodes. Despite the growing number of studies being conducted with PPy for intracortical microelectrode applications, electrochemically made PPy has a poorly defined chemical structure in which there are a significant amount of α - β couplings. The presence of defective α - β couplings along the polymer backbone induce structural disorder, limits the electrochemical response, and is contributing significantly to polymer breakdown due to over-oxidation.¹⁷¹ With these limitations in mind, new and highly stable conducting materials must be found that can endure the long-term implantation lifetime as well as attack from biological agents present in the brain tissue.

To overcome the drawbacks of PPy, poly(3,4-ethylene dioxythiophene) (PEDOT) has recently been explored as an alternative to PPy for neural interfacing electrodes. Specifically, PEDOT is more stable to oxidation and more conductive than PPy. Unlike PPy, undesired α - β couplings and structural disorder are eliminated in PEDOT by “blocking” the 3- and 4-positions of the monomer by the attachment of ethylenedioxy groups (Figure 1-14). Early studies by Cui and Martin¹⁷² explored the benefits of PEDOT as coating for neural microelectrodes. Cyclic voltammetry experiments demonstrated that PEDOT-coated electrodes were more stable than those coated with PPy. In addition, high quality acute neural signals were recorded with the PEDOT-coated Michigan-style microelectrodes in the cerebellum of guinea pig with higher signal amplitude than in reference experiments with un-coated microelectrodes with gold contacts. This is likely due to the deposition of conducting polymer (i.e. PEDOT), which decreases the impedance of the electrode (increase sensitivity). Cui and Martin’s findings are highly desirable for potential use of PEDOT as alternative conducting material for neural electrodes.

After Cui and Martin initial report, several studies followed, which further explored the use of PEDOT as electrically conductive material in intracortical microelectrode applications. For example, Xiao *et al.* modified the surface of intracortical microelectrodes using PEDOT-MeOH that was electrochemically doped with poly(styrene sulfonate) (PSS).¹⁷³ In this study, Xiao *et al.* improved the limited

processability (aqueous solubility) of PEDOT through the addition of an appropriate pendant side group onto the backbone. To this end, polar derivatives of EDOT, specifically EDOT-MeOH (the chemical structure of which has been shown in Figure 1-14) was used. Xiao *et al.* found that the PEDOT-MeOH coating decreased the impedance by almost two orders of magnitude in comparison to the uncoated Michigan-style microelectrode. Decrease in electrode impedance leads to improved charge transfer from the surrounding brain tissue to the intracortical microelectrode, which is argued to lead to more effective recording and stimulating. In another investigation, Yang *et al.*¹⁷⁴ electrochemically deposited surfactant-induced ordered PEDOT onto gold-coated Michigan-style microelectrodes. Although, this ordered PEDOT polymer coated-electrodes exhibited a lower impedance and a higher charge capacity than uncoated electrodes, it was found that the surfactant used in the preparation leached from the device when placed in a cell culture medium and killed all nearby cells in the culture.

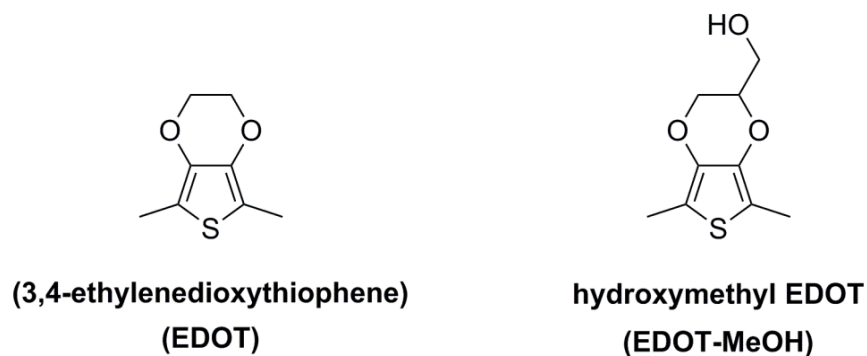


Figure 1-14. Chemical structures of monomers used to fabricate PEDOT and PEDOT-MeOH.

More recent studies by Martin and co-workers have shown that neural cells can be incorporated into PEDOT, while still maintaining cell viability and signal transduction capabilities. As a result, functional hybrid PEDOT-neural cell electrode coatings were created that can be used as highly biomimetic conductive substrates for intracortical microelectrodes. Polymerization of PEDOT around living cells has been reported *in vitro*¹⁷⁵ as well as *in vivo*¹⁷⁶ through living tissue. In one study, Richardson-Burns *et al.*¹⁷⁵

reported the electrochemical polymerization of PEDOT in the presence of live neural cells that had been cultured on in-house fabricated Au/Pd sputter-coated electrodes and/or Applied Biophysics (Troy, NY) electrodes, as shown in Figure 1-15, resulting in the formation of PEDOT film around and onto adhered neural cells. Additionally, PEDOT, PEDOT/live neurons, and neuron-templated PEDOT coatings on the electrodes significantly enhanced the electrical properties and increased charge transfer capacity. While *in vitro* experiments show successful electropolymerization of conducting polymers around neural cells, it is critical to apply the concept in animal models to fully characterize the performance of the materials to more accurately understand the contribution of this strategy to the field.

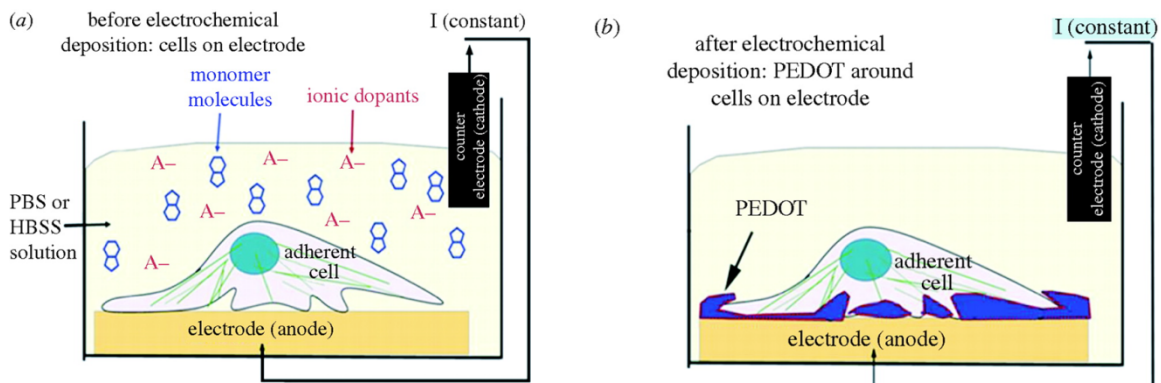


Figure 1-15. (a) Schematic of the electrochemical deposition cell and the neural cell monolayer cultured on the surface of the metal electrode prior to polymerization. (b) PEDOT polymerized around living cells. Reprinted with permission from ref. ¹⁷⁵ Copyright © 2007 Elsevier.

The first chronic, long-term neural recording studies of PEDOT-coated electrodes were conducted by Kipke and co-workers in 2006.^{160, 177} It was found that chronically implanted control microelectrodes were unable to record well-isolated unit activity due to a dramatically increased noise floor, while PEDOT-coated Michigan-style microelectrodes consistently recorded neural activity, and showed a much lower noise floor than un-coated gold-based controls over a six-week period following implantation in three male rats.¹⁷⁷

More recently, Kozai *et al.* took a further step towards long-lasting conjugated-polymer-based neural interfaces that elicit little tissue response in the brain, fabricating an integrated composite microelectrode consisting of electrically conductive carbon fiber core, a coating-based layer, and a PEDOT:PSS-based recording pad.¹⁷⁸ Specifically, electrodes were fabricated by mounting carbon fiber, which serves as the conducting core and provides the mechanical backbone of the device, with a diameter of 7 μm onto a NeuroNexus microelectrode. The carbon fibers were then coated with a 800 nm thin poly(*p*-xylylene) layer (Figure 1-16a), and subsequently a 50 nm thick layer of poly((*p*-xylylene-4-methyl-2-bromoisobutyrate)-co-(*p*-xylylene)), both with a chemical vapor deposition (CVD) process (Figure 1-16b). The later polymer provides initiator groups for a subsequent atom transfer radical polymerization (ATRP). This was used to apply a \sim 200 nm thin layer of poly(ethylene glycol) methacrylate (PEGMA) (Figure 1-16c). Finally, a carbon recording site was exposed at the tip of the neural stainless-steel wire by cutting away the insulation, and the recording site was coated with a layer of PEDOT:PSS that was applied by electrochemical deposition (Figure 1-16d). Chronic neural recordings from the inserted implants into the motor cortex of rats showed that the resulting microelectrodes provided stable single-neuron recording over five weeks in the brain. Interestingly, the electrodes also showed reduced neuro-inflammation response compared with traditional silicon electrodes. Thus far, these electrodes with mechanically-compliant coatings are the smallest implantable neural electrodes that were able to record neuronal activity in animals.

Conducting polymers aim to enhance the chronic performance of intracortical microelectrodes through providing a high surface area, and more conductive materials. Also, the charge transfer is likely improved through reduced impedance, thereby providing greater selectivity for both recording and stimulating neural applications. Despite the vast amount of research being produced in recent years on the conducting polymers for neural interfacing applications, the field is still growing and many challenges, limitations and questions remain to be answered.

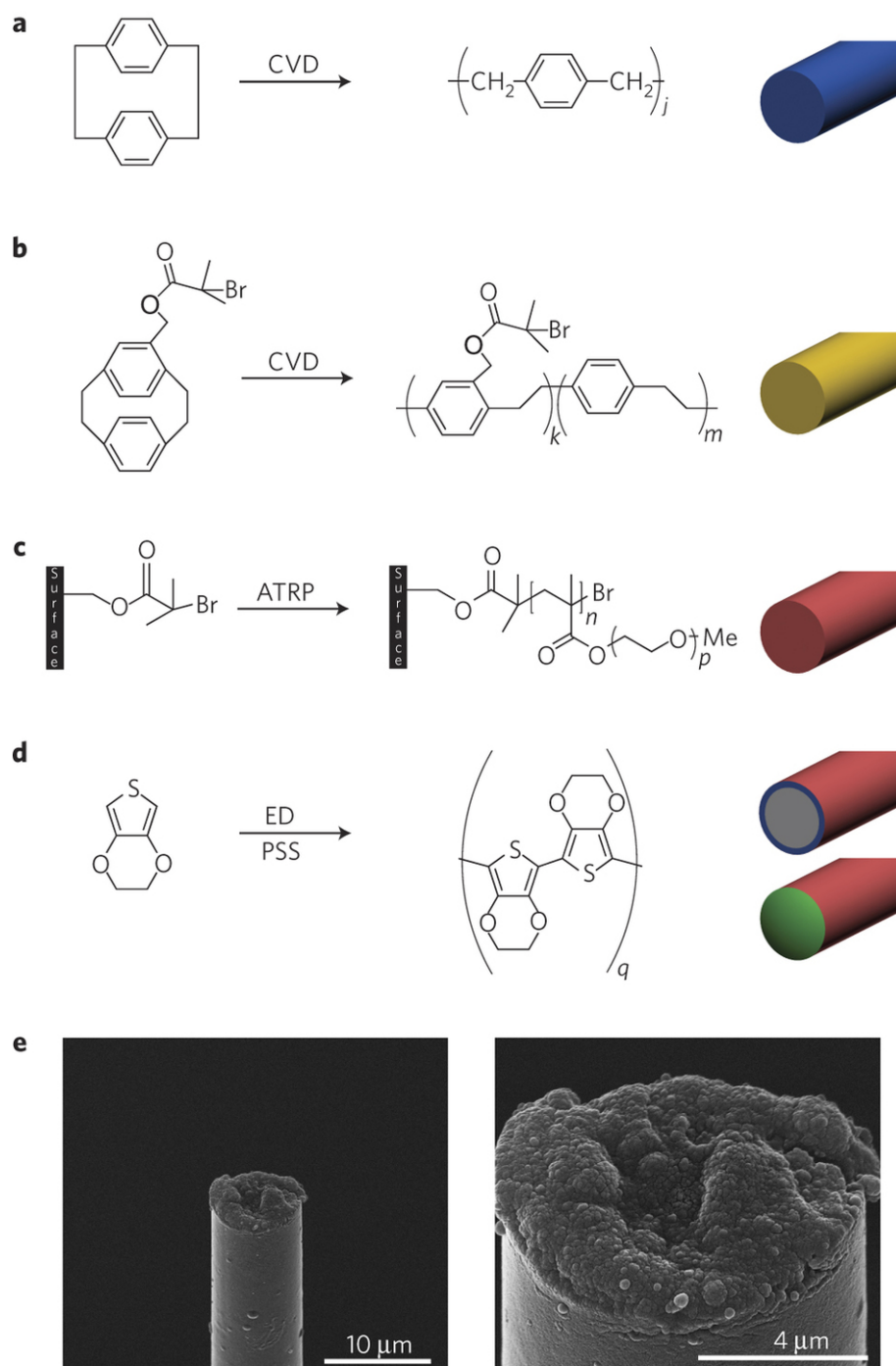


Figure 1-16. (a–d) Schematic representation of the fabrication of microtherad electrodes, and (e) SEM images of a fully assembled, functional electrode. Reprinted with permission from Ref. ¹⁷⁸. Copyright © 2012 Nature Publishing Group.

The key challenge of conducting polymers in neural interfacing applications is the preservation of the conductivity or electrochemical stability over long periods of time. For example, PPy and PEDOT films have been shown to lose up to 95% and 30% of their conductivity when subjected to 16 h of polarisation, respectively.¹⁷⁹ Also, conducting polymers are often brittle and the addition of dopants to the system in many cases exacerbates this effect.¹⁶⁶ Therefore, developing conducting polymers that are less brittle and more malleable while maintaining the conductivity and avoid delamination over time is required. Moreover, limited studies on the mechanical properties of conducting polymers for the duration of implant lifetime suggest that further research is needed to assess the durability of a coated intracortical microelectrode in animal models. This will provide an insight into possible delamination and/or mechanical erosion of conducting polymers. Another major drawback of conducting polymer systems is the diffusion of the employed dopants, unreacted monomers and typical process contaminations (e.g. solvents) into the medium, which all are slightly to moderately toxic. Unfortunately, most of the studies that have revealed a positive biological performance have been conducted *in vitro*. We believe that the cytotoxicity of released dopants is likely a limiting factor to the use of *in-situ* polymerization *in vivo*, despite the success *in vitro* – at least with the chemistries commonly explored. Thus, toxicity testing needs to be assessed using *in vivo* implantation studies to answer whether conducting polymers are useful for long-term neural implants. Today, most/all of the studies have relied on electropolymerization of conducting polymers on conductive electrodes (e.g. Au). In fact, the substrate to be coated needs to be conductive. So, the conducting polymer is really a mediator between the brain tissue and the conducting intracortical microelectrodes. Therefore, it is also of particular interest to look at printed polymer-based conductive microelectrodes for future neural interfacing applications. Finally, it is clear that long-term *in vivo* studies in this area of research is required for a better understanding of the impact of conducting polymers in improving long-term performance of intracortical microelectrodes include electrochemical stability, delamination, mechanical integrity and the maintenance of an intimate contact between the electrode and surrounding neural tissue.

1.3.4. Nanomaterials

Nanomaterials have been explored in a variety of biomedical applications due to their unique properties arising from their nanoscale dimensions.¹⁸⁰⁻¹⁸² Nanomaterials can be useful in cortical interfacing applications for several reasons. Perhaps most importantly, nanomaterials can interact with biological systems with a high degree of specificity, are able to stimulate and interact with target cells with minimizing undesirable effects, and the electronic properties of nanostructures can be tailored to match the needs associated with charge transport required for electrical/ionic level cellular interfacing.

Charge transfer reactions involving the exchange of charge between various carriers occur at the electrode–polymer and polymer–tissue interfaces.¹⁸³ In particular, it has been established that increasing the effective surface area of the interface will increase the ability for charge transfer to occur. Also, the electrical impedance of the microelectrode is inversely proportional to the surface area of the recording site.¹⁶⁷ As a result, the intrinsically large surface area of nanomaterials results in high charge transfer as well as lower overall impedance of the intracortical microelectrode.

Additionally, nanoscience approaches can present subcellular stimuli that can vary from one part of the neuron to another.¹⁸⁴ For example, a combination of photolithography and layer-by-layer (LbL) self-assembly have been used to pattern secreted phospholipase A₂ (sPLA₂), which promotes neuronal adhesion, on a non-fouling background of poly(diallyldimethylammoniumchloride) (PDDA).¹⁸⁵ The approach used by Mohammed *et al.* facilitates nanoscale patterning with complex functional architectures that are tailored to the needs of a particular experiment. LbL self-assembly has also been used by Ai *et al.* on silicon rubber to pattern alternating laminin and poly-D-lysine or fibronectin/poly-D-lysine ultrathin layers, which are 3.5-4.4 nm thick, and encourage nerve cell adhesion, and support neurite outgrowth of cerebellar neurons.¹⁸⁶ Taken together, the studies by Mohammad *et al.* and Ai *et al.* suggest that bioactive ultrathin coatings could be used to promote cell adhesion and limit immune responses, and may facilitate improved performance of intracortical microelectrodes.

Additionally, several types of nanomaterials have been utilized in neural interface

devices, including carbon nanotubes, carbon nanofibers, and graphene. The use of nanomaterials and nanotools for neuroscience has been recently reviewed.^{187, 188} In this Section, we therefore limit the discussion to the current state of the most widely investigated nanomaterials in the context of neural interfacing applications.

Carbon nanotubes (CNTs) are perhaps the most widely studied class of nanomaterials for intracortical microelectrodes,^{187, 189, 190} in view of their extraordinary strength, toughness, electrical conductivity, and surface area. As with the exploration of any new application for potential biomaterials, early work with CNTs towards intracortical microelectrodes began with *in vitro* applications. For example, Mattson *et al.* reported that multi-walled carbon nanotubes (MWCNTs) could be used as platform for neuronal growth.¹⁹¹ Since then, several studies have been devoted to evaluate neuronal growth on CNTs.¹⁹²⁻¹⁹⁶ Wang *et al.* showed the first *in vitro* stimulation of primary neurons with CNT-based electrodes.¹⁹⁷ The authors found that neurons can grow and differentiate on the microelectrode, and more importantly, that the neurons can be repeatedly stimulated with CNT electrodes. In parallel, several other groups confirmed the possibility to stimulate the neural cells via single-walled and/or multi-walled carbon nanotubes in cultured brain circuits.^{192, 198, 199} In 2008, Keefer *et al.* reported that CNT-coated metal microelectrodes improved both the recording and electrical stimulation of neurons in culture, and *in vivo* in rats and monkeys.²⁰⁰ *In vivo* recording studies of CNT-coated microelectrodes were conducted in the rat motor cortex and monkey visual cortex. It was found that CNTs-coated microelectrodes had increased the neuronal recording sensitivity as well as decreased neuronal noise compared to un-coated tungsten microelectrode controls. It was possible to record local field potential (LFPs), multiple unit activity, as well as neuronal spiking simultaneously with one CNT-coated microelectrode *in vivo*. Additionally, Keefer *et al.* found that the combination of CNTs and the conducting polymer PPy increased the charge transfer beyond that seen with CNTs alone. Further, CNT/PPy-coated microelectrodes had a significantly lower impedance (higher electrode neuronal sensitivity) than bare conventional tungsten and stainless steel microelectrodes. In a similar study, Luo *et al.* also reported that PEDOT/CNT-coated Pt microelectrodes

showed a much lower impedance than the bare Pt electrodes as characterized by electrochemical impedance spectrum (EIS) in PBS.²⁰¹ Electrochemical impedance spectroscopy was used to show that the PEDOT/CNTs decreased the impedance of Pt microelectrodes with increasing coating thickness due to the increase of the electroactive surface area, which results in a bigger capacitance. The PEDOT/CNT-coated electrodes exhibited higher charge injection than traditional electrodes and *in vitro* tests with neurons showed that the neurons attached tightly to the PEDOT/CNT surface and exhibited long neurite extensions, suggesting that PEDOT/CNT-coatings are non-neurotoxic and support the growth of neurons. Similar conducting polymer/CNT composite coatings were also studied by several other groups.^{202, 203} Lu *et al.* reported that co-deposited PPy/SWCNT coatings significantly reduce the impedance of platinum/tungsten microelectrodes. Additionally, the brain tissue response of PPy/SWCNT coated microelectrodes and un-coated Pt microelectrodes were studied with immunochemistry after a 6-week implantation in the cortex of rats. Quantitative analysis of glial fibrillary acidic protein (GFAP) expression and neuronal nuclei (NeuN) showed significantly lower GFAP and higher NeuN counts for the PPy/SWCNT coated microelectrodes within the first 100 μm from the implant/tissue interface (Figure 1-17).²⁰³

Despite the perspective advantages of CNTs for intracortical microelectrode applications, the studied devices are rigid (non-compliant) and may not be optimally suited for chronic neural *in vivo* applications. As a result, there is an increased attention towards the development of flexible CNTs-based intracortical microelectrodes by combination of flexible polymeric substrates and CNTs to overcome both the mechanical failure of more brittle CNTs-based devices, and device-mediated tissue strain. Flexible CNT-based neural electrodes were created by the combination of flexible polymeric substrates and CNT-based electrodes. Lin *et al.* were the first to fabricate a flexible CNT-based electrode array for neural recording applications.²⁰⁴ In this work, the CNT electrodes were partially embedded into a flexible Parylene-C film using a microfabrication process based on four steps: CNT growth, polymer binding, flexible film transfer, and partial

isolation. The flexible CNT electrodes produced were used to successfully record the spontaneous spikes from a crayfish nerve cord.

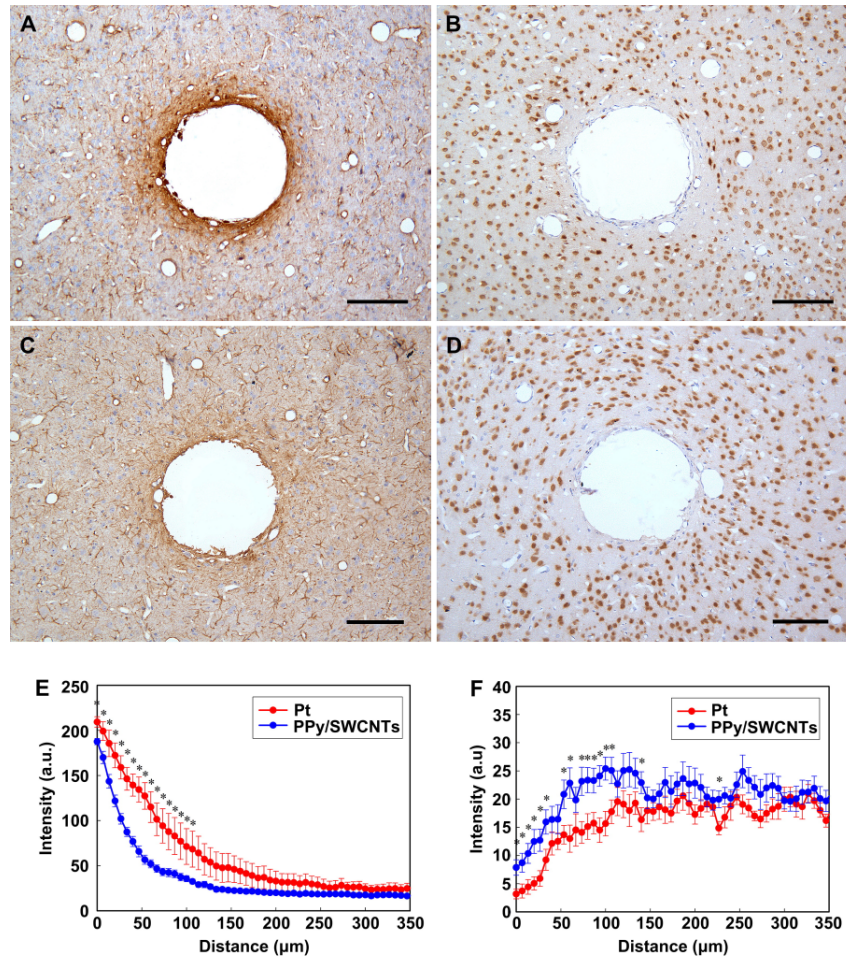


Figure 1-17. GFAP immunostaining for the Pt implant control (A) and PPy/SWCNT coated Pt implant (C) after 6 weeks post-implantation. (E) Quantitative comparison of GFAP immunoreactivity between the control and coated electrodes as a function of distance from the electrode. The survival of neurons around the implanted electrode for the control (B) and coated implant (D) at 6 weeks post-implantation. (F) Quantification comparison of neuron survival between the control and coated electrodes as a function of distance from the electrode. Scale bar = 100 μm. Reprinted with permission from Ref. ²⁰³. Copyright © 2010 Elsevier.

Alternatively, the direct growth of CNTs on flexible polyimide substrates has been reported by Hsu *et al.*²⁰⁵ Hsu *et al.* utilized UV-ozone exposure as a simple and low-cost

route to improve the interfacial properties between the CNT electrodes. UV-ozone exposure induces the formation of C-O, C=O, and O-C=O moieties on the surface of CNTs, increasing the hydrophilicity of the surface. UV-ozone treatment yielded a 50-fold impedance reduction and increased the interfacial capacitance by a factor of ten. *In culture*, UV-ozone treated CNTs electrodes promoted neuron and neurite growth in close contact with CNTs, suggesting the biocompatibility of modified CNTs for neuronal growth.²⁰⁵ In a subsequent study, spontaneous spikes were recorded from a crayfish with a signal-to-noise (SNR) ratio of 6.2. The flexible CNT electrodes were also used to record the electrocorticography (i.e. placing the electrode in the subdural region) of a rat motor cortex with a SNR of 8.7.²⁰⁶ More examples of CNT-based flexible electrodes for neural recording and simulating applications have been developed by Hanein *et al.*,^{190, 207, 208} who transferred single-walled carbon nanotubes (SWCNTs) onto a flexible PDMS substrate. Recent evoked electrical activity recording studies with chick retinas demonstrated the device capability for high efficacy neuronal recording applications.¹⁹⁰ Carbon nanofibers (CNFs), which consist of multi-walled graphene structures stacked on top of each other, like a stack of ice cream cones, have also been explored as substrates for neural interfacing applications. Researchers at NASA Ames Research Center developed forest-like vertically aligned CNFs on a Si wafer by plasma enhanced chemical vapour deposition (PECVD).²⁰⁹ After the CNF film was submerged in a liquid and dried, the CNFs irreversibly stuck together to form microbundles (Figure 1-18). Stable 3D “fuzzy” films were created by electrochemically coating the CNFs with a thin layer of electrically conducting polypyrrole. It was found that the impedance of this kind of electrode decreased significantly compared to common metal electrodes due to the large surface area of 3D nanostructured CNFs, which results in high ion mobility. Furthermore, the PPy coating was shown to improve the biocompatibility of CNF-based electrodes compared to un-coated, and further reduces the electrode impedance by more than 20 times due to the redox potentials of the polymer. A subsequent study by the same group showed that an intimate neural-electrical interface can be formed between the vertically aligned CNFs and a neuronal network of PC12 cells.²¹⁰ The addition of

neuronal growth factor (NGF) on the vertically aligned CNFs facilitated the formation of well-differentiated cells with mature neurites. Although, the freestanding CNFs coated with PPy and NGF were mechanically rigid to maintain their vertical alignment, they were found to be flexible enough to bend toward the cell body when driven by traction forces of the cells, thereby facilitating cell adhesion. Thus, it was suggested that the soft PPy coating not only improved the mechanical stability by forming a core-shell structure with the CNFs, but also promotes a better mechanical contact with neuronal cells due to a reduction of the local mechanical stresses.²¹⁰

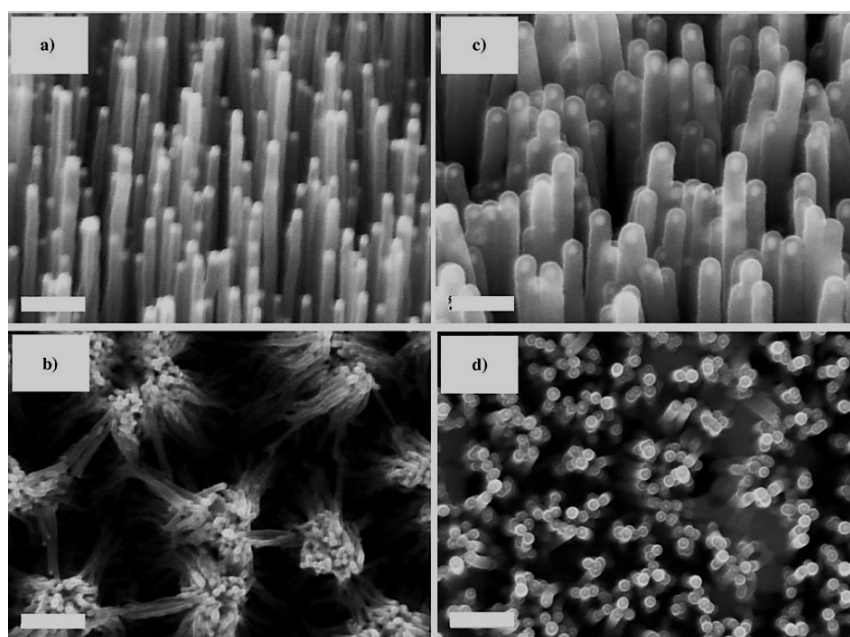


Figure 1-18. Scanning electron microscopy images of (a) An as-grown CNF array. (b) An as-grown CNF array after being soaked in water and then dried in the air. (c, d) an as-grown CNF arrays after electrodepositing a 40-nm-thick conformal polypyrrole film. (a, c) Perspective view images with scale bars = 500 nm. (b, d) Top view images with scale bars = 1.0 mm. Reprinted with permission from Ref.²⁰⁹. Copyright © 2006 Wiley-VCH.

Several studies suggest that graphene exhibits excellent biocompatibility, low cytotoxicity and supports neuronal growth.²¹¹⁻²¹³ Therefore, graphene is another carbon nanomaterial that has been recently utilized in neural interface application. Chen *et al.*²¹⁴ reported the fabrication of graphene-based neural microelectrodes, while Luo *et al.*²¹⁵

reported graphene oxide-based conducting polymer nanocomposites for potential neural interfacing applications. Chen's study showed that graphene-based microelectrodes are capable of recording neural signals in a crayfish. These graphene electrodes showed biocompatibility and non-toxicity throughout the 16 day cell culture experiment with neuronal cells. In the second investigation, Luo *et al.* electrochemically doped PEDOT with graphene oxide (GO) and demonstrated that conducting PEDOT/GO nanocomposites supported the growth of neural cells with minimal toxicity along with low electrochemical impedance.²¹⁵ To clearly demonstrate the potential of this class of graphene-based materials for neural microelectrodes, future studies need to investigate the chronic *in vivo* performance defined by both the ability to maintain a clinical viable signal quality and stimulation capabilities, as well as the biotic and abiotic failure modes (defined above). Alternatively, the Martin group^{134, 216} designed multifunctional nanobiomaterials that can be used for coating neural microelectrodes. These materials significantly decrease the electrode impedance and increase the charge density. Figure 1-19 shows the fabrication process that includes electrospinning of biodegradable nanofibers loaded with anti-inflammatory drug coating of the microelectrode/nanofiber assembly with a hydrogel layer, and subsequent electropolymerization of conducting polymer both around the nanofibers and within the hydrogel matrix. While *in vivo* data are in process and to our knowledge yet to be reported, the approach nicely demonstrates how several attractive concepts can be merged to create "smart nanobiomaterials" that are soft, have a low impedance, high charge density, and also can deliver anti-inflammatory drugs to alleviate the brain immune response to neural interfaces.

Together with the Kipke group, Martin's group also reported the use of conducting polymer nanotubes for chronic neural interfaces.²¹⁷ This work showed that poly(3,4-ethylene dioxythiophene) (PEDOT) nanotube-coated electrodes have a markedly lower impedance over a 7-week period than conventional Michigan-style microelectrodes. Figure 1-20 shows the fabrication process of such PEDOT nanotubes on the surface of Michigan-style microelectrodes.

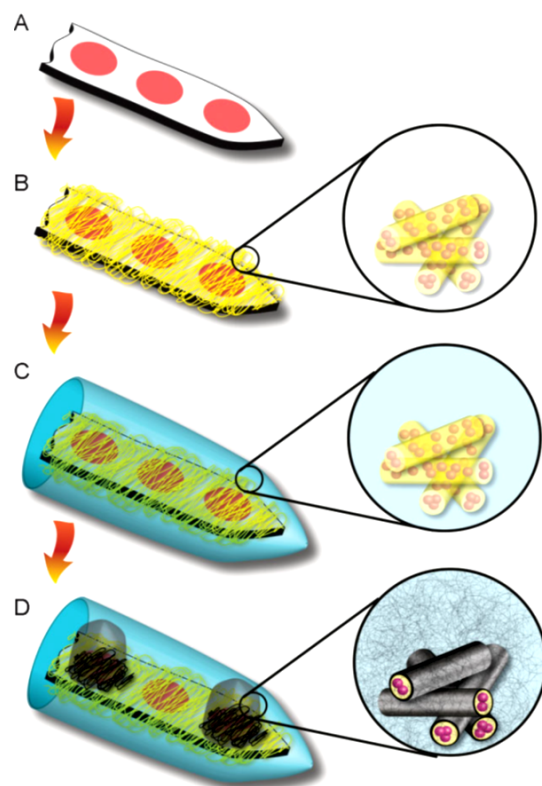


Figure 1-19. Schematic represents fabrication of multifunctional biomaterial-based microelectrode. (A) Uncoated microelectrode. (B) Electrospinning of drug-loaded nanofibers. (C) Hydrogel coating. (D) Electrochemical polymerization of a conducting polymer. Reprinted with permission from Ref. ¹³⁴. Copyright © 2008 Elsevier.

Martin and Kipke later investigated the effect of nanotube morphology on the properties of the electrodes *in vitro*.²¹⁸ Their work demonstrated that the PEDOT nanotubes decreased the impedance of the electrode site by about two orders of magnitude, and increased the capacity of charge density by about three orders of magnitude compared to bare iridium microelectrodes.²¹⁸ The team further showed that the mechanical properties of the conducting polymer can be tuned by their surface morphology. For instance, it was demonstrated that PPy and PEDOT nanotubes can adhere better to the surface of the neural electrodes than films of these polymers. For example, Figure 1-21 shows the delamination of conducting polymers films upon electrical stimulation, while nanotube mats made of the same materials did not show this undesirable effect, which would lead

to electrode failure. Despite the many incredibly attractive materials properties that nanomaterials have demonstrated towards long-term neural interfaces, several of the devices created from these materials in their current form still suffer from limitation that have chronically plagued neural electrodes (degradation and delamination). Therefore, the combination approaches, such as thus being developed by Martin and colleagues, represent the starting point towards integrating nanomaterials into intracortical microelectrodes for neural interfacing applications.

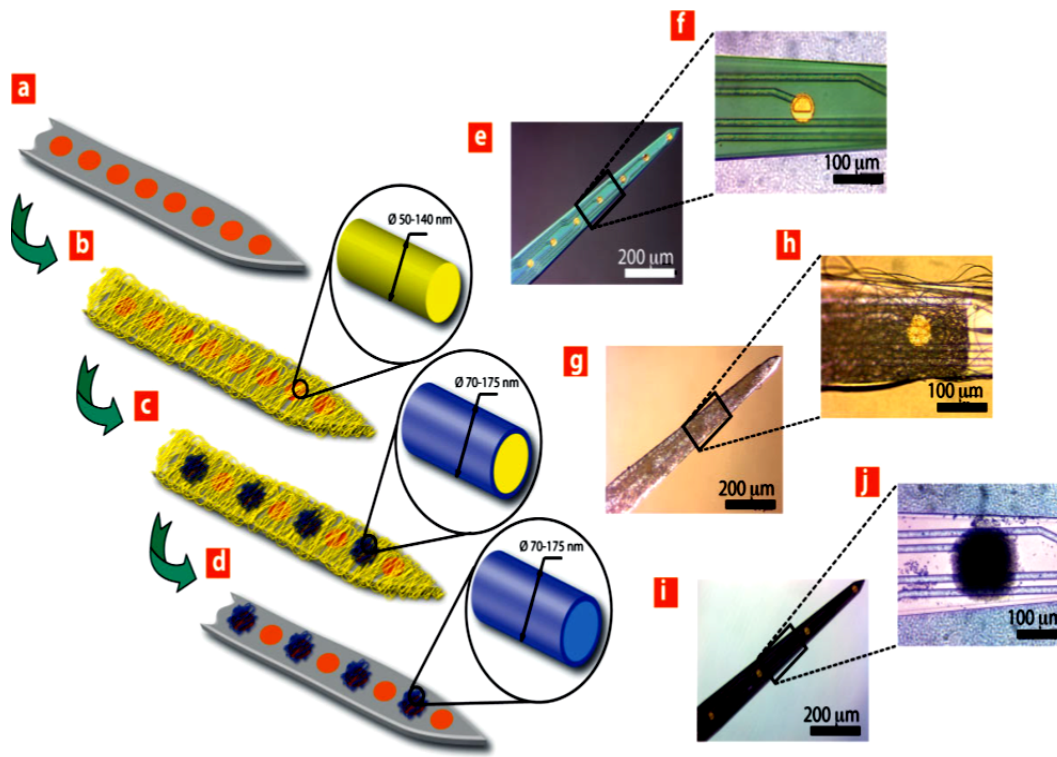


Figure 1-20. Schematic illustration of conducting polymer (PEDOT) nanotube fabrication on neural microelectrodes: (a, b) Electrospinning of polylactic acid (PLLA) nanofibers. (c) Electrochemical deposition of PEDOT. (d) Dissolution of the PLLA core. (e, f) Optical microscopy images of the entire microelectrode (e) and single electrode site (f) before surface modification. (g, h) Optical microscopy images of the entire microelectrode (g) and single electrode site (h) after electrospinning of PLLA nanofibers. (i, j) Optical microscopy images of the entire microelectrode (i) and single electrode site (j) after electrochemical deposition of PEDOT and remove of the PLLA core. Reprinted with permission from Ref. ²¹⁸. Copyright © 2009 Wiley-VCH.

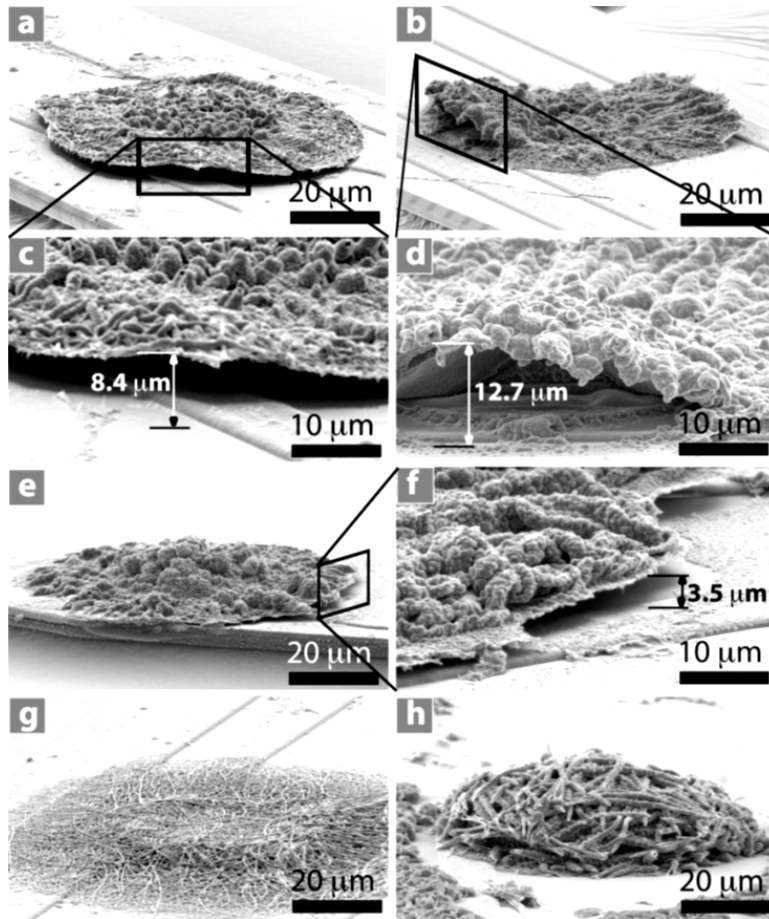


Figure 1-21. Scanning electron microscopy images of conducting polymers after CV measurements on a neural electrode: (a-d) PEDOT film, (e-f) PPy film. The images show delamination on the edge of polymer film. (g) PEDOT nanotubes. (h) PPy nanotubes. In contrast to the films, PPy nanotubes and PEDOT nanotubes remained firmly attached to the neural electrode after CV measurement. Reprinted with permission from Ref. ²¹⁸. Copyright © 2009 Wiley-VCH.

In summary the recent research activities focused on use of nanomaterials in the domain of neural interfacing applications has contributed significantly to our understanding of the development of better biocompatible intracortical microelectrodes. The application of nanomaterials in chronic neural interfaces is still in its infancy despite an impressive body of research that is emerging, partly because of the complexities associated with interacting with neural cells and the mammalian nervous system. Moreover, there are still

fundamental gaps of knowledge regarding the potential toxicity of nanomaterials within the brain that need to be addressed. We believe that there are still tremendous opportunities for nanomaterials to contribute to neural interfacing devices to generate intracortical microelectrodes that can enhance, and improve the current technologies.

Thus, herein, we present a brief outline of the most important future areas of nanomaterials in the chronic neural interfacing applications that need to be investigated:

- Integration of traditional approaches and nanomaterials to design new types of intracortical microelectrodes.
- Development of new types of nanostructured coatings offered by nanomaterials that could also increase the charge injection capacity and reduction of impedance.
- Incorporation of anti-inflammatory agents in the coatings using layer-by-layer self-assembly technique.
- Miniaturization of the traditional intracortical microelectrodes using smaller and more compliant flexible nanomaterials, while maintaining efficient electrochemical function.
- Improvement of electrical and biological properties of the neural tissue-electrode interface.
- Design of easily manufacturable, highly conductive, and mechanically strong and flexible intracortical electrodes using nanomaterials, and conductive and adaptive polymers.
- Investigation the chronic long-term potential toxicity profiles as well as delamination and degradation of nanomaterials over the period of implantation.
- Comprehensive long-term recording and stimulation studies of nanomaterials in animal models.

Finally, these exciting avenues must be tempered with the realization that the toxicity of nanomaterials is still a developing field, and that a better understanding of how nanoscale materials interact with the central nervous system is required before one can use nanomaterials widely in neural interfacing applications.

1.4. REFERENCES

1. C. B. Grundfest H, *J. Neurophysiol.*, 1942, **5**, 275-294.
2. S. R. Grundfest H, W. H. Oettinger, R. W. Gurry, *Rev. Sci. Instrum.*, 1950, **21**, 360-362.
3. F. A. Renshaw B., Morison B.R., *J. Neurophysiol.*, 1940, **3**, 74-105.
4. M. A. L. Nicolelis, *Nat. Rev. Neurosci.*, 2003, **4**, 417-422.
5. L. R. Hochberg, D. Bacher, B. Jarosiewicz, N. Y. Masse, J. D. Simeral, J. Vogel, S. Haddadin, J. Liu, S. S. Cash, P. van der Smagt and J. P. Donoghue, *Nature*, 2012, **485**, 372-375.
6. L. R. Hochberg, M. D. Serruya, G. M. Friehs, J. A. Mukand, M. Saleh, A. H. Caplan, A. Branner, D. Chen, R. D. Penn and J. P. Donoghue, *Nature*, 2006, **442**, 164-171.
7. P. R. Kennedy and R. A. Bakay, *Neuroreport*, 1998, **9**, 1707-1711.
8. P. R. Kennedy, R. A. Bakay, K. Adams and J. Goldwaithe, *IEEE Trans. Rehabil. Eng.*, 2000, **8**, 198-202.
9. P. R. Kennedy, M. T. Kirby, M. M. Moore, B. King and A. Mallory, *IEEE Trans. Neural Syst. Rehabil. Eng.*, 2004, **12**, 339-344.
10. S. Kellis, K. Miller, K. Thomson, R. Brown, P. House and B. Greger, *Conf. Proc. IEEE Eng. Med. Biol. Soc.*, 2010, **2010**, 3827-3830.
11. S. Kellis, K. Miller, K. Thomson, R. Brown, P. House and B. Greger, *J. Neural Eng.*, 2010, **7**, 056007.
12. M. A. Lebedev and M. A. Nicolelis, *Trends Neurosci.*, 2006, **29**, 536-546.
13. M. P. Ward, P. Rajdev, C. Ellison and P. P. Irazoqui, *Brain Research*, 2009, **1282**, 183-200.
14. P. A. Tresco and B. D. Winslow, *Critical Reviews in Biomedical Engineering*, 2011, **39**, 29-44.
15. X. Liu, D. B. McCreery, L. A. Bullara and W. F. Agnew, *IEEE Trans. Neural Syst. Rehabil. Eng.*, 2006, **14**, 91-100.
16. X. Liu, D. B. McCreery, R. R. Carter, L. A. Bullara, T. G. Yuen and W. F. Agnew, *IEEE Trans. Rehabil. Eng.*, 1999, **7**, 315-326.
17. D. A. Robinson, *Proceedings of the IEEE*, 1968, **56**, 1065-1071.
18. M. J. Nelson, P. Pouget, E. A. Nilsen, C. D. Patten and J. D. Schall, *J. Neurosci. Methods*, 2008, **169**, 141-157.
19. G. Buzsaki, C. A. Anastassiou and C. Koch, *Nat. Rev. Neurosci.*, 2012, **13**, 407-420.
20. S. I. H. Tillery and D. M. Taylor, *Curr. Opin. Neurobiol.*, 2004, **14**, 758-762.
21. D. M. Taylor, S. I. Tillery and A. B. Schwartz, *Science*, 2002, **296**, 1829-1832.
22. V. Gilja, C. A. Chestek, I. Diester, J. M. Henderson, K. Deisseroth and K. V. Shenoy, *IEEE Trans. Biomed. Eng.*, 2011, **58**, 1891-1899.
23. J. P. Donoghue, *Neuron*, 2008, **60**, 511-521.
24. M. R. Neuman, in *The Biomedical Engineering Handbook*, ed. J. D. Bronzino, CRC Press LLC, Boca Raton, 2000.

25. B. D. Burns, J. P. Stean and A. C. Webb, *Electroencephalogr. Clin. Neurophysiol.*, 1974, **36**, 314-318.
26. K. A. Ludwig, J. D. Uram, J. Yang, D. C. Martin and D. R. Kipke, *J Neural Eng*, 2006, **3**, 59-70.
27. M. A. Freire, E. Morya, J. Faber, J. R. Santos, J. S. Guimaraes, N. A. Lemos, K. Sameshima, A. Pereira, S. Ribeiro and M. A. Nicolelis, *PLoS One*, 2011, **6**, e27554.
28. A. Prasad, Q.-S. Xue, V. Sankar, T. Nishida, G. Shaw, W. J. Streit and J. C. Sanchez, *J. Neural Eng.*, 2012, **9**, 056015.
29. A. Prasad, Q. S. Xue, V. Sankar, T. Nishida, G. Shaw, W. J. Streit and J. C. Sanchez, *J. Neural Eng.*, 2012, **9**.
30. B. D. Winslow, M. B. Christensen, W. K. Yang, F. Solzbacher and P. A. Tresco, *Biomaterials*, 2010.
31. B. D. Winslow and P. A. Tresco, *Biomaterials*, 2010, **31**, 1558-1567.
32. R. Biran, D. C. Martin and P. A. Tresco, *Exp Neurol*, 2005, **195**, 115-126.
33. R. Biran, D. C. Martin and P. A. Tresco, *Journal of biomedical materials research. Part A*, 2007, **82**, 169-178.
34. C. S. Bjornsson, S. J. Oh, Y. A. Al-Kofahi, Y. J. Lim, K. L. Smith, J. N. Turner, S. De, B. Roysam, W. Shain and S. J. Kim, *J. Neural Eng.*, 2006, **3**, 196-207.
35. A. A. Sharp, A. M. Ortega, D. Restrepo, D. Curran-Everett and K. Gall, *IEEE Trans Biomed Eng*, 2009, **56**, 45-53.
36. S. R. Goldstein and M. Salcman, *IEEE Trans. Biomed. Eng.*, 1973, **20**, 260-269.
37. D. J. Edell, V. V. Toi, V. M. McNeil and L. D. Clark, *IEEE Trans. Biomed. Eng.*, 1992, **39**, 635-643.
38. J. P. Harris, A. E. Hess, S. J. Rowan, C. Weder, C. A. Zorman, D. J. Tyler and J. R. Capadona, *J. Neural Eng.*, 2011, **8**, 040610.
39. J. P. Harris, J. R. Capadona, R. H. Miller, B. C. Healy, K. Shanmuganathan, S. J. Rowan, C. Weder and D. J. Tyler, *J. Neural Eng.*, 2011, **8**, 066011.
40. S. R. I. Gabran, M. T. Salam, J. Dian, Y. El-Hayek, J. L. Perez-Velazquez, R. Genov, P. L. Carlen, M. M. A. Salama and R. R. Mansour, *Neural Systems and Rehabilitation Engineering, IEEE Transactions on*, 2013, **PP**, 1-12.
41. W. Jensen, K. Yoshida and U. G. Hofmann, *Biomedical Engineering, IEEE Transactions on*, 2006, **53**, 934-940.
42. A. A. Sharp, A. M. Ortega, D. Restrepo, D. Curran-Everett and K. Gall, *Biomedical Engineering, IEEE Transactions on*, 2009, **56**, 45-53.
43. W. Jensen, U. G. Hofmann and K. Yoshida, *Engineering in Medicine and Biology Society*, 2003. Proceedings of the 25th Annual International Conference of the IEEE, 2003.
44. D. Egert, R. L. Peterson and K. Najafi, *Solid-State Sensors, Actuators and Microsystems Conference (TRANSDUCERS)*, 2011 16th International, 2011.
45. T. ChunXiang and H. Jiping, *Engineering in Medicine and Biology Society*, 2005. IEEE-EMBS 2005. 27th Annual International Conference of the, 2005.
46. B. A. Wester, R. H. Lee and M. C. LaPlaca, *J. Neural Eng.*, 2009, **6**, 024002.

47. F. Beer, E. R. Johnston, J. DeWolf and D. Mazurek, *Mechanics of Materials*, 6 edn., McGraw-Hill, 2011.
48. G. C. McConnell, T. M. Schneider, D. J. Owens and R. V. Bellamkonda, *IEEE Trans. Biomed. Eng.*, 2007, **54**, 1097-1107.
49. A. E. Hess, K. A. Potter, D. J. Tyler, C. A. Zorman and J. R. Capadona, *J. Vis. Exp.*, 2013, **78**, e50078.
50. P. J. Rousche, D. S. Pellinen, D. P. Pivin, J. C. Williams, R. J. Vetter and D. R. Kipke, *IEEE Trans Biomed Eng*, 2001, **48**, 361-371.
51. J. Subbaroyan and D. R. Kipke, Conf. Proc. IEEE Eng. Med. Biol. Soc., 2006.
52. S. Takeuchi, D. Ziegler, Y. Yoshida, K. Mabuchi and T. Suzuki, *Lab Chip*, 2005, **5**, 519-523.
53. B. A. Wester, R. H. Lee and M. C. LaPlaca, *J Neural Eng*, 2009, **6**, 024002.
54. L. J. Fernandez, A. Altuna, M. Tijero, G. Gabriel, R. Villa, M. J. Rodriguez, M. Batlle, R. Vilares, J. Berganzo and F. J. Blanco, *Journal of Micromechanics and Microengineering*, 2009, **19**, 025007.
55. A. Mercanzini, P. Colin, J. C. Bensadoun, A. Bertsch and P. Renaud, *IEEE Trans. Biomed. Eng.*, 2009, **56**, 1909-1918.
56. Y. Lu, D. Wang, T. Li, X. Zhao, Y. Cao, H. Yang and Y. Y. Duan, *Biomaterials*, 2009, **30**, 4143-4151.
57. S. Lacour, S. Benmerah, E. Tarte, J. FitzGerald, J. Serra, S. McMahon, J. Fawcett, O. Graudejus, Z. Yu and B. Morrison, III, *Med. Biol. Eng. Comput.*, 2010, **48**, 945-954.
58. P. J. Rousche, D. S. Pellinen, D. P. Pivin, Jr., J. C. Williams, R. J. Vetter and D. R. Kipke, *Biomedical Engineering, IEEE Transactions on*, 2001, **48**, 361-371.
59. K. Lee, A. Singh, J. He, S. Massia, B. Kim and G. Raupp, *Sensors and Actuators B: Chemical*, 2004, **102**, 67-72.
60. K.-K. Lee, J. He, A. Singh, S. Massia, G. Ehteshami, B. Kim and G. Raupp, *Journal of Micromechanics and Microengineering*, 2004, **14**, 32-37.
61. A. Singh, K. Lee, J. He, G. Ehteshami, S. Massia and G. Raupp, Engineering in Medicine and Biology Society, 2003. Proceedings of the 25th Annual International Conference of the IEEE, 2003.
62. R. S. Clement, A. Singh, B. Olson, K. Lee and J. He, Engineering in Medicine and Biology Society, 2003. Proceedings of the 25th Annual International Conference of the IEEE, 2003.
63. K. Lee, J. He and L. Wang, *P Ann Int Ieee Embs*, 2004, **26**, 4326-4329.
64. K. Lee, J. He, R. Clement, S. Massia and B. Kim, *Biosens. Bioelectron.*, 2004, **20**, 404-407.
65. A. Singh, H. X. Zhu and J. P. He, *P Ann Int Ieee Embs*, 2004, **26**, 4298-4301.
66. A. del Campo and C. Greiner, *J. Micromech. Microeng.*, 2007, **17**, R81-R95.
67. A. Altuna, L. M. de la Prida, E. Bellistri, G. Gabriel, A. Guimera, J. Berganzo, R. Villa and L. J. Fernandez, *Biosens. Bioelectron.*, 2012, **37**, 1-5.

68. L. J. Fernández, A. Altuna, M. Tijero, G. Gabriel, R. Villa, M. J. Rodríguez, M. Batlle, R. Vilares, J. Berganzo and F. J. Blanco, *J. Micromech. Microeng.*, 2009, **19**, 025007.
69. M. Tijero, G. Gabriel, J. Caro, A. Altuna, R. Hernandez, R. Villa, J. Berganzo, F. J. Blanco, R. Salido and L. J. Fernandez, *Biosens. Bioelectron.*, 2009, **24**, 2410-2416.
70. A. Altuna, G. Gabriel, L. M. d. l. Prida, M. Tijero, A. Guimerá, J. Berganzo, R. Salido, R. Villa and L. J. Fernández, *J. Micromech. Microeng.*, 2010, **20**, 064014.
71. A. Altuna, E. Bellistri, E. Cid, P. Aivar, B. Gal, J. Berganzo, G. Gabriel, A. Guimera, R. Villa, L. J. Fernandez and L. Menendez de la Prida, *Lab Chip*, 2013, **13**, 1422-1430.
72. V. N. Vernekar, D. K. Cullen, N. Fogleman, Y. Choi, A. J. Garcia, M. G. Allen, G. J. Brewer and M. C. LaPlaca, *Journal of Biomedical Materials Research Part A*, 2009, **89A**, 138-151.
73. L. A. Guo and S. P. DeWeerth, *2009 Annual International Conference of the Ieee Engineering in Medicine and Biology Society, Vols 1-20*, 2009, 1619-1622.
74. S. A. Nikles, D. S. Pellinen, J. Kitagawa, R. M. Bradley, D. R. Kipke and K. Najafi, *Engineering in Medicine and Biology Society*, 2003. Proceedings of the 25th Annual International Conference of the IEEE, 2003.
75. S. Takeuchi, T. Suzuki, K. Mabuchi and H. Fujita, *Journal of Micromechanics and Microengineering*, 2004, **14**, 104-107.
76. T. D. Kozai and D. R. Kipke, *J. Neurosci. Methods*, 2009.
77. K.-K. Lee, J. He, A. Singh and B. Kim, *Proceedings of the International Conference on MEMS, NANO and Smart Systems*, 2003, 418- 422.
78. L. Kee-Keun and et al., *J. Micromech. Microeng.*, 2004, **14**, 32.
79. M. McClain, I. Clements, R. Shafer, R. Bellamkonda, M. LaPlaca and M. Allen, *Biomed Microdevices*, 2011, **13**, 361-373.
80. T. Li, Z. G. Suo, S. P. Lacour and S. Wagner, *J. Mater. Res.*, 2005, **20**, 3274-3277.
81. J. Xiao, A. Carlson, Z. J. Liu, Y. Huang, H. Jiang and J. A. Rogers, *Appl. Phys. Lett.*, 2008, **93**, 013109-013109-013103.
82. Y. Kato, I. Saito, T. Hoshino, T. Suzuki and K. Mabuchi, *2006 28th Annual International Conference of the IEEE Engineering in Medicine and Biology Society, Vols 1-15*, 2006, 5444-5447.
83. P. J. Gilgunn, R. Khilwani, T. D. Y. Kozai, D. J. Weber, X. T. Cui, G. Erdos, O. B. Ozdoganlar and G. K. Fedder, *IEEE 25th International Conference on Micro Electro Mechanical Systems (MEMS)*, 2012.
84. D. Y. Lewitus, K. L. Smith, W. Shain, D. Bolikal and J. Kohn, *Biomaterials*, 2011, **32**, 5543-5550.
85. X. Cui, V. A. Lee, Y. Raphael, J. A. Wiler, J. F. Hetke, D. J. Anderson and D. C. Martin, *J. Biomed. Mater. Res.*, 2001, **56**, 261-272.
86. Y. Lu, D. Wang, T. Li, X. Zhao, Y. Cao, H. Yang and Y. Y. Duan, *Biomaterials*, 2009, **30**, 4143-4151.
87. L. Rao, H. Zhou, T. Li, C. Li and Y. Y. Duan, *Acta Biomater.*, 2012, **8**, 2233-2242.

88. D.-H. Kim, J. A. Wiler, D. J. Anderson, D. R. Kipke and D. C. Martin, *Acta Biomater.*, 2010, **6**, 57-62.
89. G. Lind, C. E. Linsmeier, J. Thelin and J. Schouenborg, *J. Neural Eng.*, 2010, **7**, 046005.
90. T. D. Y. Kozai and D. R. Kipke, *J. Neurosci. Methods*, 2009, **184**, 199-205.
91. K.-K. Lee, J. He, A. Singh, S. Massia, G. Ehteshami, B. Kim and G. Raupp, *J. Micromech. Microeng.*, 2004, **14**, 32.
92. A. A. Sharp, H. V. Panchawagh, A. Ortega, R. Artale, S. Richardson-Burns, D. S. Finch, K. Gall, R. L. Mahajan and D. Restrepo, *J. Neural Eng.*, 2006, **3**, L23.
93. D. Lewitus, K. L. Smith, W. Shain and J. Kohn, *Acta Biomater.*, 2011, **7**, 2483-2491.
94. M. H. R. Magno, J. Kim, A. Srinivasan, S. McBride, D. Bolikal, A. Darr, J. O. Hollinger and J. Kohn, *J. Mater. Chem.*, 2010, **20**, 8885-8893.
95. D. Lewitus, R. J. Vogelstein, G. H. Zhen, Y. S. Choi, J. Kohn, S. Harshbarger and X. F. Jia, *IEEE Trans. Neural Syst. Rehabil. Eng.*, 2011, **19**, 204-212.
96. P. Bawa, V. Pillay, Y. E. Choonara and L. C. du Toit, *Biomedical Materials*, 2009, **4**, 022001.
97. C. d. I. H. Alarcon, S. Pennadam and C. Alexander, *Chem. Soc. Rev.*, 2005, **34**, 276-285.
98. M. A. C. Stuart, W. T. S. Huck, J. Genzer, M. Muller, C. Ober, M. Stamm, G. B. Sukhorukov, I. Szleifer, V. V. Tsukruk, M. Urban, F. Winnik, S. Zauscher, I. Luzinov and S. Minko, *Nat. Mater.*, 2010, **9**, 101-113.
99. M. W. Urban, ed., *Handbook of Stimuli-Responsive Materials*, 1 edn., Wiley-VCH, 2011.
100. J. F. Mano, *Adv. Eng. Mater.*, 2008, **10**, 515-527.
101. D. Roy, J. N. Cambre and B. S. Sumerlin, *Prog. Polym. Sci.*, 2010, **35**, 278-301.
102. J. R. Capadona, D. J. Tyler, C. A. Zorman, S. J. Rowan and C. Weder, *MRS Bull.*, 2012, **37**, 581-589.
103. T. Ware, D. Simon, R. L. Rennaker and W. Voit, *Polym. Rev. (Philadelphia, PA, U. S.)*, 2013, **53**, 108-129.
104. J. R. Capadona, K. Shanmuganathan, D. J. Tyler, S. J. Rowan and C. Weder, *Science*, 2008, **319**, 1370-1374.
105. K. Shanmuganathan, J. R. Capadona, S. J. Rowan and C. Weder, *Prog. Polym. Sci.*, 2010, **35**, 212-222.
106. K. Shanmuganathan, J. R. Capadona, S. J. Rowan and C. Weder, *ACS Appl. Mater. Interfaces*, 2010, **2**, 165-174.
107. A. Hess, J. Dunning, J. Harris, J. R. Capadona, K. Shanmuganathan, S. J. Rowan, C. Weder, D. J. Tyler and C. A. Zorman, Solid-State Sensors, Actuators and Microsystems Conference, 2009.
108. A. E. Hess, J. R. Capadona, K. Shanmuganathan, L. Hsu, S. J. Rowan, C. Weder, D. J. Tyler and C. A. Zorman, *J. Micromech. Microeng.*, 2011, **21**, 054009.
109. K. Shanmuganathan, J. R. Capadona, S. J. Rowan and C. Weder, *J. Mater. Chem.*, 2010, **20**, 180-186.

110. K. A. Potter, A. C. Buck, W. K. Self and J. R. Capadona, *J. Neural Eng.*, 2012, **9**, 046020.
111. J. K. Nguyen, K. A. Potter-Baker, D. J. Park, J. L. Skousen, A. Hess, D. J. Tyler, S. J. Rowan, C. Weder and J. R. Capadona, *Acta Biomater.*, 2014, Under Revision.
112. T. Ware, D. Simon, D. E. Arreaga-Salas, J. Reeder, R. Rennaker, E. W. Keefer and W. Voit, *Adv. Funct. Mater.*, 2012, **22**, 3470-3479.
113. A. Lendlein and S. Kelch, *Angewandte Chemie International Edition*, 2002, **41**, 2034-2057.
114. C. Liu, H. Qin and P. T. Mather, *J. Mater. Chem.*, 2007, **17**, 1543-1558.
115. T. Ware, D. Simon, K. Hearon, C. Liu, S. Shah, J. Reeder, N. Khodaparast, M. P. Kilgard, D. J. Maitland, R. L. Rennaker and W. E. Voit, *Macromol. Mater. Eng.*, 2012, **297**, 1193-1202.
116. T. Ware, D. Simon, C. Liu, T. Musa, S. Vasudevan, A. Sloan, E. W. Keefer, R. L. Rennaker and W. Voit, *Journal of Biomedical Materials Research Part B: Applied Biomaterials*, 2013, 10.1002/jbmb.32946.
117. L. W. Tien, F. Wu, M. D. Tang-Schomer, E. Yoon, F. G. Omenetto and D. L. Kaplan, *Adv. Funct. Mater.*, 2013, **23**, 3185-3193.
118. A. W. Bridges and A. J. García, *Journal of diabetes science and technology*, 2008, **2**, 984-994.
119. J. Leach, A. K. H. Achyuta and S. K. Murthy, *Front. Neuroengineering*, 2010, **2**.
120. W. He, G. C. McConnell, T. M. Schneider and R. V. Bellamkonda, *Adv. Mater.*, 2007, **19**, 3529-3533.
121. E. Azemi, C. F. Lagenaur and X. T. Cui, *Biomaterials*, 2011, **32**, 681-692.
122. E. Azemi, W. R. Stauffer, M. S. Gostock, C. F. Lagenaur and X. T. Cui, *Acta Biomater*, 2008.
123. K. Webb, E. Budko, T. J. Neuberger, S. Chen, M. Schachner and P. A. Tresco, *Biomaterials*, 2001, **22**, 1017-1028.
124. A. H. Taub, R. Hogri, A. Magal, M. Mintz and Y. Shacham-Diamand, *Journal of Biomedical Materials Research Part A*, 2012, **100A**, 1854-1858.
125. X. Cui, V. A. Lee, Y. Raphael, J. A. Wiler, J. F. Hetke, D. J. Anderson and D. C. Martin, *J Biomed Mater Res*, 2001, **56**, 261-272.
126. W. He and R. V. Bellamkonda, *Biomaterials*, 2005, **26**, 2983-2990.
127. D. H. Kim, S. M. Richardson-Burns, J. L. Hendricks, C. Sequera and D. C. Martin, *Adv. Funct. Mater.*, 2007, **17**, 79-86.
128. D. H. Kim and D. C. Martin, *Biomaterials*, 2006, **27**, 3031-3037.
129. Y. Zhong and R. V. Bellamkonda, *J. Controlled Release*, 2005, **106**, 309-318.
130. S. Chen and M. G. Allen, *MRS Bull.*, 2012, **37**, 606-613.
131. R. Wadhwa, C. F. Lagenaur and X. T. Cui, *J. Controlled Release*, 2006, **110**, 531-541.
132. D.-H. Kim and D. C. Martin, *Biomaterials*, 2006, **27**, 3031-3037.
133. Y. Zhong and R. V. Bellamkonda, *Brain Res.*, 2007, **1148**, 15-27.
134. M. R. Abidian and D. C. Martin, *Adv. Funct. Mater.*, 2009, **19**, 573-585.

135. A. Mercanzini, S. T. Reddy, D. Velluto, P. Colin, A. Maillard, J. C. Bensadoun, J. A. Hubbell and P. Renaud, *J. Controlled Release*, 2010, **145**, 196-202.
136. S. P. Massia, M. M. Holecko and G. R. Ehteshami, *Journal of Biomedical Materials Research Part A*, 2004, **68A**, 177-186.
137. W. R. Stauffer and X. T. Cui, *Biomaterials*, 2006, **27**, 2405-2413.
138. W. He, G. C. McConnell and R. V. Bellamkonda, *J. Neural Eng.*, 2006, **3**, 316.
139. E. Azemi, W. R. Stauffer, M. S. Gostock, C. F. Lagenaur and X. T. Cui, *Acta Biomater.*, 2008, **4**, 1208-1217.
140. C. L. Kolarcik, D. Bourbeau, E. Azemi, E. Rost, L. Zhang, C. F. Lagenaur, D. J. Weber and X. T. Cui, *Acta Biomater.*, 2012, **8**, 3561-3575.
141. R. A. Green, G. J. Suaning, L. A. Poole-Warren and N. H. Lovell, *Neural Engineering*, 2009. NER '09. 4th International IEEE/EMBS Conference on, 2009.
142. G. Kang, R. B. Borgens and Y. Cho, *Langmuir*, 2011, **27**, 6179-6184.
143. K. A. Potter-Baker, J. K. Nguyen, K. M. Kovach, M. M. Gitomer, T. W. Srail, W. G. Stewart, J. L. Skousen and J. R. Capadona, *Journal of Materials Chemistry B*, 2014, **Under Review**.
144. P. Heiduschka, I. Romann, H. Ecken, M. Schöning, W. Schuhmann and S. Thanos, *Electrochim. Acta*, 2001, **47**, 299-307.
145. S. P. Massia, S. S. Rao and J. A. Hubbell, *The Journal of Biological Chemistry*, 1993, **268**, 8053-8059.
146. R. A. Green, N. H. Lovell and L. A. Poole-Warren, *Biomaterials*, 2009, **30**, 3637-3644.
147. R. A. Green, N. H. Lovell and L. A. Poole-Warren, *Acta Biomater.*, 2010, **6**, 63-71.
148. R. A. Green, P. B. Matteucci, R. T. Hassarati, B. Giraud, C. W. D. Dodds, S. Chen, P. J. Byrnes-Preston, G. J. Suaning, L. A. Poole-Warren and N. H. Lovell, *J. Neural Eng.*, 2013, **10**, 016009.
149. S. Cutler, *Biomaterials*, 2003, **24**, 1759-1770.
150. R. McClelland, E. Wauthier, J. Uronis and L. Reid, *Tissue Eng. Part A*, 2008, **14**, 59-70.
151. C. Huet, C. Pisselet, B. Mandon-Pepin, P. Monget and D. Monniaux, *J. Endocrinol.*, 2001, **169**, 347-360.
152. T. L. Sellaro, A. K. Ravindra, D. B. Stolz and S. F. Badylak, *Tissue Eng.*, 2007, **13**, 2301-2310.
153. J. M. Singelyn, J. A. DeQuach, S. B. Seif-Naraghi, R. B. Littlefield, P. J. Schup-Magoffin and K. L. Christman, *Biomaterials*, 2009, **30**, 5409-5416.
154. M. M. Stern, R. L. Myers, N. Hammam, K. A. Stern, D. Eberli, S. B. Kritchevsky, S. Soker and M. Van Dyke, *Biomaterials*, 2009, **30**, 2393-2399.
155. Y. Zhang, Y. He, S. Bharadwaj, N. Hammam, K. Carnagey, R. Myers, A. Atala and M. Van Dyke, *Biomaterials*, 2009, **30**, 4021-4028.
156. S. Badylak, J. Obermiller, L. Geddes and R. Matheny, *Heart Surg. Forum*, 2003, **6**, E20-26.
157. B. N. Brown, J. E. Valentin, A. M. Stewart-Akers, G. P. McCabe and S. F. Badylak, *Biomaterials*, 2009, **30**, 1482-1491.

158. N. K. Guimard, N. Gomez and C. E. Schmidt, *Prog. Polym. Sci.*, 2007, **32**, 876-921.
159. R. Ravichandran, S. Sundarrajan, J. R. Venugopal, S. Mukherjee and S. Ramakrishna, *J. Royal Soc. Interface*, 2010, **7**, S559-S579.
160. K. A. Ludwig, J. D. Uram, J. Yang, D. C. Martin and D. R. Kipke, *J. Neural Eng.*, 2006, **3**, 59-70.
161. X. Cui, J. F. Hetke, J. A. Wiler, D. J. Anderson and D. C. Martin, *Sensors and Actuators A: Physical*, 2001, **93**, 8-18.
162. C. J. Buchko, K. M. Kozloff and D. C. Martin, *Biomaterials*, 2001, **22**, 1289-1300.
163. Y. H. Zhong and R. V. Bellamkonda, *J. Controlled Release*, 2005, **106**, 309-318.
164. J. Yang and D. C. Martin, *Sensors and Actuators B: Chemical*, 2004, **101**, 133-142.
165. A. R. Harris, S. J. Morgan, J. Chen, R. M. I. Kapsa, G. G. Wallace and A. G. Paolini, *J. Neural Eng.*, 2013, **10**, 016004.
166. R. A. Green, N. H. Lovell, G. G. Wallace and L. A. Poole-Warren, *Biomaterials*, 2008, **29**, 3393-3399.
167. *Indwelling Neural Implants: Strategies for Contending with the In Vivo Environment*, Boca Raton (FL): CRC Press, 2008.
168. D.-H. Kim, M. Abidian and D. C. Martin, *Journal of Biomedical Materials Research Part A*, 2004, **71A**, 577-585.
169. P. M. George, A. W. Lyckman, D. A. LaVan, A. Hegde, Y. Leung, R. Avasare, C. Testa, P. M. Alexander, R. Langer and M. Sur, *Biomaterials*, 2005, **26**, 3511-3519.
170. C. E. Schmidt, V. R. Shastri, J. P. Vacanti and R. Langer, *Proceedings of the National Academy of Sciences*, 1997, **94**, 8948-8953.
171. J. B. Schlenoff and H. Xu, *J. Electrochem. Soc.*, 1992, **139**, 2397-2401.
172. X. Cui and D. C. Martin, *Sensors and Actuators B: Chemical*, 2003, **89**, 92-102.
173. Y. Xiao, X. Cui, J. M. Hancock, M. Bouguettaya, J. R. Reynolds and D. C. Martin, *Sensors and Actuators B: Chemical*, 2004, **99**, 437-443.
174. J. Yang, D. H. Kim, J. L. Hendricks, M. Leach, R. Northey and D. C. Martin, *Acta Biomater.*, 2005, **1**, 125-136.
175. S. M. Richardson-Burns, J. L. Hendricks, B. Foster, L. K. Povlich, D.-H. Kim and D. C. Martin, *Biomaterials*, 2007, **28**, 1539-1552.
176. S. M. Richardson-Burns, J. L. Hendricks and D. C. Martin, *J. Neural Eng.*, 2007, **4**, L6-L13.
177. K. A. Ludwig, N. B. Langhals, M. D. Joseph, S. M. Richardson-Burns, J. L. Hendricks and D. R. Kipke, *J. Neural Eng.*, 2011, **8**, 014001.
178. T. D. Y. Kozai, N. B. Langhals, P. R. Patel, X. P. Deng, H. N. Zhang, K. L. Smith, J. Lahann, N. A. Kotov and D. R. Kipke, *Nat. Mater.*, 2012, **11**, 1065-1073.
179. H. Yamato, M. Ohwa and W. Wernet, *J. Electroanal. Chem.*, 1995, **397**, 163-170.
180. Z. Aguilar, *Nanomaterials for Medical Applications*, 1 edn., Elsevier, 2012.
181. M. R. Mozafari, ed., *Nanomaterials and Nanosystems for Biomedical Applications*, 1 edn., Springer, 2007.
182. Michael Giersig and G. B. Khomutov, eds., *Nanomaterials for Application in Medicine and Biolog*, 1 edn., Springer, 2008.

183. D. R. Merrill, M. Bikson and J. G. R. Jefferys, *J. Neurosci. Methods*, 2005, **141**, 171-198.
184. G. A. Silva, *Nat. Rev. Neurosci.*, 2006, **7**, 65-74.
185. J. S. Mohammed, M. A. DeCoster and M. J. McShane, *Biomacromolecules*, 2004, **5**, 1745-1755.
186. H. Ai, H. Meng, I. Ichinose, S. A. Jones, D. K. Mills, Y. M. Lvov and X. Qiao, *J. Neurosci. Methods*, 2003, **128**, 1-8.
187. N. A. Kotov, J. O. Winter, I. P. Clements, E. Jan, B. P. Timko, S. Campidelli, S. Pathak, A. Mazzatenta, C. M. Lieber, M. Prato, R. V. Bellamkonda, G. A. Silva, N. W. S. Kam, F. Patolsky and L. Ballerini, *Adv. Mater.*, 2009, **21**, 3970-4004.
188. A. P. Alivisatos, A. M. Andrews, E. S. Boyden, M. Chun, G. M. Church, K. Deisseroth, J. P. Donoghue, S. E. Fraser, J. Lippincott-Schwartz, L. L. Looger, S. Masmanidis, P. L. McEuen, A. V. Nurmikko, H. Park, D. S. Peterka, C. Reid, M. L. Roukes, A. Scherer, M. Schnitzer, T. J. Sejnowski, K. L. Shepard, D. Tsao, G. Turrigiano, P. S. Weiss, C. Xu, R. Yuste and X. Zhuang, *ACS Nano*, 2013, **7**, 1850-1866.
189. C. M. Voge and J. P. Stegemann, *J. Neural Eng.*, 2011, **8**, 011001.
190. Y. Hanein and L. Bareket-Keren, *Frontiers in Neural Circuits*, 2013, **6**.
191. M. Mattson, R. Haddon and A. Rao, *J. Mol. Neurosci.*, 2000, **14**, 175-182.
192. M. K. Gheith, T. C. Pappas, A. V. Liopo, V. A. Sinani, B. S. Shim, M. Motamedi, J. P. Wicksted and N. A. Kotov, *Adv. Mater.*, 2006, **18**, 2975-2979.
193. M. K. Gheith, V. A. Sinani, J. P. Wicksted, R. L. Matts and N. A. Kotov, *Adv. Mater.*, 2005, **17**, 2663-2670.
194. E. B. Malarkey, K. A. Fisher, E. Bekyarova, W. Liu, R. C. Haddon and V. Parpura, *Nano Lett.*, 2008, **9**, 264-268.
195. V. Lovat, D. Pantarotto, L. Lagostena, B. Cacciari, M. Grandolfo, M. Righi, G. Spalluto, M. Prato and L. Ballerini, *Nano Lett.*, 2005, **5**, 1107-1110.
196. H. Hu, Y. Ni, V. Montana, R. C. Haddon and V. Parpura, *Nano Lett.*, 2004, **4**, 507-511.
197. K. Wang, H. A. Fishman, H. Dai and J. S. Harris, *Nano Lett.*, 2006, **6**, 2043-2048.
198. A. Mazzatenta, M. Giugliano, S. Campidelli, L. Gambazzi, L. Businaro, H. Markram, M. Prato and L. Ballerini, *J. Neurosci.*, 2007, **27**, 6931-6936.
199. G. Cellot, E. Cilia, S. Cipollone, V. Rancic, A. Sucapane, S. Giordani, L. Gambazzi, H. Markram, M. Grandolfo, D. Scaini, F. Gelain, L. Casalis, M. Prato, M. Giugliano and L. Ballerini, *Nat. Nanotechnol.*, 2009, **4**, 126-133.
200. E. W. Keefer, B. R. Botterman, M. I. Romero, A. F. Rossi and G. W. Gross, *Nat. Nanotechnol.*, 2008, **3**, 434-439.
201. X. Luo, C. L. Weaver, D. D. Zhou, R. Greenberg and X. T. Cui, *Biomaterials*, 2011, **32**, 5551-5557.
202. G. Baranauskas, E. Maggiolini, E. Castagnola, A. Ansaldo, A. Mazzoni, G. N. Angotzi, A. Vato, D. Ricci, S. Panzeri and L. Fadiga, *J. Neural Eng.*, 2011, **8**, 066013.

203. Y. Lu, T. Li, X. Q. Zhao, M. Li, Y. L. Cao, H. X. Yang and Y. W. Y. Duan, *Biomaterials*, 2010, **31**, 5169-5181.
204. C.-M. Lin, Y.-T. Lee, S.-R. Yeh and W. Fang, *Biosens. Bioelectron.*, 2009, **24**, 2791-2797.
205. H.-L. Hsu, I. J. Teng, Y.-C. Chen, W.-L. Hsu, Y.-T. Lee, S.-J. Yen, H.-C. Su, S.-R. Yeh, H. Chen and T.-R. Yew, *Adv. Mater.*, 2010, **22**, 2177-2181.
206. Y.-C. Chen, H.-L. Hsu, Y.-T. Lee, H.-C. Su, S.-J. Yen, C.-H. Chen, W.-L. Hsu, T.-R. Yew, S.-R. Yeh, D.-J. Yao, Y.-C. Chang and H. Chen, *J. Neural Eng.*, 2011, **8**, 034001.
207. T. Gabay, M. Ben-David, I. Kalifa, R. Sorkin, Z. e. R. Abrams, E. Ben-Jacob and Y. Hanein, *Nanotechnology*, 2007, **18**, 035201.
208. Y. Hanein, *physica status solidi (b)*, 2010, **247**, 2635-2640.
209. T. D. B. Nguyen-Vu, H. Chen, A. M. Cassell, R. Andrews, M. Meyyappan and J. Li, *Small*, 2006, **2**, 89-94.
210. J. Li, T. D. B. Nguyen-Vu, H. Chen, A. M. Cassell, R. J. Andrews and M. Meyyappan, *IEEE Trans. Biomed. Eng.*, 2007, **54**, 1121-1128.
211. S. Agarwal, X. Zhou, F. Ye, Q. He, G. C. K. Chen, J. Soo, F. Boey, H. Zhang and P. Chen, *Langmuir*, 2010, **26**, 2244-2247.
212. N. Li, X. Zhang, Q. Song, R. Su, Q. Zhang, T. Kong, L. Liu, G. Jin, M. Tang and G. Cheng, *Biomaterials*, 2011, **32**, 9374-9382.
213. M. Lv, Y. Zhang, L. Liang, M. Wei, W. Hu, X. Li and Q. Huang, *Nanoscale*, 2012, **4**, 3861-3866.
214. C. H. Chen, C. T. Lin, J. J. Chen, W. L. Hsu, Y. C. Chang, S. R. Yeh, L. J. Li and D. J. Yao, Solid-State Sensors, Actuators and Microsystems Conference (TRANSDUCERS), 2011 16th International, 2011.
215. X. Luo, C. L. Weaver, S. Tan and X. T. Cui, *Journal of Materials Chemistry B*, 2013, **1**, 1340-1348.
216. M. R. Abidian and D. C. Martin, *Biomaterials*, 2008, **29**, 1273-1283.
217. M. R. Abidian, K. A. Ludwig, T. C. Marzullo, D. C. Martin and D. R. Kipke, *Adv. Mater.*, 2009, **21**, 3764-3770.
218. M. R. Abidian, J. M. Corey, D. R. Kipke and D. C. Martin, *Small*, 2010, **6**, 421-429.

Chapter 2 – Scope and Objectives

The overarching goal of this dissertation was to develop physiologically responsive mechanically adaptive materials that can be used to create adaptive implants for neural interfacing applications. Targeting materials with new property matrices that can contribute to developing an understanding for the causes of chronic neuroinflammatory responses of intracortical implants, the objectives of the present thesis were as follows:

1. To ensure reliable insertion of mechanically morphing intracortical electrodes and to reduce their cross-sectional area, it is desirable to increase the initial stiffness of physiologically responsive mechanically adaptive nanocomposites above the maximum achievable with previously reported materials (tensile storage modulus > 5 GPa). Thus, one aim of the present thesis was to explore mechanically adaptive biologically inspired nanocomposites based on poly(vinyl alcohol) as the matrix and cellulose nanocrystals derived from tunicates and cotton as the filler. This design was based on the hypothesis that the use of a polar glassy polymer that promotes significant matrix-nanocellulose interactions would result in stiffer nanocomposites than previously employed matrices. A systematic study of this system is reported in Chapter 3.
2. Based on the previous findings that anti-oxidant treatment can prevent microelectrode-mediated neurodegeneration and blood-brain barrier breach, and the hypothesis that the mechanical mismatch plays a dominant role in reactive gliosis at the microelectrode tissue interface, another objective of the present dissertation was to develop *in-situ* softening antioxidant-releasing polymeric materials, which can serve to explore if the combination of two independently effective mechanisms – softening and anti-oxidant release – leads to synergistic effect in reducing the neuroinflammation at the intracortical microelectrode-tissue interface. Thus, in Chapter 4, curcumin-releasing mechanically adaptive implants based on poly(vinyl

alcohol) and optionally cellulose nanocrystals are reported. These materials were used to create implants for an *in-vivo* study in rats, in which the faith of the cortical tissue surrounding the implants was investigated. After 4 weeks, the new curcumin-releasing, mechanically adaptive implants promoted a higher neuron survival and a more stable blood-brain barrier than the neat poly(vinyl alcohol) controls, but the benefits of the curcumin release were lost after 12 weeks, where both sets of compliant materials (with and without curcumin) had no statistically significant differences in neuronal density distribution profiles. To explore to what extent the poly(vinyl alcohol) matrix was responsible for this outcome, drug-releasing, mechanically adaptive materials based on poly(vinyl acetate), cellulose nanocrystals, and the anti-oxidants curcumin or resveratrol were made and studied. The related study is reported in Chapter 5.

3. Finally, an objective of the present dissertation was to further extend the concept of adaptive neural interfacing materials, which were initially developed to create mechanically morphing intracortical *electrodes*, to optogenetic applications. Thus, Chapter 6 discusses the first examples of physiologically responsive mechanically adaptive optical fibers for this purpose. The hypothesis was that mechanically adaptive optical fibers, which could penetrate the cortical tissue and become soft in response to the brain fluid, may mitigate the neuroinflammatory response in chronic optogenetic applications. The mechanical and optical properties of this new class of materials were investigated *in vitro* and compared to those of conventional optical fibers used in optogenetic studies.

In summary, several materials design approaches were pursued to create new materials for intracortical implants with built-in functions that are designed to reduce the glial scar formation around the implant. In Chapter 7 the most relevant results and insights gained from the experiments conducted are summarized and general conclusions are drawn in consideration of the *in-vivo* studies that are so far available. In addition, possible future directions are discussed.

Chapter 3 – Physiologically Responsive Mechanically Adaptive Bio-Nanocomposites for Biomedical Applications²

3.1. ABSTRACT

We report mechanically adaptive bio-nanocomposites based on poly(vinyl alcohol) (PVA) and cellulose nanocrystals (CNCs), whose mechanical properties change significantly upon exposure to simulated physiological conditions. These nanocomposites were made using CNCs derived from tunicates (t-CNCs) and cotton (c-CNCs) to explore how aspect ratio, surface charge density, and filler content influence the mechanical properties. Dynamic mechanical analysis data reveal a significant enhancement of the tensile storage modulus (E') upon introduction of CNCs, which scaled with the CNC type and content. For example, in the dry, glassy state at 25 °C, E' increased up to 23% (for c-CNCs) and 88% (for t-CNCs) compared to the neat polymer. Exposing the materials to simulated physiological conditions caused a drastic softening of the materials, from 9.0 GPa to 1 MPa for c-CNCs and from 13.7 GPa to 160 MPa for t-CNCs. The data show that the swelling characteristics of the nanocomposites and the extent of mechanical switching could be influenced via the amount and type of CNCs and also the processing conditions. The high stiffness in the dry state and the ability to tailor the mechanical contrast via composition and processing makes the new materials particularly useful as basis for adaptive biomedical implants.

²This chapter is adapted from Jorfi, M.; Robert, M.N.; Foster, E.J.; Weder, C. *ACS Applied Materials & Interfaces* **2013**, 5, 1517–1526. Matthew Robert prepared and characterized c-CNCs based materials.

3.2. INTRODUCTION

Materials that selectively respond to external stimuli are often referred to as “smart”, “intelligent”, or “adaptive” due to their intrinsic ability to change their physical or chemical properties on command.^{1, 2} Among many other uses, they have garnered significant attention due to their potential applications in biomedical and biotechnological fields,³⁻⁵ including their use as transient implants,^{6, 7} drug delivery carriers,^{8, 9} tissue-engineering scaffolds,^{10, 11} thermoresponsive hydrogels,¹² self-healing materials,^{13, 14} cell cultures,¹⁵ bioseparation membranes,¹⁶ sensors and actuators.^{17, 18} One intriguing feature exhibited by some of these materials is their ability to change mechanical properties “on command”.¹⁹ One recently demonstrated approach for the design of such materials relies on the preparation of polymer-based nanocomposites, which are comprised of a polymeric matrix and reinforcing nanofibers, whose interactions are stimuli-responsive and regulate the mechanical properties of the bulk material.^{19, 20} In a recent study Korley *et al.* extended this concept to polymer composites based on electrospun nanofibers as the filler, where mechanical morphing is achieved by changing the properties of the filler and not filler-filler or filler-matrix interactions.²¹

Amongst many potential nanofillers, crystalline cellulose nanofibers, referred to as “nanowhiskers”, have been widely investigated.²²⁻²⁵ Cellulose nanocrystals (CNCs) can be isolated from a variety of sources, including plants (e.g. wood, cotton, or wheat straw), marine animals (tunicates), as well as bacterial sources, such as algae, fungi, and amoeba (protozoa).²² Using CNCs isolated from tunicates, Favier *et al.* reported the first CNC-reinforced polymer nanocomposites in 1995. These materials displayed substantially enhanced mechanical properties, which were explained with the formation of a percolating, hydrogen-bonded network of CNCs within the polymer matrix.^{26, 27} This initial work was followed by a large number of studies that explored the reinforcement of a plethora of polymer matrices with CNC from a broad range of sources.^{19, 20, 22, 25} The widespread interest in CNC-based nanocomposites is explained by the low cost, outstanding mechanical properties, availability, sustainability, biodegradability, and low density of CNCs.

In a series of contributions, we demonstrated that the stiffness of CNC-based nanocomposites can be reversibly changed by controlling the degree of interactions between the rigid filler.^{20, 28-33} The CNCs form a percolating network within the matrix that is – amongst several contributing intermolecular forces – primarily held together by hydrogen-bonds among the surface hydroxyl groups, although CNC-polymer interactions also as important as other systems in which interactions between filler and polymer matrix play an important role.³⁴⁻³⁶ This causes a significant reinforcement of the polymer matrix. Upon exposure to chemicals that can competitively hydrogen-bond to the CNCs or interfere with intermolecular van der Waals forces, e.g. water, the interactions between individual CNCs are reduced and the nanocomposite softens considerably, as predicted by mechanical models. Our first generation of such mechanically adaptive nanocomposites was based on a rubbery ethylene oxide-epichlorohydrin copolymer (EO-EPI) and t-CNCs.^{28, 37} Incorporation of 19% v/v t-CNCs into EO-EPI results in an increase of the storage modulus, E' , from 3.7 MPa (neat EO-EPI) to 800 MPa (EO-EPI/t-CNC nanocomposite) at 25 °C. These materials undergo a pronounced and reversible modulus reduction from 800 to 20 MPa upon exposure to water. Plasticization of the polymer matrix upon aqueous swelling has been shown to reinforce the effect, for example in nanocomposites based on poly(vinyl acetate) (PVAc) and t-CNCs or c-CNCs.^{29, 30} The PVAc/t-CNC nanocomposites showed an increase of the E' from 1.8 GPa (neat PVAc) to 5.2 GPa for a nanocomposite containing 16.5% v/v t-CNCs. Due to the glassy nature of the PVAc matrix, these materials exhibit a much higher initial stiffness than the EO-EPI based systems, but soften greatly (5.2 GPa to 12 MPa) upon exposure to water due to matrix plasticization and t-CNCs decoupling.

We have shown that such biologically-inspired mechanically adaptive materials are potentially useful as substrates for medical devices, for example intracortical microelectrodes.^{38, 39} Such neural prosthetic devices, which connect the brain with the outside world, promise to be useful for many clinical applications, but it has proven difficult to achieve long-term connectivity, presumably on account of the mechanical-mismatch between current electrode materials and the cortical tissue.⁴⁰ Initial *in-vivo*

experiments with PVAc/t-CNC nanocomposites suggest that mechanically adaptive intracortical neural prosthetics can more rapidly stabilize neural cell populations at the interface than rigid systems, which bodes well for improving the functionality of intracortical devices.^{39, 41} The realization of such intracortical electrodes,³⁸ and other medical devices would benefit significantly, if mechanically adaptive materials with a higher than currently available stiffness ($E' = 5.2$ GPa)³⁰ could be made available. Thus, we have explored mechanically adaptive stimuli-responsive nanocomposites based on PVA as the matrix and CNCs derived from tunicates (t-CNCs) and cotton (c-CNCs) as the filler. This design was based on the hypothesis that the use of a polar glassy polymer that promotes significant matrix-CNC interactions would result in stiffer nanocomposites than previously employed matrices. With this perspective, PVA was chosen for this purpose because it can be water-soluble (depending on the degree of hydrolysis and heat treatment),⁴² and has many hydroxyl groups that can interact with the surface hydroxyls of CNCs. Moreover, PVA is biocompatible, nontoxic and already used in a wide variety of biomedical applications such as contact lenses⁴³⁻⁴⁵ and FDA-approved nerve grafts.⁴⁶ Several studies have reported PVA-based nanocomposites with t-CNCs⁴⁷ and c-CNCs,⁴⁸⁻⁵⁰ as well as microfibrillated cellulose.⁵¹ While previous work has shown dynamic mechanical properties of such nanocomposites by exposing them to humid atmosphere, we herein investigate the dynamic mechanical properties by complete submersion into a simulated physiological fluid to explore the properties under more relevant conditions for use in biomedical applications. We demonstrate that by particular processing conditions, it is possible to control the aqueous swelling of the material and the degree of softening it experiences.

3.3. EXPERIMENTAL SECTION

Materials. Poly(vinyl alcohol) (PVA) 99% hydrolyzed ($M_w = 85,000$ - $124,000$ g/mol; $\delta = 1.26$ g/mL) and all reagents were purchased from Sigma-Aldrich and used without further purification. Artificial cerebrospinal fluid (ACSF) was prepared by dissolving the following materials in 1 L of deionized water: NaCl = 7.25 g, KCl = 0.22 g, NaHCO₃ =

2.18 g, $\text{CaCl}_2 \cdot 2\text{H}_2\text{O} = 0.29$ g, $\text{KH}_2\text{PO}_4 = 0.17$ g, $\text{MgSO}_4 \cdot 7\text{H}_2\text{O} = 0.25$ g, and *D*-glucose = 1.80 g.⁵² A literature value of 1.46 g/mL was used for the density of the CNCs.⁵³

Isolation of Cellulose Nanocrystals from Tunicates. t-CNCs were isolated from tunicates (*Styela clava*) collected from floating docks in Point View Marina (Narragansett, RI). The t-CNCs were prepared by sulfuric acid hydrolysis of the cellulose pulp. The protocol was based on the method described by Favier *et al.*,²⁶ utilized modifications reported by Shanmuganathan *et al.*,³⁰ and relied on minor changes that are detailed in the Appendix.

Isolation of Cellulose Nanocrystals from Cotton. c-CNCs were isolated from Whatman filter paper with minor modifications to a previously published procedure.⁵⁴ After sulfuric acid hydrolysis and dialysis treatment, the resulting dispersion was sonicated for 3 h and left to settle at room temperature for 18 h. The supernatant was then decanted off and the c-CNC dispersion was spray-dried using a Büchi Mini Spray Dryer (Model B-191) to yield dried c-CNCs as a white powder. The drying parameters were an inlet temperature of 110 °C, a flow rate of 4 mL/min, a nozzle airflow of 700 mL/min, an aspiration rate of 70%, and an outlet temperature of 60 °C.

Preparation of PVA/CNC Nanocomposites. Lyophilized t-CNCs or spray-dried c-CNCs were dispersed in deionized water at a concentration of 5 mg/mL by sonicating for 10 h and 7 h, respectively. PVA was dissolved in deionized water at a concentration of 50 mg/mL by stirring for 2 h at 90 °C. Nanocomposites comprising 4-16% v/v CNCs were prepared by combining the appropriate amounts of the CNC dispersion and PVA solution to cast a film weighing 1 g. This mixture was stirred at room temperature for 30 min, followed by sonication for 30 min, and the resulting homogeneous mixtures were cast into Teflon Petri dishes of a diameter of 100 mm. The dishes were placed into an oven at 35 °C for 5 days to evaporate the water, and the resulting films were then further dried in the oven at 70 °C for 24 h. The films were compression-molded between spacers in a Carver laboratory press (1000 psi for 2 min, followed by an increase of pressure to 2000

psi for 15 min). Unless otherwise stated, PVA/t-CNC films were compression-molded at 150 °C, and PVA/c-CNC films were compression molded at 120 °C. Both types of films were allowed to cool to ~70 °C over the course of ca. 90 min under the applied pressure to yield 70-100 µm thin nanocomposite films. The thickness of the films was measured using an electronic digital caliper (Fowler) and micrometer (Millimess Inductive Digital Comparator Extramess 200, Mahr). For reference purposes, neat PVA films were prepared in a similar manner by solution-casting and subsequent compression-molding at 120 °C and 150 °C.

Atomic Force Microscopy (AFM). Atomic force microscopy was carried out on a NanoWizard II (JPK Instruments) microscope. 10 µL of dilute aqueous CNC dispersions (0.1 mg/mL) were deposited onto freshly cleaved mica (SPI Supplies Division of Structure Probe, Inc.) and allowed to dry at 70 °C for 2 h. The scans were performed in tapping mode in air using silicon cantilevers (NANO WORLD, TESPA-50) with a scan rate of 1 line/sec.

Transmission Electron Microscopy (TEM). The dimensions of the CNCs and the homogeneity of the CNC dispersion in the PVA/CNC nanocomposites were examined by transmission electron microscopy (TEM) using a Hitachi H-1700 microscope operating at an accelerating voltage of 75 kV. To assess the CNCs dimensions, lyophilized CNCs were dispersed in deionized water at a concentration of 0.1 mg/mL by sonication. Subsequently, 3 µL of the aqueous CNC dispersions were deposited on carbon-coated grids (Electron Microscopy Sciences) and allowed to dry at 70 °C for 2 h. CNC dimensions were determined by analyzing 10 TEM images of CNCs with a total of more than 100 individual CNCs of which length and width were measured. The dimensions thus determined are reported as average values ± standard error.

Conductometric Titration. Conductometric titrations were performed to quantify the surface charges of CNCs. 50 mg of the CNCs were suspended into 10-15 mL of aqueous 0.01 M hydrochloric acid. After 5 min of stirring and 30 min of sonication, the

suspensions were titrated with 0.01 M NaOH. The titration curves were evaluated by considering the following three regions: the titration of the excess of HCl, a weak acid corresponding to the sulfate-ester surface groups, a finally the excess NaOH present after titration of all of the acid (see Figure A3-1 in the Appendix). The three regions were separately fit to lines, and the volume of NaOH used to titrate the sulfate-ester groups was determined by the volume comprised within the points at which the linear fits intersect one another (shown graphically in Figure A3-1). To assess the accuracy of this titration volume with regard to other weakly acidic species being in solution, such as dissolved CO₂, a blank titration was performed without CNCs present in solution. This volume was calculated to be 0.08 mL of NaOH and was subtracted from the volumes determined for titrations containing CNCs to further calculate the sulfate charge density. The concentration of sulfate groups was calculated following the equation:

$$\frac{\text{mmol } SO_4^-}{\text{kg cellulose}} = \frac{C_{NaOH} * V_{NaOH}}{W_{CNC}} * 10^6 \quad (3 - 1)$$

where, C_{NaOH} is the concentration of the base (0.01 M), V_{NaOH} is the volume (L) of NaOH used to titrate the weak acid, and W_{CNC} is the weight of S-CNCs employed for the measurement (g).

Swelling Behavior. The swelling behavior of the PVA/CNC nanocomposites was investigated by immersing the materials in artificial cerebrospinal fluid (ACSF) at human body temperature (37 °C) over the course of 2 months. The degree of swelling was determined by measuring the weight of the samples pre- and post-swelling:

$$\text{Degree of swelling (\%)} = \frac{\text{Mass of wet sample} - \text{Mass of dry sample}}{\text{Mass of dry sample}} \times 100 \quad (3 - 2)$$

To minimize the error in measuring the degree of swelling, once the wet samples were taken out of the ACSF, they were placed on paper tissue to wick any excess ACSF from the surface; the samples were then immediately weighed.

Dynamic Mechanical Analysis (DMA). The mechanical properties of the PVA/CNC nanocomposites were characterized by dynamic mechanical analysis (DMA) using a TA Instruments Model Q800. Tests were conducted in tensile mode using a temperature sweep method (0-140 °C) at a fixed frequency of 1 Hz, a strain amplitude of 30 μm , a heating rate of 5 °C/min and a gap distance between the jaws of \sim 10 mm. The samples were prepared by cutting strips from the films with a width of \sim 6 mm. To determine the mechanical properties of the films in the wet state, the samples were swelled in ACSF at 37 °C for periods of 1 week and 1 month. DMA experiments were conducted in tensile mode with a submersion clamp, which allowed measurements while the samples were immersed in ACSF. In this case, the temperature sweeps were done in the range of 23-75 °C with a heating rate of 1 °C/min, a constant frequency of 1 Hz, a strain amplitude of 30 μm and a fixed gap distance between jaws of 15 mm.

Stress-Strain Measurements. Stress-strain measurements of PVA/CNCs nanocomposites were performed using a TA Instruments Model Q800 dynamic mechanical analyzer. Tests were carried out at 25 °C with a strain rate of 0.5%/min, a preload force of 0.01N, a gap distance between the jaws of \sim 10 mm, and using dog-bone shaped films having a width of 2.1 mm. Tensile moduli were calculated from the slopes of the linear region between 0 and 0.3% strain.

Differential Scanning Calorimetry (DSC). Differential scanning calorimetry experiments were carried out with a Mettler Toledo STAR instrument under N₂ atmosphere. The typical procedure included heating and cooling cycles of approximately 10 mg sample in a DSC pan from -50 to 250 °C using a heating rate of 10 °C/min. The glass transition temperature (T_g) was determined from the midpoint of the specific heat increment at the glass-rubber transition, while the melting temperature (T_m) was taken by the highest temperature point of the melting endotherm.

3.4. RESULTS AND DISCUSSION

3.4.1. Isolation and Physical Properties of Cellulose Nanocrystals

The CNCs used in this study were isolated from tunicates (t-CNCs) and cotton (c-CNCs) by sulfuric acid hydrolysis, using protocols that represent modified versions of well-established methods. In the case of c-CNCs, spray-drying was used to isolate the dry CNCs (see Experimental Section). Polymer nanocomposites with t-CNCs have consistently been shown to exhibit superior mechanical properties than those with c-CNCs, a fact that is mainly credited to their higher aspect ratio (~ 70 vs. ~ 10),^{23, 24} and on-axis stiffness (tensile modulus ~ 143 vs. ~ 105 GPa).^{55, 56} c-CNCs, on the other hand, are more viable for commercial exploitation, because they are isolated from an abundant and sustainable bio-source. Due to their high density of strongly interacting surface hydroxyl groups, CNCs have a strong tendency for self-association.^{37, 54, 57} Transmission electron microscopy (TEM) and atomic force microscopy (AFM) images of the CNCs confirm that re-dispersion of the dried materials in water is readily possible (Figure 3-1, and Figures A3-2, A3-3, and A3-4). The dimensions of the t-CNCs, determined from TEM micrographs, were an average length and width of 2500 ± 1000 nm and 30 ± 5 nm, respectively. The average aspect ratio (A , defined as length to width ratio, l/w) of the t-CNCs is therefore 83. The charge density of negatively charged sulfate esters on the CNC surface that are introduced during hydrolysis has been suggested to modulate CNC-CNC interactions and to affect their dispersability. By conductometric titration, the density of sulfate groups of the present t-CNCs was determined to be ~ 75 mmol/kg (Figure A3-1a in the Appendix).

The c-CNCs used here were measured to have an average length and width of 220 ± 70 nm and 22 ± 6 nm, respectively, resulting in an aspect ratio of 10. In addition to exhibiting a lower aspect ratio than the t-CNCs, the charge density on the surface of c-CNCs (~ 25 mmol/kg, Figures A3-1b and A3-1c in the Appendix), is significantly lower than that of t-CNCs. While t-CNCs were dried and isolated by lyophilization, spray-drying was used for c-CNCs. In order to assess any influence of the drying process on the physical properties of the c-CNCs, one batch of as-prepared c-CNCs was, after dialysis

and sonication, split into two portions, which were dried by lyophilization and spray drying, respectively. TEM and conductometric titration data suggest that the drying method has no influence on the physical dimensions of the c-CNCs or on their surface charge density and morphology (Figures A3-1, A3-2, and A3-3).

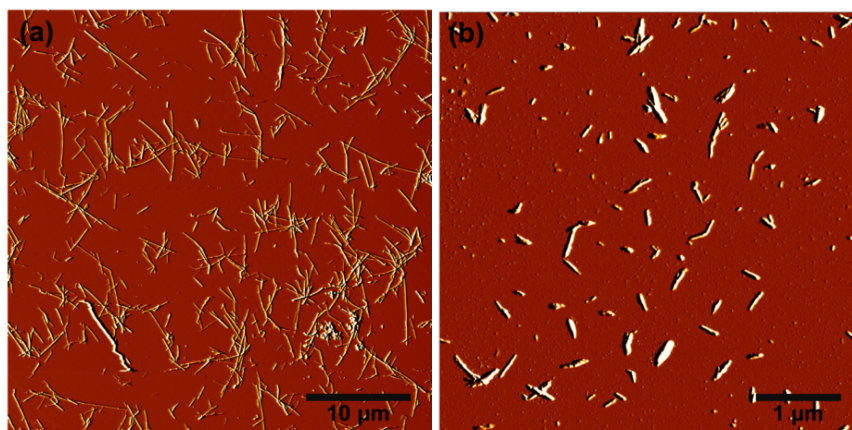


Figure 3-1. AFM amplitude images for (a) lyophilized t-CNCs, and (b) spray-dried c-CNCs deposited from aqueous dispersions (0.1 mg/mL) onto freshly cleaved mica surfaces.

3.4.2. Nanocomposite Processing

PVA solutions and CNC dispersions were combined, and after solution-casting and evaporation of solvent, the resulting films were re-shaped by compression-molding to result films of the nanocomposite with 4-16% v/v CNCs and a thickness of 70-100 μm . Due to the limited thermal stability of the nanocomposites above the melting temperature (T_m) of PVA (~ 220 $^{\circ}\text{C}$), the films were compressed at a temperature much below T_m . PVA/t-CNC nanocomposites were compression-molded at 150 $^{\circ}\text{C}$ without any visible color changes, while PVA/c-CNC nanocomposites yellowed, when processed at this temperature (Figure A5 in the Appendix). As a consequence, PVA/c-CNC nanocomposites were processed at 120 $^{\circ}\text{C}$, unless otherwise noted. Several explanations have been proposed in the literature regarding the degradation of CNCs,⁵⁸⁻⁶⁰ and we speculate the differences in thermal degradation arise from differences related to the source of CNCs.

3.4.3. Thermal Properties

The thermal properties of PVA/CNC nanocomposites were determined using differential scanning calorimetry (DSC, Table 3-1). The DSC curves (Figure A3-6 in the Appendix) show that the T_g (68 and 71 °C) and T_m (216 and 217 °C) of the neat PVA only slightly depends on the temperature at which the films were compression-molded. In both cases, the incorporation of CNCs led to an increase of T_g by approximately 10 °C, which interestingly was independent of the CNC content. The T_g of the polymer nanocomposites is strongly influenced by the extent of interactions between nanoparticles and polymer chains.⁶¹ In the present work, both the polymer matrix and reinforcing phase are rather hydrophilic. Hence, strong molecular interactions (hydrogen bonding and/or van der Waals forces) between the polymer and CNCs can be expected, which can restrict the segmental mobility of the macromolecules and thereby increase T_g . A similar trend was found in PVA-based nanocomposites, comprising CNCs,⁵⁰ bacterial cellulose nanocrystals,⁶² or nanoclay particles.⁶³ In addition, upon introduction of CNCs the width of the melting peak increases, and the degree of crystallinity (χ_c) increases slightly. This shows that the CNCs perhaps act as small nucleation sites for the crystallization of PVA. Also this effect was largely independent of the CNC content.

3.4.4. Mechanical Properties of Dry PVA/CNC Nanocomposites

The mechanical properties of the nanocomposites were established using dynamic mechanical analysis (DMA, Table 3-2). Figure 3-3a shows the tensile storage moduli (E') of the PVA/t-CNC nanocomposites and a neat PVA reference film in the dry state as a function of temperature. At room temperature (25 °C), the neat PVA matrix, processed at 150 °C exhibits an E' of 7.3 GPa. Upon increasing the temperature, E' drastically decreases to 840 MPa at 100 °C ($\sim T_g + 30$ °C) due to a transition from the glassy to the rubbery regime at ~ 70 °C, which is seen as a maximum in the $\tan \delta$ curves (Figure 3-2b). PVA/t-CNC nanocomposites containing 4 to 16% v/v t-CNCs showed a significant increase in E' compared to the neat matrix below and above the T_g . At 25 °C, E' increased from 7.3 GPa (neat PVA) to 13.7 GPa for the nanocomposite containing 16% v/v t-CNCs

(Figure 3-2a, and Table 3-2). A more significant reinforcement was observed above T_g . At 100 °C, the nanocomposite containing 16% v/v t-CNCs shows an E' of 5.4 GPa, which represents a seven-fold increase over the stiffness of the neat PVA (840 MPa) at this temperature. At temperatures well above T_g where the softening of the material is attributed to higher polymer chain mobility, the significantly higher stiffness of the nanocomposites at these temperatures supports the notion that a percolating network of stiff CNCs reinforces the surrounding soft polymer matrix. Theoretically, further reinforcement is possible with higher loadings, although practical limitations regarding the brittleness of the material make 16% v/v loading a reasonable upper limit.

Table 3-1. Thermal properties of neat PVA and PVA/CNC nanocomposites as a function of CNC type and content.

Sample	CNC Content (% v/v)	T_g (°C) ^a	T_m (°C) ^a	ΔH_m (J/g)	χ_c (%) ^b
Neat PVA ^c		71	217	43.9	27
PVA/t-CNC	4	81	218	50.2	33
	8	83	214	49.7	34
	12	82	220	48.8	35
	16	82	215	44.1	34
Neat PVA ^d		68	216	49.6	31
PVA/c-CNC	4	79	216	58.5	38
	8	80	213	52.4	36
	12	81	212	47.3	34
	16	82	210	40.9	31

^aThe data obtained from the second heating scan of DSC measurements. ^b $\chi_c = \frac{\Delta H_m}{w\Delta H_0}$, where w is the weight fraction of polymer matrix in the nanocomposites, ΔH_m is the measured melting enthalpy and ΔH_0 is the enthalpy of 100% crystalline PVA (161 J/g).⁶⁴ ^cFilms were compression-molded at 150 °C. ^dFilms were compression-molded at 120 °C.

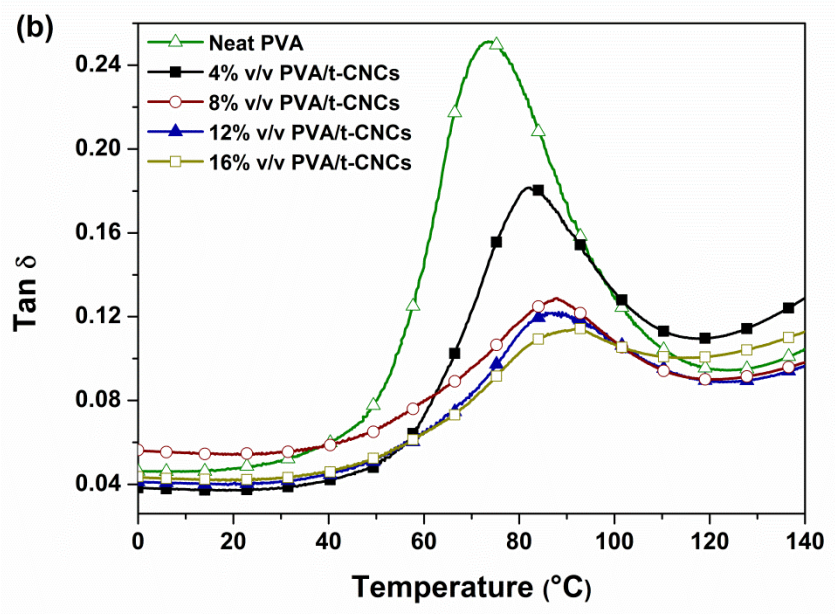
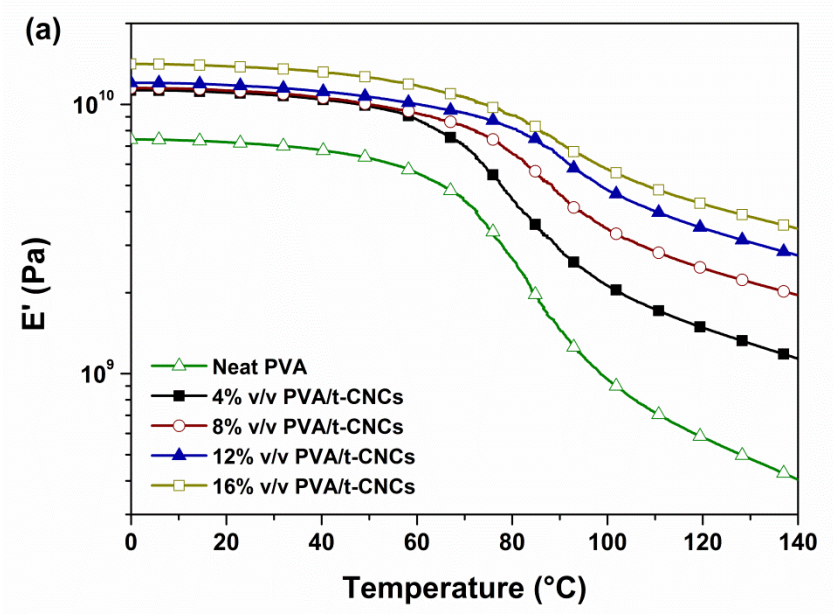
The E' of nanocomposites prepared with c-CNCs exhibits a similar trend as observed for the t-CNC nanocomposites, although the stiffness increase was more modest. As discussed above, PVA/c-CNC nanocomposite films yellowed upon compression molding at 150 °C and were thus processed at 120 °C. At all temperatures, the E' of dry PVA reference films, processed at 120 °C, was found to be slightly lower than that of the neat

PVA processed at 150 °C (Figures 3-2a, 3-2c, Table 3-2). For example, at 25 °C E' values of 7.3 and 7.0 GPa were measured. PVA/c-CNC nanocomposite with 16% v/v c-CNCs exhibited a E' of 9.0 GPa at 25 °C, which is higher than that of the neat PVA (7.0 GPa), but lower than the E' of 13.7 GPa of the t-CNC nanocomposite with the same CNC content. Above T_g (at 100 °C) E' of this nanocomposite was 1.4 GPa, which represent a two-fold enhancement over the stiffness of the neat polymer (Figure 3-2c and Table 3-2). The lower reinforcement displayed by the c-CNCs compared to the t-CNCs is consistent with previous findings and can be attributed to lower aspect ratio and stiffness of c-CNCs.²⁰

Table 3-2. Tensile storage moduli (E') of dry and ACSF-swollen films of neat PVA and PVA/CNC nanocomposites determined by DMA. Data represent averages (N = 4-7).

Sample	CNC Content (% v/v)	Dry Nanocomposites		Swollen Nanocomposites	
		E' at 25 °C (GPa)	E' at 100 °C (GPa)	E' at 37 °C after 1 week in ACSF (MPa)	E' at 37 °C after 1 month in ACSF (MPa)
Neat PVA ^a		7.3	0.84	11.1	6.9
PVA/t-CNC	4	10.5	2.1	45.4	46.8
	8	11.1	3.7	78.3	85.2
	12	11.7	4.7	124	108
	16	13.7	5.4	164	173
	16 ^b	12.3	3.0	60 ^c	n.m.
Neat PVA ^b		7.0	0.7	1.4 ^c	n.m.
PVA/c-CNC	4	6.8	0.5	1.5 ^c	n.m.
	8	7.7	0.8	3.6 ^c	n.m.
	12	8.3	1.0	1.6 ^c	n.m.
	16	9.0	1.4	1.9 ^c	n.m.
	16 ^a	8.4	2.1	13 ^c	n.m.

^aFilms were compression-molded at 150 °C. ^bFilms were compression-molded at 120 °C. ^cSamples were measured after 1 day immersed in ACSF. n.m. = not measured.



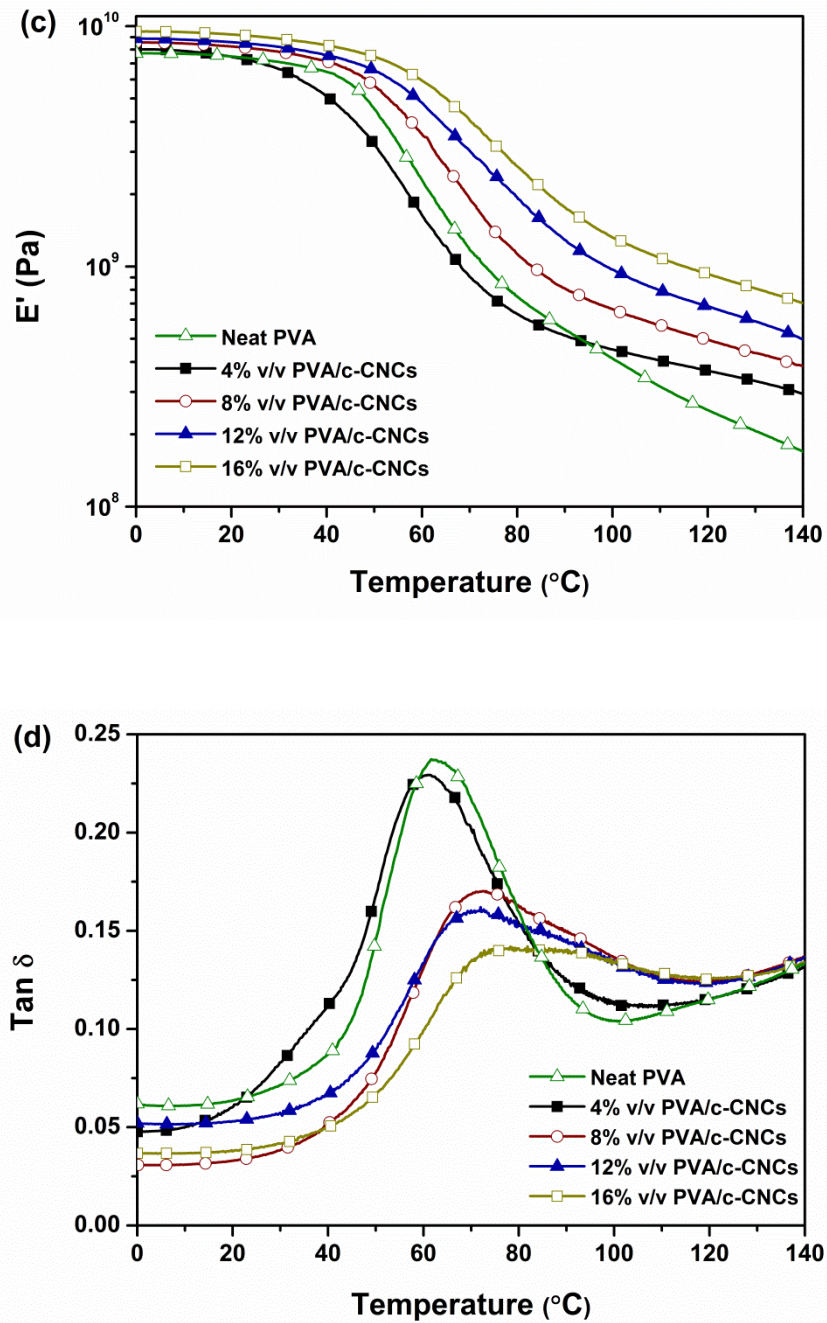


Figure 3-2. Dynamic mechanical analysis (DMA) data of dry PVA and dry PVA/CNC nanocomposites as a function of temperature and CNC content. (a) Tensile storage moduli (E') and (b) loss tangent ($\tan \delta$) of PVA/t-CNC nanocomposites. (c) Tensile storage moduli (E') and (d) loss tangent ($\tan \delta$) of PVA/c-CNC nanocomposites.

Figures 3-2b and 3-2d display the loss factor ($\tan \delta$) curves of neat PVA and the two series of nanocomposites as a function of temperature. $\tan \delta$ is the ratio of loss modulus to storage modulus E''/E' of the material and is indicative of its damping behavior. All curves show a single relaxation peak centered at T_a , which corresponds to the T_g determined by DSC. The introduction of CNCs led to a reduction in peak intensity (I_a) and a shift of T_a to higher temperature compared to the neat PVA films. The peak intensity of the curve is indicative of the magnitude of energy loss due to relaxation processes in the material, which in this case reflect polymer chain relaxation due to the onset of the glass transition. The trend of decreasing I_a and increasing T_a is attributed to the reduced mobility of PVA chains in the amorphous phase due to the presence of the CNCs, but it is, unfortunately, not possible to deduce to what extent CNC-CNC or CNC-PVA interactions contribute to this effect. Above a CNC content of 8% v/v, i.e., in a regime where the CNC concentration is above the percolation threshold, the changes in I_a and T_a seem to level off.

Table 3 shows a comparison of the E' values of the dry PVA/CNC nanocomposites studied here with previously reported mechanically adaptive nanocomposites based on a range of polymer matrices. The data are quoted for a filler content of ~16% v/v. The comparison shows that the stiffness of the present PVA/t-CNC nanocomposites at 25 °C is more than three times higher than that of the stiffest mechanically adaptive nanocomposites reported to date. This implies that a good dispersion of the CNCs has been achieved in the PVA matrix and supports the conclusion that strong molecular interactions such as H-bonding⁵⁰ and/or van der Waals forces⁶⁵ between the CNCs and the polymer matrix indeed increase the reinforcing effect of the cellulose. Similar observations have been reported for other PVA-based nanocomposites with strong polymer-filler interactions.^{50, 66, 67}

Table 3-3. Comparison of tensile storage moduli (E') of current materials with previous mechanically adaptive nanocomposites comprising ~16% v/v of CNCs.

CNC Type	Polymer Matrix	E' of Neat Polymer at 25 °C (GPa)	E' of Nanocomposite at 25 °C (GPa)	Reference
Tunicate	EO-EPI	0.004	0.8	28
Tunicate	PBMA	0.6	3.8	20
Tunicate	PVAc	2.0	5.2	20
Cotton	PVAc	2.0	4.0	29
Tunicate	PVA	7.3 ^a	13.7	this work
Cotton	PVA	7.0 ^b	9.0	this work

^aPVA film was compression-molded at 150 °C. ^bPVA film was compression-molded at 120 °C.

In order to further evaluate the reinforcing effect of the CNCs on the mechanical properties of the nanocomposites, the Young's moduli of the nanocomposites with 8 and 16% v/v CNC content were determined by way of tensile testing (Figure A3-7). The Young's modulus changed in a similar manner as E' (i.e, from 12.2 GPa for the neat PVA to 15.3 and 17.1 GPa for nanocomposites with 8 and 16% v/v t-CNC and to 13.8 and 15.5 GPa for nanocomposites with 8 and 16% v/v c-CNC). The maximum stress increased from 104 MPa for the neat PVA to 130 and 140 MPa for nanocomposites with 8 and 16% v/v t-CNC and to 126 and 110 MPa for nanocomposites with 8 and 16% v/v c-CNC.

3.4.5. Analysis of Mechanical Data in the Framework of the Percolation Model

The mechanical reinforcement in optimally assembled CNC nanocomposites is caused by the formation of a percolating CNC network, in which stress transfer is facilitated by intermolecular interactions between the CNCs.²⁶ The stiffness of these materials can be described by a percolation model that has been successfully used to predict the mechanical behavior of heterogeneous materials, such as polymer blends⁶⁸ and nanocomposites.^{28-30, 37, 69} Detailed information about the percolation model and its use for modeling CNCs-based nanocomposites can be found elsewhere.²⁵ Within the framework of this model, E' of the nanocomposite can be expressed by:

$$E' = \frac{(1 - 2\psi + \psi X_r)E'_s E'_r + (1 - X_r)\psi E'_r{}^2}{(1 - X_r)E'_r + (X_r - \psi)E'_s} \quad (3 - 3)$$

The subscripts s and r refer to the soft phase (polymer matrix) and rigid phase (CNCs), respectively. ψ is the volume fraction of the percolating rigid phase (CNCs) that participates in the load transfer, which can be written as:

$$\psi = X_r \left(\frac{X_r - X_c}{1 - X_c} \right)^{0.4} \quad (3 - 4)$$

Where $X_r \geq X_c$; X_r is the volume fraction of CNCs and X_c is the critical CNC volume fraction (percolation threshold) which was calculated by $0.7/A$. Figures 3-3a and 3-3b show the predictions for the two series of nanocomposites studied here, along with experimentally determined E' values of dry PVA/CNC nanocomposites at 100 °C, i.e., at $\sim T_g + 30$ °C. For the calculations, aspect ratios (A) of 83 and 10 (as determined by TEM) were used for t-CNCs and c-CNCs, respectively, and storage moduli E'_s of 840 MPa (for the PVA processed at 150 °C) and 700 MPa (for the PVA processed at 120 °C) were employed for the neat polymer matrix at 100 °C (as determined by DMA). The tensile storage modulus of the CNC phase, E'_r , was in previous studies derived by either measuring the stiffness of a neat t-CNC or c-CNC film or by fitting the model against the experimentally determined properties of the nanocomposites and using E'_r as a fit parameter. While the morphology (and therewith the stiffness) of a neat CNCs film depends strongly on the processing conditions and has little resemblance to that of a CNC network within a polymer matrix, the E'_r values of 5-24 GPa for t-CNC-based,^{28, 30, 70} and 0.6 - 5 GPa for c-CNC-based^{29, 37, 70} nanocomposites determined by these approaches appeared to roughly match. Interestingly, E'_r values of 80 GPa and 10 GPa are required to fit the model to the data for the t-CNC-based and c-CNC-based nanocomposites with PVA studied here (Figures 3-3a, and 3-3b). A comparison of the data for several other t-CNC-based nanocomposites shows that for a given CNC content, E' increases with the polarity of the polymer matrix (PS³⁷<PVAc³⁰<Epoxy⁷⁰), suggesting that systems with

pronounced CNC-polymer interactions may exhibit larger reinforcement due to factors that are not explicitly accounted for in the percolation model.⁷⁰ This conclusion is consistent with the results of Dufresne and co-workers, who also reported difficulty in fitting data for PVA/c-CNC nanocomposites according to the methods used for similar materials.⁵⁰

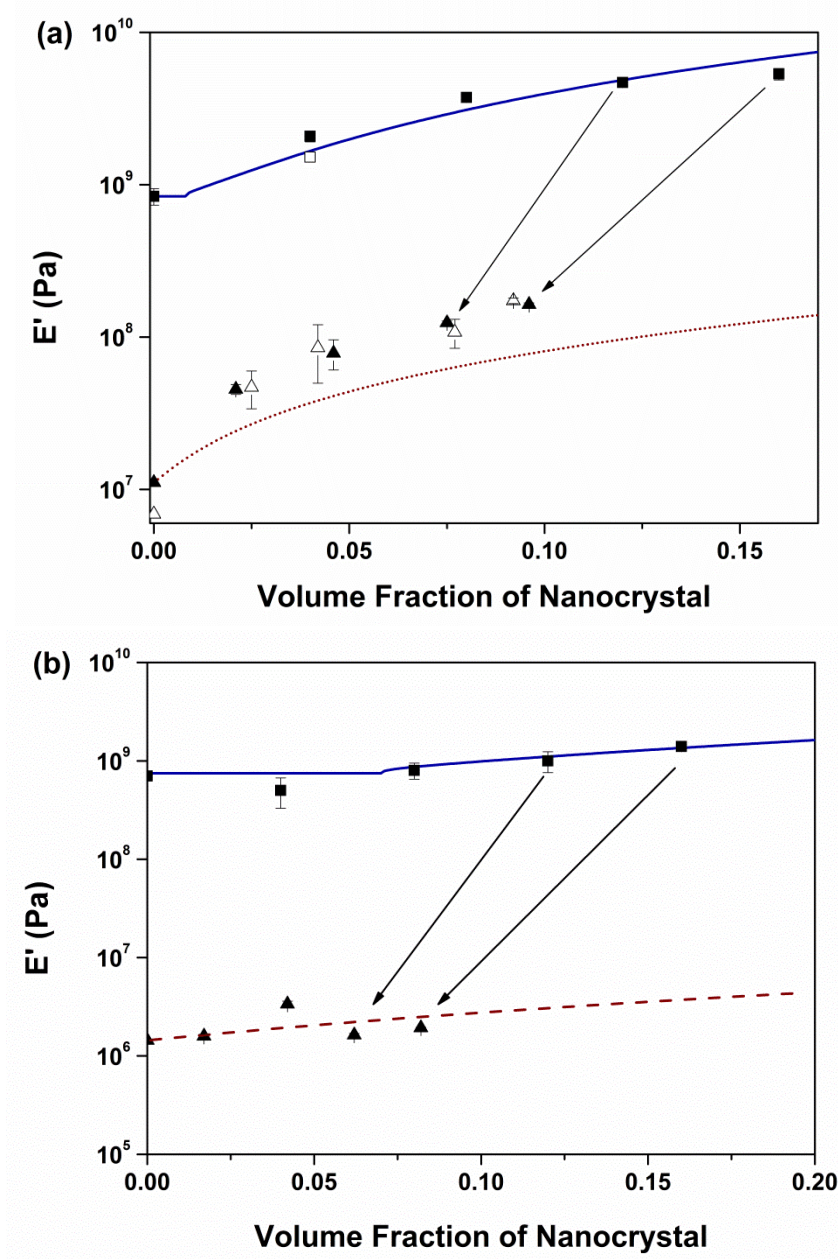


Figure 3-3. (a) Tensile storage moduli (E') of neat PVA and PVA/t-CNC nanocomposites as a function of CNC content in the dry state at 100 °C (\square), re-dried after swelling with ACSF for 1 week (\square), ACSF-swollen after immersion in ACSF at 37 °C for 1 week (\square) and 1 month (Δ). The solid line shows values predicted by the percolation model for the dry state ($E'_r = 80$ GPa). The dotted line shows values predicted by the Halpin-Kardos model for samples conditioned in ACSF at 37 °C ($E'_{tr} = 130$ GPa, $E'_{tr} = 5$ GPa, $E'_s = 11$ MPa, $G'_r = 1.77$ GPa, $G'_s = 3.9$ MPa, $\nu_r = 0.3$, $\nu_s = 0.44$).⁷¹ (b) Tensile storage moduli (E') of neat PVA and PVA/c-CNC nanocomposites as a function of CNC content in the dry state at 100 °C (\square), and ACSF-swollen after immersion in ACSF at 37 °C for 1 week (\square). The solid line shows values predicted by the percolation model ($E'_r = 10$ GPa). The dotted line shows the prediction by the Halpin-Kardos model for samples conditioned in ACSF at 37 °C ($E'_{tr} = 130$ GPa, $E'_{tr} = 5$ GPa, $E'_s = 1.44$ MPa, $G'_r = 1.77$ GPa, $G'_s = 0.5$ MPa, $\nu_r = 0.3$, $\nu_s = 0.44$).⁷¹ Because of solvent uptake the volume fraction of CNCs in ACSF-swollen samples is lower than in the dry state. Data points represent averages of $N = 3-6$ measurements \pm s.d.

3.4.6. Swelling Behavior

The swelling behavior of the nanocomposites in physiological conditions was investigated by immersing the materials into artificial cerebrospinal fluid (ACSF) at 37 °C to mimic physiological conditions. It is known that heat-treated, PVA is no longer water soluble,⁴² and that the processing temperature of PVA affects the permeability of the material and thereby the potential for water uptake.⁷² Indeed, the swelling characteristics of the materials studied here were found to be strongly dependent on the temperature used for compression-molding, but not the type or content of CNCs. Neat PVA and PVA/t-CNC nanocomposite films processed at 150 °C exhibit ~40% w/w swelling, whereas neat PVA films and PVA/c-CNC nanocomposites processed at 120 °C exhibit approximately ~120% w/w swelling (Figure 3-4), regardless of the CNC content. The results indicate that the water uptake of the PVA/CNC nanocomposites is reduced by heat-treatment, likely on account of heat-induced cross-linking.⁷³ The conclusion that the processing temperature is the primary factor for the swelling behavior was further supported by swelling PVA/c-CNC nanocomposites, which were processed at 150 °C, and PVA/t-CNC nanocomposites, which were processed at 120 °C (Figure 3-4). Compared to the other nanocomposites, these samples exhibited swelling that was consistent with their processing temperature rather than the type of CNC. Swelling

experiments in ACSF were extended over the course of two months to investigate the possible changes that might occur during prolonged biological implantation of the material (Table 3-4). The data show that for the PVA/t-CNC nanocomposites processed at 150 °C equilibrium swelling is reached within 24 hours and that these materials do not degrade over the course of two months. Similarly, PVA/c-CNC nanocomposite films reached an equilibrated swelling within 24 hours and maintained their integrity for at least one week. A comparison of the swelling data of the present PVA/t-CNC and the previously investigated PVAc/t-CNC nanocomposites³⁰ shows that the PVA-based nanocomposites swell much less than their PVAc-based counterparts. For instance, the PVAc/t-CNC nanocomposites comprising 16.5% v/v t-CNCs displayed a degree of swelling of ~80%, while the PVA/t-CNC nanocomposites shows ~40% w/w of swelling with 16% v/v CNCs.

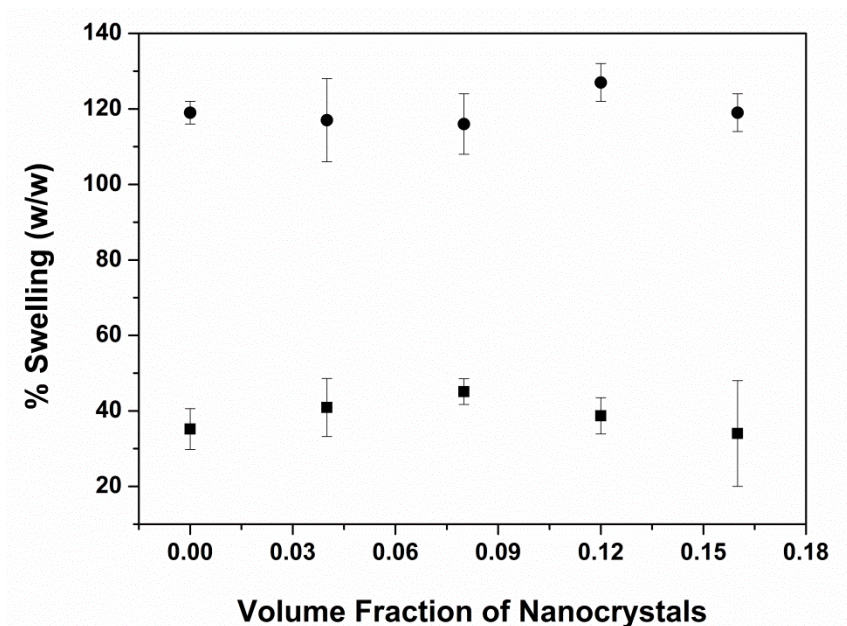


Figure 3-4. Swelling of PVA/t-CNC nanocomposites compression-molded at 150 °C (■), PVA/c-CNC nanocomposites compression-molded at 120 °C (●), a PVA/t-CNC nanocomposite compression-molded at 120 °C (○), and a PVA/c-CNC nanocomposite compression-molded at 150 °C (□) as a function of CNC content, after the samples were immersed in ACSF at 37 °C for 1 day. Data represent averages of N = 3 measurements \pm s.d.

Table 3-4. Swelling data of neat PVA and PVA/t-CNC nanocomposites at 37 °C in ACSF as a function of t-CNC content. Data represent averages ($N = 3$) \pm s.d.

Sample	t-CNC Content (% v/v)	After 1 Day (% w/w)	After 3 Days (% w/w)	After 1 Week (% w/w)	After 1 Month (% w/w)	After 2 Months (% w/w)
Neat PVA		35 \pm 5	43 \pm 4	38 \pm 2	43 \pm 4	45 \pm 6
PVA/t-CNC	4	41 \pm 8	40 \pm 6	48 \pm 2	37 \pm 8	50 \pm 3
	8	45 \pm 3	44 \pm 7	42 \pm 5	47 \pm 9	48 \pm 6
	12	39 \pm 5	46 \pm 9	37 \pm 5	36 \pm 5	46 \pm 8
	16	34 \pm 1	42 \pm 3	40 \pm 8	42 \pm 5	41 \pm 2

3.4.7. Mechanical Properties of ACSF-Swollen Nanocomposites

The mechanical properties of ACSF-swollen PVA/CNC nanocomposites were determined by DMA using a submersion clamp set-up, which allowed the samples to be immersed in ACSF during the measurements. Neat PVA films softened substantially upon submersion in ACSF for one week and exhibited mechanical properties that appear to be correlated with their swelling behavior. Neat PVA films processed at 150 °C displayed a change in E' from ~ 7.3 GPa (dry) to ~ 11 MPa (ACSF-swollen), whereas E' for neat PVA films processed at 120 °C changed from 7.0 GPa to ~ 1 MPa. The ACSF-swollen PVA/t-CNC nanocomposites display an E' that is higher than of the neat PVA films (Figure 3-5a and Figure A3-8 in the Appendix), but considerably lower than that of the corresponding materials in the dry state. For example, E' of the material comprising 16% v/v t-CNCs dropped from 13.7 GPa (dry, RT) to ~ 160 MPa (ACSF-swollen at 37 °C). The data in Figure 3-3 and Table 3-2 show that the switching is reversible and that ACSF exposure for 1 week and 1 month has the same effect. Moreover, the data in Figure 3-3a show that the relation between E' of the ACSF-swollen PVA/t-CNC nanocomposites and the t-CNC content is fairly well described by the Halpin-Kardos model, whose application to the modeling of CNCs-based nanocomposites has been reported elsewhere.^{29, 30} Parameters used for the modeling (see caption to Figure 3-3) were taken from Ref. 71, except E'_s of 11 MPa and 1.44 MPa for materials processed at 150 and 120 °C, respectively, which were measured by DMA. The fact that the model underestimates E' suggests that the CNC-CNC and perhaps also CNC-matrix interactions

are reduced upon swelling with ACSF, but – perhaps on account to the abundance of hydroxyl groups on the matrix polymer and the CNCs that can interact with water – not entirely switched off. All of the ACSF-swollen samples show a significant drop of E' at ~ 60 °C. Since this temperature is below the T_g of the plasticized PVA and far below the T_m of the matrix (~ 220 °C), we speculate that this transition is related to the dissolution of the matrix.

The ACSF-swollen PVA and PVA/c-CNC films, which were processed at 120 °C and display considerably more swelling than the above discussed t-CNC-based materials, exhibit an E' of 1 - 4 MPa at 37 °C (Figures 3-3b and 3-5b, Table 3-2). Due to the rather low modulus, these measurements feature a significant error, and it is therefore not possible to draw a firm conclusion about how the nanocomposite composition affects the modulus of the ACSF-swollen materials. The fact that the ACSF-induced mechanical switching was very significant and the finding that similar values were observed for both the neat PVA and the nanocomposites suggest that the mechanical properties of these materials were largely governed by the swollen polymer matrix, supporting the notion that the water effectively reduced interactions between the CNCs and interrupted their continuous reinforcing network.

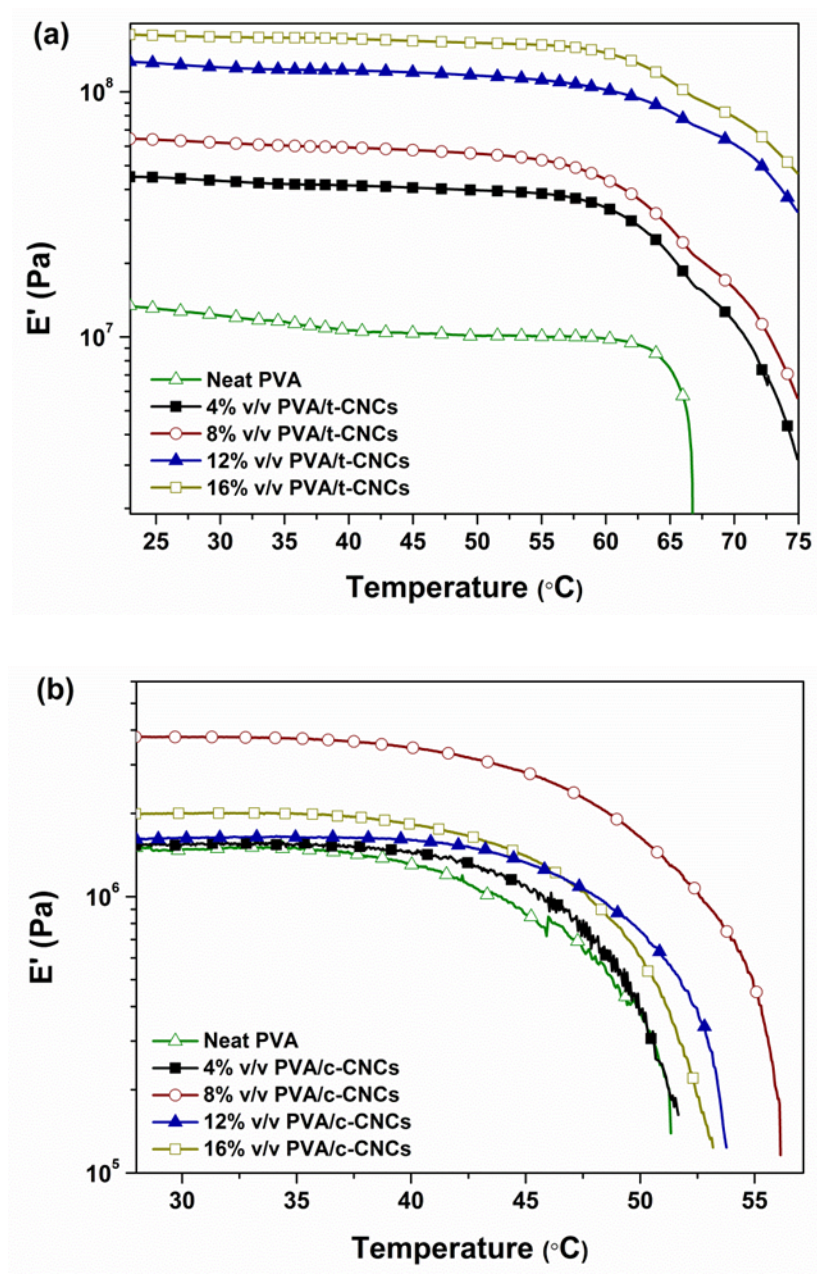


Figure 3-5. Dynamic mechanical analysis (DMA) data of ACSF-swollen films of (a) neat PVA and PVA/t-CNC nanocomposites and (b) PVA/c-CNC nanocomposites as a function of temperature and CNC content after immersion in ACSF at 37 $^{\circ}\text{C}$ for 1 week.

In order to further probe the influence of the processing temperature on the mechanical switching, the tensile storage moduli (E') of nanocomposites with 16% v/v t-CNCs that

had been compression-molded at 120 °C and 150 °C were compared (Table 3-2). It was found that the E' of PVA/t-CNC films processed at 150 °C, switched from 13.7 GPa (dry, RT) to 164 MPa (ACSF-swollen at 37 °C), whereas the material processed at 120 °C switched from 12.3 GPa to 60 MPa (Figure A3-9 in the Appendix). A similar result, was observed for the ACSF-swollen PVA/c-CNC films, which if processed at 150 °C exhibited an E' of 13 MPa at 37 °C, while the same composition processed at 120 °C, showed an E' of 2 MPa at 37 °C (Figure A3-10 in the Appendix). A lower processing temperature therefore not only influences the mechanical properties of the materials in the dry state, but also reduces E' of the ACSF-swollen state considerably. While the PVA/c-CNC films processed at 150 °C show some yellowing, their dry-state mechanical properties are largely comparable to those of the material processed at 120 °C, and (on account of less swelling) a higher modulus in the soft state is achieved, suggesting that whatever effect is responsible for the yellowing, it is not negatively impacting the material's mechanical characteristics. Thus, it appears that if PVA is used as a matrix, not only the CNC type and content but also the processing temperature can be used to tailor the mechanical contrast of CNCs-based, water-responsive, mechanically adaptive nanocomposites.

3.5. CONCLUSIONS

In summary, water-responsive, mechanically adaptive nanocomposites based on PVA and t-CNCs or c-CNCs offer an initial stiffness that is significantly higher than that of previous generations of such responsive materials. The use of PVA as a matrix polymer into which CNCs are incorporated proved useful for several reasons. The tensile storage moduli of PVA/CNC nanocomposites were - in both the glassy and rubbery regime - significantly higher than those of comparable nanocomposites. It appears that in addition to CNC-CNC interactions, polymer-CNC interactions, which could be promoted by the strong propensity of PVA to form hydrogen bonds and provide a compatible polymer-filler interface, are a significant factor in this context. Another significant factor is the possibility of controlling the swelling characteristics of the PVA matrix, and therewith

the properties of water- or ACSF-swollen nanocomposites, via the processing conditions. Using this tool, the switching “contrast” of the t-CNC-based nanocomposites upon exposure to ACSF could be varied between a 90-fold to a 200-fold modulus reduction. The results suggest that other ranges can be dialed in via the processing temperature, which (in relative terms) affects mainly the soft state. Although not as stiff initially in the dry state, PVA/c-CNC nanocomposites exhibit a larger mechanical contrast (up to 900-fold), as they soften much more than the t-CNC-based materials. This effect is related to the lower reinforcing power of c-CNCs. Despite the fact that decomposition of the c-CNC-containing materials starts around 150 °C, the nanocomposites maintain useful mechanical properties. Therefore, one could envision employing a higher processing temperature for PVA/c-CNC nanocomposites to further increase the stiffness of the water-swollen state. Overall, we have demonstrated that varying the CNC type and concentration and the processing temperature allows one to tailor the mechanical properties of “hard” and “soft” state over a broad range. The hitherto unavailable contrasts accessible by the new materials make them potentially useful as substrates for neural prosthetic devices. Ongoing work *in vivo* studies seek to quantify the potential benefits of these mechanically-switchable materials as basis for adaptive neural interfaces.

3.6. REFERENCES

1. M. W. Urban, ed., *Handbook of Stimuli-Responsive Materials*, 1 edn., Wiley-VCH, 2011.
2. M. Shahinpoor and H. J. Schneider, eds., *Intelligent Materials*, 1 edn., RSC Publishing, 2007.
3. M. A. C. Stuart, W. T. S. Huck, J. Genzer, M. Muller, C. Ober, M. Stamm, G. B. Sukhorukov, I. Szleifer, V. V. Tsukruk, M. Urban, F. Winnik, S. Zauscher, I. Luzinov and S. Minko, *Nat. Mater.*, 2010, 9, 101-113.
4. Y. Qiu and K. Park, *Adv. Drug Delivery Rev.*, 2001, 53, 321-339.
5. C. d. I. H. Alarcon, S. Pennadam and C. Alexander, *Chem. Soc. Rev.*, 2005, 34, 276-285.
6. Y. J. Kim, S. Choi, J. J. Koh, M. Lee, K. S. Ko and S. W. Kim, *Pharm. Res.*, 2001, 18, 548-550.
7. A. J. Rosengart, M. D. Kaminski, H. T. Chen, P. L. Caviness, A. D. Ebner and J. A. Ritter, *J. Magn. Magn. Mater.*, 2005, 293, 633-638.
8. D. Needham and M. W. Dewhirst, *Adv. Drug Delivery Rev.*, 2001, 53, 285-305.
9. N. A. Peppas, J. Z. Hilt, A. Khademhosseini and R. Langer, *Adv. Mater.*, 2006, 18, 1345-1360.
10. E. M. Bachelder, T. T. Beaudette, K. E. Broaders, J. Dashe and J. M. J. Frechet, *J. Am. Chem. Soc.*, 2008, 130, 10494-10495.
11. F. M. Chen, Y. M. Zhao, H. H. Sun, T. Jin, Q. T. Wang, W. Zhou, Z. F. Wu and Y. Jin, *J. Controlled Release*, 2007, 118, 65-77.
12. J. Yang, M. Yamato, C. Kohno, A. Nishimoto, H. Sekine, F. Fukai and T. Okano, *Biomaterials*, 2005, 26, 6415-6422.
13. S. R. White, N. R. Sottos, P. H. Geubelle, J. S. Moore, M. R. Kessler, S. R. Sriram, E. N. Brown and S. Viswanathan, *Nature*, 2001, 409, 794-797.
14. S. H. Cho, H. M. Andersson, S. R. White, N. R. Sottos and P. V. Braun, *Adv. Mater.*, 2006, 18, 997-1000.
15. O. H. Kwon, A. Kikuchi, M. Yamato, Y. Sakurai and T. Okano, *J. Biomed. Mater. Res.*, 2000, 50, 82-89.
16. H. Lee and T. G. Park, *Biotechnol. Prog.*, 1998, 14, 508-516.
17. R. Pelrine, R. Kornbluh, Q. B. Pei and J. Joseph, *Science*, 2000, 287, 836-839.
18. V. H. Ebron, Z. W. Yang, D. J. Seyer, M. E. Kozlov, J. Y. Oh, H. Xie, J. Razal, L. J. Hall, J. P. Ferraris, A. G. MacDiarmid and R. H. Baughman, *Science*, 2006, 311, 1580-1583.
19. L. Hsu, C. Weder and S. J. Rowan, *J. Mater. Chem.*, 2011, 21, 2812-2822.
20. K. Shanmuganathan, J. R. Capadona, S. J. Rowan and C. Weder, *Prog. Polym. Sci.*, 2010, 35, 212-222.
21. D. A. Stone, N. D. Wanasekara, D. H. Jones, N. R. Wheeler, E. Wilusz, W. Zukas, G. E. Wnek and L. T. J. Korley, *ACS Macro Letters*, 2011, 1, 80-83.
22. S. J. Eichhorn, A. Dufresne, M. Aranguren, N. E. Marcovich, J. R. Capadona, S. J. Rowan, C. Weder, W. Thielemans, M. Roman, S. Renneckar, W. Gindl, S. Veigel, J.

- Keckes, H. Yano, K. Abe, M. Nogi, A. N. Nakagaito, A. Mangalam, J. Simonsen, A. S. Benight, A. Bismarck, L. A. Berglund and T. Peijs, *J. Mater. Sci.*, 2010, 45, 1-33.
23. Y. Habibi, L. A. Lucia and O. J. Rojas, *Chem. Rev.*, 2010, 110, 3479-3500.
 24. S. J. Eichhorn, *Soft Matter*, 2011, 7, 303-315.
 25. M. A. S. A. Samir, F. Alloin and A. Dufresne, *Biomacromolecules*, 2005, 6, 612-626.
 26. V. Favier, H. Chanzy and J. Y. Cavaille, *Macromolecules*, 1995, 28, 6365-6367.
 27. V. Favier, G. R. Canova, J. Y. Cavaille, H. Chanzy, A. Dufresne and C. Gauthier, *Polym. Adv. Technol.*, 1995, 6, 351-355.
 28. J. R. Capadona, K. Shanmuganathan, D. J. Tyler, S. J. Rowan and C. Weder, *Science*, 2008, 319, 1370-1374.
 29. K. Shanmuganathan, J. R. Capadona, S. J. Rowan and C. Weder, *J. Mater. Chem.*, 2010, 20, 180-186.
 30. K. Shanmuganathan, J. R. Capadona, S. J. Rowan and C. Weder, *ACS Appl. Mater. Interfaces*, 2010, 2, 165-174.
 31. J. Mendez, P. K. Annamalai, S. J. Eichhorn, R. Rusli, S. J. Rowan, E. J. Foster and C. Weder, *Macromolecules*, 2011, 44, 6827-6835.
 32. A. E. Way, L. Hsu, K. Shanmuganathan, C. Weder and S. J. Rowan, *ACS Macro Letters*, 2012, 1, 1001-1006.
 33. K. L. Dagnon, K. Shanmuganathan, C. Weder and S. J. Rowan, *Macromolecules*, 2012, 45, 4707-4715.
 34. M. K. Shin, G. M. Spinks, S. R. Shin, S. I. Kim and S. J. Kim, *Adv. Mater.*, 2009, 21, 1712-1715.
 35. D. J. Schmidt, F. C. Cebeci, Z. I. Kalcioğlu, S. G. Wyman, C. Ortiz, K. J. Van Vliet and P. T. Hammond, *ACS Nano*, 2009, 3, 2207-2216.
 36. G. M. Spinks, V. Mottaghitalab, M. Bahrami-Samani, P. G. Whitten and G. G. Wallace, *Adv. Mater.*, 2006, 18, 637-640.
 37. J. R. Capadona, O. Van Den Berg, L. A. Capadona, M. Schroeter, S. J. Rowan, D. J. Tyler and C. Weder, *Nat. Nanotechnol.*, 2007, 2, 765-769.
 38. A. E. Hess, J. R. Capadona, K. Shanmuganathan, L. Hsu, S. J. Rowan, C. Weder, D. J. Tyler and C. A. Zorman, *J. Micromech. Microeng.*, 2011, 21, 054009.
 39. J. P. Harris, A. E. Hess, S. J. Rowan, C. Weder, C. A. Zorman, D. J. Tyler and J. R. Capadona, *J. Neural Eng.*, 2011, 8, 040610.
 40. J. R. Capadona, D. J. Tyler, C. A. Zorman, S. J. Rowan and C. Weder, *MRS Bull.*, 2012, 37, 581-589.
 41. J. P. Harris, J. R. Capadona, R. H. Miller, B. C. Healy, K. Shanmuganathan, S. J. Rowan, C. Weder and D. J. Tyler, *J. Neural Eng.*, 2011, 8, 066011.
 42. E. Chiellini, P. Cinelli, V. I. Hieva and M. Martera, *Biomacromolecules*, 2008, 9, 1007-1013.
 43. S. H. Hyon, Y. Ikada, Method of molding a polyvinyl alcohol contact lenses. US Patent 4874562, Oct 17, 1989.
 44. P. I. Lee, Production of borate cross-linked polyvinyl alcohol contact lenses. US Patent 4559186, Dec 17, 1985.

45. R. A. Janssen, P. I. Lee, E. M. Ajello, Preparation of stable polyvinyl alcohol hydrogel contact lens. US Patent 5174929, Dec 29, 1992.
46. A. R. Nectow, K. G. Marra and D. L. Kaplan, *Tissue Eng Part B*, 2012, 18, 40-50.
47. A. J. Uddin, J. Araki and Y. Gotoh, *Polym. Int.*, 2011, 60, 1230–1239.
48. A. J. Uddin, J. Araki and Y. Gotoh, *Biomacromolecules*, 2011, 12, 617-624.
49. S. A. Paralikar, J. Simonsen and J. Lombardi, *J. Membr. Sci.*, 2008, 320, 248-258.
50. M. Roohani, Y. Habibi, N. M. Belgacem, G. Ebrahim, A. N. Karimi and A. Dufresne, *European Polymer Journal*, 2008, 44, 2489-2498.
51. J. Lue, T. Wang and L. T. Drzal, *Composites Part A*, 2008, 39, 738–746.
52. www.alzet.com/products/cfs_prep.php, Accessed 08/04/2009.
53. C. C. Sun, *J. Pharm. Sci.*, 2005, 94, 2132–2134.
54. J. R. Capadona, K. Shanmuganathan, S. Triftschuh, S. Seidel, S. J. Rowan and C. Weder, *Biomacromolecules*, 2009, 10, 712-716.
55. A. Sturcova, G. R. Davies and S. J. Eichhorn, *Biomacromolecules*, 2005, 6, 1055-1061.
56. R. Rusli and S. J. Eichhorn, *Appl. Phys. Lett.*, 2008, 93.
57. O. van den Berg, J. R. Capadona and C. Weder, *Biomacromolecules*, 2007, 8, 1353-1357.
58. M. Roman and W. T. Winter, *Biomacromolecules*, 2004, 5, 1671-1677.
59. M. F. Rosa, E. S. Medeiros, J. A. Malmonge, K. S. Gregorski, D. F. Wood, L. H. C. Mattoso, G. Glenn, W. J. Orts and S. H. Imam, *Carbohydr. Polym.*, 2010, 81, 83-92.
60. F. Alloin, A. D'Aprèa, N. E. Kissi, A. Dufresne and F. Bossard, *Electrochim. Acta*, 2010, 55, 5186-5194.
61. J. M. Kropka, K. W. Putz, V. Pryamitsyn, V. Ganesan and P. F. Green, *Macromolecules*, 2007, 40, 5424-5432.
62. J. George, K. V. Ramana, A. S. Bawa and Siddaramaiah, *Int. J. Biol. Macromol.*, 2011, 48, 50-57.
63. G. Johnsy, K. K. R. Datta, V. A. Sajeevkumar, S. N. Sabapathy, A. S. Bawa and M. Eswaramoorthy, *ACS Appl. Mater. Interfaces*, 2009, 1, 2796-2803.
64. S. Kubo and J. F. Kadla, *Biomacromolecules*, 2003, 4, 561-567.
65. Q. Zhang, H. Brumer, H. Ågren and Y. Tu, *Carbohydr. Res.*, 2011, 346, 2595-2602.
66. J. J. Liang, Y. Huang, L. Zhang, Y. Wang, Y. F. Ma, T. Y. Guo and Y. S. Chen, *Adv. Funct. Mater.*, 2009, 19, 2297-2302.
67. L. Q. Liu, A. H. Barber, S. Nuriel and H. D. Wagner, *Adv. Funct. Mater.*, 2005, 15, 975-980.
68. A. Dufresne and M. Vincendon, *Macromolecules*, 2000, 33, 2998-3008.
69. A. Morin and A. Dufresne, *Macromolecules*, 2002, 35, 2190-2199.
70. L. M. Tang and C. Weder, *ACS Appl. Mater. Interfaces*, 2010, 2, 3396-3396.
71. P. Hajji, J. Y. Cavaille, V. Favier, C. Gauthier and G. Vigier, *Polym. Compos.*, 1996, 17, 612-619.
72. L. Y. Lim and L. S. C. Wan, *Drug Dev. Ind. Pharm.*, 1995, 21, 369-373.
73. J. Sriupayo, P. Supaphol, J. Blackwell and R. Rujiravanit, *Polymer*, 2005, 46, 5637-5644.

3.7. APPENDIX

Isolation of Cellulose Nanocrystals from Tunicates. The bleached tunicate mantles were blended at high speed, yielding a fine cellulose pulp. Sulfuric acid (95-97%, 600 mL) was slowly (over the course of 2 h) added under vigorous mechanical stirring to an ice-cooled suspension of tunicate cellulose pulp in deionized water (6 g in 600 mL, 20 °C). After 500 mL of the acid had been added, the dispersion was removed from the ice bath and was heated to 40 °C during the addition of the final 100 mL of acid. After the acid addition was complete, the dispersion was heated to 60 °C and was kept at this temperature for 1 h under continuous stirring. The mixture was then cooled to room temperature, centrifuged (30 min at 3300 rpm), and the supernatant solution was decanted. Deionized water was added and the centrifugation step was repeated until the pH of the dispersion reached about 5. After the last centrifugation the resulting CNCs were dialyzed in three successive 24 h treatments against deionized water to remove the last residues of the sulfuric acid. The suspension was diluted with deionized water (total volume 1 L) and sonicated for 18 h, before it was filtered through a No. 1 glass filter in order to remove any remaining aggregates. The concentration of the CNCs in the final dispersion was determined gravimetrically to be ~3 mg/mL. This dispersion was freeze-dried using a VirTis BenchTop 2K XL lyophilizer with an initial temperature of 25 °C and a condenser temperature of -78 °C. The t-CNCs aerogel those produced was stored and used as needed.

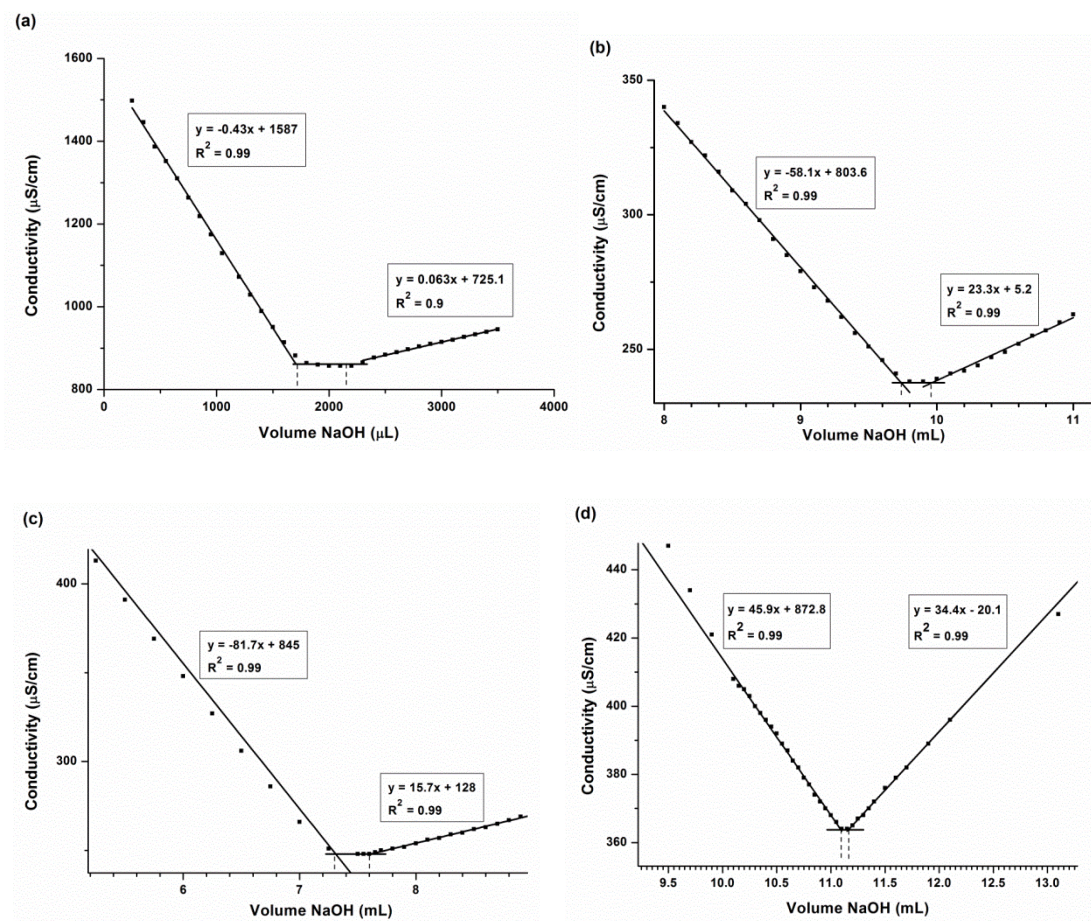


Figure A3-1. Conductometric titration curves of CNCs. (a) Lyophilized t-CNCs, (b) spray-dried c-CNCs, (c) lyophilized c-CNCs, and (d) a blank titration without CNCs.

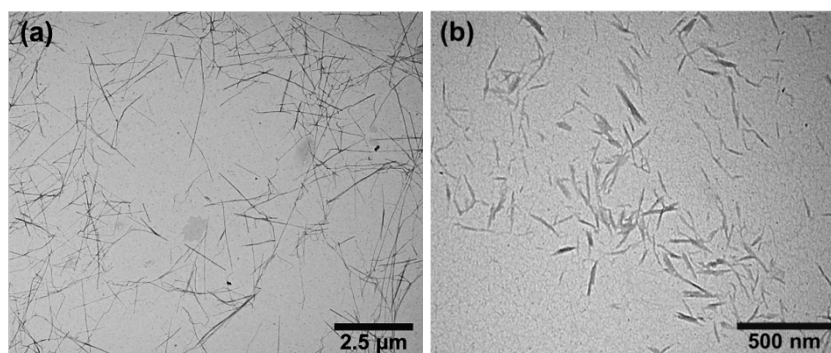


Figure A3-2. Representative transition electron microscopy (TEM) images of CNCs. (a) lyophilized t-CNCs, and (b) spray-dried c-CNCs deposited from aqueous dispersions (0.1 mg/mL).

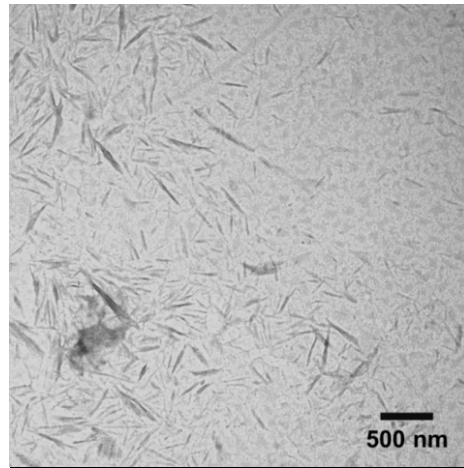


Figure A3-3. Transition electron microscopy (TEM) images lyophilized c-CNCs deposited from aqueous dispersions (0.1 mg/mL).

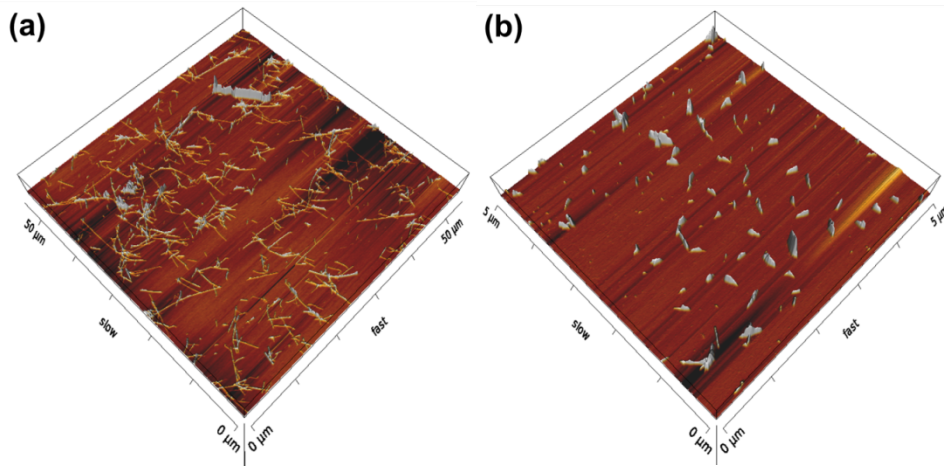


Figure A3-4. Three-dimensional AFM topographic (height) images for (a) lyophilized t-CNCs, and (b) spray-dried c-CNCs deposited from aqueous dispersions (0.1 mg/mL) onto freshly cleaved mica surfaces.

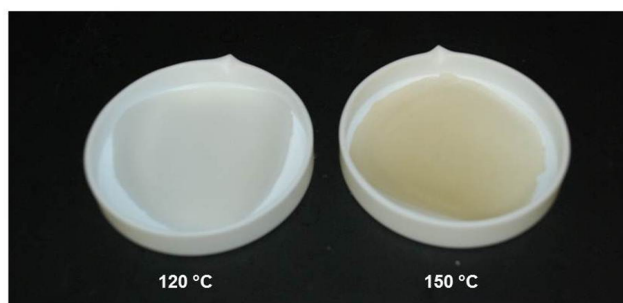
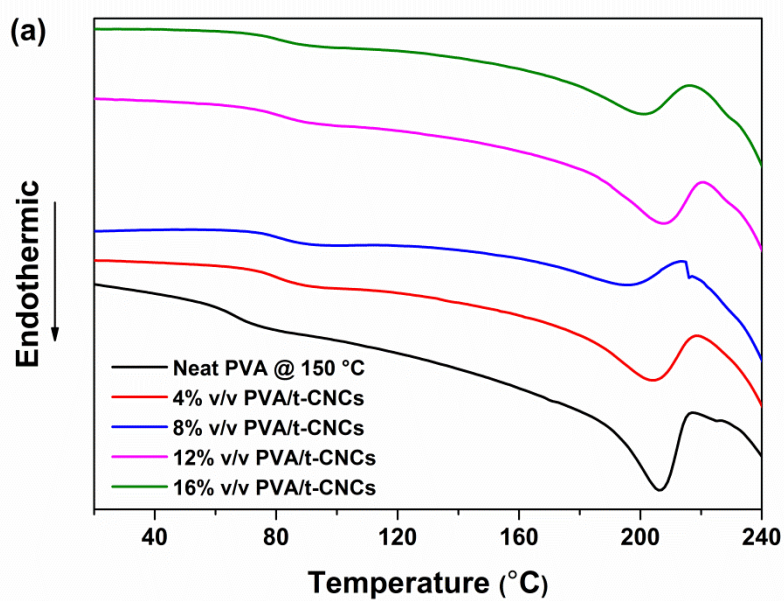


Figure A3-5. Photographs of solution-cast and compression-molded PVA/c-CNC nanocomposite films (16% v/v c-CNCs) processed at 120 (left) and 150 °C (right), respectively.



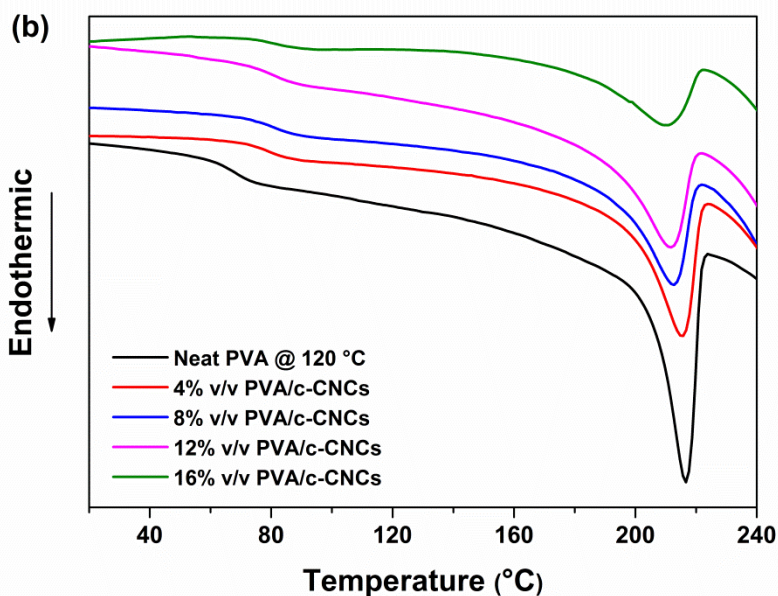


Figure A3-6. DSC thermograms (second heating) of (a) PVA/t-CNC and (b) PVA/c-CNC nanocomposites and neat PVA films compression-molded at (a) 150 °C and (b) 120 °C, respectively.

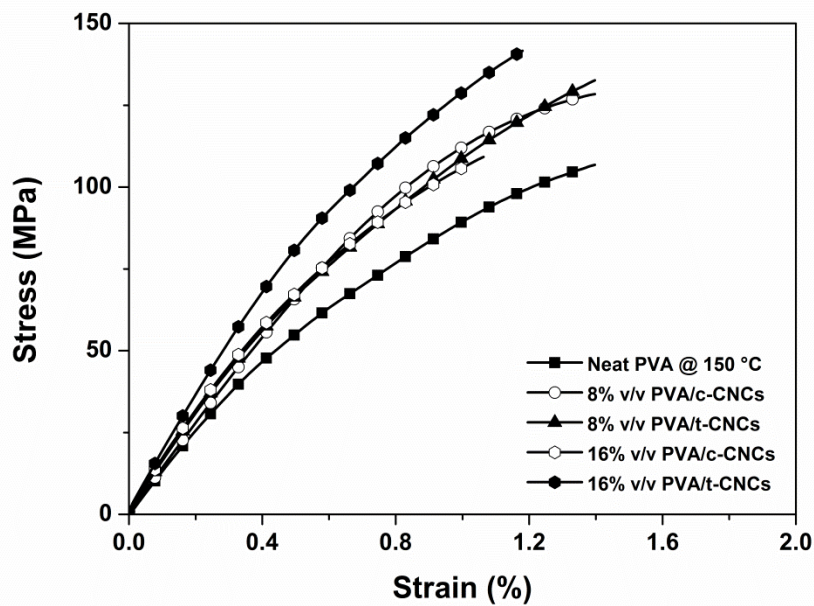


Figure A3-7. Chart showing the stress-strain curves of neat PVA and PVA/CNC nanocomposites as a function of CNC content (all data acquired at 25 °C).

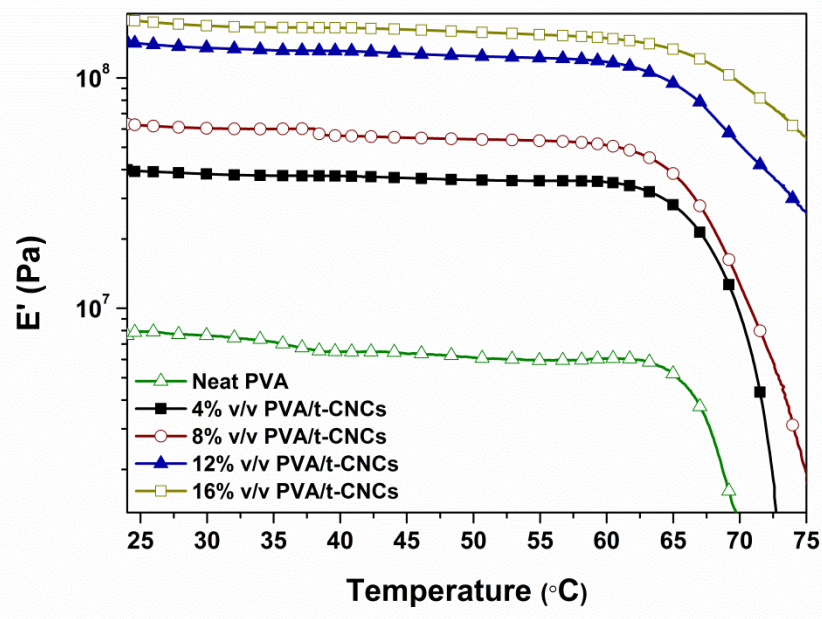


Figure A3-8. DMA data of ACSF-swollen films of neat PVA and PVA/t-CNC nanocomposites after immersion in ACSF at 37 °C for 1 month.

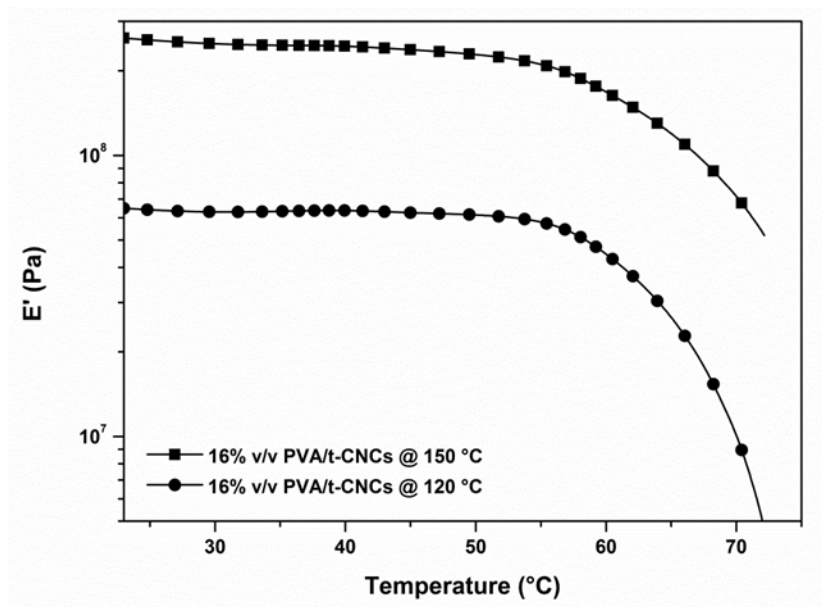


Figure A3-9. DMA data of ACSF-swollen films of 16% v/v PVA/t-CNC nanocomposites after immersion in ACSF at 37 °C for 1 day. The processing temperature is indicated in the Figure.

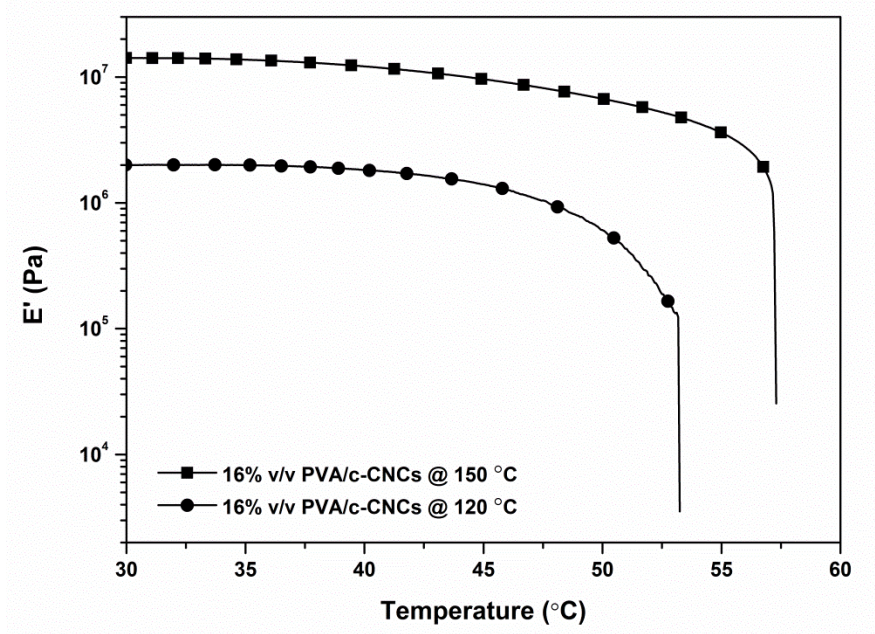


Figure A3-10. DMA data of ACSF-swollen films of 16% v/v PVA/c-CNC nanocomposites after immersion in ACSF at 37 $^{\circ}\text{C}$ for 1 day. The processing temperature is indicated in the Figure.

Chapter 4 – Curcumin-Releasing Mechanically Adaptive Intracortical Implants Improve Proximal Neuronal Density and Blood-Brain Barrier Stability³

4.1. ABSTRACT

The cellular and molecular mechanism by which neuroinflammatory pathways respond to and propagate the reactive tissue response to intracortical microelectrodes remains an active area of research. We previously demonstrated that both, the mechanical mismatch between rigid implants and the much softer brain tissue, as well as oxidative stress contribute to the neurodegenerative reactive tissue response to intracortical implants. In this study, we utilize physiologically-responsive, mechanically adaptive polymer implants based on poly(vinyl alcohol), with the capability to also locally administer the anti-oxidant curcumin. The goal of this study is to investigate if the combination of two independently effective mechanisms – softening of the implant and anti-oxidant release – leads to synergistic effects *in vivo*. Over the first four weeks of the implantation, curcumin-releasing, mechanically-adaptive implants were associated with higher neuron survival and a more stable blood-brain barrier at the implant-tissue interface than the neat poly(vinyl alcohol) controls. Twelve weeks post implantation, the benefits of the curcumin release were lost, and both sets of compliant materials (with and without curcumin) had no statistically significant differences in neuronal density distribution profiles. Overall, however, the curcumin-releasing softening polymer implants cause minimal implant-mediated neuroinflammation, and embody the new concept of localized drug delivery from mechanically adaptive intracortical implants.

³This chapter is adopted from Potter, K.A.*; Jorfi, M.*; Householder, K.T.; Foster, E.J.; Weder, C.; Capadona, J.R. *Acta Biomaterialia*, **2014**, 10, 2209–2222 (*Co-first authors). Kelsey Potter and Kyle Householder carried out all *in vivo* studies.

4.2. INTRODUCTION

Chronic intracortical microelectrode arrays allow neural firing patterns of many single neurons to be monitored over time from specific structures within the brain. In paralyzed individuals, chronic microelectrode recordings provide a way for their neural signals to directly control various assistive devices.^{1, 2} Chronic recordings in animals can advance our fundamental understanding of the brain function in both normal and diseased states.³ ⁴ However, despite the ability of intracortical microelectrodes to record the activity of single- and/or multi-unit neuron activity early after implantation, a common issue surfaces. Eventually, neurodegenerative processes critically impair signal quality to the point that single neurons can no longer be detected across most electrodes.

One widely accepted theory concerning microelectrode failure centers on changes in the viability and function of neuronal targets at the microelectrode recording sites. It has been shown by several groups that a reduction of viable neurons proximal to the implant occurs weeks to months after implantation.⁵⁻⁸ Further, neuronal processes that remain near the electrodes have been shown to be degenerative, with decreases in myelin and dendrite density.^{9, 10} The ability of intracortical microelectrodes to record activity from single neurons is directly related to the proximity of viable neurons, and thus the neurodegenerative process has significant ramifications for device performance.¹¹ To fully realize the potential of brain-machine interface technology, the deterioration of local proximal neurons must be overcome.

Significant efforts have been made to minimize the reactive tissue response to intracortical microelectrodes. Both materials-based and therapeutic strategies have been employed, with various degrees of success.^{12, 13} Additionally, Each of these approaches, as well as others, has demonstrated a clear short-term improvement in the neuroinflammatory response to implanted intracortical microelectrodes. However, the dominant mechanism leading to functional loss following intracortical implantation is unresolved.

We have recently observed that the long-term neuroinflammatory response to traditional, rigid silicon microelectrodes is multiphasic.⁷ Additionally, we have also recently

proposed that the long-term neuroinflammatory response is self-perpetuating through the continual breach of the blood-brain barrier.¹⁰ The potential significance of our hypothesis is supported by recent results of Saxena *et al.*, who demonstrated that the chronic blood-brain barrier breach impacts microelectrode function.¹⁴ Many factors can contribute to the perpetual disruption of the blood-brain barrier, including (i) reactive microglia released pro-inflammatory molecules and reactive oxygen species in response to implanted microelectrodes^{6, 10, 15, 16} and (ii) the mechanical contrast between ‘stiff’ microelectrodes and ‘soft’ brain tissue resulting in micromotion-mediated tissue strain.¹⁷⁻¹⁹

To further investigate these leading hypotheses, we have previously explored each aspect individually. For example, Potter *et al.* demonstrated that anti-oxidant treatment can prevent microelectrode-mediated neurodegeneration and blood-brain barrier breach.¹⁰ In addition, we developed a new class of physiologically-responsive, mechanically adaptive polymer nanocomposites. The nanocomposite implants are sufficiently rigid to allow insertion into the cortex, but soften considerably after implantation, to investigate the role of microelectrode-tissue mechanical mismatch.²⁰⁻²⁶ The polymer alone softens considerably upon exposure to physiological conditions due to plasticization upon absorption of water. The introduction of physiologically benign rigid, rod-like CNCs further increases the stiffness of the dry material. This is particularly important for polymers that are not stiff enough to penetrate the brain as small implant dimensions. Additionally, the high stiffness in the dry state and the ability to tailor the mechanical contrast via composition and processing renders nanocomposites particularly useful as basis for adaptive biomedical implants. Our previous nanocomposite work is in agreement with both *in silico* and *in vivo* studies proposing the hypothesis that the mechanical mismatch plays a dominant role in reactive gliosis at the microelectrode tissue interface.^{18, 27}

Together, our previous studies with nanocomposite-derived microelectrodes and anti-oxidant therapeutics have shown a significant contribution of both oxidative stress and mechanical mismatch to the reactive tissue response to implanted intracortical implants. However, the interplay between the two mechanisms and possible synergies that may

arise from implanting mechanically adaptive implants with a drug-releasing feature has yet to be explored. Here, we employ our latest generation of mechanically adaptive polymer implants based on poly(vinyl alcohol) (PVA), and optionally cellulose nanocrystals (CNCs),²⁴ to investigate the efficacy of the local delivery of anti-oxidant therapies at the intracortical implant-tissue interface.

4.3. EXPERIMENTAL SECTION

Materials. Poly(vinyl alcohol) (PVA) 99% hydrolyzed ($M_w = 85,000\text{--}124,000$ g/mol; $\delta = 1.26$ g/mL), curcumin (Figure 4-1), 2,2-diphenyl-1-picrylhydrazyl (DPPH), Tween 80, sucrose, Triton-X 100, and all other reagents used for material processing were purchased from Sigma Aldrich and used without further purification. 1X Phosphate buffered saline (PBS Buffer) was purchased from CellGro.

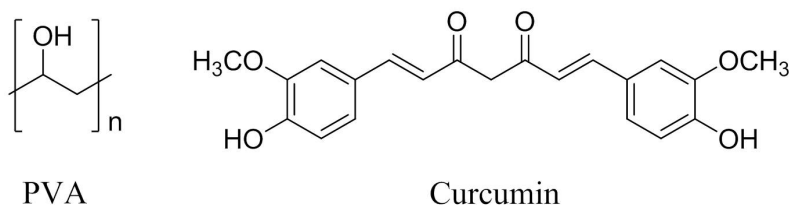


Figure 4-1. Chemical structure of poly(vinyl alcohol) (PVA) and curcumin.

Isolation of Cellulose Nanocrystals from Tunicates. Cellulose nanocrystals (CNCs) were isolated from tunicates (*Styela clava*) collected from floating docks in Point View Marina (Narragansett, RI). The CNCs were prepared by sulfuric acid hydrolysis of the cellulose pulp, according to established protocols,²⁸ with slight modifications, as previously reported.²⁴ Transmission electron microscopy (TEM), atomic force microscopy (AFM) and conductometric titration were used to characterize the physical dimensions, surface charge density, and morphology of the isolated CNCs (Figures A4-1 and A4-2).

Preparation of Curcumin/Polymer Films. A PVA stock solution was prepared by dissolving PVA in dimethyl sulfoxide (DMSO) at a concentration of 50 mg/mL by stirring for 3 hours at 90 °C. Similarly, a curcumin stock solution was made by dissolving curcumin in DMSO (10 mg/mL) by stirring for 1 hour at room temperature (RT). Films containing either 1% or 3% w/w curcumin were made by combining appropriate amounts of the above stock solutions, stirring the mixture for 30 minutes at RT and then sonicating for 30 minutes. The solutions were next cast into a Teflon[®] Petri dish, dried at 60 °C for 5 days and further dried at 120 °C under high vacuum oven for an additional 24 hours to evaporate all of the solvent. After drying, films were compression-molded between spacers in a Carver[®] laboratory press (1000 psi for 2 minutes, followed by an increase of pressure to 2000 psi for 15 minutes) at 150 °C, and then allowed to cool to ~70 °C for a minimum of 90 minutes under the applied pressure to yield 70-110 µm thin films. The thickness of the films was measured using an electronic digital caliper (Fowler) and a micrometer (Millimess Inductive Digital Comparator Extramess 200, Mahr). For reference purposes, neat PVA control films were prepared in a similar manner by solution-casting and subsequent compression-molding. The curcumin/PVA films thus produced were stored in a desiccator at ambient temperature.

Preparation of Curcumin/Polymer/CNCs Films. Films containing CNCs were prepared in a manner that mirrored the fabrication of curcumin/polymer films described above. However, in the case of CNC-containing films, CNC dispersions were combined with the appropriate amounts of the PVA and curcumin stock solutions, so that the CNC content in the final material was 8% v/v. Of note, lyophilized CNCs were dispersed in DMSO at a concentration of 3 mg/mL by sonicating for 10 hours.

Swelling Behavior. Prior to *in vivo* evaluation, the physical and mechanical properties of the prepared films were characterized in the dry state and under simulated physiological conditions. To simulate the ionic composition of endogenous brain fluid, artificial

cerebrospinal fluid (ACSF) was used. ACSF was prepared following established protocols²⁹ by dissolving the following materials in 1 liter of deionized water: sodium chloride (NaCl) = 7.25 g, potassium chloride (KCl) = 0.22 g, sodium bicarbonate (NaHCO₃) = 2.18 g, calcium chloride dihydrate (CaCl₂·2H₂O) = 0.29 g, monopotassium phosphate (KH₂PO₄) = 0.17 g, magnesium sulfate heptahydrate (MgSO₄·7H₂O) = 0.25 g, and *D*-glucose = 1.80 g.

The swelling behavior of the neat PVA control and the curcumin-loaded films was investigated by cutting the films into ~30 mm × ~6 mm × 70-110 μm rectangular strips and immersing the samples in ACSF at the physiological temperature of 37 °C for one week. After one week incubation in ACSF, the degree of film swelling was calculated by comparing the weight of the films pre- and post-swelling:

$$\text{Degree of swelling (\%)} = \frac{(W_s - W_d)}{W_d} \times 100 \quad (4 - 1)$$

where W_d is the weight of the dry film prior to swelling and W_s is the weight of the swollen film. After swollen films were removed from ACSF, the samples were briefly placed on a small piece of tissue paper to wick any excess ACSF from the surface, and the samples were immediately weighed (Table 4-1). This experiment was repeated four times, and the results are expressed as mean ± standard deviation.

Mechanical Characterization. The mechanical properties of the films were characterized by dynamic mechanical analysis (DMA, TA Instruments, Model Q800). Tests were conducted in tensile mode, sweeping the temperature between 0-140 °C at a fixed frequency of 1 Hz, and using a strain amplitude of 30 μm, a heating rate of 5 °C/min, and a gap of ~10 mm between the jaws. Samples for mechanical testing were prepared by cutting strips (~30 mm × ~6 mm × 70-110 μm) from the films. To determine the mechanical properties of the films in the wet state, samples were first swelled in ACSF at 37 °C for one week. After the degree of swelling had been measured, DMA experiments were conducted in tensile mode with a submersion clamp, which allowed

measurements while the samples were immersed in ACSF. For wet samples, the temperature sweeps were carried out in the range of 25-55 °C with a heating rate of 1 °C/min, a constant frequency of 1 Hz, strain amplitude of 30 μm, and a gap of ~15 mm between the jaws. These experiments were repeated three to five times, and the result was expressed as mean ± standard deviation (Table A4-2).

***In vitro* Curcumin Release.** To determine the release rates of curcumin from anti-oxidant loaded films, samples (~30 mm × ~6 mm × 70-110 μm) were incubated at 37 °C in a mixture of 20 mL of 99.5% v/v ACSF and 0.5% v/v Tween-80, which was added to increase the solubility of the curcumin in water. Here, polymer sample sizes were chosen to ensure that released curcumin could be detected spectrophotometrically. In set time intervals (t=1, 2, 4, 6, 8, 10, 24, 29, 33, and 48 h), 1 mL aliquots of the solution were withdrawn, diluted with 1.5 mL of the neat solvent (99.5% v/v ACSF and 0.5% v/v Tween-80), and the amount of curcumin released was detected spectrophotometrically (UV 2401-PC spectrophotometer, Shimadzu). The concentration of released curcumin was calculated using a calibration curve established by measuring the absorbance at 425 nm of a series of solutions of the drug (5-30 μg/mL) in ACSF/Tween 80. The amount of curcumin released (relative to the amount of curcumin originally present in the material) was calculated using Equation 4-2, Where $[Cur]_{UV}$ is the concentration of curcumin measured by UV (mg/mL), V_{Sample} the volume of the sample in mL, W_{Film} the weight of the film in mg, and $[Cur]_{Film}$ is the nominal concentration of the curcumin in the film (mg/mg). This experiment was repeated four times, and the result was expressed as mean ± standard deviation.

$$\text{Release (\%)} = \frac{[Cur]_{UV} \times V_{Sample}}{W_{Film} \times [Cur]_{Film}} \times 100 \quad (4 - 2)$$

Measurement of Anti-oxidative Activity of Curcumin. The anti-oxidative activity of curcumin-releasing films was assessed using 2,2-diphenyl-1-picrylhydrazyl (DPPH) following a previously reported method,³⁰ with slight modifications. Here, the absorbance

of DPPH, a stable free radical, at 516 nm was monitored to quantify the anti-oxidant activity of curcumin, which is known to reduce DPPH, and thereby decreases its absorbance at 516 nm. Briefly, the films were cut into rectangular pieces (~30 mm × ~6 mm) and placed into a methanolic solution of DPPH (100 μM). Samples were incubated at 37 °C in the dark. The absorbance of the solution was measured spectrophotometrically at 516 nm in regular time intervals ($t = 0, 1, 3, 5, 7, 9, 24, 30,$ and 48 h). The radical scavenging activity of curcumin-loaded films was expressed using Equation 4-3, where A and B are the absorbance values at time t , of the neat DPPH solution (A) and the DPPH solution in the presence of the anti-oxidant loaded film (B), respectively. All samples were tested three times to ensure repeatability of measurements.

$$\text{DPPH Scavenging Activity} = \left(\frac{A - B}{A} \right) \quad (4 - 3)$$

Animals and Surgical Implantation. Forty male Sprague Dawley rats (225–300 g) (Charles River) were used in this study and sacrificed either 2, 4 or 12 weeks after implantation. A minimum of five animals were used for each implanted condition and end point. In addition to surgically implanted animals, a minimum of two non-implanted, age-matched sham animals were used for each end point, as controls to assess background histological information. All procedures and animal care practices were performed in accordance with the Louis Stokes Department of Veterans Affairs Institutional Animal Care and Use Committee.

Surgical procedures closely followed our established protocols.^{7, 10, 31} Briefly, animals were initially anesthetized using a mixture of ketamine (Butler Schein) (80 mg/kg) and xylazine (Butler Schein) (10 mg/kg) given intraperitoneally (IP). Depth of anesthesia was monitored using a pulse oximeter and toe-pinch reflex, and if required, isoflurane (Butler Schein) (0.5-2%) was used to maintain anesthesia for the duration of the procedure. Animal temperature was maintained using a circulating water heating pad, placed below the stereotaxic frame. Ophthalmic ointment (Butler Schein) was used throughout the procedure to prevent retinal drying. Prior to surgery, each animal received cefazolin

(Butler Schein) (16 mg/kg) and meloxicam (Butler Schein) (1 mg/kg) subcutaneously (SQ) to prevent infection and manage pain, respectively. Following initial anesthesia, the surgical area was thoroughly shaved and the animal was mounted onto a stereotaxic frame. Local anesthesia was provided using a SQ injection of Marcaine (Butler Schein) (0.5%) at the incision site. Prior to incision, a sterile surgical field was obtained by three alternating passes of betadine solution and 70% isopropanol over the surgical site.

To perform the craniotomy, the skull was exposed by using a one-inch incision down midline and retracting surrounding tissue. Next, a 3-mm biopsy punch (PSS Select) was used to manually create a hole in the skull approximately 3 mm lateral to midline and 4 mm caudal to bregma. The dura matter was gently reflected using a 45° dura pick and visible vasculature was avoided. Here, animals each received either a single sterile shank PVA implant (2 mm × ~100 μm × ~100 μm) or 3% Cur/PVA Curcumin implant (2 mm × ~100 μm × ~100 μm). All samples were prepared to uniform dimensions by laser micromachining, and confirmed under a microscope. All implants used in this study were sterilized using ethylene oxide gas (14 hour cycle; University Hospitals Cleveland, OH) and were allowed to out gas a minimum of 72 hours prior to implantation. Implants were inserted carefully by hand until approximately 100 μm of the polymer shank remained above the cortical tissue. Prior to sample tethering, a silicone gel (Kwik-Sil, World Precision Instruments) was applied over each craniotomy to prevent cortical tissue dehydration. Polymer implants were then securely anchored to the skull using ultra-violet (UV) curing dental acrylic (Fusio/Flow-it ALC, Pentron Dental). The surgical site was closed using 5-0 monofilament polypropylene suture and triple antibiotic ointment was applied over the incision to prevent drying and localized infection around the surgical site. After recovery, animals received SQ injections of cefazolin (16 mg/kg) twice the day after surgery and meloxicam (1 mg/kg) daily for two days to prevent infection and manage pain, respectively. To minimize variability, the same surgeon performed all craniotomies.

Histological Tissue Processing. The inflammatory response to implanted devices was assessed by allowing animals to survive to controlled time points that correlated with different stages of inflammation.⁷ Prior to perfusion, animals were deeply anesthetized using a mixture of ketamine (80 mg/kg) and xylazine (10 mg/kg) administered IP. Each animal was then perfused transcardially with 1X phosphate buffer saline (PBS) at a rate of 50 mL per minute until the exudate was clear and then fixed with 4% paraformaldehyde at the same flow rate. The brain was then carefully extracted, placed in fresh 4% paraformaldehyde, stored at 4 °C and allowed to post-fix for 24 hours. Following fixation and prior to sectioning, the tissue was cryoprotected by equilibrating in a step-wise gradient of sucrose (10%-20%-30%) in 1X PBS at 4 °C. Tissue was equilibrated in sucrose until it ‘sunk’ to the bottom of the vial. Typically, tissue was equilibrated in 10% and 20% sucrose solution for 24 hours. In the case of 30% sucrose, tissue was equilibrated twice, initially for 48 hours, then the solution was replaced with fresh 30% sucrose and equilibrated for an additional 24 hours. The brain tissue was then frozen at -80 °C in optimal cutting temperature compound (OCT) (Tissue-Tek), sliced axially in 20 µm sections in a cryostat, and mounted directly onto slides to be stored at -80 °C until immunohistochemical labeling.

Immunohistochemistry. Immunohistochemical analysis of common central nervous system inflammatory markers was used to evaluate the extent of inflammation and necrosis around the implants. The primary antibodies utilized in this study included: mouse anti-glial fibrillary acidic protein (GFAP) (1:500, #A-21282, Invitrogen), rabbit anti-IBA-1 (1:250, #019-1974, Wako), mouse anti-CD68 (1:100, #MAB1435, Millipore), mouse anti-neuronal nuclei (NeuN) (1:250, #MAB377, Millipore), rabbit anti-immunoglobulin G (IgG) (1:100, #618601, AbD Serotec) and rabbit anti-high mobility group box 1 (HMGB1) (1:250, #ab18256, Abcam).

Immunohistochemical labeling of microglia/macrophages (IBA-1, CD68), astrocytes (GFAP), neuronal nuclei (NeuN), blood brain barrier stability (IgG), and TLR4-mediated mechanisms of inflammation and damage (HMGB1) was done using a previously

reported methodology.^{7, 10, 31, 32} Briefly, brain slices were allowed to equilibrate to RT to promote adhesion to microscope slides. Sections were then washed quickly three times with 1X PBS to remove remaining OCT, and permeated with 1X PBS containing 0.1% Triton-X 100 (Sigma) (1X PBS-T) for 15 minutes. All slides were then blocked for an hour at RT in blocking buffer (4% v/v goat serum (Invitrogen), 0.3% v/v Triton-X 100, 0.1% w/v sodium azide (Sigma)). Following blocking, primary antibodies were applied directly to samples and allowed to incubate overnight at 4 °C. Unbound primary antibodies were then removed using six subsequent 5 minutes washes with 1X PBS-T. Next, species-specific secondary antibodies (goat anti-rabbit or mouse Alexa-Fluor 488 and goat anti-rabbit or mouse Alexa-Fluor 594, Molecular Probes) were diluted 1:1000 in blocking buffer and applied to the tissue sections for 2 hours at RT. In addition to secondary antibodies, 4,6-diamidino-2-phenylindole (DAPI, 1:36,000) (Invitrogen) was used to co-label total cell nuclei. Unbound secondary antibodies were removed with six subsequent 5 minutes washes with 1X PBS-T. Following washing, tissue autofluorescence was removed with a 10 minutes treatment with 0.5 mM copper sulfate buffer (50 mM ammonium acetate, pH 5.0).³¹ Slides were finally thoroughly rinsed with deionized water, mounted with Fluoromount-G (Southern Biotech), allowed to dry at RT and then stored at 4 °C in the dark until imaged.

Imaging and Quantitative Analysis. All immunohistological images in this study were acquired fluorescently using a 10X objective on an AxioObserver Z1 (Zeiss Inc.) and an AxioCam MRm (Zeiss Inc.). To allow for a wider field of view, without sacrificing image resolution, MosaiX software (Zeiss Inc.) was used to stitch together 16 individual 10X images for each analyzed region of interest. Prior to analysis, stitched images were exported as unmodified 16-bit tagged image files (TIFs). Images were analyzed in the raw acquired form, with no further modifications.

The quantification of inflammatory markers was done with two different methods. For all markers except neuronal nuclei, intensities were quantified using an in-house, freely available, written MATLAB program, MINUTE.³¹ Within the graphic user interface

(GUI), the implant region was defined and the surrounding image intensity quantified using expanding 2 μm rings from the defined region of interest. Intensities were quantified up to 1500 μm away from the implant interface. Quantified intensities were then normalized to a background region to obtain a normalized intensity profile for each analyzed marker. Here, background was defined as approximately 1200-1400 μm from the defined interface and held constant for any given stain, for all time points and analyzed conditions. To allow for statistical evaluation, the area under the curve of the normalized intensity plots was then obtained using MATLAB for all tested conditions. For clarity, data is presented as normalized intensity profiles as a function of distance from the implant. The area under the curve values were only used to find significance between conditions, and not otherwise reported. The following bins were used to determine significance: 0 to 50 μm , 50 to 75 μm , 75 to 100 μm , 100 to 125 μm , 125 to 150 μm , 150 to 175 μm , 175 to 200 μm and then 100 μm bins out to 1000 μm from the implant. Binning intervals were defined based on those reported by multiple groups in the field^{5, 33, 34} and modeling studies by Busaki et al which outlined critical distance to maintain functional neural recordings.¹¹

In addition to the area under the curve, exponential curve fitting was applied to each normalized intensity plot to quantify the cellular and molecular distribution of labeled antigens. Using previously reported methods,⁷ curve fitting was done using the Nelder-Mead method and the sum of the squared residuals was normalized to the variables λ and a . Lambda (λ) values, denoting the distance at which 63.2% of the total observed fluorescent intensity had returned to background levels, were obtained for each analyzed image (see Equation 4-4). Lambda values were only used if a R^2 value of 0.9 was achieved after curve fitting.

$$y(x) = a \cdot e^{\left(\frac{-x}{\lambda}\right)} \quad (4 - 4)$$

Neuronal nuclei (NeuN) densities around implanted materials were quantified using Adobe Photoshop. Similar to above, the implant region was defined and expanding

concentric rings at fixed radii were drawn up to 600 μm from the region of interest. Then, the area within each region and total number of neuronal nuclei were determined, manually. For all conditions and analyzed end points, neuronal nuclei density was normalized to age-matched, non-surgical control animals. Neurons in the sham tissue were counted using the same quantification as implanted animals and the densities were defined as 2757 ± 275 , 2042 ± 156 , and 1432 ± 184 cells per mm^2 for 2 weeks, 4 weeks, and 12 weeks, respectively. All neuronal nuclei densities were reported relative to the sham values for a given end point.

Statistical Analysis. For each analyzed marker, a minimum of 15 tissue sections from a minimum of five rats were used for statistical comparison. Each image was treated as an independent measurement and then averaged within a given cohort. For all comparisons between time of implant and material type, statistical analyses using a general linearized model two-way analysis of variance (ANOVA) were run using Minitab 16 (Minitab Inc.). Pair-wise comparisons were conducted using a Tukey's post-hoc test. Significance was defined as a p-value less than 0.05.

4.4. RESULTS

4.4.1. Characterization of Curcumin-Loaded Materials

The swelling behavior of the curcumin-loaded materials (with and without CNCs) and the neat PVA control in emulated physiological conditions was investigated by immersing the materials into ACSF at 37 $^{\circ}\text{C}$ (Table 4-1). The water uptake was found to be ~30 - 40% w/w for all compositions, and no dependence of the drug or CNC content is apparent. The thermal properties of anti-oxidant loaded materials were determined using differential scanning calorimetry (DSC, Table A4-1). The DSC data show that the incorporation of CNCs and/or anti-oxidant led to an increase of the glass transition temperature (T_g) by approximately 10 $^{\circ}\text{C}$ in comparison to the neat PVA (~68 $^{\circ}\text{C}$). A melting temperature (T_m) of ~220 $^{\circ}\text{C}$ was observed, independent of the presence of CNCs and/or anti-oxidant. However, the degree of crystallinity (χ_c) increased slightly (Table

A4-1), suggesting that the CNCs and the curcumin act as nucleation sites for the crystallization of PVA.

Table 4-1. Swelling properties of neat PVA and curcumin-loaded films.

Polymer Film	Swelling (% w/w)
Neat PVA Control	40 ± 6.0
1% Curcumin/PVA	30 ± 10
3% Curcumin/PVA	35 ± 2.0
PVA/CNCs Control	40 ± 5.0
1% Curcumin/PVA/CNCs	30 ± 5.0
3% Curcumin/PVA/CNCs	27 ± 8.0

4.4.2. Mechanically Adaptive Properties of Curcumin-Loaded Materials

The mechanical properties of both curcumin-loaded PVA and PVA/CNC films were investigated using dynamic mechanical analysis (DMA). Figures 4-2 and A4-3 show the tensile storage moduli (E') of the curcumin-loaded PVA (Cur/PVA) and the curcumin-loaded PVA/CNC nanocomposites (Cur/PVA/CNCs) as well as a neat PVA reference film in the dry and ACSF-swollen state as a function of temperature. The curves reveal a nearly temperature-independent tensile storage modulus E' of ~10 GPa at temperatures below ~20 °C. E' is reduced as the temperature is increased towards the T_g (~68 °C), and reaches a rubbery plateau above ~100 °C. The incorporation of CNCs led to an increase of the E' , in particular above T_g .

All curcumin-loaded materials softened substantially upon submersion in ACSF. For example, 3% Cur/PVA films display a reduction of E' from ~9 GPa (dry, RT) to ~12 MPa (ACSF-swollen, 37 °C) (Figure 4-2). The ACSF-swollen Cur/PVA/CNC nanocomposite films display an E' that is higher than that of the Cur/PVA films (Figures 4-2 and A4-3), but considerably lower than that of the corresponding materials before swelling. For example, E' of the 1% Cur/PVA/CNC dropped from ~11 GPa (dry, RT) to ~130 MPa (ACSF-swollen, 37 °C). Thus, mechanical tests confirm that all materials

studied here are rigid when dry, but soften considerably upon swelling in (emulated) physiological conditions, as targeted for the intended intracortical microelectrode applications.

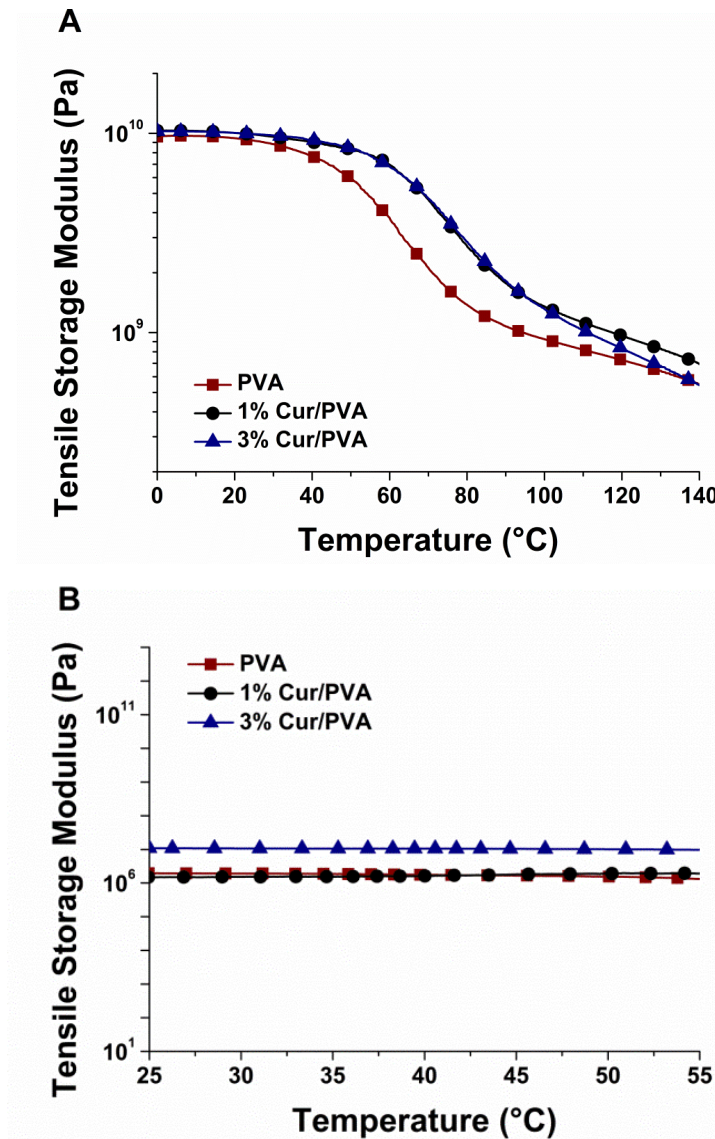


Figure 4-2. Representative dynamic mechanical analysis (DMA) traces showing the tensile storage moduli of (A) dry and (B) ACSF-swollen curcumin-loaded poly(vinyl alcohol) (PVA) samples as a function of temperature and curcumin content (1 or 3% w/w). Neat PVA was also studied for reference purposes. Average data of multiple experiments are compiled in Table A4-2.

4.4.3. Curcumin Release Profiles

In vitro curcumin release studies were carried out by submersing curcumin-loaded films in ACSF at 37 °C and monitoring the absorbance of curcumin in the solution as a function of time. The release, relative to the total amount of curcumin nominally included in the composition, is shown in Figure 4-3 and Figure A4-4. The data reveal a burst release, where most of the drug elution occurs within a timeframe of ~10 hours. Interestingly, only about ~15-25% w/w of the curcumin comprised in the PVA was released into the ACSF medium, with no clear correlation to the curcumin content in the material (1 or 3% w/w) or the presence or absence of CNCs. The absolute amount released from the samples scaled with the curcumin content; the 3% curcumin-loaded PVA films released ca. 3.1 times more curcumin than the 1% curcumin-loaded PVA films and the 3% curcumin-loaded PVA/CNC nanocomposite films released ca. 2.2 times more curcumin than the 1% curcumin-loaded PVA/CNC nanocomposites.

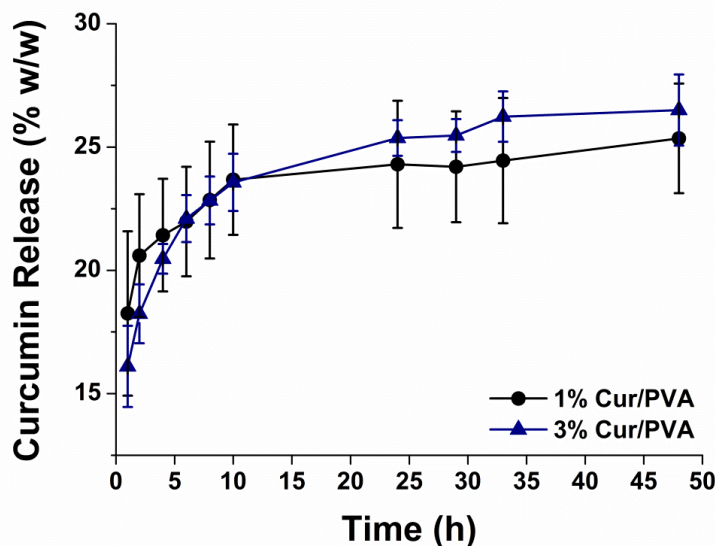


Figure 4-3. Cumulative *in vitro* release profile of curcumin-loaded polymers in ACSF at 37 °C. Values represent mean \pm S.D. (n = 4), and relative to the original nominal amount of curcumin in the materials.

4.4.4. Anti-oxidative Activity of Curcumin-Loaded Materials

The antioxidant activity of the curcumin-loaded materials was investigated utilizing the ability of curcumin to scavenge DPPH radicals. The corresponding reaction changes the absorption of the DPPH and can be readily monitored. The neat DPPH solution shows slow discoloration over time (Figures A4-5 and A4-6), which is due to slow reaction with the hydrogen-donating solvent (i.e. methanol), and requires that the spectroscopic scavenging data are referenced to this baseline. The function did not change when films of the neat PVA or the PVA/CNC nanocomposites were placed into the DPPH solution (Figures 4-4A and A4-7A). By contrast, the decrease was accelerated in the case of PVA or PVA/CNC loaded with 1% w/w curcumin, and even more so in the case of samples comprising 3% w/w curcumin (Figures 4-4A and A4-7A). The relative antioxidant activity of the curcumin-loaded PVA films containing 1 and 3% curcumin after 48 h incubation was ~0.23 and ~0.68, respectively, while that of the curcumin-loaded PVA/CNC films containing 1 and 3% curcumin was ~0.11 and ~0.65, respectively (Figures 4-4B and A4-7B).

4.4.5. *In vivo* Studies

Following material validation *in vitro*, initial *in vivo* characterization of the curcumin-loaded PVA materials was performed. Here, based on the performance in the DPPH anti-oxidative activity assay, 3% curcumin-loaded PVA (3% Cur/PVA) was chosen for *in vivo* testing. Neat PVA was used as a control for histological assessment. Forty male Sprague Dawley rats (225–300 g) (Charles River) were used in this study and sacrificed either 2, 4 or 12 weeks after implantation.

4.4.6. Neuronal Nuclei Density (NeuN)

Theoretical modeling has suggested that neuronal cell bodies must be within 50 μm of the intracortical microelectrode, in order to enable recordings of action potentials from individual neurons.¹¹ To quantify the number of neurons around the implants used here, we utilized the NeuN antibody, which selectively stains for neuronal nuclei.³⁵ All neuron

counts are presented as a percentage to condition and age-matched no surgery control animals.

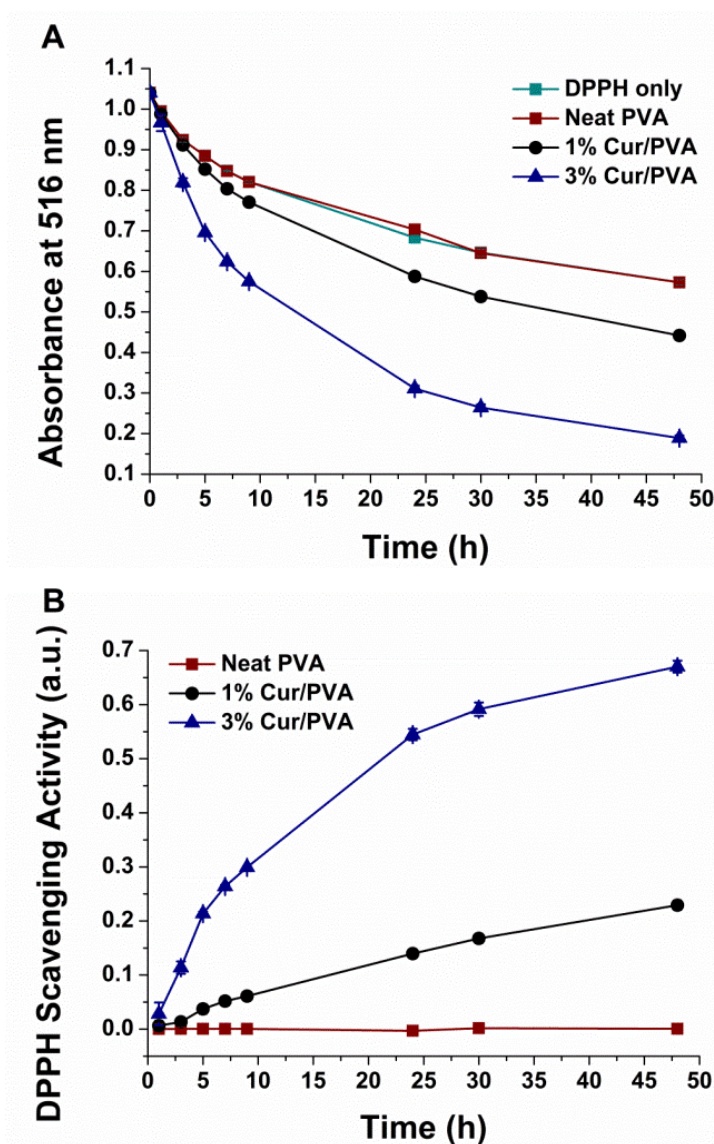


Figure 4-4. (A) Plot showing the absorbance at 516 nm of a methanolic solution of DPPH (100 μ M) as a function of time, and of the same solution in the presence of films consisting of neat PVA, or PVA with 1 or 3% w/w curcumin, respectively, incubated at 37 $^{\circ}$ C in the dark for up to 48 hours. (B) DPPH scavenging activity calculated from the results shown in (A) according to equation 3. The results shown are means \pm standard deviation of three independent experiments.

At 2 weeks after implantation, we observed that animals implanted with 3% Cur/PVA implants presented higher densities of NeuN⁺ neurons up to 200 μm from the implant surface ($p < 0.04$) than animals in which neat PVA control was implanted (Figure 4-5A, B). The asterisks in Figure 4-5 indicate conditions in which the binning intervals were statistically reduced from native sham tissue backgrounds ($p < 0.05$). Note, neat PVA control implants demonstrated significantly lower NeuN⁺ neuron densities in comparison to background from 0 to 600 μm from the implant surface, except for from 400 – 500 μm from the implant surface at 2 weeks post implantation (Figure 4-5B). However, by 100 μm from the implant surface, at the same time point, 3% Cur/PVA implants had returned to background levels of neuron densities, except for from 400 – 500 μm from the implant surface (Figure 4-5B). Reduction in neuronal densities at extended distances from the implant are most likely due to the craniotomy.³⁶

At 4 weeks after implantation, 3% Cur/PVA implants presented higher densities of NeuN⁺ neurons from 0 to 100 μm and 200 to 400 μm from the implant surface in comparison to neat PVA controls ($p < 0.04$; Figure 4-5C). Additionally, only neat PVA control implants from 0 to 50 μm from the implant surface demonstrated significantly lower NeuN⁺ neuron densities in comparison the background. Animals implanted with curcumin-releasing implants showed densities insignificant from background for all binning intervals at 4 weeks after implantation (Figure 4-5C). However, at 12 weeks post-implantation, similar neuronal densities were noted between both polymer implants, with 3% Cur/PVA implants only presenting higher densities of NeuN⁺ neurons from 100 to 200 μm from the implant surface (Figure 4-5D). In addition, both the neat PVA and the 3% Cur/PVA implants demonstrated significantly lower NeuN⁺ neuron densities in comparison to background from 0 to 50 μm from the implant surface, while neither material set was statistically different from background beyond 50 μm.

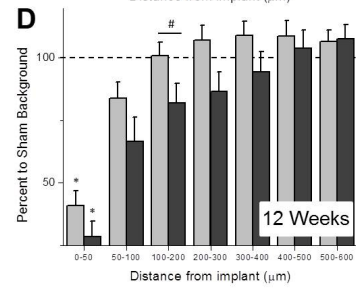
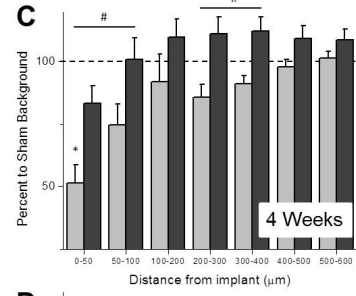
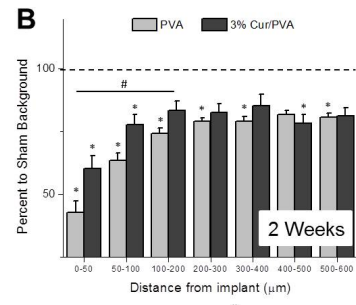
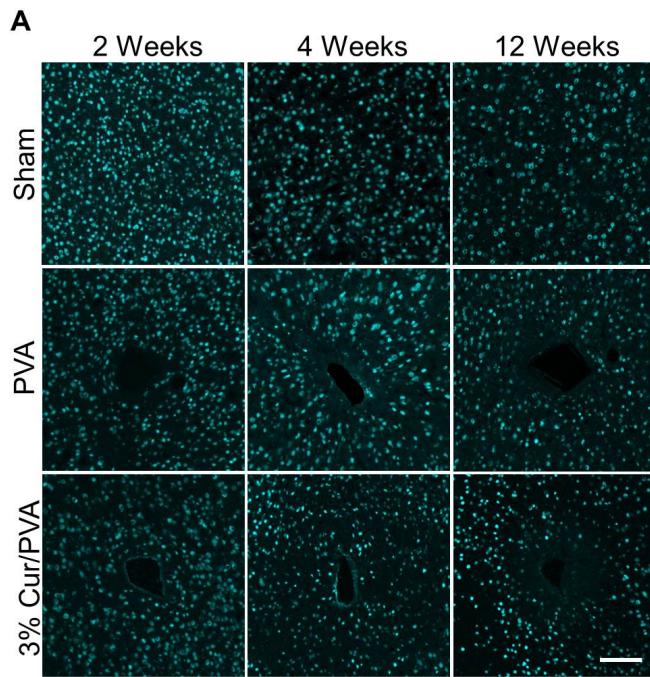


Figure 4-5. Neuronal nuclei populations surrounding neat PVA control and curcumin-releasing PVA implants. Neuronal (NeuN) density was investigated at 2, 4 and 12 weeks after polymer implantation up to 600 μm from the implant interface. At 2 weeks, neat PVA implants demonstrated significantly lower neuronal densities than non-surgery sham controls at all binning intervals investigated, except from 400 to 500 μm from the implant ($*p < 0.05$) (A, B). Animals implanted with curcumin-releasing PVA, however, only demonstrated densities significant from background up to 100 μm from the implant interface (B). In addition, significant differences in neuronal populations were noted between the two types of polymer implants up to 200 μm at 2 weeks ($\square p < 0.04$) (B). By 4 weeks post implantation, similar background densities of neurons, in comparison to non-surgery sham controls, were noted at all binning intervals, except from 0 to 50 μm in neat PVA implanted animals (A, C). In addition, significant differences between polymer types were noted from 0 to 100 μm and 200 to 400 μm ($\square p < 0.04$) (C). At 12 weeks post-surgical implantation, neat PVA and curcumin-releasing PVA demonstrated similar neuronal densities, with significant differences between the two samples only noted from 100 to 200 μm from the interface (D). In addition, neuronal densities lower than sham backgrounds were only noted from 0 to 50 μm at this time point in both conditions (D). Scale = 100 μm . Data is represented as an average \pm s.e.m.

4.4.7. Blood Brain Barrier Permeability (IgG)

Saxena *et al.* recently demonstrated a correlation between chronic blood-brain barrier (BBB) breach and microelectrode function.¹⁴ Therefore, we sought to explore the stability of the BBB after implanting the new mechanically adaptive, curcumin-releasing materials. The ability of the BBB to repair itself over time can be correlated to the amount of immunoglobulin G (IgG) present within the surrounding tissue.^{5, 16} If a microelectrode is implanted into the cortex and quickly removed, the BBB heals, as measured through the lack of IgG present in the tissue.⁷ Therefore, in order to investigate BBB integrity, the amount of IgG present at the implant site was examined.

Representative images and quantitative analysis from immunohistological staining of IgG indicated that the blood-brain barrier surrounding the neat PVA control implants was significantly more compromised than the blood-brain barrier surrounding 3% Cur/PVA implants at both 2 and 4 weeks post-implantation, but not at 12 weeks post-implantation (Figure 4-6). At 2 weeks post-implantation (Figure 6A), higher levels of IgG infiltration

within the cortical tissue surrounding neat PVA implants was seen across all binning intervals from the implant-tissue interface extending to 1 mm from the implant surface ($p < 0.03$ vs. curcumin-loaded implants). Further, the molecular distribution of IgG infiltration (λ) was significantly higher ($p < 0.003$) in animals receiving neat PVA control implants, indicating a much wider diffusion of accumulated serum proteins (Table 4-2). No significant differences in λ were noted at 4 or 12 weeks for IgG reactive tissue. Additionally, at 4 weeks post-implantation in the neat PVA control implants (Figure 6B), higher levels of IgG infiltration within the cortical tissue were seen from 200 μm to 400 μm from the implant surface ($p < 0.03$). By 12 weeks post-implantation, comparisons between both material sets failed to demonstrate significant differences in IgG infiltration within cortical tissue surrounding the implants (Figure 4-6C).

Table 2. Lambda Values of Inflammatory Markers

		Two Weeks	Four Weeks	Twelve Weeks
IgG	PVA	434.94 \pm 64.59*	188.95 \pm 38.06	135.97 \pm 36.52
	3% Cur/PVA	108.23 \pm 38.37*	113.24 \pm 20.41	117.03 \pm 15.86
GFAP	PVA	188.18 \pm 20.21	81.55 \pm 24.59	53.67 \pm 6.70
	3% Cur/PVA	154.19 \pm 19.37	88.92 \pm 13.70	77.25 \pm 9.36
IBA-1	PVA	86.59 \pm 20.20	49.57 \pm 4.98	49.02 \pm 5.23
	3% Cur/PVA	92.46 \pm 13.42	45.16 \pm 6.78	37.90 \pm 5.97
CD68	PVA	50.36 \pm 19.20	46.48 \pm 5.73	38.06 \pm 3.91
	3% Cur/PVA	60.17 \pm 8.84	44.06 \pm 5.17	49.52 \pm 7.77

*denotes significance between polymer types

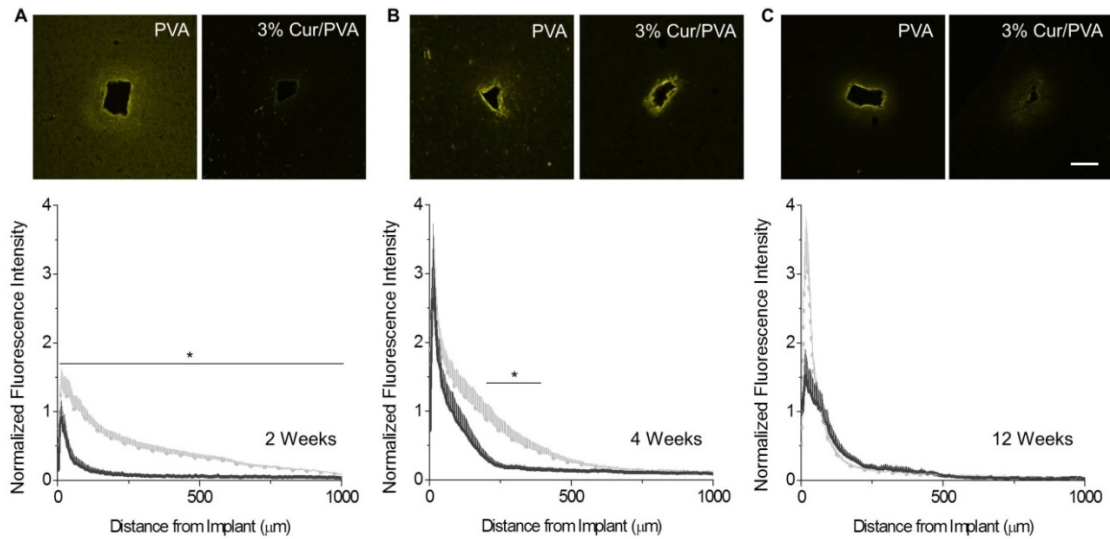


Figure 4-6. Infiltration of immunoglobulin-g (IgG) around neat PVA controls and curcumin-releasing PVA implants. The extent of blood brain barrier permeability around the implanted polymers was examined using labeling of immunoglobulin-g (IgG). At 2 weeks, poly(vinyl alcohol) (PVA) (light grey-dashed line) implants demonstrated significantly higher IgG infiltration in comparison to curcumin-releasing samples (solid dark grey line) up to 1000 μm away from the implant ($*p < 0.03$) (A). By 4 weeks, similar IgG profiles were noted between implanted conditions, with only significant differences noted from 200 to 400 μm away from the implant ($*p < 0.03$) (B). No significant differences between conditions were noted between the two materials at 12 weeks after implantation (C). Scale = 100 μm . Data is represented as an average \pm s.e.m.

4.4.8. Astrocytic Scar Formation: Astrogliosis (GFAP)

Immunostaining for GFAP⁺ cells allows for the monitoring of both immature/mature resting or activated astrocytes,³⁷ both of which play a dominant role in repair following CNS injury. Further, many researchers hypothesize that the astrocytic diffusion barrier may play a beneficial role in restricting the impact of macrophage-secreted factors on the surrounding tissue, as well as mechanically shielding the surrounding tissue from micromotion-induced strains surrounding the historically stiff microelectrodes.^{8, 38, 39} However, astrogliosis may also increase the tissue's impedance to small ion transport, potentially limiting recording function as first suggested by Schmidt and co-workers.^{40, 41}

Here, immunostaining for GFAP⁺ astrocytes showed that at 2 weeks post-implantation, 3% Cur/PVA implants demonstrated significantly more GFAP⁺ cells within the first 100 μm from the implant surface (Figure 4-7A, $p < 0.01$) than the neat PVA control implants. Interestingly, at 4 weeks post-implantation, the trend reversed, and the neat PVA control implants presented with more GFAP⁺ cells than the 3% Cur/PVA implants from 0 to 200 μm from the implant surface (Figure 4-7B, $p < 0.01$). However, by 12 weeks post-implantation, the distribution of GFAP⁺ cells encompassing both the neat and curcumin-loaded PVA implants were statistically similar (Figure 4-7C). No significant effect on lambda was noted between polymer types for any investigated time point (Table 4-2).

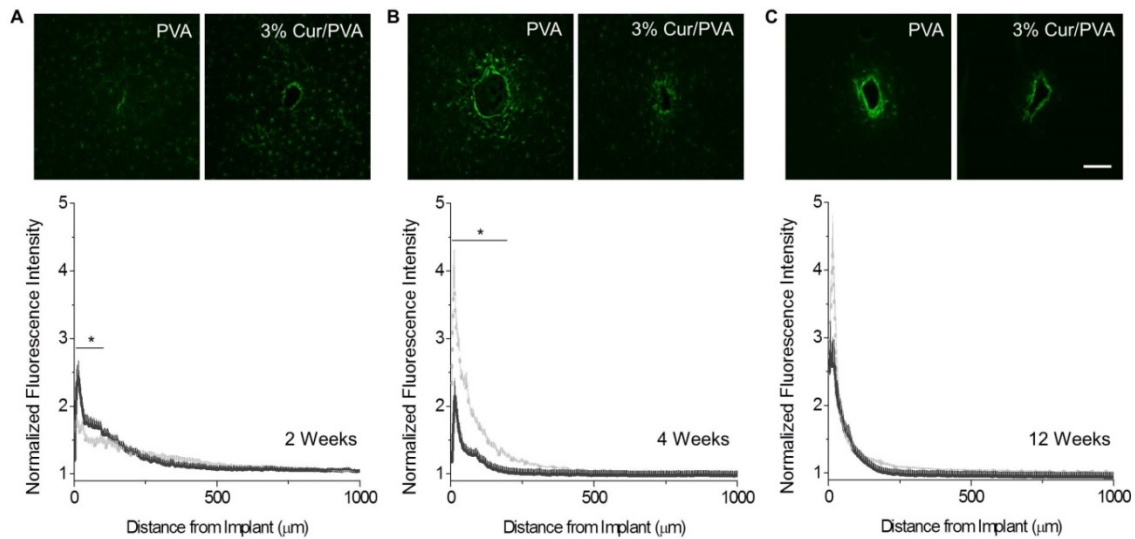


Figure 4-7. Astroglial response surrounding neat PVA control and curcumin-loaded PVA implants in the cortex. The extent of astrocytic scarring around the implanted polymers was investigated using labeling of glial fibrillar acidic protein (GFAP). At 2 weeks post implantation, neat PVA control implants (light grey dashed line) had significantly less astrocytic scarring up to 100 μm away from the implant interface in comparison to curcumin-loaded implants (dark solid grey line) ($*p < 0.01$) (A). In contrast, by 4 weeks, curcumin-releasing implants had significantly lower intensities of GFAP⁺ cells at the implant interface up to 200 μm away from the implant than the neat PVA controls ($*p < 0.01$) (B). No significant differences were noted between the two materials at 12 weeks post implantation (C). Scale = 100 μm . Data is represented as an average \pm s.e.m.

4.4.9. Microglia and Macrophage Density (total – IBA-1; activated – CD-68)

Microglia/macrophages mediate the inflammatory and immune response to minimize bacterial/viral invaders,⁴² as well as infiltrating serum proteins within the CNS (microglia).⁴³ When activated, microglia and macrophages release several inflammatory factors that can become neurotoxic, and have been implicated to propagate the neuroinflammatory response to implanted intracortical microelectrodes.^{10, 15, 16} Therefore, many studies of the tissue response to intracortical electrodes have focused on microglia/macrophage activation in response to indwelling implants.

The ionized calcium binding adapter molecule (IBA-1), which is involved in aspects of motility-associated rearrangement of the actin cytoskeleton, is a selective marker for both resting and activated microglia/macrophages.⁴⁴ Immunostaining for IBA-1 provides information for total microglial and macrophage density and distribution around cortical implants. Here, immunohistological assessment demonstrated a significant increased density of IBA-1⁺ cells at the implant surface in comparison to background IBA-1⁺ expression (Figure 4-8; $p < 0.001$). The increased density of IBA-1⁺ cells declined over the first 150-250 μm , back to background levels at all time points investigated post-implantation. No statistically significant difference between the neat PVA control and 3% Cur/PVA implants were identified for any of the three time points examined. Further, no significant effect on lambda was noted between polymer types for any investigated time point (Table 4-2).

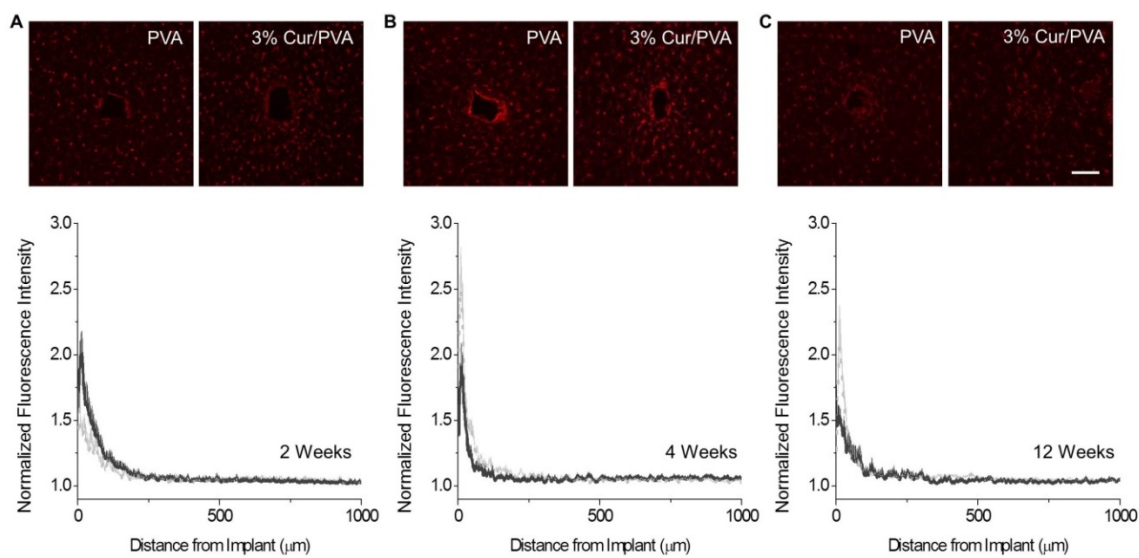


Figure 4-8. Total microglia and macrophage accumulation (IBA-1⁺ cells) around neat PVA controls and curcumin-releasing polymer implants. The total population of microglia and macrophages around implanted polymers was investigated by labeling IBA-1⁺ cells. Here, similar microglia/macrophage infiltration was noted and there were no significant differences between the two polymer materials for all assessed time points. Dark grey solid line denotes 3% Cur/PVA and dashed light grey line denotes neat PVA control. Scale = 100 μm. Data is represented as an average ± s.e.m.

CD68 is a cytoplasmic antigen found only in activated microglia and macrophages.⁴⁵ Therefore, CD68 is more regularly used to identify activated microglia/macrophages, which are likely to be secreting pro-inflammatory molecules. As with IBA-1, immunohistological assessment of CD68 expression demonstrated a significant increased density at the implant surface in comparison to background CD68 expression (Figure 4-9; $p < 0.001$). At 2 weeks post-implantation, the increased intensity of CD68⁺ cells declined over the first ~150 μm, back to background levels (Figure 4-9A). Additionally, no statistically significant differences between neat PVA controls and 3% Cur/PVA implants were identified. However, at 4 weeks post-implantation, CD68 reactive tissue expanded to ~450 μm for the neat PVA control and ~250 μm for the 3% Cur/PVA implants (Figure 4-11B). Additionally, expression levels of CD68 were statistically higher for the neat PVA implants from 0 to 300 μm from the implant surface ($p < 0.04$). At 12 weeks post-implantation, peak intensities of CD68 expression for both the neat PVA control and the 3% Cur/PVA more than doubled the expression levels at 2 or 4 weeks post-implantation

(Figure 4-9C). Nevertheless, no statistically significant difference between neat PVA control and 3% Cur/PVA implants were identified. In addition, no significant effect on lambda was noted between polymer types for any investigated time point (Table 4-2).

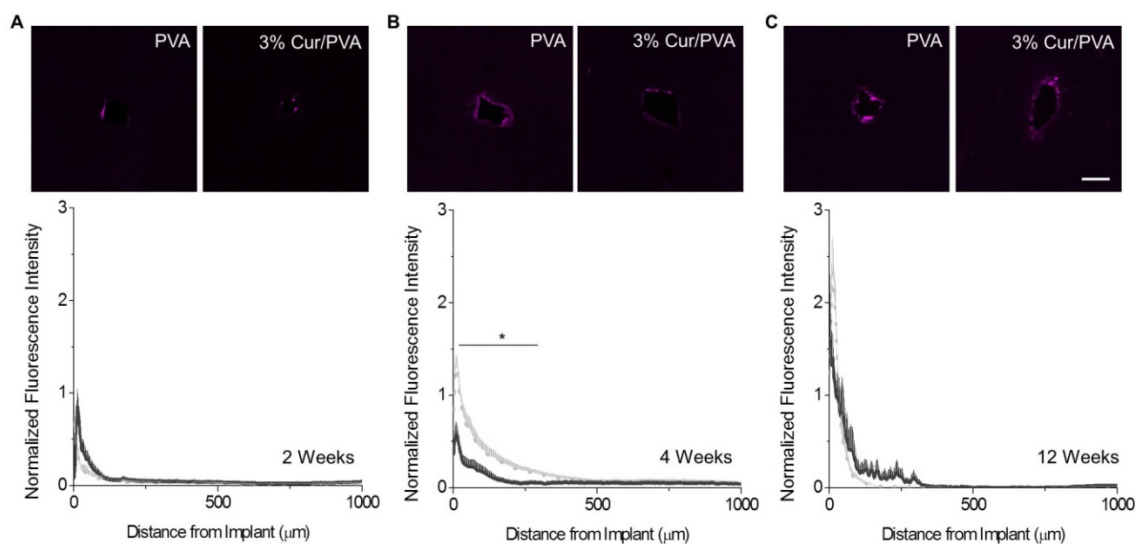


Figure 4-9. Accumulation of activated microglia and macrophages (CD68⁺) around neat PVA controls and curcumin-releasing implants. The presence of activated microglia and macrophages (CD68⁺) around implanted polymers at 2, 4 and 12 weeks post implantation was investigated. At 2 weeks, no notable differences between the two materials were demonstrated (A). However, by 4 weeks post implantation, significantly higher amounts of CD68⁺ cells were accumulated around neat PVA controls (light grey dashed line) than in the case of curcumin-releasing implants (dark grey solid line) up to 300 μm away from the implant interface (*p<0.04) (B). Similar to 2 weeks post implantation, no statistical differences between the two materials was noted at 12 weeks post implantation (C). Scale = 100 μm. Data is represented as an average ± s.e.m.

4.4.10. Wound Healing (HMGB-1)

Wound healing is a critical component following device implantation in the central nervous system. Recently, we demonstrated that acute suppression of wound healing events by anti-oxidant therapy was correlated with higher populations of viable neurons around implanted devices in the cortex.¹⁰ To investigate if curcumin-releasing implants support similar molecular mechanisms, the expression of high mobility group box-1

(HMGB-1), a cytokine that has been shown to inhibit wound healing^{46, 47} was quantified at 2, 4 and 12 weeks post implantation.

Notably, we found that curcumin-releasing implants had higher amounts of HMGB-1 at both 2 and 4 weeks in comparison to neat PVA control, with the highest amounts noted at 2 weeks after implantation (Figure 4-10). By 12 weeks, however, the reverse trend was noted, where neat PVA implants had higher levels of HMGB-1 at the implant interface in comparison to curcumin-loaded implants.

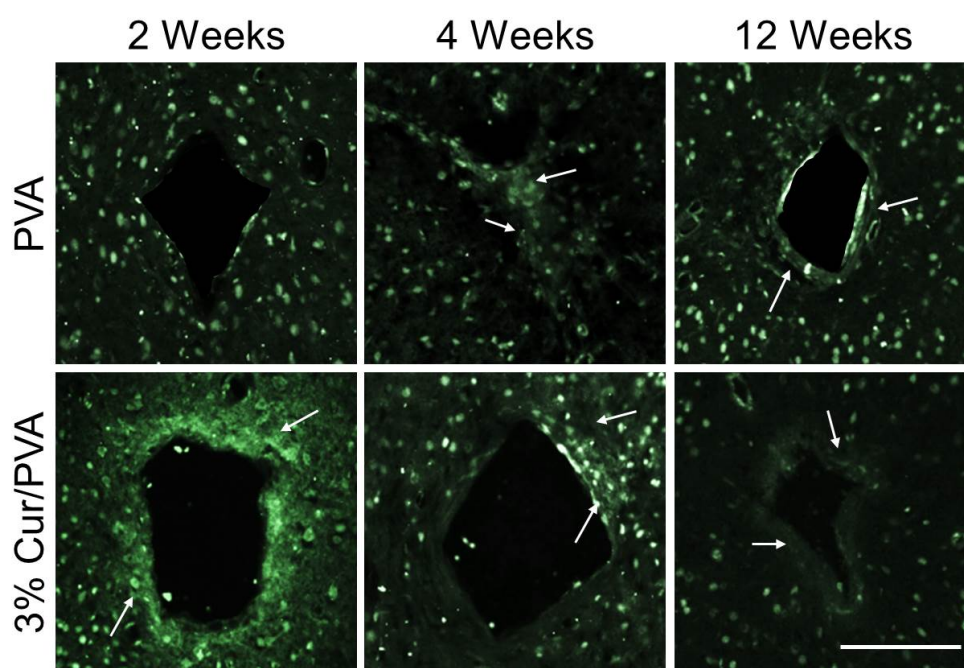


Figure 4-10. Expression of High Mobility Group Box-1 (HMGB-1) around neat PVA controls and curcumin-releasing PVA implants. A qualitative assessment of intra- and extracellular high mobility group box-1 (HMGB-1) expression was investigated around both polymers at 2, 4 and 12 weeks after implantation. At 2 weeks, animals with curcumin-releasing implants had slightly higher amounts of HMGB-1 at the device interface. Notably, high amounts (intra- and extracellular) of HMGB-1 were noted in both polymers at 4 weeks after implantation, with higher levels noted in animals receiving a 3% Cur/PVA implant. In contrast, by 12 weeks after implantation, neat PVA implants demonstrated larger amounts of HMGB-1 expression around the implant. Arrows denote extracellular accumulations of soluble HMGB-1 around implanted polymer samples. Scale = 100 μ m.

4.5. DISCUSSION

Intracortical microelectrodes have been developed from all classes of materials. Regardless of the combination of materials that have been employed, all suffer a similar fate. Early in the implant periods, activity of many neurons can be recorded. However, while such early results are encouraging, devices are often plagued by inconsistent long-term recording stability and performance. Unfortunately, there has been much debate in the literature and conference circle over the mechanism of device failure.⁴⁸⁻⁵⁰ The debate has perpetuated primarily due to the believed inconsistency between the time course of the inflammatory response to the implant,^{5, 51-53} and the longest reported functional devices in animal and human models.^{54-56 57 58} In part due to the recent flux of funding by the Defense Advanced Research Projects Agency (DARPA), under the Histology for Interface Stability over Time program,^{14, 49, 59} several studies have been reported on the relative contribution of both the biotic and abiotic failure modes (not DARPA funded⁴⁸). A number of failure modes likely influence chronic recording stability and quality, including 1) direct mechanical damage, 2) corrosion of electrical contacts, 3) degradation of passivation layers and insulating coatings, and 4) the neuro-inflammatory response that the brain mounts against chronically implanted devices.⁴⁸⁻⁵⁰ Utilizing 16-channel 50 μm tungsten microwire arrays, the Sanchez group assessed the biotic and abiotic failure modes of for up to 9 months in 25 rats.⁴⁹ Their study concluded that mechanisms of failure were multi-faceted. Further, Sanchez felt that failure modes occur concurrently, and are incapable of isolation. Of note, Sanchez also reported a high level of ferritin expression, intraparenchymal bleeding and microglia degeneration; factors were attributed to oxidative stress.

The Bellamkonda group has also linked oxidative stress to late-onset neurodegeneration at the microelectrode tissue interface.⁵ More recently, the Bellamkonda group has expended on their initial findings, and was among the first to demonstrate a direct correlation between electrode performance and the histological response.¹⁴ In agreement with the Sanchez group, Bellamkonda and team suggested that the blood-brain barrier status is the most critical physiological determinant of the performance of the

microelectrode.¹⁴ Further, Bellamkonda has demonstrated that increased expression of inflammatory signaling molecules, specifically cytokines and chemokines, directly correlate with histology and device performance.⁵⁹ Findings from both Sanchez and Bellamkonda supported the seminal work by Biran *et al.* from 2005.⁵² In Biran's study, the Tresco group demonstrated that microglia and macrophages cultured from explanted intracortical microelectrodes secreted increased levels of MCP-1 and TNF- α , both known to increase blood-brain barrier permeability in high levels. Most recently, the Donoghue group reported a 17 year retrospective of Utah electrode arrays in non-human primates.⁴⁸ In their extensive analysis, the Donoghue group reported that nearly half of the failed devices were acute mechanical failures. Mechanical failures can be largely due to the brittleness of the materials, and are a significant contributor to the recent exploration of polymeric alternatives to silicon and ceramic. Of the remaining failed devices, 46% of those were due to the biological response, 25% were reported as materials failure, and the remaining 28% were unknown. Degradation of insulating materials resulting in device failure can be catalyzed by the oxidative inflammatory response, further supporting finding by Sanchez stating that failure modes occur concurrently, and are incapable of isolation. The combined work of Sanchez, Bellamkonda, Tresco, Donoghue, and many more has directed the field to the significant interconnected role that both the blood-brain barrier and oxidative stress play on the performance of intracortical microelectrodes. Therefore, we have explored several mechanisms that have been suggested to either promote a decline in the stability of the blood-brain barrier or the inflammatory-mediated oxidative environment around intracortical microelectrodes. Specifically, we have previously shown that both anti-oxidative treatment and the use of mechanically adaptive materials are effective strategies to temporally mitigate the neuroinflammatory response to intracortical microelectrodes.^{8, 10} However, as discussed above, both mechanisms are interconnected, and synergistic approaches are yet to be reported. Here we investigated the use of anti-oxidant-releasing, mechanically adaptive polymers to begin to elucidate the potential use of a synergistic approach to address the variable neuronal viability and inflammatory processes.

Our group has developed physiologically-responsive, mechanically adaptive materials for use as “smart” substrates for intracortical microelectrodes,^{22, 26, 60} Our hypothesis is that mechanically adaptive materials are useful for intracortical microelectrodes that initially require a stiff material for easy insertion, but are chronically compliant to minimize strain on the surrounding brain tissue. Most of our reported materials are nanocomposites that are comprised of a polymeric matrix and reinforcing nanofibers. Our nanocomposite materials are engineered to be stimuli-responsive and regulate the mechanical properties of the bulk material. Among several materials series based on this architecture,^{25, 61, 62} we recently reported nanocomposites based on poly(vinyl alcohol) (PVA) and cellulose nanocrystals (CNCs) derived from tunicates.²⁴ Unlike several of the polymer systems we have used previously, PVA has been FDA-approved for applications in nerve grafts.⁶³ Most processing conditions result in PVA that is water-soluble. However, the specific melt-processing protocol we employed renders the PVA materials water-insoluble. Additionally, curcumin is a natural polyphenol derived from the rhizome of the herb *Curcuma longa* having a wide range of therapeutic activities such as anti-cancer, anti-inflammatory, anti-oxidant, wound healing, and neuroprotective effects.^{64, 65} Further, phase I clinical trials showed that curcumin is safe at very high doses (12 g/day) in humans.^{66, 67} Therefore, the system developed here utilized PVA and PVA/CNC nanocomposites capable of releasing curcumin short term.

Prior to *in vivo* testing, the physiochemical characteristics (mechanical and thermal properties, swelling behavior), drug release, and anti-oxidant activity of a subset of four antioxidant-loaded PVA compositions with either 1% and 3% w/w curcumin and either no CNCs or 8% v/v CNCs were tested *in vitro* (ACSF, 37 °C). Swelling experiments in such emulated physiological conditions showed that the present materials swell by about 30-40% w/w independent of the composition (Table 4-1). Further, all of the materials studied here undergo a pronounced and reversible modulus reduction from ~8-11 GPa to ~1-130 MPa upon exposure to emulated physiological conditions (Figures 4-2 and A4-3). We have previously described that the reversible modulus change is due to matrix plasticization and/or decoupling of hydrogen bonding between CNCs. As expected based

on previous data, the CNC-containing nanocomposites show a higher tensile storage modulus in the ACSF-swollen state (~130 and ~40 MPa for materials containing 1% and 3% w/w curcumin, respectively) than the CNC-free PVA loaded with the drug (~1 and ~13 MPa). The higher modulus of PVA/CNC nanocomposites in emulated physiological conditions is consistent with demonstrated examples of modest reinforcement, even when the CNCs are decoupled.²² *In vitro* drug release studies were performed to establish the timeframe in which the curcumin is released under physiological conditions. Curcumin showed burst release kinetics from PVA films followed by a slower sustained release into the medium after 2 days (Figures 4-3 and A4-4). Qualitatively, the data match swelling-induced release profiles.⁶⁸ The fact that in all cases only a fraction of the incorporated drug is released from annealed PVA-matrices has been observed before,⁶⁹ and was attributed to the semicrystalline nature of the matrix polymer, which hinders the diffusion of the drug molecules.⁷⁰ The rate of curcumin release from these materials enables localized delivery of curcumin directly at the trauma site. Specifically, the size of cortical implants was capable of facilitating a localized release of 1.5 μM (1% curcumin containing polymers), 2.5 μM (3% curcumin loaded PVA/CNC) and 4.5 μM (3% curcumin loaded PVA) after 48 hours respectively. Since curcumin has previously shown to be effective *in vitro* from 0.1 μM to 5 μM ,^{71, 72} all engineered polymer systems investigated here were capable of maintaining a therapeutic dose of curcumin for at least 48 hours. Of the four anti-oxidant loaded samples studied, the two compositions loaded with 3% curcumin had higher DPPH scavenging activity than the materials with 1% curcumin. Since the 3% curcumin-loaded PVA demonstrated the largest mechanical contrast with the lowest stiffness after exposure to the physiological conditions (Figures 4-2 and A4-3), is compositionally simpler than the nanocomposites, and displays a high absolute curcumin release, this composition was chosen for the *in vivo* studies.

Specifically, 3% Cur/PVA and neat PVA intracortical probes were implanted into the motor cortex of rats and investigated the neuroinflammatory response surrounding the implant. Loss of viable neurons within 50 μm of the microelectrode could result in the inability to properly record individual neural activity¹¹. Therefore, we investigated the

effect our polymer system would have on the neuronal populations surrounding the intracortical implant. Notably, we found that the short-term release of curcumin from the implant directly impacted neuronal populations surrounding the device. Curcumin-loaded implants provided significant neuronal protection at both 2 and 4 weeks after implantation (Figure 4-5). In addition, we found that at 2 weeks post-implantation, neat PVA control implants were unable to return to sham background densities for all investigated binning intervals, except 400 to 500 μm from the implant. The incorporation of curcumin into the chronically compliant polymer implants resulted in neuronal recovery by 100 μm at 2 weeks post implantation, with only the binning interval of 400 to 500 μm being significant from background densities. Similar trends were noted at 4 weeks, where background neuronal densities were noted in all binning intervals for curcumin-loaded implants. In contrast, neat PVA control implants had significantly lower densities than background from 0 to 50 μm from the interface. Together, these results suggest that a mechanically compliant implant based on PVA was alone insufficient to maintain background densities of neurons around the implant, especially at 2 and 4 weeks following implantation. However, the incorporation of localized anti-oxidant, curcumin, aided in maintaining higher neuronal densities locally and globally around the implant. Fluctuations in neuronal populations around cortical implants have been shown to be time-dependent and directly correlated to the inflammatory response and vasculature stability following surgical implantation.^{5, 7, 73} Further, the use of anti-oxidants or mechanically compliant materials has shown variable effects on the neuroinflammatory response.^{8, 10} Therefore, in order to better characterize our new polymer system and gain insight into events mediating neuronal survival, neuroinflammatory and blood-brain barrier stability were monitored at three distinct time points during the inflammatory cascade.

At 2 weeks after implantation, in comparison to neat PVA controls, curcumin-releasing implants were found to significantly reduce blood-brain barrier (BBB) permeability up to 1000 μm from the implant interface (Figure 4-6). Interestingly, at the same time point, infiltration and activation of resident microglia/macrophages were statistically

insignificant between curcumin-loaded and neat PVA implants (Figures 4-8A, 4-9A). Additionally, animals receiving curcumin-loaded implants also exhibited a significantly more robust glial scar than animals implanted with neat PVA implants (Figure 4-7A). Many groups, including our own, have demonstrated the role of glial scar compaction and pro-inflammatory molecules on neuronal survival and BBB stability surrounding intracortical microelectrodes.^{7, 74, 75} In fact, it has been suggested that astrogliosis is critical in providing a physical barrier between neurotoxic cytokines and soluble factors released by activated microglia/macrophages and the neuronal environment.⁷⁶ In addition, curcumin has been shown to up-regulate pathways responsible for the breakdown or down regulation of pro-inflammatory molecules in activated inflammatory cells.⁷⁷ Therefore collectively, our results at 2 weeks further support the hypothesis that blood-brain barrier stability is associated with neuronal survival. Wherein, for our model, improvements in neuronal survival and BBB stability are due to a synergistic effect between glial scar compaction and/or a likely reduction of pro-inflammatory biomolecules accumulation from activated inflammatory cells.

It is important to note, however, that within an inflammatory system a dichotomy between a pro- and anti-inflammatory state exists.^{78, 79} Therefore, therapeutic intervention within the system can bolster or deteriorate the surrounding tissue homeostasis depending on time of administration and therapeutic dosage. Specifically, Rennaker *et al.* demonstrated that short term dosing (5 days) with minocycline following intracortical microelectrode implantation was capable of sustaining a viable neuronal recording environment for up to 4 weeks after implantation.⁸⁰ In addition, we recently demonstrated that dosing with resveratrol, a naturally derived anti-oxidant, the day before and after electrode implantation, could facilitate more viable neurons around intracortical microelectrodes for up to 4 weeks after implantation.¹⁰ Short-term therapeutic intervention in neurodegenerative disease models, such as traumatic brain injury and spinal cord injury, has also demonstrated similar neuroprotective effects.^{81, 82} Hence, it is not surprising that in our model, a short-term release of curcumin from polymer implants

resulted in conferred neuroprotection up to 4 weeks after surgical implantation (Figure 4-5).

However, neuronal populations surrounding intracortical microelectrodes have been shown to be multi-phasic, with lowest densities occurring at early (2 weeks) and late (>12 weeks) time points.^{5, 7} Therefore, in order to fully determine if our polymer system was capable of providing long-term neuroprotection, we also investigated the neuroinflammatory response surrounding our PVA-based cortical implants at 12 weeks post-implantation. By 12 weeks, we found that both curcumin-loaded and neat PVA control implants had statistically similar neuronal populations at the interface, with statistical differences only noted at 100 to 200 μm away from the implant (Figure 4-5). Further, all other quantified neuroinflammatory markers were statistically comparable at the same time point between both polymer films. Together with the 2 and 4 week data, our data suggest that the short-term release of curcumin from the mechanically adaptive PVA system was unable to facilitate neuroprotection around the implant at late chronic time points. Specifically, in combination with our *in vitro* assessment, curcumin loaded polymer implants were only capable of releasing up to 4.5 μM for 48 hours after implantation. Due to this finding, we hypothesize that multiple exposures to an anti-oxidant (localized or systemic) may be required to maintain neuroprotection around the device throughout the lifetime of the implant. Alternatively, the solubility of PVA may increase due to long-term exposure to harsh inflammatory cell laden environments, resulting in a delayed or secondary neuroinflammatory response. Consequently, we also propose that other mechanically adaptive polymer substrates be explored in combined anti-oxidant releasing systems.

Further, we suggest that future design and use of mechanically adaptive polymer systems for neural interfaces must account for the degree of swelling demonstrated by the polymer systems. Here we found that our PVA polymer systems had a maximum swelling range of approximately 35% to 40%, but still had the ability to mediate the neuroinflammatory response occurring after cortical implantation. In addition, prior reports by our group and others have utilized polymer systems with similar or higher

degrees of swelling and also shown the ability of their various polymer systems in reducing the neuroinflammatory response to cortical implants.^{8, 83, 84} Thus, given the high potential our and similar polymer systems have had in stabilizing the neuroinflammatory response, we have previously reported on a manufacturing process to account for large degrees of swelling for mechanically adaptive polymer systems for the application of intracortical microelectrodes.²⁶ Briefly, our previously described manufacturing processes would allow direct substitution of the silicon backbone for the mechanically adaptive polymer. Therefore, regardless of swelling, the electrical contacts along the device shank would still maintain functionality after implantation.

Finally, curcumin has also been shown to impact wound healing.^{64, 85} Therefore, to examine the effects that curcumin-loaded implants had on wound healing in our intracortical microelectrode model, we investigated the expression of high mobility group box-1 (HMGB-1) around implanted polymer implants. Previous reports have shown HMGB-1 expression and release to be directly implicated in preventing collagen synthesis during wound healing.⁴⁷ Notably, we found an increase of HMGB-1 expression around implanted curcumin-loaded PVA implants at 2 and 4 weeks in comparison to neat PVA controls (Figure 4-10). Interestingly, high levels of HMGB-1 expression were correlated with neuroprotection around the implants (Figure 4-5). Therefore, similar to our previous findings,¹⁰ a delayed wound healing response to intracortical implants may be beneficial in facilitating neuroprotection around the device. Further, given the similarities in neuronal populations between conditions at 12 weeks, our results suggest that initial delays in wound healing may not significantly affect the chronic response to the implanted device.

4.6. CONCLUSIONS

In summary, our results show that the incorporation of the anti-oxidant curcumin into the mechanically adaptive polymer poly(vinyl alcohol) provided significant improvements in neuronal densities surrounding cortical implants in comparison to neat polymer films up to 4 weeks after implantation. However, at 12 weeks post implantation, no significant

differences between curcumin-releasing and neat PVA reference implants were apparent for all investigated markers. Taken together, our results suggest that acute attenuation of inflammatory events using localized drug delivery mechanisms, such as release of curcumin, would not cause detrimental effects at more chronic time points. Further the results presented here provide exciting opportunities to better understand the importance and optimal timing of wound healing events around cortical implants such that neuronal degeneration is prevented. Building on our proof-of-concept study, we suggest that future studies should continue to investigate the use of mechanically adaptive polymer systems, in conjunction with anti-oxidant release to mediate acute and chronic neuroinflammatory events surrounding intracortical microelectrodes. In order to better understand if the effects of short-term local release of antioxidant therapies are sufficient for long-term neuroprotection surrounding intracortical microelectrodes, it is imperative that future studies investigate the use of additional anti-oxidants and alternative mechanically adaptive polymer systems with improved long-term *in vivo* stability.

4.7. REFERENCES

1. M. A. L. Nicolelis, *Nat. Rev. Neurosci.*, 2003, **4**, 417-422.
2. A. B. Schwartz, *Annu. Rev. Neurosci.*, 2004, **27**, 487-507.
3. D. M. Taylor, S. I. H. Tillery and A. B. Schwartz, *Science*, 2002, **296**, 1829-1832.
4. C. A. Chestek, V. Gilja, P. Nuyujukian, J. D. Foster, J. M. Fan, M. T. Kaufman, M. M. Churchland, Z. Rivera-Alvidrez, J. P. Cunningham, S. I. Ryu and K. V. Shenoy, *J. Neural Eng.*, 2011, **8**, 045005.
5. G. C. McConnell, H. D. Rees, A. I. Levey, C.-A. Gutekunst, R. E. Gross and R. V. Bellamkonda, *J. Neural Eng.*, 2009, **6**, 056003.
6. R. Biran, D. C. Martin and P. A. Tresco, *Exp. Neurol.*, 2005, **195**, 115-126.
7. K. A. Potter, A. C. Buck, W. K. Self and J. R. Capadona, *J. Neural Eng.*, 2012, **9**, 046020.
8. J. P. Harris, J. R. Capadona, R. H. Miller, B. C. Healy, K. Shanmuganathan, S. J. Rowan, C. Weder and D. J. Tyler, *J. Neural Eng.*, 2011, **8**, 066011.
9. B. D. Winslow, M. B. Christensen, W. K. Yang, F. Solzbacher and P. A. Tresco, *Biomaterials*, 2010, **31**, 9163-9172.
10. K. A. Potter, A. C. Buck, W. K. Self, M. E. Callanan, S. Sunil and J. R. Capadona, *Biomaterials*, 2013, **34**, 7001-7015.
11. G. Buzsaki, *Nat. Neurosci.*, 2004, **7**, 446-451.
12. P. A. Tresco and B. D. Winslow, *Critical Reviews in Biomedical Engineering*, 2011, **39**, 29-44.
13. M. Jorfi, J. L. Skousen, C. Weder and J. R. Capadona, *J. Neural Eng.* 2015, **12**, 011001.
14. T. Saxena, L. Karumbaiah, E. A. Gaupp, R. Patkar, K. Patil, M. Betancur, G. B. Stanley and R. V. Bellamkonda, *Biomaterials*, 2013, **34**, 4703-4713.
15. W. He and R. V. Bellamkonda, in *Indwelling Neural Implants: Strategies for Contending with the In Vivo Environment* ed. W. M. Reichert, 2008.
16. J. Skousen, S. Merriam, O. Srivannavit, G. Perlin, K. Wise and P. Tresco, *Prog. Brain Res.*, 2011, **194C**, 167-180.
17. T. Ware, D. Simon, D. E. Arreaga-Salas, J. Reeder, R. Rennaker, E. W. Keefer and W. Voit, *Adv. Funct. Mater.*, 2012, **22**, 3470-3479.
18. J. R. Capadona, D. J. Tyler, C. A. Zorman, S. J. Rowan and C. Weder, *MRS Bull.*, 2012, **37**, 581-589.
19. L. W. Tien, F. Wu, M. D. Tang-Schomer, E. Yoon, F. G. Omenetto and D. L. Kaplan, *Adv. Funct. Mater.*, 2013, **23**, 3185-3193.
20. K. Shanmuganathan, J. R. Capadona, S. J. Rowan and C. Weder, *Prog. Polym. Sci.*, 2010, **35**, 212-222.
21. A. E. Hess, K. A. Potter, D. J. Tyler, C. A. Zorman and J. R. Capadona, *J. Vis. Exp.*, 2013, **78**, e50078.
22. J. R. Capadona, K. Shanmuganathan, D. J. Tyler, S. J. Rowan and C. Weder, *Science*, 2008, **319**, 1370-1374.

23. J. R. Capadona, O. Van Den Berg, L. A. Capadona, M. Schroeter, S. J. Rowan, D. J. Tyler and C. Weder, *Nat. Nanotechnol.*, 2007, **2**, 765-769.
24. M. Jorfi, M. N. Roberts, E. J. Foster and C. Weder, *ACS Appl. Mater. Interfaces*, 2013, **5**, 1517-1526.
25. J. D. Fox, J. R. Capadona, P. D. Marasco and S. J. Rowan, *J. Am. Chem. Soc.*, 2013, **135**, 5167-5174.
26. A. E. Hess, J. R. Capadona, K. Shanmuganathan, L. Hsu, S. J. Rowan, C. Weder, D. J. Tyler and C. A. Zorman, *J. Micromech. Microeng.*, 2011, **21**, 054009.
27. T. Ware, D. Simon, R. L. Rennaker and W. Voit, *Polym. Rev. (Philadelphia, PA, U. S.)*, 2013, **53**, 108-129.
28. V. Favier, H. Chanzy and J. Y. Cavaille, *Macromolecules*, 1995, **28**, 6365-6367.
29. www.alzet.com/products/cfs_prep.php, Accessed 08/04/2009.
30. Y. Zou, Y. Lu and D. Wei, *J. Agric. Food Chem.*, 2004, **52**, 5032-5039.
31. K. A. Potter, J. S. Simon, B. Velagapudi and J. R. Capadona, *J. Neurosci. Methods*, 2012, **203**, 96-105.
32. M. Ravikumar, S. Jain, R. H. Miller, J. R. Capadona and S. M. Selkirk, *J. Neurosci. Methods*, 2012, **211**, 280-288.
33. B. D. Winslow and P. A. Tresco, *Biomaterials*, 2010, **31**, 1558-1567.
34. E. Azemi, C. F. Lagenaur and X. T. Cui, *Biomaterials*, 2011, **32**, 681-692.
35. R. J. Mullen, C. R. Buck and A. M. Smith, *Development*, 1992, **116**, 201-211.
36. J. Cole, A. Yarnell, W. Kean, E. Gold, B. Lewis, M. Ren, D. McMullen, D. Jacobowitz, H. Pollard, J. O'Neill, N. Grunberg, C. Dalgard, J. Frank and W. Watson, *J. Neurotrauma*, 2011, **28**, 359-369.
37. M. Eddleston and L. Mucke, *Neuroscience*, 1993, **54**, 15-36.
38. M. Aschner, U. Sonnewald and K. H. Tan, *Brain Pathol*, 2002, **12**, 475-481.
39. G. C. McConnell, T. M. Schneider, D. J. Owens and R. V. Bellamkonda, *IEEE TRANSACTIONS ON BIOMEDICAL ENGINEERING*, 2007, **54**, 1097-1107.
40. E. M. Schmidt, M. J. Bak and J. S. McIntosh, *Exp Neurol*, 1976, **52**, 496-506.
41. J. C. Williams, J. A. Hippensteel, J. Dilgen, W. Shain and D. R. Kipke, *J. Neural Eng.*, 2007, **4**, 410-423.
42. G. W. Kreutzberg, *Trends Neurosci.*, 1996, **19**, 312-318.
43. D. S. Arroyo, J. A. Soria, E. A. Gaviglio, M. C. Rodriguez-Galan and P. Iribarren, *Int. Immunopharmacol.*, 2011, **11**, 1415-1421.
44. D. Ito, Y. Imai, K. Ohsawa, K. Nakajima, Y. Fukuuchi and S. Kohsaka, *Molecular Brain Research*, 1998, **57**, 1-9.
45. C. Dijkstra, E. Dopp, P. Joling and G. Kraal, *Immunology*, 1985, **54**, 589-599.
46. H. Yang, H. Wang, C. J. Czura and K. J. Tracey, *Journal of Leukocyte Biology*, 2005, **78**, 1-8.
47. Q. Zhang, S. O'Hearn, S. L. Kavalukas and A. Barbul, *J. Surg. Res.*, 2012, **176**, 343-347.
48. J. C. Barrese, N. Rao, K. Paroo, C. Triebwasser, C. Vargas-Irwin, L. Franquemont and J. P. Donoghue, *J Neural Eng*, 2013, **10**, 066014.

49. A. Prasad, Q.-S. Xue, V. Sankar, T. Nishida, G. Shaw, W. J. Streit and J. C. Sanchez, *J. Neural Eng.*, 2012, **9**, 056015.
50. M. P. Ward, P. Rajdev, C. Ellison and P. P. Irazoqui, *Brain Res*, 2009, **1282**, 183-200.
51. K. A. Potter, A. C. Buck, W. K. Self and J. R. Capadona, *J Neural Eng*, 2012, **9**.
52. R. Biran, D. Martin and P. Tresco, *Exp. Neurol.*, 2005, **195**, 115-126.
53. R. Biran, D. C. Martin and P. A. Tresco, *Journal of Biomedical Materials Research Part A*, 2007, **82A**, 169-178.
54. J. D. Simeral, S. P. Kim, M. J. Black, J. P. Donoghue and L. R. Hochberg, *J Neural Eng*, 2011, **8**, 025027.
55. R. J. Vetter, J. C. Williams, J. F. Hetke, E. A. Nunamaker and D. R. Kipke, *IEEE TRANSACTIONS ON BIOMEDICAL ENGINEERING*, 2004, **51**, 896-904.
56. D. R. Kipke, R. J. Vetter, J. C. Williams and J. F. Hetke, *IEEE Trans Neural Syst Rehabil Eng*, 2003, **11**, 151-155.
57. S. Suner, M. R. Fellows, C. Vargas-Irwin, G. K. Nakata and J. P. Donoghue, *IEEE Trans. on Rehabilitation Engineering*, 2005, **13**, 524-541.
58. A. B. Schwartz, X. T. Cui, D. J. Weber and D. W. Moran, *Neuron*, 2006, **52**, 205-220.
59. L. Karumbaiah, T. Saxena, D. Carlson, K. Patil, R. Patkar, E. A. Gaupp, M. Betancur, G. B. Stanley, L. Carin and R. V. Bellamkonda, *Biomaterials*, 2013.
60. J. P. Harris, A. E. Hess, S. J. Rowan, C. Weder, C. A. Zorman, D. J. Tyler and J. R. Capadona, *J. Neural Eng.*, 2011, **8**, 040610.
61. A. E. Way, L. Hsu, K. Shanmuganathan, C. Weder and S. J. Rowan, *ACS Macro Letters*, 2012, **1**, 1001-1006.
62. J. Mendez, P. K. Annamalai, S. J. Eichhorn, R. Rusli, S. J. Rowan, E. J. Foster and C. Weder, *Macromolecules*, 2011, **44**, 6827-6835.
63. A. R. Nectow, K. G. Marra and D. L. Kaplan, *Tissue Eng Part B-Re*, 2012, **18**, 40-50.
64. L. Pari, D. Tewas and J. Eckel, *Arch. Physiol. Biochem.*, 2008, **114**, 127-149.
65. V. Menon and A. Sudheer, in *The Molecular Targets and Therapeutic Uses of Curcumin in Health and Disease*, eds. B. Aggarwal, Y.-J. Surh and S. Shishodia, Springer US, 2007, vol. 595, pp. 105-125.
66. C. D. Lao, M. T. t. Ruffin, D. Normolle, D. D. Heath, S. I. Murray, J. M. Bailey, M. E. Boggs, J. Crowell, C. L. Rock and D. E. Brenner, *BMC Complement. Altern. Med.*, 2006, **6**, 10.
67. A. L. Cheng, C. H. Hsu, J. K. Lin, M. M. Hsu, Y. F. Ho, T. S. Shen, J. Y. Ko, J. T. Lin, B. R. Lin, W. Ming-Shiang, H. S. Yu, S. H. Jee, G. S. Chen, T. M. Chen, C. A. Chen, M. K. Lai, Y. S. Pu, M. H. Pan, Y. J. Wang, C. C. Tsai and C. Y. Hsieh, *Anticancer Res.*, 2001, **21**, 2895-2900.
68. C. S. Brazel and N. A. Peppas, *Eur. J. Pharm. Biopharm.*, 2000, **49**, 47-58.
69. L. S. C. Wan and L. Y. Lim, *Drug Dev. Ind. Pharm.*, 1992, **18**, 1895-1906.
70. S. K. Mallapragada and N. A. Peppas, *J. Controlled Release*, 1997, **45**, 87-94.
71. W. H. Chan, C. C. Wu and J. S. Yu, *J. Cell. Biochem.*, 2003, **90**, 327-338.

72. C. T. Tu, Q. Y. Yao, B. L. Xu, J. Y. Wang, C. H. Zhou and S. C. Zhang, *Food and chemical toxicology : an international journal published for the British Industrial Biological Research Association*, 2012, **50**, 3343-3351.
73. S. M. Gutowski, K. L. Templeman, A. B. South, J. C. Gaulding, J. T. Shoemaker, M. C. LaPlaca, R. V. Bellamkonda, L. A. Lyon and A. J. García, *Journal of Biomedical Materials Research Part A*, 2013, DOI: 10.1002/jbm.a.34799.
74. J. Skousen, K. Bolick, M. Bridge and P. Tresco, *IFESS*, 2012.
75. M. Ravikumar, D. J. Hageman, W. H. Tomaszewski, G. M. Chandra, J. L. Skousen and J. R. Capadona, *Biomaterials*, 2013, Under Review.
76. M. V. Sofroniew, *Trends Neurosci.*, 2009, **32**, 638-647.
77. C.-t. Tu, Q.-y. Yao, B.-l. Xu, J.-y. Wang, C.-h. Zhou and S.-c. Zhang, *Food Chem. Toxicol.*, 2012, **50**, 3343-3351.
78. J. P. O'Callaghan, K. Sriram and D. B. Miller, *Ann. N. Y. Acad. Sci.*, 2008, **1139**, 318-330.
79. T. C. Frank-Cannon, L. T. Alto, F. E. McAlpine and M. G. Tansey, *Mol. Neurodegener.*, 2009, **4**, 47.
80. R. L. Rennaker, J. Miller, H. Tang and D. A. Wilson, *J. Neural Eng.*, 2007, **4**, L1-L5.
81. O. Ates, S. Cayli, E. Altinoz, I. Gurses, N. Yucel, M. Sener, A. Kocak and S. Yologlu, *Mol. Cell. Biochem.*, 2007, **294**, 137-144.
82. C. J. Liu, Z. B. Shi, L. H. Fan, C. Zhang, K. Z. Wang and B. Wang, *Brain Res.*, 2011, **1374**, 100-109.
83. T. Ware, D. Simon, K. Hearon, T. H. Kang, D. J. Maitland and W. Voit, *Macromolecular Bioscience*, 2013, n/a-n/a.
84. L. W. Tien, F. Wu, M. D. Tang-Schomer, E. Yoon, F. G. Omenetto and D. L. Kaplan, *Adv. Funct. Mater.*, 2013, **23**, 3185-3193.
85. T. K. Biswas and B. Mukherjee, *Int. J. Low. Extrem. Wounds*, 2003, **2**, 25-39.

4.8. APPENDIX

Atomic Force Microscopy (AFM). Atomic force microscopy of CNCs was carried out on a NanoWizard II (JPK Instruments) microscope. 5 μL of the CNCs re-dispersed in DMSO (0.1 mg/ml, 30 min sonication) was placed on freshly cleaved mica (SPI Supplies Division of Structure Probe, Inc.) and allowed to dry. The scans were performed in tapping mode in air using silicon cantilevers (NANO WORLD, TESPA-50) with a scan rate of 1 line/sec.

Transmission Electron Microscopy (TEM). The dimensions of the CNCs and the homogeneity of the CNC dispersion were examined by transmission electron microscopy (TEM) using a Hitachi H-1700 microscope operating at an accelerating voltage of 75 kV. To assess the CNCs dimensions, lyophilized CNCs were dispersed in deionized water at a concentration of 0.1 mg/mL by sonication. Subsequently, 3 μL of the aqueous CNC dispersions were deposited on carbon-coated grids (Electron Microscopy Sciences) and allowed to dry at 70 $^{\circ}\text{C}$ for 2 h. CNC dimensions were determined by analyzing 10 TEM images of CNCs with a total of more than 100 individual CNCs of which length and width were measured. The dimensions thus determined are reported as average values \pm standard error.

Differential scanning calorimetry Analysis. Differential scanning calorimetry (DSC, METTLER TOLEDO STAR) experiments were carried out under an N_2 atmosphere. Heating and cooling cycles were conducted on a 10 mg film sample (-50 to 250 $^{\circ}\text{C}$ using a heating rate of 10 $^{\circ}\text{C}/\text{min}$). The glass transition temperature (T_g) was defined as the temperature from the midpoint of the specific heat increment at the glass-rubber transition, while the melting temperature (T_m) was taken as the peak temperature of the melting endotherm.

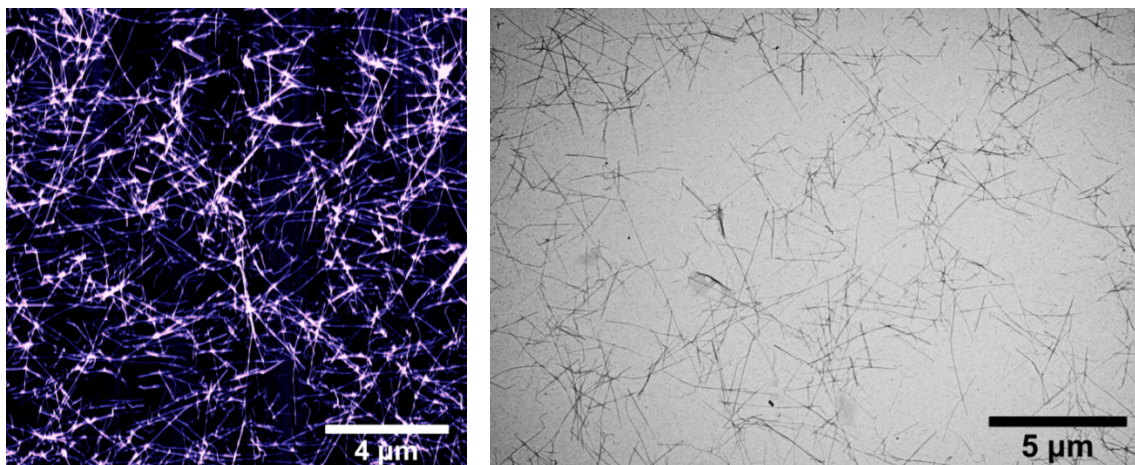


Figure A4-1. (Left) AFM height image of CNCs derived from tunicates and deposited from DMSO re-dispersion (1 mg/mL) onto freshly cleaved mica surface. (Right) Representative transmission electron microscopy (TEM) image of lyophilized CNCs, deposited from aqueous dispersions (0.1 mg/mL).

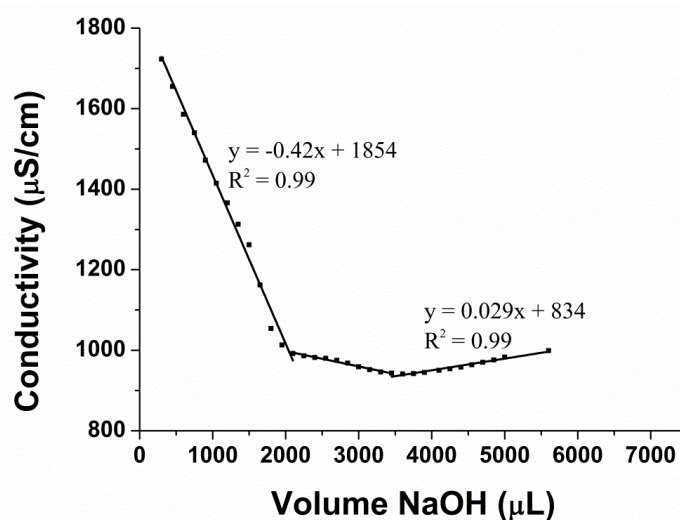


Figure A4-2. Conductometric titration curve of lyophilized CNCs. Conductometric titrations were performed to quantify the density of surface charges of CNCs due to sulfate ester groups introduced during hydrolysis. 50 mg of the CNCs were suspended into 15 mL of aqueous 0.01 M hydrochloric acid (HCl). After 5 min of stirring and 30 min of sonication, the suspensions were titrated with 0.01 M NaOH. The representative titration curve shows the presence of a strong acid, corresponding to the excess of HCl, and a weak acid corresponding to the sulfate ester surface groups (88 ± 3.0 mmol/kg).

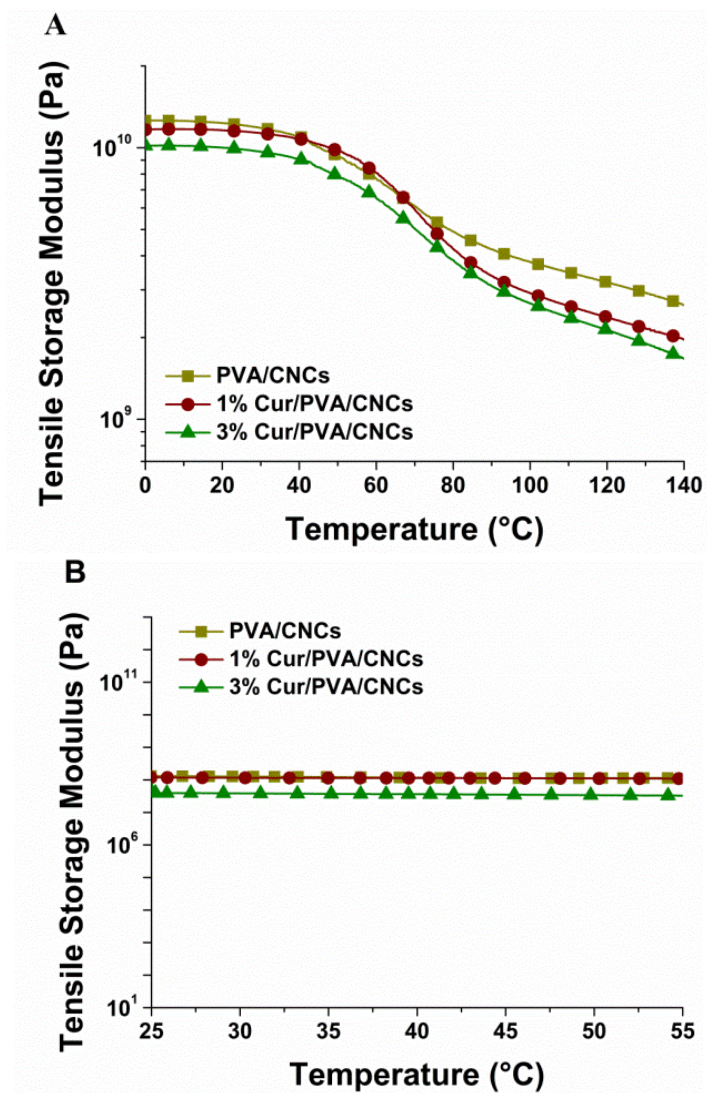


Figure A4-3. Representative dynamic mechanical analysis (DMA) traces showing the tensile storage moduli of (A) dry and (B) wet curcumin-loaded PVA/CNCs polymers as a function of temperature. Average data of multiple experiments are compiled in Table A4-2.

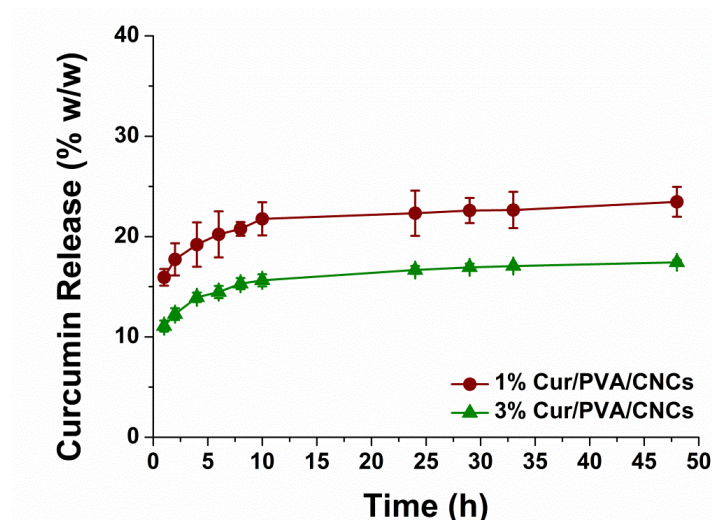
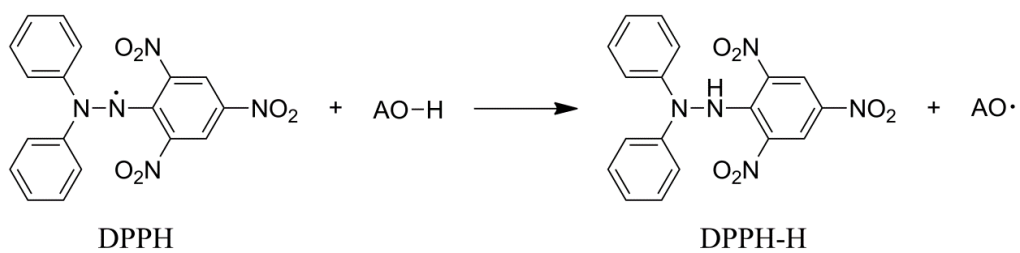


Figure A4-4. Cumulative *in vitro* release profile of curcumin-loaded materials in ACSF at 37 °C. Values represent mean \pm S.D. ($n = 4$), and relative to the original nominal amount of curcumin in the materials.



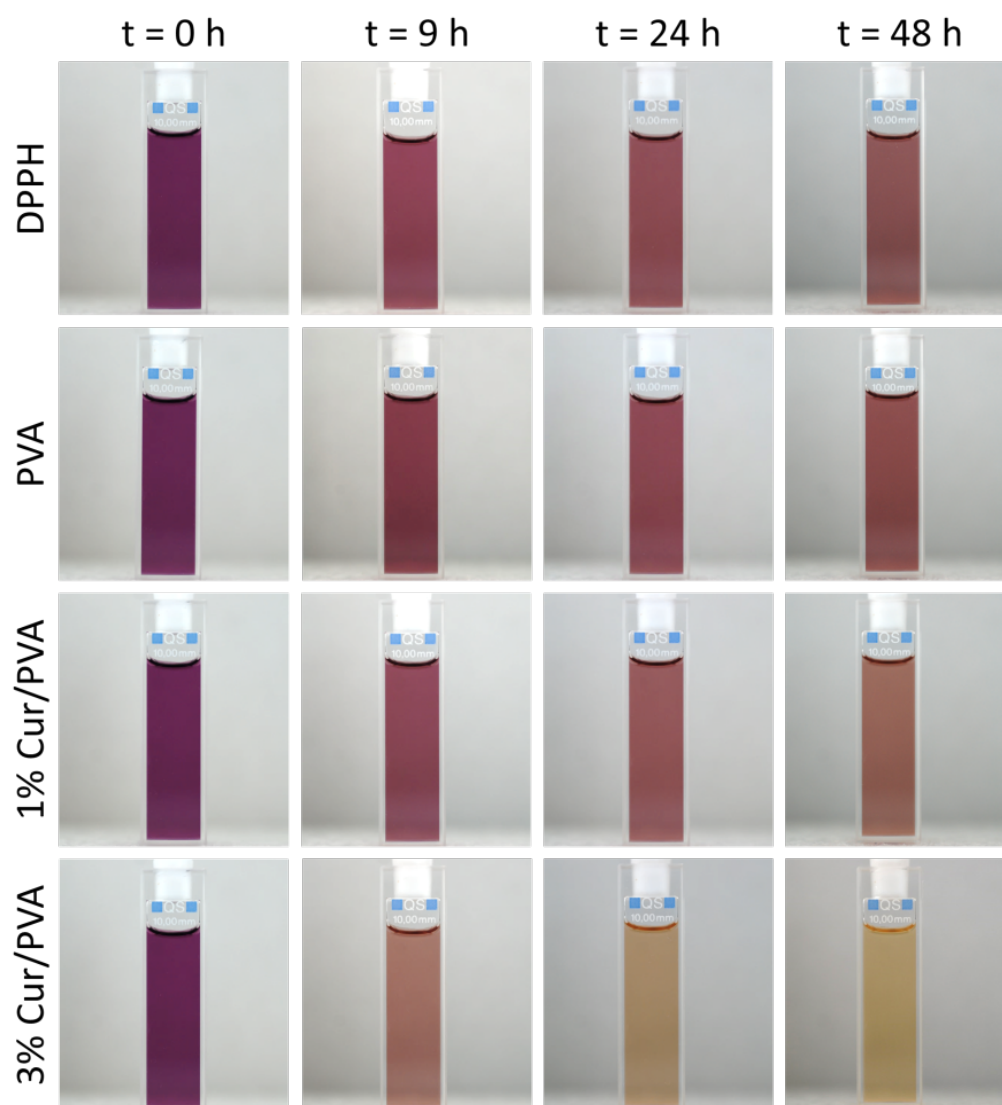


Figure A4-5. (Top) Chemical structure of DPPH and its reaction with an anti-oxidant (AO-H). (Bottom) Representative photographs of solutions of DPPH in methanol (100 μ M, 3 mL) at 0, 9, 24 and 48 hours and after placing a film of the neat PVA control, or the curcumin-loaded PVA films into the DPPH solution. All samples were kept at 37 $^{\circ}$ C in the dark.

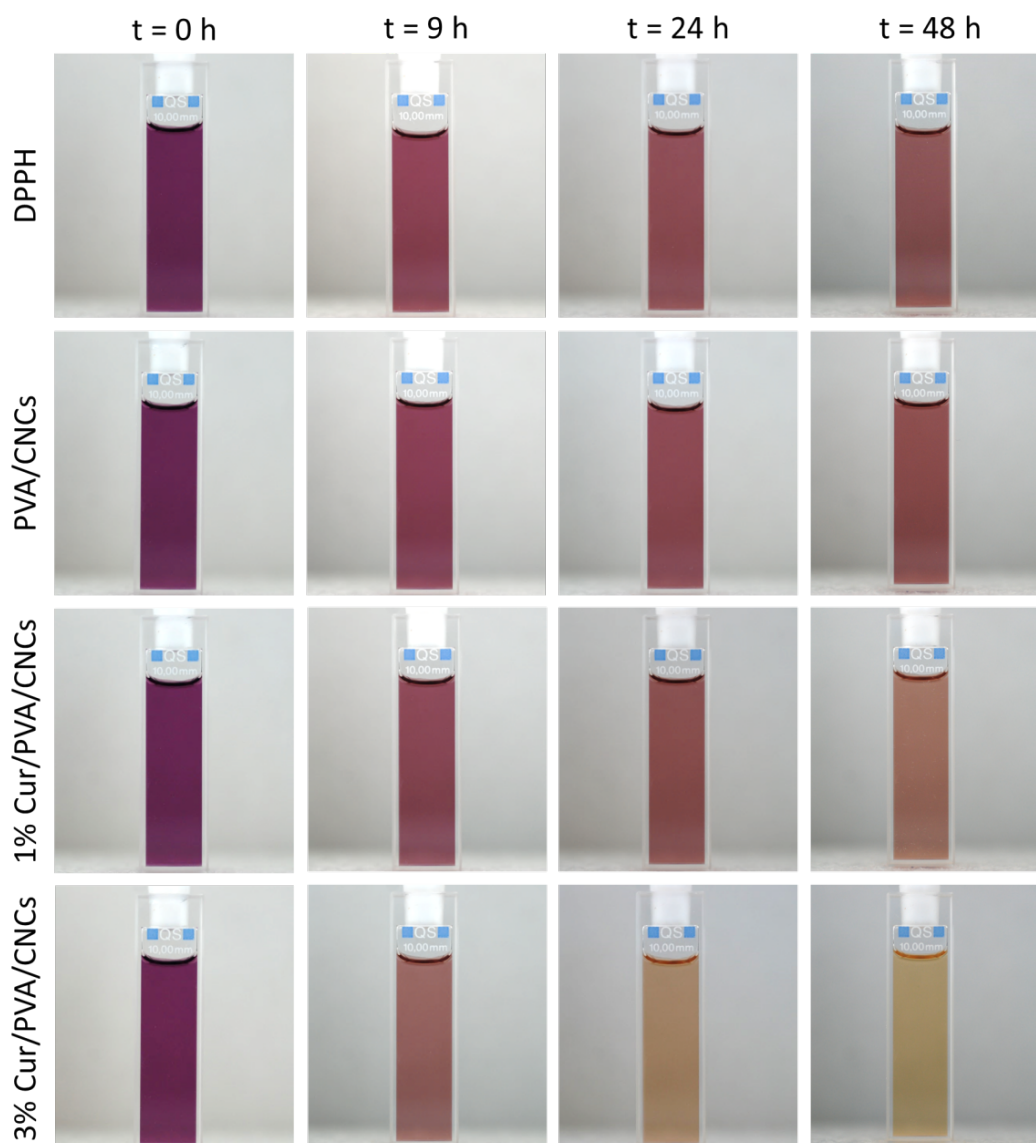


Figure A4-6. Representative photographs of solutions of DPPH in methanol (100 μ M, 3 mL) at 0, 9, 24 and 48 hours and after placing a film of the neat PVA/CNC control, or the curcumin-loaded PVA/CNC films into the DPPH solution. All samples were kept at 37 $^{\circ}$ C in the dark.

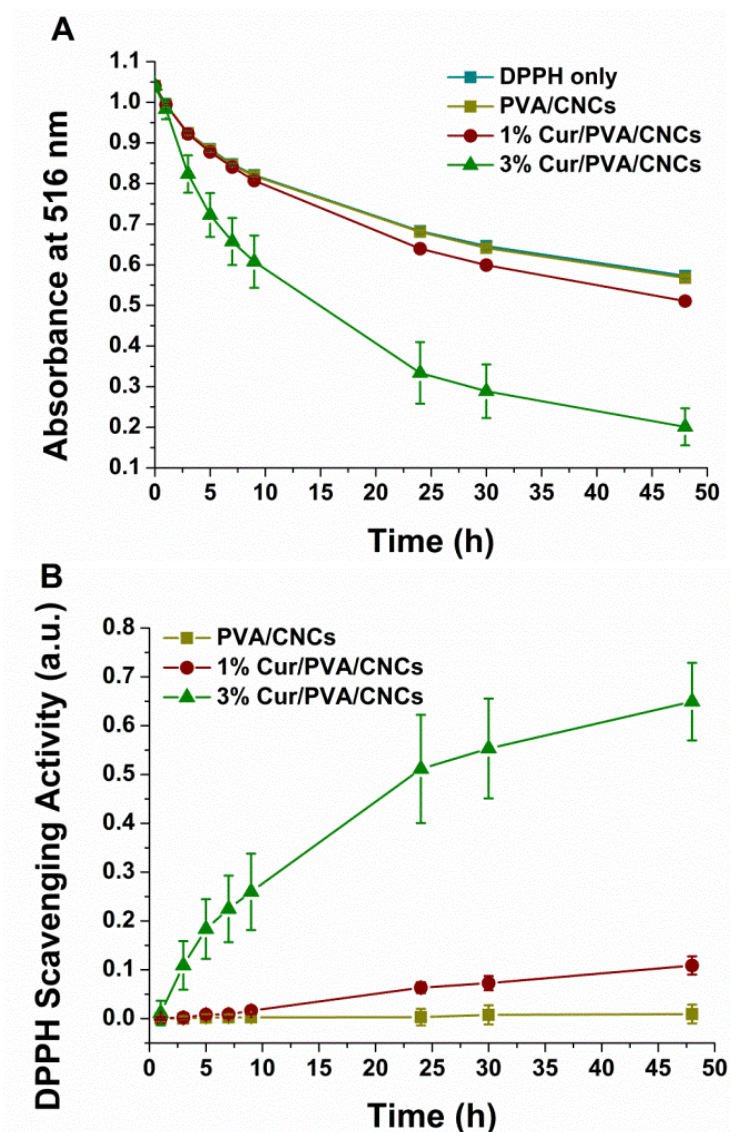


Figure A4-7. (A) Plot showing the absorbance at 516 nm of a methanolic solution of DPPH (100 μ M) as a function of time, and of the same solution in the presence of films consisting of the neat PVA/CNC nanocomposite, or the PVA/CNC nanocomposites with 1 or 3% w/w curcumin, respectively, incubated at 37 $^{\circ}$ C in the dark for up to 48 hours. (B) DPPH scavenging activity calculated from the results shown in (A) according to equation 3. The results shown are means \pm standard deviation of three independent experiments.

Table A4-1. Thermal properties of materials studied.

Films	T_g ($^{\circ}C$)	T_m ($^{\circ}C$)	ΔH_m (J/g)	χ_c (%) ^a
Neat PVA	68	218	46.5	28
PVA/CNCs	80	215	44.6	31
1% Cur/PVA	78	219	55.9	35
3% Cur/PVA	78	220	50.2	32
1% Cur/PVA/CNCs	82	216	47.2	33
3% Cur/PVA/CNCs	88	219	44.9	32

^a The data obtained from the second heating scan of DSC measurements. $^a\chi_c = (\Delta H_m)/(w\Delta H_0)$, where w is the weight fraction of polymer matrix in the nanocomposites, ΔH_m is the measured melting enthalpy and ΔH_0 is the enthalpy of 100% crystalline PVA (161 J/g).

Table A4-2. Tensile storage moduli (E') of dry and ACSF-swollen films determined by dynamic mechanical analyzer.^a

Sample	Drug Content (% w/w)	E' of dry materials		E' at 37 $^{\circ}C$ of ACSF-swollen materials after 1 week in ACSF (MPa)
		at 25 $^{\circ}C$ (GPa)	at 100 $^{\circ}C$ (GPa)	
Neat PVA		8.8 ± 0.7	1.0 ± 0.07	7.0 ± 5.0
Cur/PVA	1	9.9 ± 0.9	1.2 ± 0.11	5.0 ± 4.0
	3	9.3 ± 0.9	1.1 ± 0.19	13 ± 4.0
PVA/CNCs		11.7 ± 0.5	3.3 ± 0.44	180 ± 80
Cur/PVA/CNCs	1	11.6 ± 0.5	3.0 ± 0.14	130 ± 70
	3	10.3 ± 0.6	2.4 ± 0.27	50 ± 15

^a Data represent averages ($N = 3-5$) \pm s.d.

Chapter 5 – Physiologically Responsive Mechanically Adaptive Antioxidant-Releasing Nanocomposites for Cortical Implants with Improved Neural Integration

5.1. ABSTRACT

Building on previous findings that antioxidant treatment can prevent neurodegeneration and blood-brain barrier (BBB) breach around intracortical implants, and the hypothesis that the mechanical mismatch plays a dominant role in reactive gliosis at the implant/tissue interface, *in-situ* softening antioxidant-releasing polymeric materials were developed, which can serve to explore if the combination of two independently effective mechanisms – softening and antioxidant release – leads to synergistic effect in reducing the neuroinflammation at the intracortical microelectrode-tissue interface. A first series of curcumin-releasing mechanically adaptive implants based on poly(vinyl alcohol) (PVA) and optionally cellulose nanocrystals (CNCs) were reported in Chapter 4. An *in-vivo* study in rats showed that after 4 weeks, the new curcumin-releasing, mechanically adaptive implants promoted a higher neuron survival and a more stable BBB than the neat PVA controls, but the benefits of the curcumin release were lost after 12 weeks, where the antioxidant-releasing compliant materials caused no statistically significant differences in neuronal density distribution profiles viz the PVA reference. To explore to what extent the PVA matrix used in the study was responsible for this outcome, antioxidant-releasing, mechanically adaptive materials based on poly(vinyl acetate) (PVAc), CNCs, and the antioxidants curcumin or resveratrol were made and studied. Exposing the nanocomposites to (emulated) physiological conditions caused a drastic softening; the tensile storage modulus E' was reduced from ca. ~6000 MPa (dry, 25 °C) to ~10 MPa. The ability of these physiologically responsive, mechanically adaptive nanocomposites to release the anti-oxidants was also studied.

5.2. INTRODUCTION

Several types of medical devices are used within the central nervous system (CNS) with various levels of clinical success. In the case of intracortical microelectrodes, a decline in performance can be directly linked to the foreign body response to the implanted device.¹ ² Previously, it was shown that the inflammatory response to intracortical microelectrodes has a biphasic response.³ Potter *et al.* reported that a single systemic administration of the antioxidant resveratrol can reduce the neuroinflammatory response at acute time points.⁴ Additionally, our group has developed several generations of mechanically adaptive materials for use as substrates for intracortical microelectrodes.⁵⁻¹⁰ Such softening materials are useful in intracortical microelectrodes that initially require a stiff material for easy insertion, but benefit from subsequent softening upon exposure to physiological conditions so that the implant becomes mechanically more compatible with the surrounding soft brain tissue. Most of our reported materials are nanocomposites that are comprised of a polymeric matrix and reinforcing nanofillers, whose interactions are stimuli-responsive and regulate the mechanical properties of the bulk material. We have demonstrated that mechanically adaptive polymer implants are able to reduce the chronic neuroinflammatory response by reducing the mechanical mismatch between traditionally stiff microelectrode materials and neural tissue.¹¹ Taken together, to date, it was shown that both antioxidative treatment and the use of mechanically compliant microelectrodes are strategies to temporally mitigate the neuroinflammatory response to intracortical microelectrodes.^{4, 11}

In order to explore if the combination of two independently effective mechanisms – softening and antioxidant release – leads to synergistic effect in reducing the neuroinflammation at the intracortical microelectrode-tissue interface, we recently developed a first series of curcumin-releasing mechanically adaptive implants based on poly(vinyl alcohol) (PVA) and optionally cellulose nanocrystals (CNCs) (Chapter 4).¹⁰ An *in-vivo* study in rats showed that after 4 weeks, the new curcumin-releasing, mechanically adaptive implants promoted a higher neuron survival and a more stable BBB than the neat PVA controls, but the benefits of the curcumin release were lost after

12 weeks, where the antioxidant-releasing compliant materials caused no statistically significant differences in neuronal density distribution profiles viz the PVA reference. Thus, to date no approach has been able to provide continual neuroprotection, throughout the multiphasic tissue response that exists to implanted microelectrodes.^{3, 12} To explore to what extent the PVA matrix used in our study was responsible for this outcome, antioxidant-releasing, mechanically adaptive materials based on poly(vinyl acetate) (PVAc), CNCs, and the antioxidants curcumin or resveratrol were made and studied. The first *in vivo* evaluation of the neuro-inflammatory response to mechanically adaptable PVAc/CNC nanocomposites as substrate for penetrating microelectrodes was reported by Harris *et al.*¹¹ Initial histological evaluations of these materials demonstrated that at four weeks post-implantation, compliant implants more rapidly stabilize neural cell populations within 200 μm of the implant than rigid, non-dynamic systems.¹¹ In addition to a wide range of therapeutic activities of curcumin, resveratrol is a natural polyphenol that found in red wine and grapes, which has several health benefits including anti-oxidant, anti-cancer, cardioprotective and anti-inflammatory effects.¹³ Recently, resveratrol has been shown to protect against various neurological disorders including brain ischemia, seizures, and neurodegenerative disease models,¹³ and to be capable of providing neuroprotection through its reactive oxygen species-scavenging properties towards activated microglia.¹⁴

5.3. EXPERIMENTAL SECTION

Materials. Pharmaceutical grade, 99% pure trans-resveratrol powder was purchased from Mega Resveratrol (Danbury, CT) and 99% pure curcumin was obtained from ChromaDex[®] (Figure 5-1). Poly(vinyl acetate) (PVAc, $M_w = 100,000$), 2,2-diphenyl-1-picrylhydrazyl (DPPH), Triton-X 100, and all other reagents were purchased from Sigma Aldrich and were used without further purification. Cellulose nanocrystals (CNCs) in this study were isolated from tunicate (*Styela clava*) collected from floating docks in Point View Marina (Narragansett, RI), and prepared by sulfuric acid hydrolysis of the cellulose pulp, according to established protocols, as previously reported.^{9, 15} To simulate the ionic

composition of endogenous brain fluid, artificial cerebrospinal fluid (ACSF) was prepared following an established protocol¹⁶ by dissolving the following materials in one liter of deionized water: sodium chloride (NaCl) = 7.25 g, potassium chloride (KCl) = 0.22 g, sodium bicarbonate (NaHCO₃) = 2.18 g, calcium chloride dihydrate (CaCl₂·2H₂O) = 0.29 g, monopotassium phosphate (KH₂PO₄) = 0.17 g, magnesium sulfate heptahydrate (MgSO₄·7H₂O) = 0.25 g, and *D*-glucose = 1.80 g.

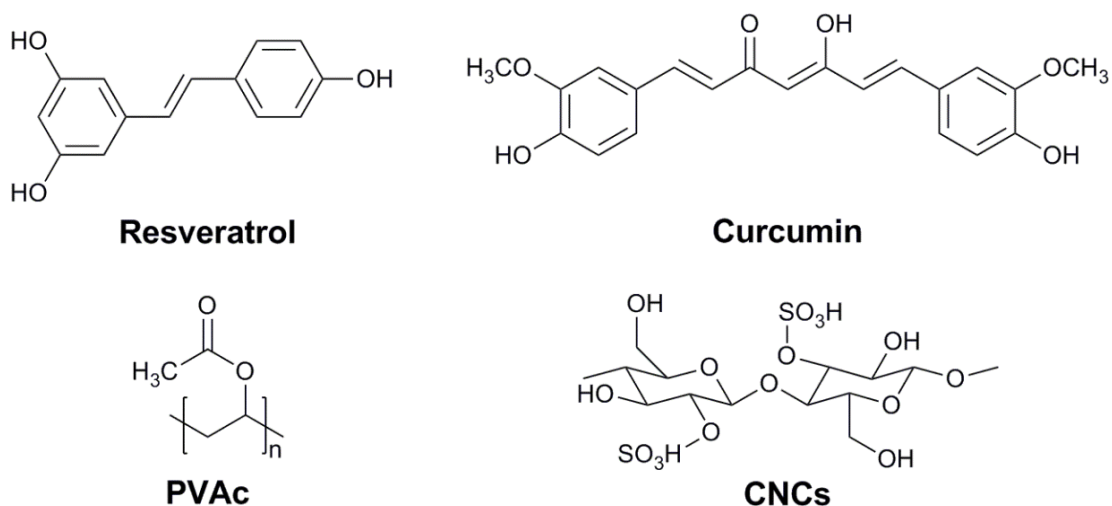


Figure 5-1. Chemical structures of materials used in this study.

Preparation of Antioxidant-Releasing Nanocomposites. A poly(vinyl acetate) (PVAc) stock solution was prepared by dissolving PVAc in dimethylformamide (DMF) at a concentration of 50 mg/mL by stirring for 3 hours at room temperature (RT). Similarly, stock solutions containing curcumin or resveratrol were made by separately dissolving the antioxidants in DMF (10 mg/mL) by stirring for 1 hour at RT. Lyophilized CNCs were dispersed in DMF at a concentration of 5 mg/mL by sonicating for 10 hours at room temperature using BANDELIN SONOREX TECHNIK RL 70 UH sonicator operating at 40 kHz. Films containing either 0, 0.005, 0.01, 1.0 or 3.0% w/w of the antioxidant (*i.e.* curcumin or resveratrol) and 15% w/w CNCs were made by combining appropriate amounts of the above stock solutions, and CNC dispersion, and stirring the mixture for 30

minutes at RT. The mixtures were then cast into a Teflon[®] Petri dish, dried at 70 °C for 5 days and further dried at 120 °C under high vacuum in an oven for an additional 24 hours to evaporate all of the solvent. After drying, nanocomposite films were compression-molded between spacers in a Carver[®] laboratory press (1000 psi for 2 minutes, followed by an increase of pressure to 3000 psi for 10 minutes) at 90 °C, to yield ~100 μm thin films. The drug-releasing films thus produced were stored in a desiccator at ambient temperature.

Microscopy Studies. Atomic force microscopy (AFM) and transmission electron microscopy (TEM) were used to characterize the morphology and physical dimensions of the isolated CNCs. Atomic force microscopy of CNCs was carried out on a NanoWizard II (JPK Instruments) microscope. 5 μL of the CNCs re-dispersed in DMF (0.01 mg/mL, 30 min sonication) was placed on freshly cleaved mica (SPI Supplies Division of Structure Probe, Inc.) and allowed to dry. The scans were performed in tapping mode in air using silicon cantilevers (NANO WORLD, TESPA-50) with a scan rate of 1 line/second.

A Hitachi H-1700 microscope operating at an accelerating voltage of 75 kV was used to examine the dimensions of the CNCs and the homogeneity of the CNC dispersion by TEM micrographs. To assess the CNCs dimensions, samples were prepared by dropping 3 μL of the aqueous CNC dispersions (0.01 mg/mL) on carbon-coated grids (Electron Microscopy Sciences) and allowed to dry in an oven at 70 °C for 2 h.

Swelling Behavior. The swelling behavior of the PVAc/CNC control nanocomposite and the antioxidant-loaded nanocomposite films was investigated by cutting the films into ~30 mm × ~6 mm × ~100 μm rectangular strips and immersing the samples in artificial cerebrospinal fluid (ACSF) at the physiological temperature of 37 °C for one week. After one week incubation in ACSF, the degree of swelling was calculated by comparing the weight of the films pre- and post-swelling:

$$\text{Degree of swelling (\%)} = \frac{(W_s - W_d)}{W_d} \times 100 \quad (5 - 1)$$

where W_d is the weight of the dry film prior to swelling and W_s is the weight of the swollen film. After the swollen films were removed from the ACSF, the samples were briefly placed on a small piece of tissue paper to wick any excess ACSF from the surface, and the samples were immediately weighed. This experiment was repeated four times, and the results are expressed as mean \pm standard deviation.

Thermogravimetric Analysis. Thermogravimetric (TGA) analysis of the PVAc/CNC reference materials and the antioxidant releasing PVAc/CNC nanocomposites were performed with a thermogravimetric analyzer (Mettler Toledo STAR). Each sample (~10 mg) was heated in an aluminum pan from 30 to 600 °C at a flow rate of 10 °C/min under nitrogen.

Mechanical Characterization. The mechanical properties of the antioxidant-releasing nanocomposite films were characterized by dynamic mechanical analysis (DMA, TA Instruments, Model Q800). Tests were conducted in tensile mode, sweeping the temperature between 23-80 °C at a fixed frequency of 1 Hz, and using a strain amplitude of 15 μm , a heating rate of 5 °C/min. Samples for mechanical testing were prepared by cutting strips (~30 mm \times ~6 mm \times ~100 μm) from the films. To determine the mechanical properties of the films in the wet state, samples were first swelled in ACSF at 37 °C for one week. After the degree of swelling had been measured, DMA experiments were conducted in submersion clamp using tensile mode, which allowed mechanical measurements while the nanocomposite films were immersed in ACSF. In submersion measurements, the temperature sweeps in the range of 25-50 °C with a heating rate of 1 °C/min, a constant frequency of 1 Hz, and strain amplitude of 15 μm . These experiments were repeated five times, and the result was expressed as mean \pm standard deviation.

***In vitro* Drug Release.** To determine the release rates of resveratrol or curcumin from the antioxidant-loaded nanocomposite films, samples (~30 mm \times ~6 mm \times ~100 μm) were

incubated at 37 °C in a mixture of 20 mL of 99.5% v/v ACSF and 0.5% v/v Tween-80, which was added to increase the solubility of the drug in the ACSF. In set time intervals ($t=1, 2, 4, 6, 8, 10, 24, 29, 34, 48, 55,$ and 72 hours), 1 mL aliquots of the solutions were withdrawn, diluted with 1.5 mL of the neat solvent (99.5% v/v ACSF and 0.5% v/v Tween-80), and the amount of antioxidant released was detected spectrophotometrically (UV-vis 2401-PC spectrophotometer, Shimadzu). The concentration of antioxidant released was calculated using a calibration curve established by measuring the absorbance at 425 nm and 308 nm of solutions series of curcumin and resveratrol (5-30 $\mu\text{g/mL}$) in ACSF/Tween 80, respectively. The amount of antioxidant released (relative to the amount of antioxidant originally present in the nanocomposites) was calculated using Equation 5-2, where $[\text{Antioxidant}]_{\text{UV}}$ is the concentration of the antioxidant measured by UV (mg/mL), V_{Sample} the volume of the sample in mL, W_{Film} the weight of the film in mg, and $[\text{Antioxidant}]_{\text{Film}}$ is the nominal concentration of the antioxidant in the film (mg/mg). This experiment was repeated four times, and the result was expressed as mean \pm standard deviation.

$$\text{Antioxidant Release (\%)} = \frac{[\text{Antioxidant}]_{\text{UV}} \times V_{\text{Sample}}}{W_{\text{Film}} \times [\text{Antioxidant}]_{\text{Film}}} \times 100 \quad (5 - 2)$$

Measurement of Anti-Oxidative Activity of Antioxidant-Releasing Nanocomposites.

The anti-oxidative activity of antioxidant-releasing nanocomposite films was assessed using 2,2-diphenyl-1-picrylhydrazyl (DPPH) following a previously reported method¹⁷ with slight modifications. Here, the absorbance of DPPH, a stable free radical, at 516 nm was monitored to quantify the antioxidant activity of curcumin and resveratrol, which are known to reduce DPPH, and thereby decrease its absorbance at 516 nm. Briefly, the films were cut into rectangular pieces ($\sim 15 \text{ mm} \times \sim 6 \text{ mm} \times \sim 100 \mu\text{m}$) and placed into a 20 mL methanolic solution of DPPH (100 μM). Samples were incubated at 37 °C in the dark. The absorbance of the solution was measured spectrophotometrically at 516 nm in regular time intervals ($t = 0, 1, 3, 5, 21, 25, 29,$ and 48 hours). The radical scavenging activity of curcumin-loaded films was expressed using Equation 5-3:

$$\text{DPPH Scavenging Activity} = \left(\frac{A - B}{A} \right) \quad (5 - 3)$$

where A and B are the absorbance values at time t , of the neat DPPH solution (A) and the DPPH solution in the presence of the antioxidant loaded film (B), respectively. All samples were tested three times to ensure repeatability of measurements.

5.4. RESULTS AND DISCUSSION

5.4.1. Processing and Characterization of Materials

The cellulose nanocrystals (CNCs) used in the present study were isolated from tunicates by sulfuric acid hydrolysis based on established protocols with a few modifications as previously reported.⁹ Atomic force microscopy (AFM) and transmission electron microscopy (TEM) were used to characterize the morphology and physical dimensions of the isolated CNCs (Figures 5-2 and A5-1). The dimensions of the CNCs, determined from TEM micrographs, were an average length and width of 2650 ± 1100 nm and 30 ± 4 , respectively (average aspect ratio ~ 88). The CNC dispersions, PVAc and stock solutions of the antioxidants resveratrol (Res) and curcumin (Cur) were combined, and after solution-casting, the resulting films were compression-molded to obtain nanocomposite films with 15% w/w CNCs and four different concentrations of antioxidant drug (0.005, 0.01, 1.0, and 3.0% w/w). Based on previous studies, PVAc nanocomposites with 16.5% v/v CNCs exhibited an adequate mechanical switching upon exposure to physiological conditions and upon implantation into cortical tissue ($E' = 5.1$ GPa for a dry/pre-insertion and 12 MPa for ACSF-swollen nanocomposite).^{6, 7, 18} It was shown that dry implants of this nanocomposite can readily be inserted through the *pia mater* into the cerebral cortex of a rat without the need for assistive devices. Also, a range of antioxidant concentrations was used to test cytotoxicity at various resveratrol and curcumin concentrations to choose the optimal drug concentration for *in vivo* implantation. Figure 5-3 shows representative photographs of solution-cast antioxidant releasing nanocomposite films containing either 0.005% or 0.01% w/w of the

antioxidants. The morphology of the antioxidant-free reference nanocomposites was investigated by AFM imaging of ultrathin films ($\sim 30 \mu\text{m}$). Figure A5-2 shows the corresponding AFM images, in which individual CNCs can be clearly distinguished show a good homogeneous dispersion of CNCs in the PVAc matrix.

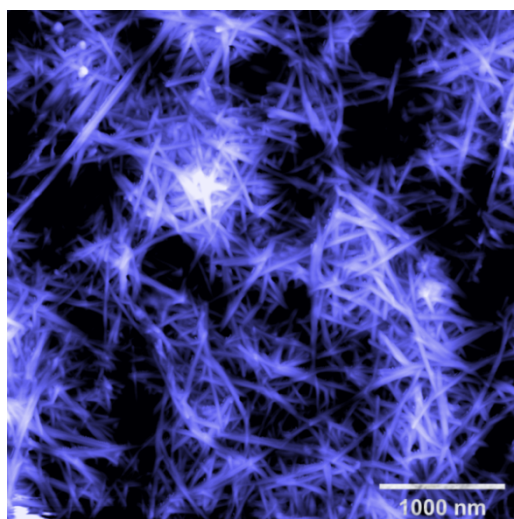


Figure 5-2. Atomic force microscopy (AFM) image of lyophilized CNCs isolated from tunicates. The CNCs were deposited from aqueous dispersions (0.01 mg/mL) onto freshly cleaved mica surfaces.

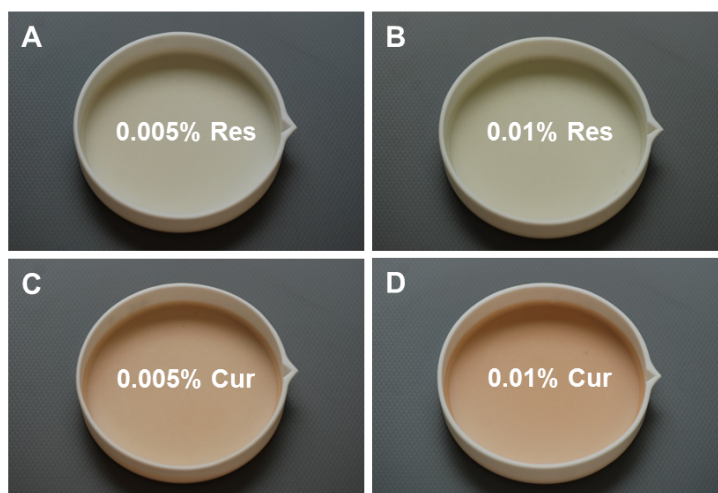


Figure 5-3. Photographs of solution-cast PVAc/CNC nanocomposite films (15% w/w CNCs) with either 0.005% or 0.01% w/w resveratrol (Res, A and B) or curcumin (Cur, C and D).

The swelling behavior of the antioxidant-loaded (either with curcumin or resveratrol) and the PVAc/CNC control nanocomposites in (emulated) physiological conditions was investigated by immersing the materials into ACSF at 37 °C (Figure 5-4). As expected on the basis of previous studies on neat PVAc/CNC nanocomposites,^{7, 19} the water uptake was found to be ~75 - 85% w/w for all materials, and no dependence of the drug content or drug type is apparent. Additionally, the thermogravimetric properties of antioxidant-loaded materials were determined using thermogravimetric analysis (TGA, Figure 5-5). The TGA curves show that the onset degradation for all nanocomposites was at approximately ~300 °C, confirmed that no solvent residues were present in the nanocomposite films after solution-casting and solvent evaporation. From the TGA analysis, it is clear that the processing technique for preparation of the antioxidant-loaded nanocomposite films presented in this study was reliable.

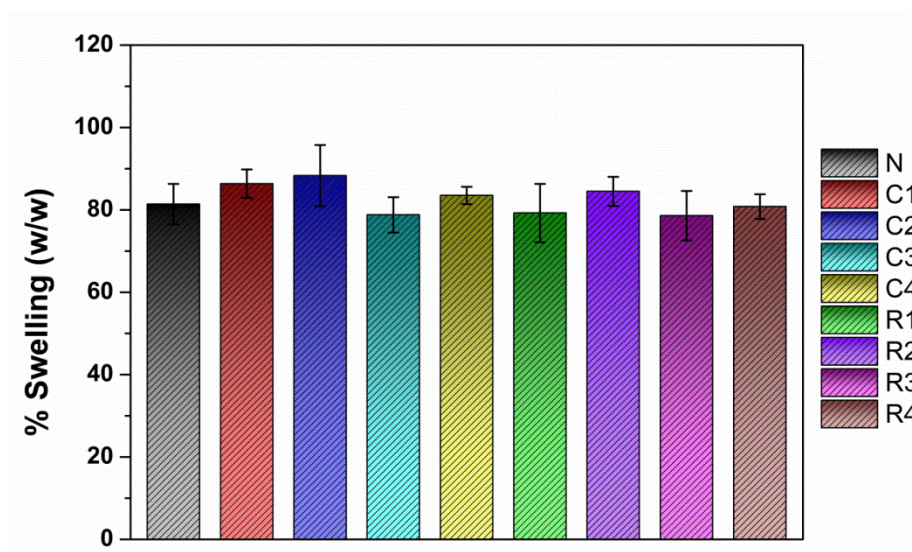


Figure 5-4. Swelling behavior of PVAc/CNC nanocomposites (15% w/w CNCs) with different amounts of antioxidants after the films were immersed in ACSF at 37 °C for 1 week. (N) neat PVAc/CNC nanocomposite; (C1) 0.005% w/w curcumin (Cur); (C2) 0.01% w/w Cur; (C3) 1.0% w/w Cur; (C4) 3.0% w/w Cur; (R1) 0.005% w/w resveratrol (Res); (R2) 0.01% w/w Res; (R3) 1.0% w/w Res; and (R4) 3.0% w/w Res-loaded nanocomposites. Data represent averages of N = 3 measurements \pm standard deviations.

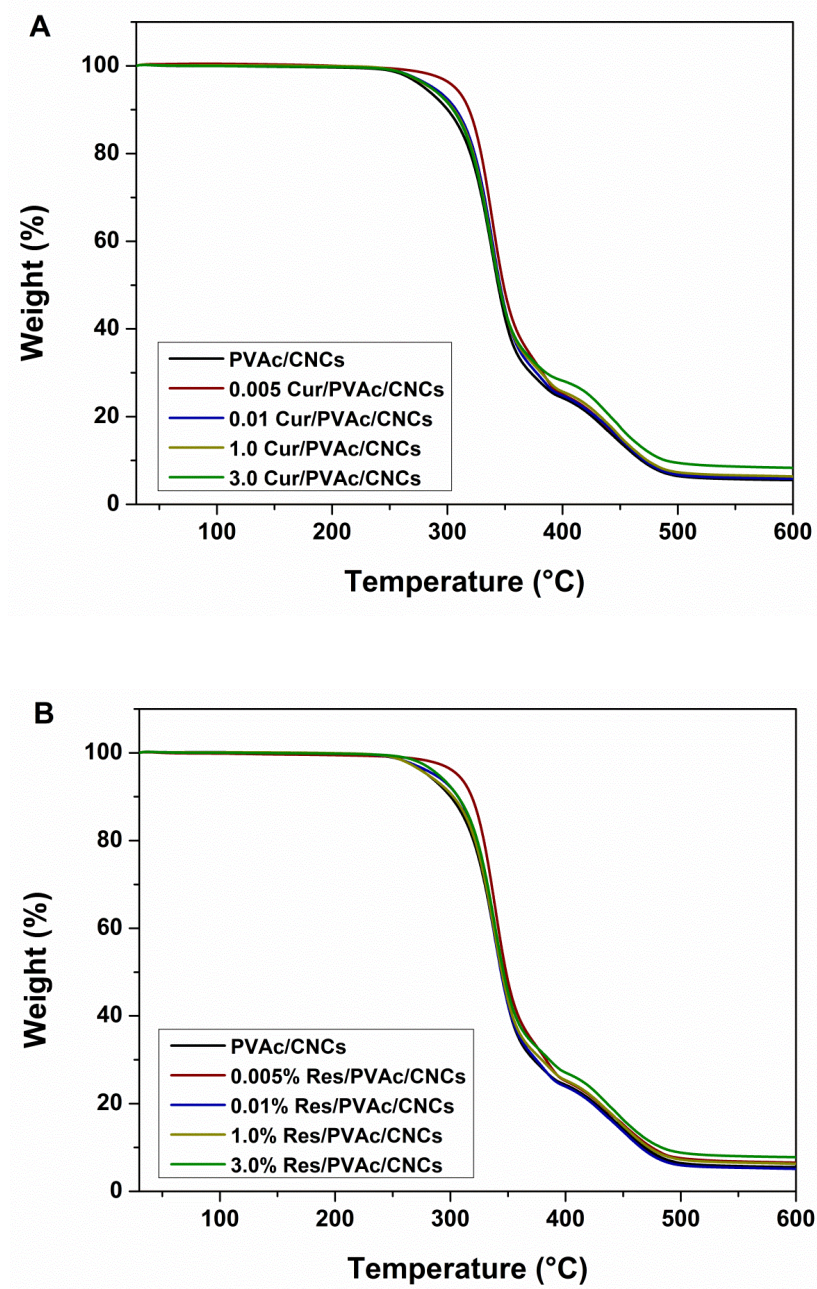


Figure 5-5. Thermogravimetric analysis traces of (A) curcumin (Cur) and (B) resveratrol (Res) loaded PVAc/CNC nanocomposites (15% w/w CNCs) as a function of temperature.

5.4.2. Mechanically Adaptive Properties of Antioxidant-Loaded Materials

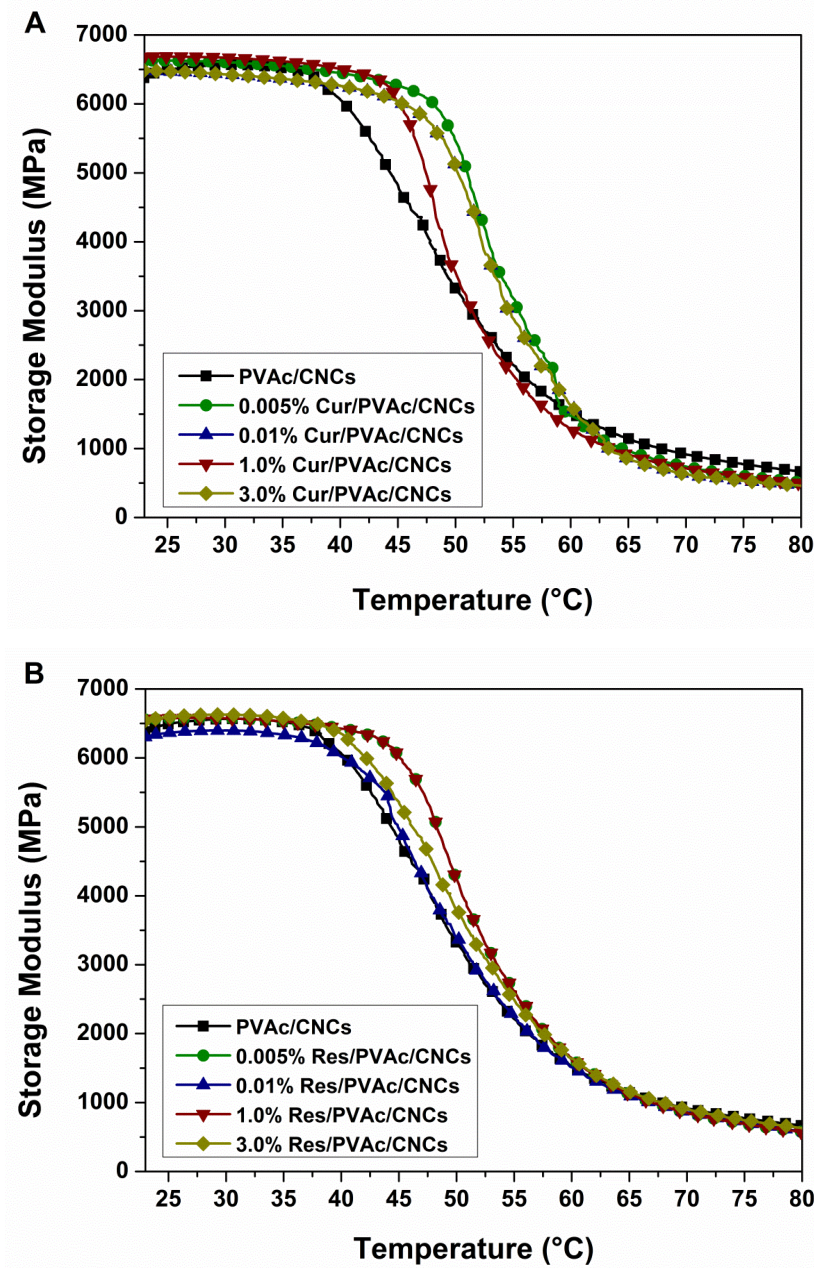
The mechanical properties of both curcumin-loaded and resveratrol-loaded PVAc/CNC nanocomposite films were investigated using dynamic mechanical analysis (DMA). Figure 5-6 shows the tensile storage moduli (E') of the antioxidant-loaded PVAc/CNC nanocomposites as well as the neat PVAc/CNC control nanocomposite film in the dry and ACSF-swollen state as a function of temperature. The curves reveal a nearly temperature-independent tensile storage modulus E' of ~6000-6400 MPa below the glass transition temperature ($T_g \sim 45$ °C). E' is reduced as the temperature is increased towards the T_g , and reaches a rubbery plateau above ~65 °C (Figure 5-6, Table 5-1).

Table 5-1. Storage moduli (E') of dry and ACSF-swollen PVAc/CNC nanocomposites determined by DMA. Data represent averages (N = 5) and are shown for the neat PVAc/CNC reference nanocomposite as well as for curcumin (Cur) and resveratrol (Res) releasing nanocomposites loaded with different contents of these antioxidants.

Nanocomposite	Antioxidant Content (% w/w)	Dry Nanocomposites		Swollen Nanocomposites
		E' at 25 °C (MPa)	E' at 70 °C (MPa)	E' at 37 °C after 1 week in ACSF (MPa)
Neat PVAc/CNC		6300 ± 190	720 ± 180	13 ± 1.8
Cur/PVAc/ CNC	0.005	6300 ± 270	930 ± 98	9.0 ± 2.5
	0.01	6000 ± 300	810 ± 75	7.2 ± 3.2
	1.0	6100 ± 27	680 ± 45	10 ± 1.0
	3.0	6346 ± 100	740 ± 99	14 ± 1.4
Res/PVAc/CNC	0.005	6100 ± 350	970 ± 72	7.0 ± 3.6
	0.01	6050 ± 140	900 ± 85	6.0 ± 1.5
	1.0	6100 ± 197	851 ± 67	13 ± 2.0
	3.0	6340 ± 135	840 ± 205	14 ± 2.5

All of the materials studied undergo a pronounced modulus reduction from ~6000 MPa to ~10 MPa upon exposure to (emulated) physiological conditions, due to matrix plasticization and/or decoupling of CNCs on account of competitive hydrogen bonding with water. For example, the 3% w/w Cur/PVAc/CNC nanocomposite films display a reduction of E' from 6346 MPa (dry, RT) to 14 MPa (ACSF-swollen, 37 °C), and the 3% w/w Res/PVA/CNC nanocomposite films exhibit a similar reduction of E' from 6340 MPa (dry, RT) to 14 MPa (ACSF-swollen, 37 °C) (Figure 5-6, and Table 5-1). Table 5-1

shows that in the compositional range studied, neither the amount nor the nature of the antioxidant had a significant influence on the mechanical properties. Thus, mechanical analysis confirm that all materials studied here are rigid when dry, but soften considerably upon swelling in (emulated) physiological conditions, as targeted for the intended penetrating intracortical microelectrode applications.



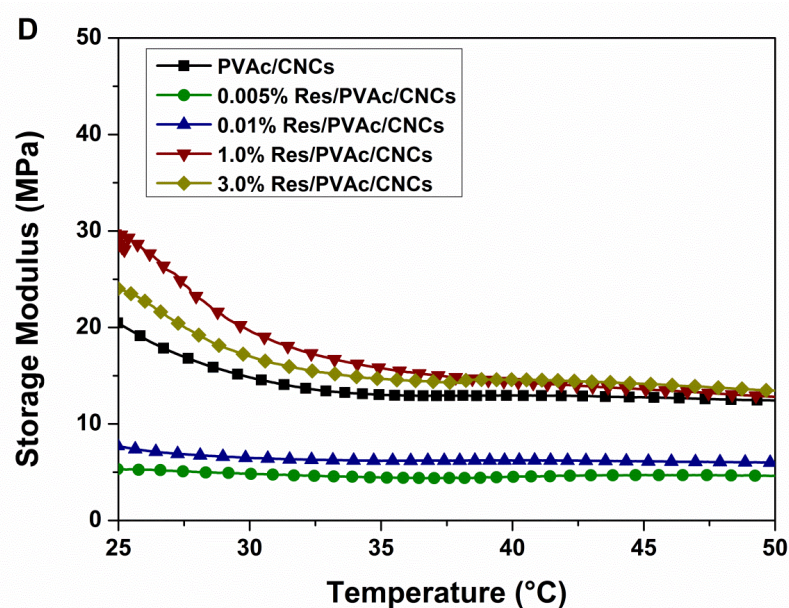
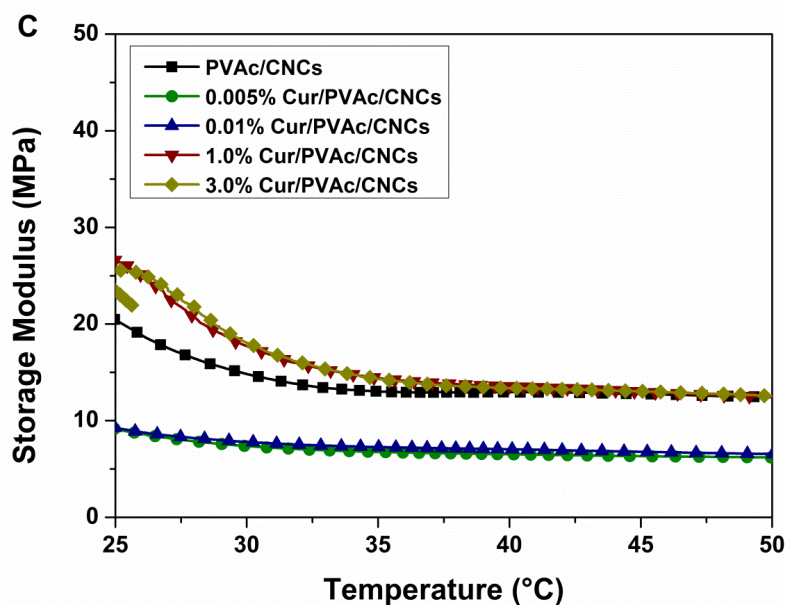


Figure 5-6. Representative dynamic mechanical analysis (DMA) traces showing the storage moduli E' of (A) dry Cur/PVAc/CNC, (B) dry Res/PVAc/CNC, (C) ACSF-swollen Cur/PVAc/CNC, and (D) ACSF-swollen Res/PVAc/CNC nanocomposites as a function of temperature and drug content (0.005, 0.01, 1.0 or 3.0% w/w). The neat PVAc/CNC nanocomposite was also studied for reference purposes and all PVAc/CNC nanocomposites contain 15% w/w CNCs. Average data of multiple experiments are compiled in Table 5-1.

5.4.3. Drug Release Studies

In vitro antioxidant release studies were performed to establish the timeframe in which the antioxidants are released from the nanocomposites under (emulated) physiological conditions. The release studies were carried out by submersing antioxidant-loaded nanocomposite films in ACSF at 37 °C and monitoring the UV absorbance of curcumin and resveratrol in the supernatant solution as a function of time. The cumulative release percentage, relative to the total amount of antioxidants nominally included in the composition, is shown in Table 5-2. After the drug release experiments were carried out, the drug-loaded films were found to be colorless, indicating that almost all of the antioxidants loaded in PVAc/CNC nanocomposite films were released (100% release) into the medium within a timeframe of ~70 hours. While, only about ~45% w/w of the curcumin and ~60% w/w of the resveratrol comprised in the nanocomposites was detected by UV-vis after 72 hours (See Table 5-2).

Table 5-2. Cumulative release (%) data of curcumin (Cur)-loaded PVAc/CNC nanocomposites and resveratrol (Res)-loaded PVAc/CNC nanocomposites in ACSF at 37 °C determined by UV-vis. All PVAc/CNC nanocomposites contain 15% w/w CNCs and 1 or 3% Cur or Res, as indicated in the Table. Values represent means \pm standard deviations of N = 4 experiments, and relative to the original nominal amount of drug loaded in the nanocomposites.

Time (hour)	1% w/w Cur/PVAc/CNCs	3% w/w Cur/PVAc/CNCs	1% w/w Res/PVAc/CNCs	3% w/w Res/PVAc/CNCs
1	5.4 \pm 1.6	3.0 \pm 0.9	10.9 \pm 2.2	6.7 \pm 0.4
2	7.5 \pm 2.0	4.1 \pm 0.9	13.3 \pm 3.3	10.1 \pm 0.7
4	9.6 \pm 2.6	8.4 \pm 0.4	19.8 \pm 0.8	15.1 \pm 2.2
6	16.5 \pm 2.6	12.4 \pm 0.6	24.0 \pm 0.8	20.2 \pm 1.8
8	17.9 \pm 1.5	14.9 \pm 0.8	27.8 \pm 1.6	23.2 \pm 3.4
10	19.9 \pm 2.9	18.0 \pm 0.3	30.7 \pm 4.5	27.3 \pm 4.4
24	31.3 \pm 2.4	32.5 \pm 2.7	45.8 \pm 5.5	44.0 \pm 5.1
29	32.4 \pm 3.0	34.5 \pm 2.8	47.0 \pm 5.2	47.8 \pm 2.4
34	34.7 \pm 3.5	37.5 \pm 1.8	50.1 \pm 3.5	50.0 \pm 4.8
48	43.4 \pm 3.7	42.0 \pm 2.0	59.1 \pm 4.1	55.4 \pm 4.6
55	44.9 \pm 4.2	43.8 \pm 2.4	61.2 \pm 4.2	56.8 \pm 5.2
72	48.7 \pm 4.8	46.1 \pm 1.9	64.3 \pm 4.0	59.4 \pm 4.6

The fact that the percentage of the weight of antioxidants released from the drug-loaded nanocomposite films was lower than 100% w/w could be due to a number of factors, e.g., decomposition of fractional amount of the antioxidants during processing conditions which can cause undesirable hydrolysis reactions in the active antioxidant compounds. Several factors have been reported in the literature regarding to the degradation of either curcumin or resveratrol such as light, solvents or pH conditions.^{20, 21} We found (data not shown) that antioxidants studied here are decomposed upon exposure the antioxidant solutions (dissolved in DMF) to oxygen at room temperature. Based on these results, the data presented in Table 5-2 were normalized as antioxidant released percentage versus time (Figure 5-7). Additionally, as expected, the absolute amount released from the films scaled with the drug content; the 3% curcumin-loaded nanocomposite films released ca. 3.0 times more curcumin than the 1% curcumin-loaded PVAc/CNC films and the 3% resveratrol-loaded nanocomposite films released ca. 3.5 times more resveratrol than the 1% resveratrol-loaded nanocomposite films after 72 hours incubation in ACSF at 37 °C. In comparison to our previous poly(vinyl alcohol) (PVA) drug-releasing generation, the antioxidant release from the PVAc-based nanocomposites studied here is slower and qualitatively higher than PVA-based nanocomposites after 50 hours incubation in physiological conditions. For example, 3% Cur/PVA/CNC nanocomposites released only about ~25% w/w of the curcumin comprised in the film even after 50 hours, while 3% Cur/PVAc/CNC nanocomposites released ~45% w/w of the curcumin relative to the total amount of curcumin nominally incorporated in the film. This is indeed attributed to the semicrystalline nature of the polymer matrix PVA, which hinders the diffusion of the drug molecules.²² Unfortunately, it was not possible to detect the release of the antioxidants photometrically in low dose nanocomposites (0.005 and 0.01% w/w) due to the limited sensitivity of the technique. Assuming the same drug release profile, the drug-loaded nanocomposite films were tested further by DPPH scavenging assay to investigate the materials antioxidant activity *in vitro*.

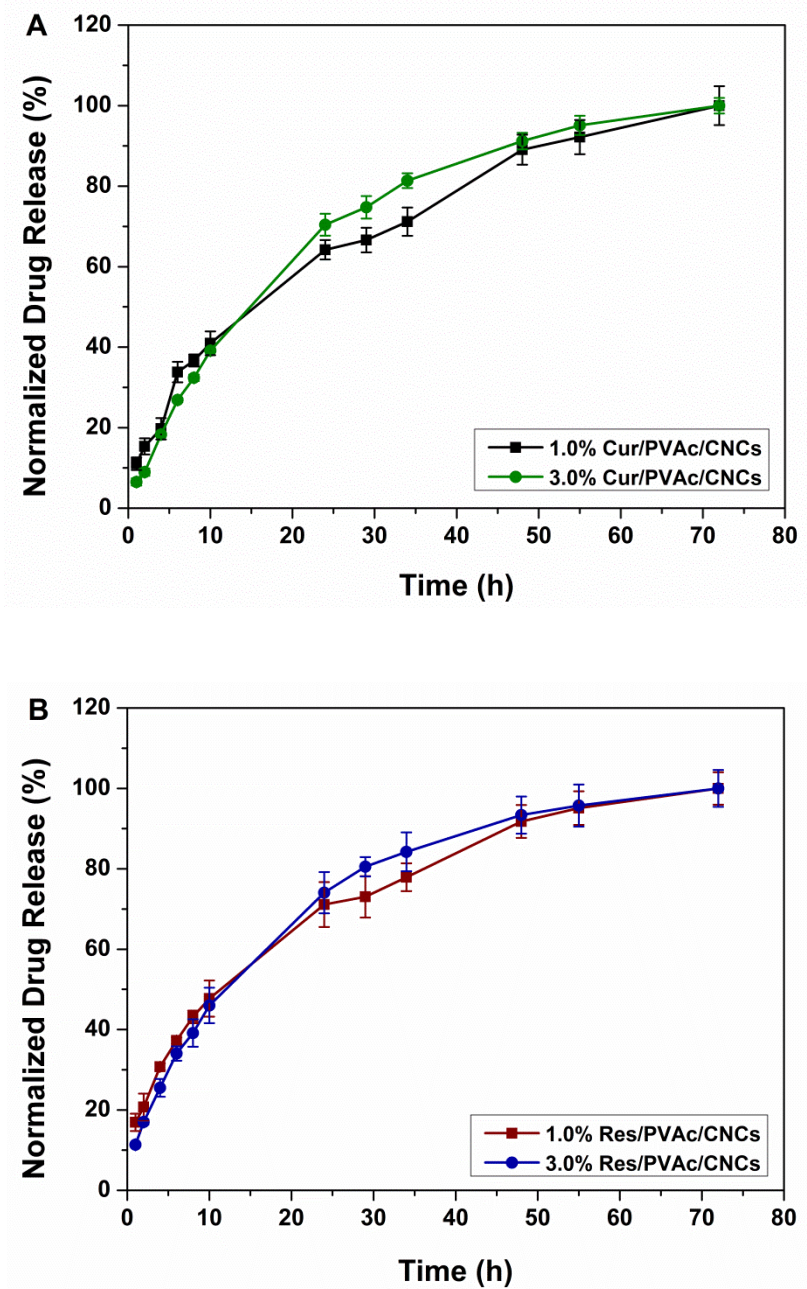


Figure 5-7. Drug release percentage (normalized drug release) of (A) curcumin (Cur)-loaded PVAc/CNC nanocomposites and (B) resveratrol (Res)-loaded PVAc/CNC nanocomposites in ACSF at 37 °C. All PVAc/CNC nanocomposites contain 15% w/w CNCs and 1 or 3% Cur or Res, as indicated in the figure. Values represent means \pm standard deviations of N = 4 experiments.

5.4.4. Antioxidative Activity of Drug-Loaded Nanocomposites

The DPPH scavenging assay was employed to test the antioxidant activity of the nanocomposites studied. DPPH is a stable free radical with an absorption band at 516 nm, which loses this adsorption in the presence of antioxidants.²³ This results in a noticeable discoloration of DPPH from purple to yellow (Figure 5-8). The corresponding reaction can be readily monitored spectrophotometrically (Figure 5-9). It was found that the absorbance of DPPH alone decline over the period of the experiments in the absence of any antioxidant-loaded nanocomposite films, which is due to slow reaction with the hydrogen-donating solvent (i.e. methanol),²⁴ and requires that the spectroscopic scavenging data are referenced to this baseline. The function did not change when films of the PVAc/CNC control nanocomposites were placed into the DPPH solution (Figure 5-9). By contrast, the decrease was accelerated in the case of PVA/CNC loaded with either 1% w/w curcumin or resveratrol, and even more so in the case of nanocomposite films comprising 3% w/w antioxidants (Figures 5-9A and B). The relative antioxidant activity of the curcumin-loaded PVAc/CNC nanocomposites containing 1% curcumin after 21 h incubation in methanol was ~0.7, while that of the resveratrol-loaded PVAc/CNC nanocomposites containing 3% resveratrol was ~0.6 (Figures 5-9C and D). Based on our previous studies,¹⁰ there is indeed no correlation between the drug release kinetic and the antioxidant activity of the drugs, however, there is a clear correlation between the antioxidant activity and the relative amount of the drug incorporated in the nanocomposite films (Figures 5-8 and 5-9).

The results on the DPPH scavenging ability of the antioxidant-loaded materials confirm that the activity of the antioxidants was not affected during material processing. The percentage of DPPH free radical scavenging shows a linear increase with increasing concentration of antioxidants in the nanocomposite films. Of the eight tested antioxidant-loaded materials, the 3% w/w antioxidant-containing PVAc/CNC nanocomposites were the most effective compositions in scavenging all the DPPH radicals within 5 hours of incubation. This is simply due to the antioxidant concentration released into the medium was significantly higher than the free DPPH radicals available in the medium. For

example, 3% Cur/PVAc/CNC scavenged all the free radicals (100%) of the DPPH within 5 hours of incubation at 37 °C, while 0.005% Cur/PVAc/CNC scavenged ~4.3% of the DPPH after 48 hours. By contrast, resveratrol-loaded PVA/CNC nanocomposites with 0.005% and 3% w/w resveratrol showed ~2.4% (after 48 hours) and 100% scavenging activity (after 5 hours), respectively. In addition to this, DPPH assay studies showed that curcumin has greater antioxidant activity than resveratrol, for example 3% Cur/PVAc/CNC scavenged ~78% of the DPPH radicals after 1 hour incubation at 37 °C, while 3% Res/PVAc/CNC scavenged ~73% of the DPPH radical. This is consistent with the literature which already has been reported that curcumin has potent antioxidant activity compared to other well-known antioxidants such as resveratrol and quercetin.²⁵

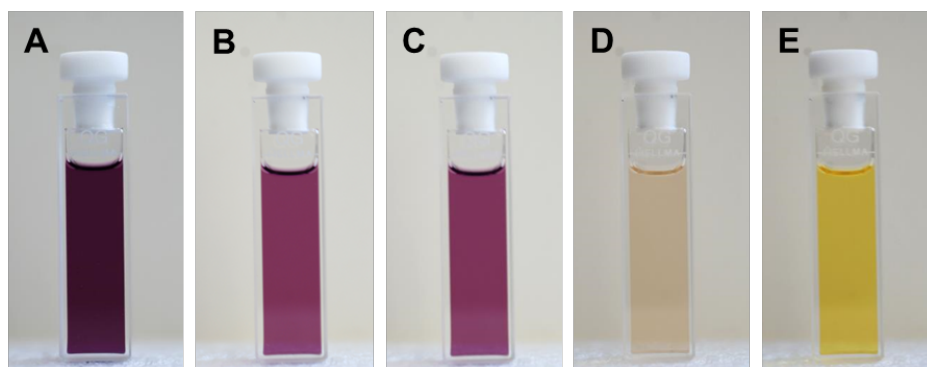
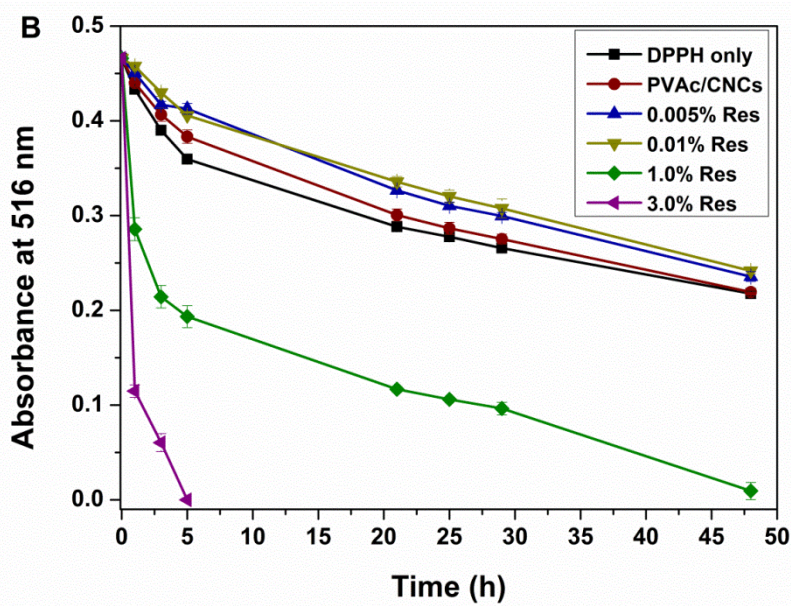
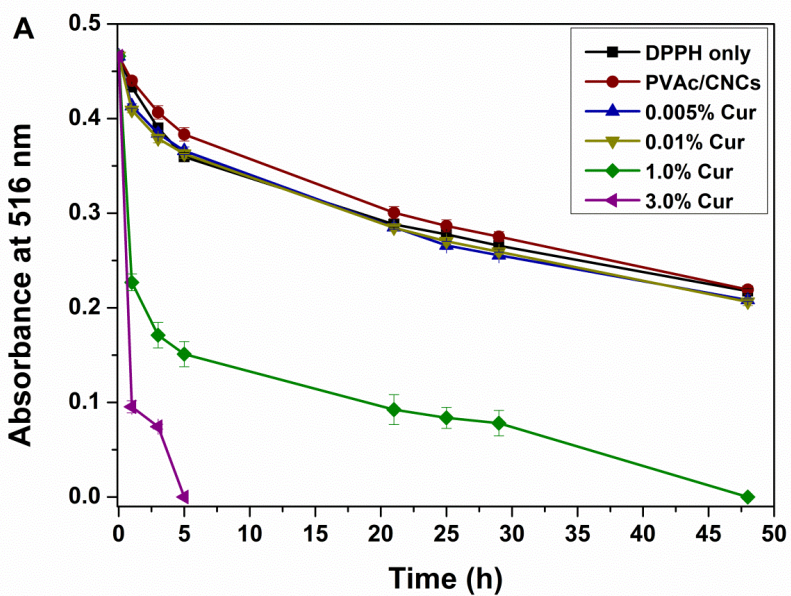


Figure 5-8. Representative photographs of solutions of DPPH in methanol (100 μ M, 3 mL) at time $t = 0$ (A) and 1 h (B) and after placing films of the neat PVAc/CNC control (C), or the PVAc/CNC nanocomposites with 3% w/w Res (D), or 3% w/w Cur (E) into the DPPH solution after 1 h. All samples were kept at 37 °C in the dark. All PVAc/CNC nanocomposites contain 15% w/w CNCs.



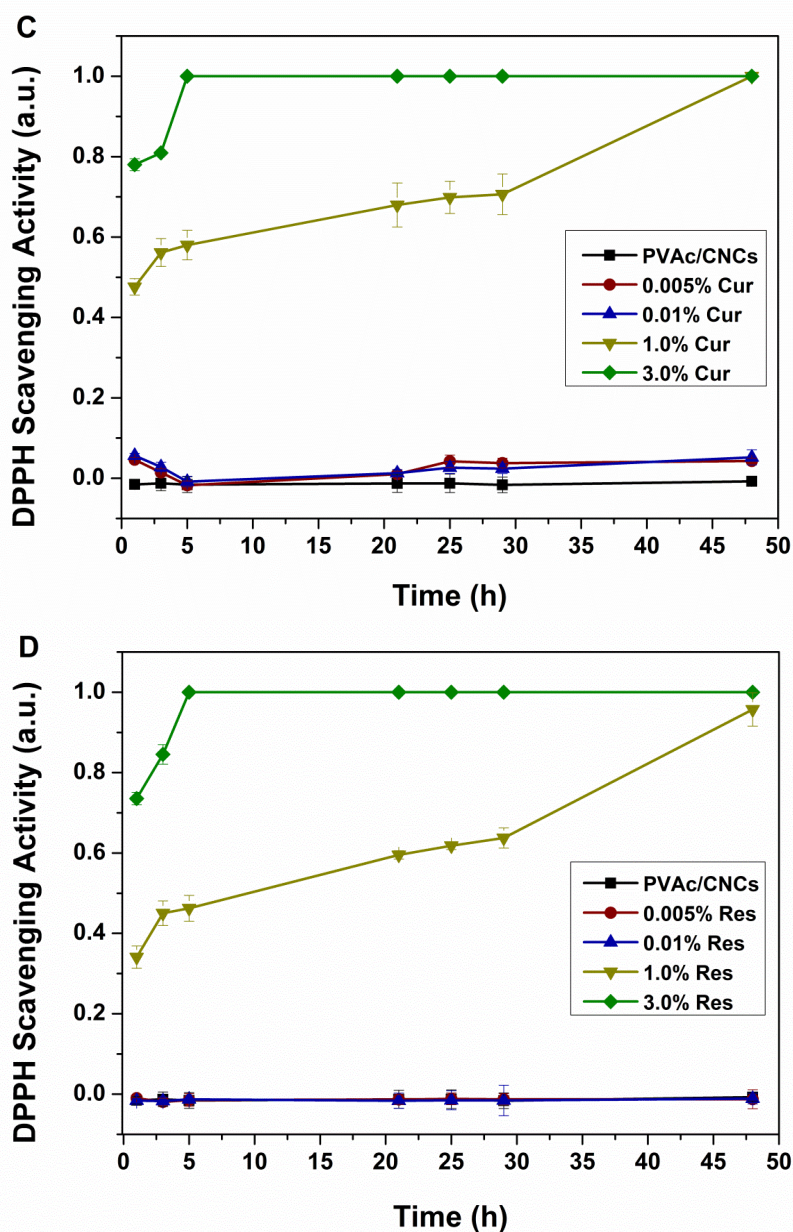


Figure 5-9. (A, B) Plots showing the absorbance at 516 nm of a methanolic solution of DPPH (100 μ M) as function of time, and of the same solution in the presence of nanocomposite films consisting of the neat PVAc/CNC reference nanocomposite, or PVAc/CNC nanocomposites with different content of curcumin (Cur, A) or resveratrol (Res, B), respectively. (C, D) DPPH scavenging activity of curcumin-loaded (C) or resveratrol-loaded nanocomposites (D) calculated from the data shown in (A) and (B) according to equation 3. The results shown are means \pm standard deviations of N = 3 experiments. All PVAc/CNC nanocomposites contain 15% w/w CNCs.

5.5. CONCLUSIONS

There are a variety of factors that contribute to the neuroinflammatory response to intracortical microelectrodes. Therefore, a synergistic approach addressing various aspects of the foreign body response is needed to improve material design and long-term performance for neural implants. Our system utilizes anti-oxidant therapy and material modulus to affect the inflammatory response at acute time points. In summary, biologically-inspired mechanically adaptive nanocomposites based on PVAc and CNCs with the capability to release natural anti-oxidant agents (i.e. curcumin or resveratrol) locally within 72 hours of incubation in emulated physiological conditions. The nanocomposites soften substantially upon immersion in artificial cerebrospinal fluid at body temperature; tensile modulus reduced from ~6000 MPa to ~10 MPa (~600-fold). Additionally, curcumin-releasing mechanically adaptive nanocomposite exhibited greater antioxidant activity *in vitro* than their counterparts. Ongoing *in vivo* histological studies tend to quantify the benefits of synergistic effects of mechanically adaptive materials combined with anti-oxidant releasing properties to mediate acute neuroinflammatory events surrounding intracortical microelectrodes.

5.6. REFERENCES

1. V. S. Polikov, P. A. Tresco and W. M. Reichert, *J. Neurosci. Methods*, 2005, **148**, 1-18.
2. P. A. Tresco and B. D. Winslow, *Crit. Rev. Biomed. Eng.*, 2011, **39**, 29-44.
3. K. A. Potter, A. C. Buck, W. K. Self and J. R. Capadona, *J. Neural Eng.*, 2012, **9**, 046020.
4. K. A. Potter, A. C. Buck, W. K. Self, M. E. Callanan, S. Sunil and J. R. Capadona, *Biomaterials*, 2013, **34**, 7001-7015.
5. A. E. Hess, J. R. Capadona, K. Shanmuganathan, L. Hsu, S. J. Rowan, C. Weder, D. J. Tyler and C. A. Zorman, *J. Micromech. Microeng.*, 2011, **21**, 054009.
6. J. P. Harris, A. E. Hess, S. J. Rowan, C. Weder, C. A. Zorman, D. J. Tyler and J. R. Capadona, *J. Neural Eng.*, 2011, **8**, 040610.
7. M. Jorfi and E. J. Foster, *J. Appl. Polym. Sci.*, 2015, **32**, 41719.
8. J. R. Capadona, D. J. Tyler, C. A. Zorman, S. J. Rowan and C. Weder, *MRS Bull.*, 2012, **37**, 581-589.
9. M. Jorfi, M. N. Roberts, E. J. Foster and C. Weder, *ACS Appl. Mater. Interfaces*, 2013, **5**, 1517-1526.
10. K. A. Potter, M. Jorfi, K. T. Householder, E. Johan Foster, C. Weder and J. R. Capadona, *Acta Biomater.*, 2014, **10**, 2209-2222.
11. J. P. Harris, J. R. Capadona, R. H. Miller, B. C. Healy, K. Shanmuganathan, S. J. Rowan, C. Weder and D. J. Tyler, *J. Neural Eng.*, 2011, **8**, 066011.
12. G. C. McConnell, H. D. Rees, A. I. Levey, C.-A. Gutekunst, R. E. Gross and R. V. Bellamkonda, *J. Neural Eng.*, 2009, **6**, 056003.
13. F. Zhang, J. Liu and J. S. Shi, *Eur. J. Pharmacol.*, 2010, **636**, 1-7.
14. E. Candelario-Jalil, A. C. P. de Oliveira, S. Graf, H. S. Bhatia, M. Hull, E. Munoz and B. L. Fiebich, *J. Neuroinflammation*, 2007, **4**.
15. V. Favier, H. Chanzy and J. Y. Cavaille, *Macromolecules*, 1995, **28**, 6365-6367.
16. www.alzet.com/products/cfs_prep.php, Accessed 08/04/2009.
17. Y. Zou, Y. Lu and D. Wei, *J. Agric. Food Chem.*, 2004, **52**, 5032-5039.
18. J. R. Capadona, K. Shanmuganathan, D. J. Tyler, S. J. Rowan and C. Weder, *Science*, 2008, **319**, 1370-1374.
19. K. Shanmuganathan, J. R. Capadona, S. J. Rowan and C. Weder, *ACS Appl. Mater. Interfaces*, 2010, **2**, 165-174.
20. Y.-J. Wang, M.-H. Pan, A.-L. Cheng, L.-I. Lin, Y.-S. Ho, C.-Y. Hsieh and J.-K. Lin, *J. Pharm. Biomed. Anal.*, 1997, **15**, 1867-1876.
21. J. S. Jensen, C. F. Wertz and V. A. O'Neill, *J. Agric. Food Chem.*, 2010, **58**, 1685-1690.
22. S. K. Mallapragada and N. A. Peppas, *J. Controlled Release*, 1997, **45**, 87-94.
23. P. Goupy, C. Dufour, M. Loonis and O. Dangles, *J. Agric. Food Chem.*, 2003, **51**, 615-622.
24. K. Pyrzynska and A. Pekal, *Anal Methods-Uk*, 2013, **5**, 4288-4295.
25. N. Aftab and A. Vieira, *Phytother. Res.*, 2010, **24**, 500-502.

5.7. APPENDIX

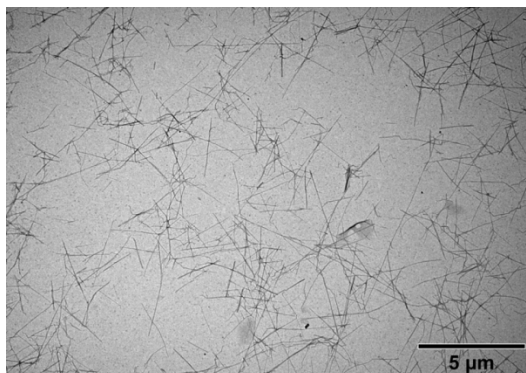


Figure A5-1. Representative transition electron microscopy (TEM) image of CNCs isolated from tunicates. For TEM imaging, lyophilized CNCs were re-dispersed in water at a concentration of 0.01 mg/mL and was deposited on carbon-coated grids.

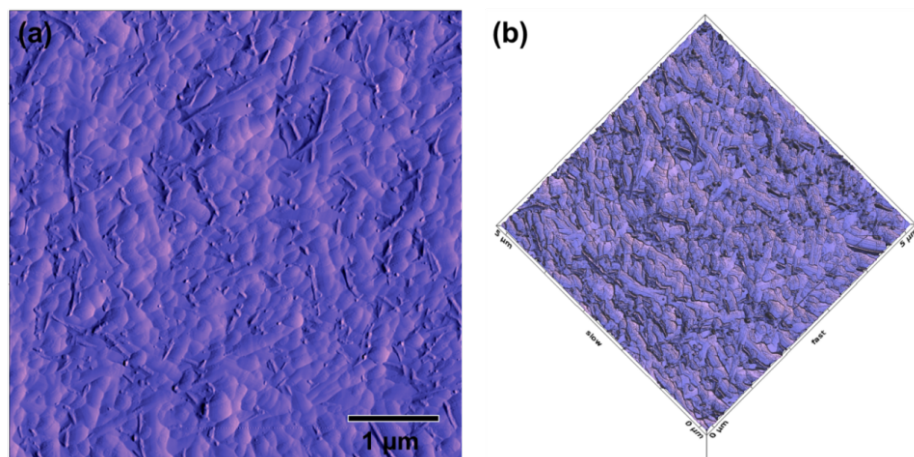


Figure A5-2. Atomic force microscopy (AFM) images of a PVAc/CNC nanocomposite film showing the dispersion of cellulose nanocrystals within the polymer matrix as made surface.

Chapter 6 – Physiologically Responsive Mechanically Adaptive Polymer Optical Fibers for Optogenetics⁴

6.1. ABSTRACT

The capability to deliver light to specific locations within the brain using optogenetic tools has opened up new possibilities in the field of neural interfacing. In this context, optical fibers are commonly inserted into the brain to activate or mute neurons using photosensitive proteins. While chronic optogenetic stimulation studies are just beginning to emerge, knowledge gathered in connection with electrophysiological implants suggests that the mechanical mismatch of conventional optical fibers and the cortical tissue may be a significant contributor to neuroinflammatory response. We here present the design and fabrication of physiologically responsive mechanically adaptive optical fibers made of poly(vinyl alcohol) (PVA) that may mitigate this problem. Produced by a one-step dry-jet wet-spinning process, the fibers display a tensile storage modulus, E' of ~ 7000 MPa in the dry state at 25 °C and can thus readily be inserted into cortical tissue. Exposure to water causes a drastic reduction of E' to ~ 35 MPa, on account of modest swelling with the water. The optical properties at 470 and 590 nm were comparable with losses of 0.7 ± 0.04 dB/cm at 470 nm and 0.6 ± 0.1 dB/cm at 590 nm in the dry and 1.1 ± 0.1 dB/cm at 470 nm and 0.9 ± 0.3 dB/cm at 590 nm in the wet state. The dry end of a partially switched fiber of a length of 10 cm was coupled with a light-emitting diode with an output of 10.1 mW to deliver light with a power density of >500 mW/cm² from the wet end, which is more than sufficient to stimulate neurons *in vivo*. Thus, even without a low-refractive index cladding, the physiologically responsive mechanically adaptive optical fibers presented here appear to be a most useful new tool for future optogenetic studies.

⁴This chapter is adopted from Jorfi, M.; Voirin, G.; Foster, E.J.; Weder, C. *Opt. Lett.* **2014**, 39, 2872-2875.

6.2. INTRODUCTION

Neural interfaces, which (re)connect the brain with the outside world, are enabling tools for studies of the brain function and also essential elements for a broad range of clinical applications.¹ While intracortical microelectrodes, which can electrically record or stimulate the activity of individual or small populations of neurons, have been known for decades,² the discovery that optical signals can be used to interface with neurons is a more recent development. In particular the possibility to activate or mute neurons using photosensitive proteins has opened up new possibilities in the field of neural interfacing.³ Optogenetic technology is thus generating considerable excitement in neuroscience and biomedical engineering, and has quickly become a widely used toolbox to investigate the brain function and behavior in a broad variety of organisms that ranges from zebrafish to rodents to nonhuman primates.⁴⁻⁷

The majority of optogenetics studies conducted *in vivo* use optical fibers, which are often guided through an implanted cannula and/or combined with a tungsten microelectrode.^{8,9} In a recent study, Zorzos *et al.* extended the design concept to three-dimensional micro-waveguides, which are capable of delivering light to targets distributed in a 3D pattern throughout the brain.¹⁰ While such optical interfaces have successfully been used in many short-term animal experiments, long-term *in vivo* studies are only emerging.^{11, 12} The possibility to use optogenetic tools under chronic conditions, ideally in freely moving animals and with minimal neuroinflammatory response, is desirable for both fundamental studies and possible clinical applications, but reliable chronic interfaces have proved difficult to realize.¹³ A growing body of work gathered in connection with electrophysiological implants suggests that the mechanical mismatch of rigid neural implants and the much softer cortical tissue is a contributing factor to the cell-mediated inflammatory responses, neuronal dieback, and eventual encapsulation of cortical implants.^{13, 14} One can speculate that the mechanical mismatch of conventional optical fibers and the cortical tissue may cause similar effects in chronic optogenetic applications. One recent approach to alleviate the problems arising from such mechanical

mismatch between neural microelectrodes and the cortical tissue is the development of physiologically responsive mechanically adaptive materials, which are sufficiently rigid to permit insertion of small-diameter implants, but which soften considerably upon exposure to emulated physiological conditions.¹⁵⁻¹⁸ Such adaptive materials can be made by creating nanocomposites consisting of polymers and rigid nanofillers, in which the interactions between the nanofiller particles, and therewith the overall mechanical properties, can be influenced by exposure to water.¹⁹⁻²² For example, the tensile storage modulus (E') of nanocomposites based on poly(vinyl alcohol) (PVA) and cellulose nanocrystals is reduced from ~14 GPa in the dry state at room temperature to ~10 MPa upon exposure to simulated physiological conditions.²³ Since the introduction of nanocellulose into polymers is normally accompanied by increased light scattering, such nanocomposites are not well suited as basis for adaptive optical fibers and alternative design approaches are needed.

Poly(vinyl alcohol) (PVA) has been used in a wide variety of biomedical applications including contact lenses^{24, 25} and FDA-approved nerve grafts.²⁶ We have recently shown that heat-treated, water-insoluble PVA shows water-induced mechanical switching, on account of plasticization upon minimal swelling.^{23, 27} Here we report the fabrication and characteristics of physiologically responsive, mechanically adaptive optical fibers based on PVA, which were fabricated by dry-jet wet-spinning and subsequent annealing.

6.3. EXPERIMENTAL SECTION

Materials. Poly(vinyl alcohol) (PVA, 99% hydrolyzed, $M_w = 85000-124000$ g/mol) and all the chemical reagents were purchased from Sigma Aldrich and were used without further purifications.

Fabrication of Optical Fibers. A dry-jet wet-spinning process was used to spin a 10 mg/mL solution of PVA in a 4:1 v/v DMSO/water mixture into a coagulation bath of methanol cooled to -20 °C, using a spinneret with a diameter of 0.8 mm and a flow rate of 0.36 mL/min. The as-spun PVA fibers were kept immersed in the coagulation bath for

24 h at -20 °C and for another 24 h at room temperature. The methanol-swollen fibers were subsequently aligned and fixated on an aluminum sheet, dried for 24 h in an oven at 50 °C, and finally heat-treated at 150 °C for 15 min.

Microscopy Studies. To measure the morphology and dimensions of the PVA optical fibers, optical microscopy images were taken on Olympus BX51 microscope equipped with DP72 digital camera.

Swelling Behavior. To evaluate the swelling behavior of the optical fibers in water at 37 °C, the degree of swelling was calculated by measuring the weight of the fibers pre- and post-swelling:

$$\text{Degree of swelling (\%)} = \frac{(W_s - W_d)}{W_d} \times 100 \quad (6 - 1)$$

Where W_d is the weight of the dry film before swelling, and W_s is the weight of the swollen film at a definite time interval. To minimize the error in measuring the degree of swelling, once the swollen films were taken out of the water, they were placed on paper tissue to wick any excess water from the surface; the samples were then immediately weighed.

Dynamic Mechanical Analyses. DMA measurements of the commercial single mode optical fibers and the PVA fibers were performed using a TA Instruments Model Q800 dynamic mechanical analyzer. All tests were carried out in tensile mode using a temperature sweep method from 0 °C to 140 °C and applying an oscillatory deformation with a frequency of 1 Hz and a strain with an amplitude of 15 μm . To determine the mechanical properties of the water-swollen optical fibers in the wet state, the fibers were first immersed in water at 37 °C for 1 day. Then, the mechanical tests were conducted in a submersion clamp, which allowed measurements while the fibers were immersed in water. In this method, the temperature sweeps were done in the range of 23-60 °C with a heating rate of 1 °C/min, and a strain amplitude of 15 μm using the tensile mode.

Optical Measurements. Blue (470 nm, M470F1, 10.1 mW, ThorLabs) and amber (590 nm, M590F1, 3.2 mW, ThorLabs) fiber-coupled high-power LEDs were used to characterize the PVA fibers' optical properties. The light transmission of the PVA fibers was quantified by determining the loss of light using a cutback method,^{28, 29} in which the optical fibers were truncated and the intensity of the transmitted light was measured using a photodiode (S120VC, ThorLabs) coupled with a photometer (PM100USB, ThorLabs). To characterize the optical properties in the wet state, the fiber was threaded through two ferrules embedded in opposite windows of a 1 cm x 1 cm x 5 cm polystyrene cuvette such that the two fiber extremities remained dry while the middle portion could be exposed to a fluid.

6.4. RESULTS AND DISCUSSION

The various steps of the fabrication process employed are schematically shown in Figure 6-1. A dry-jet wet-spinning process was used to spin a 10 mg/mL solution of in a 4:1 v/v DMSO/water mixture into a coagulation bath of methanol cooled to -20 °C, using a spinneret with a diameter of 0.8 mm and a flow rate of 0.36 mL/min. The as-spun PVA fibers were kept immersed in the coagulation bath for 24 h at -20 °C and for another 24 h at room temperature. The methanol-swollen fibers were subsequently aligned and fixated on an aluminum sheet, dried for 24 h in an oven at 50 °C, and finally heat-treated at 150 °C for 15 min. This method afforded fibers with a diameter of ~150 μm. Optical microscopy images show rather homogeneous cross-sections and smooth surfaces (Figure 6-2a,b), while polarized optical microscopy images reveal a high degree of uniaxial orientation (Figure 6-2c,d). For this initial study no further cladding was used.

The swelling behavior of the PVA fibers was investigated by immersing them in deionized water at physiological temperature of 37 °C for one day. After one day of incubation in water, the degree of swelling was determined by measuring the weight of the fibers pre- and post- swelling as reported before,²³ yielding an equilibrium water uptake of $35 \pm 4.5\%$ w/w.

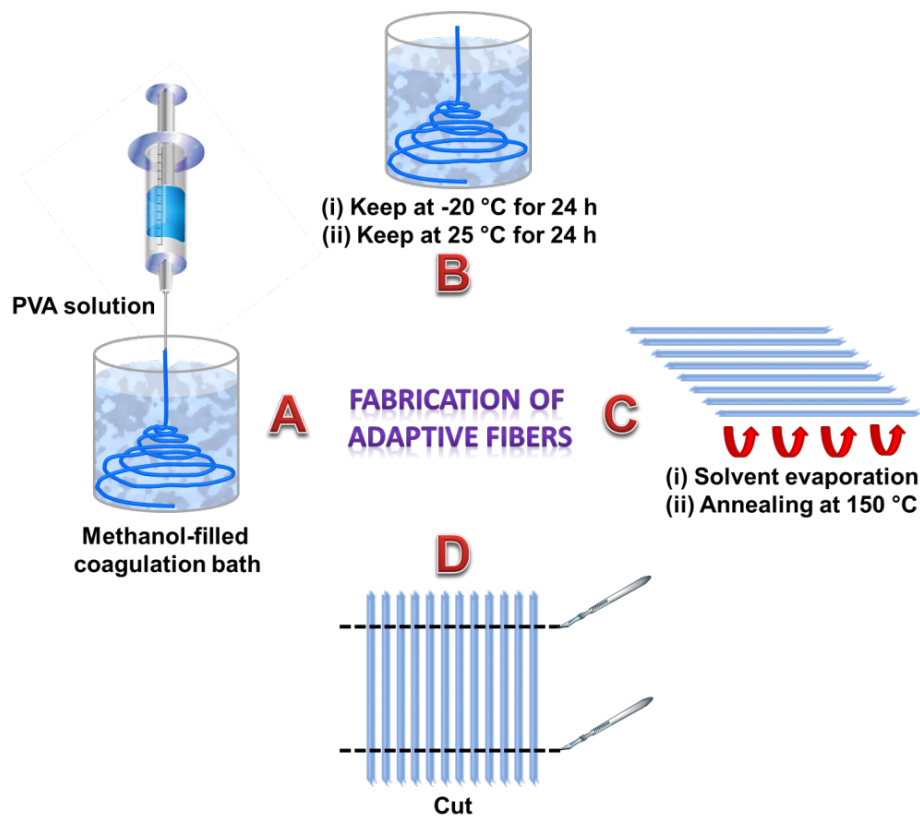


Figure 6-1. Schematic representation of the various processing steps used to fabricate physiologically-responsive, mechanically adaptive optical fibers based on PVA.

Dynamic mechanical analysis (DMA) experiments were carried out to determine the tensile storage modulus (E') of the fibers in the dry and wet state. The adaptive PVA fibers display an initial tensile storage modulus E' of 7100 ± 230 MPa (dry state at 25 °C, Figure 6-3), which is reduced as the temperature is increased above the T_g (~ 68 °C) to reach a rubbery plateau with an E' of 1630 ± 400 MPa at 100 °C (data not shown, $N = 3$). Upon immersion in deionized water for 1 day at 37 °C, the PVA fibers softened substantially to reach an E' of ~ 35 MPa after equilibration.

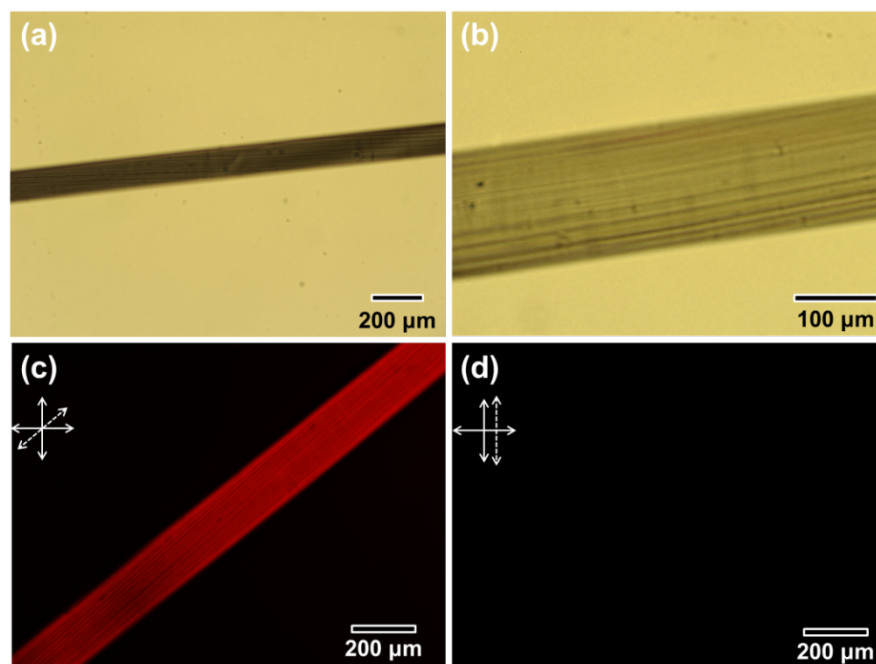


Figure 6-2. Optical microscopic images of a PVA optical fiber (a, b). Cross-polarized optical micrographs of a PVA optical fiber arranged with its long axis oriented with angles of 45° (c) and 0° (d) relative to the analyzer; the orientation of the polarizers (solid arrows) and sample (dashed arrows) is also shown.

Figure 6-3 shows time-dependent measurements of the tensile storage modulus E' of a PVA fiber and a single mode optical fiber which is a silica core coated with dual acrylate (S405-XP, ThorLabs) as reference, starting in the dry state at room temperature and upon addition of water at 37°C . In the case of the PVA fiber, a rapid (4 min) decrease of E' is observed, while the mechanical properties of the conventional SM optical fiber remain unchanged. Thus, mechanical tests confirm unequivocally that the PVA fibers investigated here are rigid when dry, but soften considerably upon swelling in water.

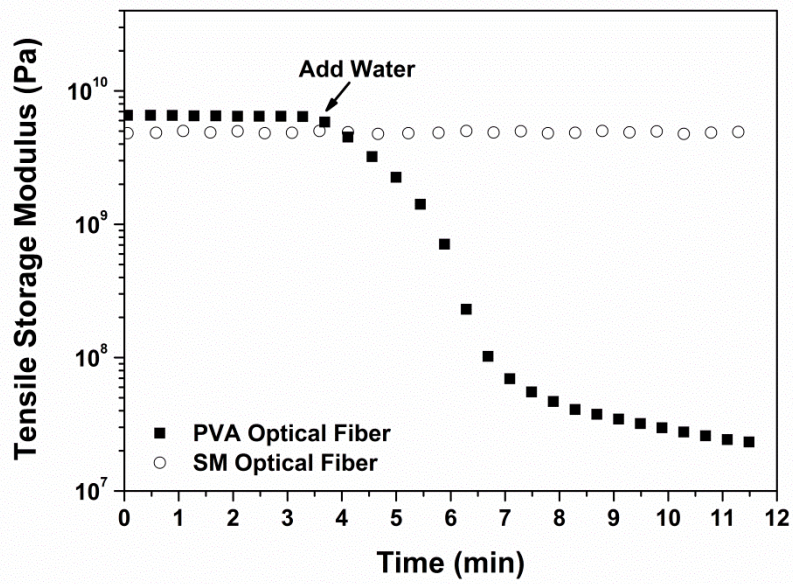


Figure 6-3. Tensile storage modulus (E') of an adaptive PVA fiber and a commercial single mode (SM) optical fiber (S405-XP, ThorLabs) as a function of immersion time in water at 37 °C. The water was added after 3.5 min, as indicated in the figure.

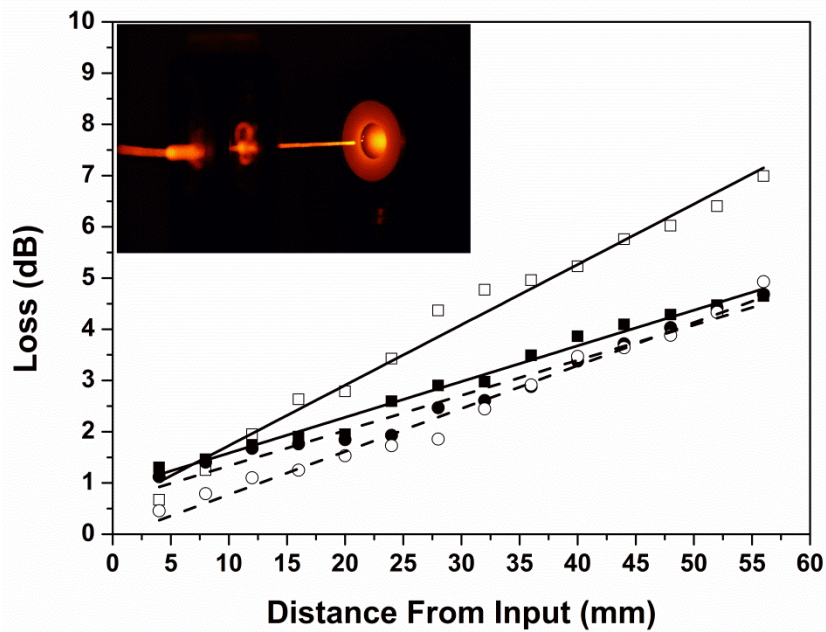


Figure 6-4. Optical losses of PVA optical fibers in the dry and wet state as function of fiber length. Data are shown for 470 (dry, □; wet, □) and 590 nm (dry, □; wet, □) incident light and represent of $N=5$ samples \pm standard deviation. Solid (470 nm) and dashed (590 nm) lines are least square fits. The inset shows a photograph of a fiber transmitting 590 nm light in the dry, rigid state.

Blue (470 nm, M470F1, 10.1 mW, ThorLabs) and amber (590 nm, M590F1, 3.2 mW, ThorLabs) fiber-coupled high-power LEDs were used to demonstrate the PVA fibers' ability to deliver light of different wavelengths as they are commonly used in optogenetic applications. The light transmission of the PVA fibers was quantified by determining the loss of light using a cutback method,^{28, 29} in which the optical fibers were truncated and the intensity of the transmitted light was measured using a photodiode (S120VC, ThorLabs) coupled with a photometer (PM100USB, ThorLabs). Figure 6-4 shows the light loss as function of fiber length, wavelength, and switching state. The propagation losses determined through linear regression of the data sets are 0.7 ± 0.04 dB/cm at 470 nm and 0.6 ± 0.1 dB/cm at 590 nm ($N = 5$) in the dry state.

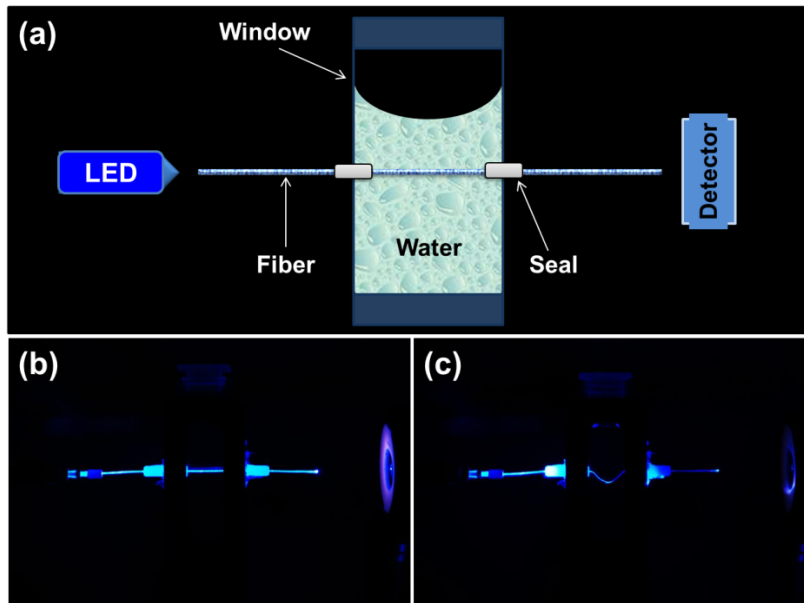


Figure 6-5. (a) Schematic representation of the cell used to operate optical fibers in the dry and water-swollen state. (b, c) Photographs of a 5 cm long PVA fiber transmitting 470 nm light in the dry state (b) and after adding water of a temperature of 25 °C (c).

The setup sketched in Figure 6-5a was used to measure the optical transmission through the fibers in the rigid dry and wet soft state. The fiber was threaded through two ferrules embedded in opposite windows of a 1 cm x 1 cm x 5 cm polystyrene cuvette such that the two fiber extremities remained dry while the middle portion could be exposed to a fluid. Light from a 470 nm LED with an output of 10.1 mW was coupled into one end of the fiber. Figures 6-5b and 6-5c, which show the setup in the dry and water-filled state, reveal no qualitative differences in light transmission and scattering. However, in the water-swollen state the PVA fiber can be readily bent (Figure 6-5c). Figure 6-6 shows how the transmitted power and power density change over time as the fiber is repeatedly softened by addition of deionized water, and rigidified upon drying. In a first 5 h dry phase, light transmission is stable as expected. Upon addition of water (refractive index $n = 1.33$) a brief increase of the transmitted power (density) of $\sim 10\%$ is observed, which is likely related to increased total internal reflection in the fiber ($n = 1.46$). Upon swelling/softening, the transmission is rapidly decreased by $\sim 15\%$. We speculate that the reduction of the fibers' refractive index on account of swelling with water ($n = 1.33$) and reduced total internal reflection as well increased scattering effects contribute to these relatively small losses; a similar trend was observed by Dupuis *et al.* for microstructured polymer optical fibers made from cellulose butyrate³⁰. Figure 6-6 shows that drying and another wetting and drying cycle permitted to reversibly switch the transmission characteristics of the PVA fibers and that under unchanged conditions the transmission stabilized quickly and was then stable for many hours. The propagation loss of the PVA fibers in the water-swollen soft state, measured after immersion for 30 min in water at room temperature, was 1.1 ± 0.1 dB/cm at 470 nm and 0.9 ± 0.3 dB/cm at 590 nm (Figure 6-4, $N = 5$), i.e., slightly higher than in the dry state. The linear losses vs. distance functions confirm that the optical properties are homogeneous along the PVA fiber and that smooth bents introduce negligible losses. Due to significant scattering losses imparted by the slightly crystalline polymer, the optical losses of the current PVA

fibers are higher than in conventional optical fibers, but their optical properties are clearly sufficient (*vide infra*) for the targeted application.

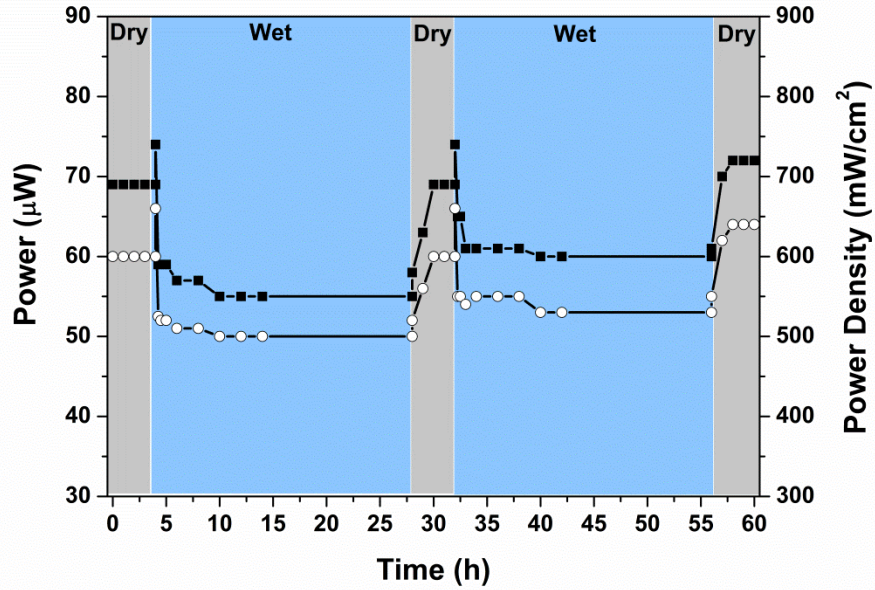


Figure 6-6. Changes of transmitted power (□) and power density (□) over time as a 10 cm long PVA fiber transporting 470 nm light from a 10.1 mW fiber-coupled high-power LED is switched from the dry, rigid state to the water-swollen soft state (room temperature) and back.

The illumination power density required for optogenetic applications is typically in the range of 10-1000 mW/cm².³¹ The data in Figure 6-6 show that this level can be met with the current PVA fibers. For example, if a LED with an output of 10.1 mW is used, a 150 μm thick, 10 cm long PVA fiber had an output power density of ~700 and ~500 mW/cm² in the dry and wet state, respectively. Thus, the illumination power achievable with the physiologically responsive, mechanically adaptive PVA fibers described here is adequate to activate neurons in the brain, which bodes well for future *in vivo* optogenetic applications.

6.5. CONCLUSIONS

In summary, we have demonstrated the design and fabrication of physiologically-responsive, mechanically adaptive optical fibers from poly(vinyl alcohol). These fibers offer an initial stiffness of ~ 7 GPa, which is slightly higher than those of commercial single mode optical fibers and permits facile insertion of small-diameter implants into the cortex. Upon exposure to water the fibers swell slightly and their stiffness is reduced 200-fold, while the concomitant changes to the fiber's optical properties are small. Clearly, the optical properties of the PVA fibers studied are not comparable to those of conventional optical fibers; the semicrystalline nature of the polymer, which causes scattering, and the absence of a cladding contribute to significant losses. However, the targeted application in optogenetics requires fibers that are only a few mm long. We have shown that the optical characteristics of the, at this point largely unoptimized, PVA fibers produced here are already sufficient to meet the demands of this application, and permit to deliver light of a range of wavelengths that is sufficiently intense to stimulate neurons in the brain. The hitherto unavailable mechanical morphing feature of the PVA optical fibers promises to be useful for chronic optogenetics technology and *in vivo* studies are planned that seek to quantify the potential benefits in terms of reduced neuroinflammatory response and improved neural integration.

6.6. REFERENCES

1. M. A. L. Nicolelis, *Nat. Rev. Neurosci.*, 2003, **4**, 417-422.
2. A. B. Schwartz, *Annu. Rev. Neurosci.*, 2004, **27**, 487-507.
3. E. S. Boyden, F. Zhang, E. Bamberg, G. Nagel and K. Deisseroth, *Nat. Neurosci.*, 2005, **8**, 1263-1268.
4. K. Deisseroth, *Nat. Methods*, 2011, **8**, 26-29.
5. R. T. LaLumiere, *Brain Stimul*, 2011, **4**, 1-6.
6. J. G. Bernstein, P. A. Garrity and E. S. Boyden, *Curr. Opin. Neurobiol.*, 2012, **22**, 61-71.
7. A. Gerits, R. Farivar, B. R. Rosen, L. L. Wald, E. S. Boyden and W. Vanduffel, *Curr. Biol.*, 2012, **22**, 1722-1726.
8. V. Gradinaru, M. Mogri, K. R. Thompson, J. M. Henderson and K. Deisseroth, *Science*, 2009, **324**, 354-359.
9. Y. Lu, Y. L. Li, J. Q. Pan, P. F. Wei, N. Liu, B. F. Wu, J. B. Cheng, C. Y. Lu and L. P. Wang, *Biomaterials*, 2012, **33**, 378-394.
10. A. N. Zorzos, J. Scholvin, E. S. Boyden and C. G. Fonstad, *Opt. Lett.*, 2012, **37**, 4841-4843.
11. D. R. Sparta, A. M. Stamatakis, J. L. Phillips, N. Hovelso, R. van Zessen and G. D. Stuber, *Nat. Protoc.*, 2012, **7**, 12-23.
12. K. Ung and B. R. Arenkiel, 2012, e50004.
13. V. S. Polikov, P. A. Tresco and W. M. Reichert, *J. Neurosci. Methods*, 2005, **148**, 1-18.
14. J. R. Capadona, D. J. Tyler, C. A. Zorman, S. J. Rowan and C. Weder, *MRS Bull.*, 2012, **37**, 581-589.
15. A. Hess, J. Dunning, J. Harris, J. R. Capadona, K. Shanmuganathan, S. J. Rowan, C. Weder, D. J. Tyler and C. A. Zorman, Solid-State Sensors, Actuators and Microsystems Conference, 2009.
16. J. P. Harris, A. E. Hess, S. J. Rowan, C. Weder, C. A. Zorman, D. J. Tyler and J. R. Capadona, *J. Neural Eng.*, 2011, **8**, 040610.
17. J. P. Harris, J. R. Capadona, R. H. Miller, B. C. Healy, K. Shanmuganathan, S. J. Rowan, C. Weder and D. J. Tyler, *J. Neural Eng.*, 2011, **8**, 066011.
18. T. Ware, D. Simon, D. E. Arreaga-Salas, J. Reeder, R. Rennaker, E. W. Keefer and W. Voit, *Adv. Funct. Mater.*, 2012, **22**, 3470-3479.
19. J. R. Capadona, K. Shanmuganathan, D. J. Tyler, S. J. Rowan and C. Weder, *Science*, 2008, **319**, 1370-1374.
20. K. Shanmuganathan, J. R. Capadona, S. J. Rowan and C. Weder, *Prog. Polym. Sci.*, 2010, **35**, 212-222.
21. A. E. Way, L. Hsu, K. Shanmuganathan, C. Weder and S. J. Rowan, *ACS Macro Letters*, 2012, **1**, 1001-1006.
22. L. Hsu, C. Weder and S. J. Rowan, *J. Mater. Chem.*, 2011, **21**, 2812-2822.

23. M. Jorfi, M. N. Roberts, E. J. Foster and C. Weder, *ACS Appl. Mater. Interfaces*, 2013, **5**, 1517-1526.
24. S. H. Hyon, Y. Ikada, Method of molding a polyvinyl alcohol contact lenses. U.S. Patent, 4874562, 1989.
25. R. A. Janssen, P. I. Lee, E. M. Ajello, Preparation of stable polyvinyl alcohol hydrogel contact lens, 5174929, 1992.
26. A. R. Nectow, K. G. Marra and D. L. Kaplan, *Tissue Eng Part B-Re*, 2012, **18**, 40-50.
27. K. A. Potter, M. Jorfi, K. T. Householder, E. Johan Foster, C. Weder and J. R. Capadona, *Acta Biomater.*, 2014, 10, 2209–2222.
28. G. T. Reed, Measurements on Optical Devices, IEE Colloquium on, 1992.
29. A. Zhang and K. T. Chan, Optoelectronics, Proceedings of the Sixth Chinese Symposium, 2003.
30. A. Dupuis, N. Guo, Y. Gao, N. Godbout, S. Lacroix, C. Dubois and M. Skorobogatiy, *Opt. Lett.*, 2007, **32**, 109-111.
31. J. G. Bernstein and E. S. Boyden, *Trends in cognitive sciences*, 2011, **15**, 592-600.

Chapter 7 – Conclusions and Outlook

7.1. CONCLUSIONS

The present dissertation presents the design, preparation, and investigation of a new platform of physiologically responsive mechanically adaptive materials for neural interfacing applications, which alter their mechanical characteristics in response to physiological conditions. The materials are sufficiently rigid to facilitate implantation of the cortical devices into the cortex, but once in place, the materials will respond to the chemical environment of the cortex, soften substantially to closely match the mechanics of the surrounding tissue, and thus become “mechanically invisible” to minimize brain tissue response. The mechanical morphing of these materials relies on either plasticization of the polymer matrix upon absorption of water and/or on a nanocomposite architecture where physiologically benign rigid, rod-like cellulose nanocrystals are introduced into a polymer of interest. The high stiffness in the dry state and the ability to tailor the mechanical contrast via composition and processing renders these materials particularly useful for a wide variety of adaptive biomedical implants (patents pending^{5,6,7}) such as intracortical microelectrodes. The chapters in this dissertation have been presented in a chronological fashion to illustrate the development of this new class of physiologically responsive biomaterials.

Chapter 3 described chemo-responsive mechanically adaptive nanocomposites based on poly(vinyl alcohol) (PVA) and cellulose nanocrystals (CNCs), which offer an initial stiffness that is significantly higher than that of previous generations of such adaptive materials. The use of PVA as a matrix polymer into which CNCs are incorporated proved

⁵Polymer Nanocomposites Having Switchable Mechanical Properties; European Patent Application 61/701,000, Patent Filed 9/14/2012.

⁶Medical Injection Device; European Patent Application 61/700,995, Patent Filed 9/14/2012.

⁷Physiologically Responsive Mechanically Adaptive Polymer Optical Fibers, Production and Methods of Use; US Provisional Patent Application 61/939,893, Patent Filed 2/14/2014.

useful for several reasons. The tensile storage moduli of the nanocomposites were significantly higher than those of comparable nanocomposites in both the glassy and rubbery regime. It appears that in addition to CNC-CNC interactions, polymer-CNC interactions, which could be promoted by the strong propensity of PVA to form hydrogen bonds and provide a compatible polymer-filler interface, are a significant factor in this context. Another significant factor is the possibility of controlling the swelling characteristics of the PVA matrix, and therefore the properties of water- or artificial cerebrospinal fluid-swollen materials, via the processing conditions. Using this tool, the switching “contrast” of the materials upon exposure to physiological conditions could be varied between a 90-fold to a 200-fold modulus reduction depending on the source of cellulose nanocrystals. The results suggest that other ranges are accessible via the processing temperature, which (in relative terms) affects mainly the soft state. Although not as stiff initially in the dry state, materials fabricated from cotton cellulose nanocrystals exhibit a larger mechanical contrast (up to 900-fold), as they soften much more than the tunicate-based materials. This effect is related to the lower reinforcing power of cotton. Overall, we have demonstrated that varying the CNC type and concentration and the processing temperature allows one to tailor the mechanical properties of “hard” and “soft” state over a broad range. The hitherto unavailable contrasts accessible by these materials make them potentially useful as substrates for next generation of neural prosthetic devices.

Chapters 4 and 5 dealt with the development of new class of drug-releasing mechanically adaptive materials. In Chapter 4, *in situ* softening antioxidant releasing polymeric materials were developed to explore if the combination of two independently effective mechanisms, softening vs. antioxidant release, leads to a synergistic effect in reducing the neuroinflammation at the intracortical microelectrode-tissue interface. Results showed that the incorporation of the antioxidant curcumin into the mechanically adaptive poly(vinyl alcohol) provided significant improvements in neuronal densities surrounding cortical implants in comparison to neat polymer films up to 4 weeks after implantation. However, at 12 weeks post-implantation, there were no significant differences between

curcumin-releasing and neat PVA reference implants for all investigated markers. Taken together, our results suggested that acute attenuation of inflammatory events using localized drug delivery mechanisms, such as release of curcumin, would not cause detrimental effects in the long-term. Further, the results presented here provide exciting opportunities to better understand the importance and optimal timing of wound healing events around cortical implants such that neuronal degeneration is prevented.

Building on our proof-of-concept study in Chapter 4, we suggested that future studies should continue to investigate the use of mechanically adaptive polymer systems in conjunction with antioxidant release to mediate acute and chronic neuroinflammatory events surrounding intracortical microelectrodes. In order to better understand if the effects of short-term local release of antioxidant therapies are sufficient for long-term neuroprotection surrounding intracortical microelectrodes, it is imperative that future studies screen both additional antioxidants and alternative mechanically adaptive polymer systems with improved long-term *in vivo* stability. Therefore, in Chapter 5, mechanically adaptive materials based on poly(vinyl acetate) and CNCs with the ability to release two different natural antioxidant drugs (i.e. curcumin or resveratrol) locally within 72 hours of incubation in emulated physiological conditions were investigated. The nanocomposites softened substantially upon immersion in artificial cerebrospinal fluid at body temperature; tensile modulus decreased from ~6000 MPa to ~10 MPa (~600-fold). Additionally, curcumin-releasing mechanically adaptive nanocomposite exhibited greater antioxidant activity *in vitro* than their counterparts. Ongoing *in vivo* histological studies seek to quantify the benefits of synergistic effects of mechanically adaptive materials with antioxidant releasing properties to mediate acute and chronic neuroinflammatory events surrounding intracortical microelectrodes in comparison to commercial silicon-based intracortical microelectrodes.

Chapter 6 discussed expanding the idea of mechanically adaptive neural interfacing materials towards optogenetic applications. A different approach was taken to design and fabricate physiologically responsive, mechanically adaptive optical fibers from poly(vinyl alcohol). These fibers offer an initial stiffness of ~7000 MPa, which is slightly

higher than those of commercial optical fibers and permits facile insertion of small-diameter implants into the cortex. Upon exposure to emulated physiological conditions the fibers swell slightly with water and their stiffness is reduced 200-fold, while the concomitant changes to the fiber's optical properties are small. We have shown that the optical characteristics of the fibers produced here are already sufficient to meet the demands of this application, and permit the delivery of light in a range of wavelengths that is intense enough to stimulate neurons in the brain. The mechanical morphing feature of these optical fibers promises to be useful for chronic optogenetics technology and *in vivo* studies are planned that will quantify the potential benefits in terms of reduced neuroinflammatory response and improved neural integration.

This dissertation derived fundamental insights into the structure-property relationships by controlling the adaptive nature of these materials through composition (i.e. different polymer matrices, types and amount of nanofiller, and therapeutic agents) and also processing conditions. While *in vivo* studies using the new materials presented here have only recently begun, it is already clear that the materials made and studied in this dissertation will be useful to advance the understanding of how stimuli-responsive polymeric materials can help to decrease the neuroinflammation effects associated with intracortical implants.

7.2. OUTLOOK

The hypothesis that the mechanical mismatch between current metallic- or silicon-based intracortical microelectrodes and brain tissue propagates neuroinflammation, an event leading to microelectrode failure, has led to the development of new family of *in situ* softening polymeric materials as presented in this dissertation. The application of mechanically adaptive materials in chronic neural interfaces is still in its infancy despite an impressive body of emerging research, partly because of the complexities associated with interacting with neural cells and the mammalian nervous system. Moreover, there are fundamental gaps of knowledge that need to be addressed. In addition to the areas investigated in the present dissertation, there are still many opportunities for *in situ*

softening materials to enhance and improve current technologies in neural interfacing devices. While initial histological studies of implants based on mechanically adaptive polymers suggest that adaptive materials can better stabilize neural cell populations at the neural tissue/electrode interface than rigid electrodes (up to eight weeks), there are still several challenges that need to be addressed. First, the mechanical strain placed on cortical tissue by stiffer implants played a less important role soon after implantation than at more long-term times. Therefore, histological studies for such adaptive materials must be conducted for long-term implantation times to better understand the impact of mechanically adaptive materials in improving long-term performance of intracortical microelectrodes. It is also important to note that, at present, tissue histochemistry alone does not predict neural recording quality of intracortical electrodes. Future research activities in mechanically adaptive materials for intracortical microelectrode applications must focus, in parallel with histological studies, on investigating the transition of this platform technology to actual recording electrodes. Second, if such *in vivo* tissue response studies confirm that adaptive materials are indeed better than previously developed rigid electrodes, one must next determine how soft they need to be. In other words, could even softer materials (~kPa) further improve the tissue response? While the adaptive polymeric materials are several orders of magnitude softer than traditionally used materials, the materials are still two or three orders of magnitude stiffer than brain tissue. Answers to these questions are important to the development of this field. Additionally, limited studies on the mechanical properties of dynamic materials for the duration of implant lifetime suggest that further research is needed to assess the durability of softening polymeric-based intracortical microelectrodes in animal models. This will provide an insight into possible degradation of such adaptive polymer systems.

The work presented in this dissertation also suggests the potential for synergistic effects of combinatorial approaches throughout the progressive inflammatory response. For example, one could envision the incorporation of bioactive molecules such as anti-inflammatory, antioxidant therapies and/or proteins on or within the mechanically dynamic neural electrode devices to mitigate initial trauma, coupled with a chronically

compliant device to dictate scar mechanics and mediate chronic tissue strain. One limitation of drug-releasing implants is their limited effective duration. There are currently few if any viable options for locally delivering drugs for the extended periods of time that may be clinically relevant for intracortical microelectrode applications. Therefore, the field should also seek to develop sustained drug-releasing implants for long-term cortical applications.

Finally, a proof of concept has been successfully established in Chapter 6 to expand the concept of mechanically adaptive polymeric materials towards other central nervous system applications; optogenetics. This developed platform technology can be tailored to a variety of biomedical applications, such as sensing, to create interesting polymeric optical fibers with mechanically dynamic properties. One could develop stimuli-responsive adaptive polymeric fibers that could react to different stimuli such as pH. In the case of optogenetic applications, it is clear that long-term *in vivo* studies are necessary to better investigate the effect and behavior of such physiologically responsive mechanically adaptive optical fibers in the brain compared to commercial optical fibers.

It is also important to note that despite the vast amount of research being developed recently on polymeric materials for neural interfacing applications; in most cases researchers have simply repurposed polymers developed for different applications for use in intracortical microelectrodes. Although the development of such materials-based intracortical microelectrodes has contributed significantly to our understanding of the technology, one should think of designing novel materials, strategies and concepts for the purposes of this field. Furthermore, due to the exciting advances in the fields of materials science, neural engineering and bioengineering, we should foster dynamic multi-disciplinary teams, in order to accumulate the skills and knowledge to design, test, and integrate the next generation intracortical microelectrodes, capable of long-term clinical deployment for neuro-rehabilitative applications, and beyond.

Mehdi Jorfi, Ph.D.

Curriculum Vitae

RESEARCH EXPERTISE AND INTERESTS

Advanced Healthcare Biomaterials: Polymeric Biomaterials, Drug Delivery, Nanomaterials, Microfluidics, Layer-by-Layer Assembly, Biologically-Inspired Materials, Polymeric (Nano)-Microcapsules, Bioengineering, Printing Materials, Polymer Nanocomposites, Regenerative Medicine, Hydrogels, Tissue Engineering, Stem Cells

EDUCATION

Ph.D., Biomaterials Science March 2014
University of Fribourg, Switzerland

Thesis Title: Physiologically Responsive Mechanically Adaptive Polymeric Materials for Biomedical Applications

Advisor: Prof. Dr. Christoph Weder

M.S., Chemistry January 2008
Shahid Chamran University of Ahvaz, Iran

Thesis Title: Synthesis and Study of Some Transition Metals Group (VIII) Oxidants

Advisor: Prof. Mohammad Kooti

B.S., Chemistry July 2005
University of Kashan, Iran

Education as Chemistry Teacher, Degree awarded: High School and College Teacher License

RESEARCH EXPERIENCE

Research Assistant Nov. 2010 – Present
Adolphe Merkle Institute, University of Fribourg, Switzerland – with Prof. Christoph Weder

Synthesis, processing and investigation of biologically-inspired polymer nanocomposites as mechanically adaptive substrates for intracortical microelectrodes

Development and investigation of drug-releasing mechanically dynamic biomaterials for cortical microelectrodes to minimize neurodegeneration

Development of sustained drug release systems based on cellulose nanocrystals, biodegradable polymeric nanoparticles, and mechanically adaptive nanocomposites for CNS applications

Development of advanced polymer materials as mechanically adaptive optical fibers for optogenetics

Visiting Researcher

Summer 2012

L. Stokes Cleveland Veteran's Affairs Medical Center and Department of Biomedical Engineering at Case Western Reserve University, United States – with Prof. Jeffrey R. Capadona

Assessment of inflammatory response to drug-eluting mechanically adaptive materials as substrate for intracortical microelectrodes

Research Assistant

Sep. 2006 – Jan. 2008

Department of Chemistry, Shahid Chamran University of Ahvaz, Iran – with Prof. Mohammad Kooti

Synthesis and characterization of novel Ferrate (VI) compounds

Synthesis and characterization of nanosized NiO₂ and NiO in the presence of various surfactants

Oxidation of various organic substrates by nanosized nickel peroxide in the presence of different catalysts

HONORS AND AWARDS

2014	SNSF Early Postdoctoral Mobility Fellowship
2013	First Place – Adolphe Merkle Institute Image Award
2013	SCNAT/SCS Chemistry Travel Award
2011	Second Place – Adolphe Merkle Institute Image Award
2009	Iran Nanotechnology Initiative Council Award
2008	Excellent Graduate Thesis in Chemistry, Shahid Chamran University

PUBLICATIONS

Peer-Reviewed Articles

1. Jorfi, M.; Foster, E.J. Recent Advances in Nanocellulose for Biomedical Applications *J. Appl. Polym. Sci.* 2015, 132, 41719.
2. Jorfi, M.; Skousen, J.L.; Weder, C.; Capadona, J.R. Progress towards Biocompatible Intracortical Microelectrodes for Neural Interfacing Applications. *J. Neural Eng.* 2015, 12, 011001.
3. Biyani, M.V.; Jorfi, M.; Weder, C. Foster, E.J.; Light-Stimulated Mechanically Switchable, Photopatternable Cellulose Nanocomposites *Polym. Chem.* 2014, 5, 5716.
4. Jorfi, M.; Foster, E.J.; Weder, C. Physiologically Responsive Mechanically Adaptive Polymer Optical Fibers for Optogenetics *Opt. Lett.* 2014, 39, 2872-2875.

5. Sacui, I.A.; Nieuwendaal, R.C.; Szmecinski, H.; Burnett, D.J.; Stranick, S.J.; Jorfi, M.; Weder, C.; Foster, E.J.; Olsson, R.T.; Gilman, J.W. Comparison of the properties of cellulose nanocrystals and cellulose nanofibrils isolated from bacteria, tunicate, and wood processed using acid, enzymatic, mechanical, and oxidative methods *ACS Appl. Mater. Interfaces* 2014, 6, 6127-6138.
6. Jorfi, M.*; Potter, K.A.*; Householder, K.T.; Foster, E.J.; Weder, C.; Capadona, J.R. Curcumin-Releasing Mechanically adaptive Intracortical Implants Improve the Proximal Neuronal Density and Blood-Brain Barrier Stability *Acta Biomater.* 2014, 10, 2209–2222 (*Equal Contribution).
7. Jorfi, M.; Robert, M.N.; Foster, E.J.; Weder, C. Physiologically-Responsive, Mechanically adaptive Bio-Nanocomposites for Biomedical Applications *ACS Appl. Mater. Interfaces* 2013, 5, 1517–1526.
8. Kooti, M.; Jorfi, M.; Javadi, H. Rapid Chemical Synthesis of Four Ferrate Compounds *J. Iran. Chem. Soc.* 2010, 7, 814-819.
9. Kooti, M.; Jorfi, M. Synthesis and Characterization of Nanosized NiO₂ and NiO Using Triton[®] X-100 *Cent. Eur. J. Chem.* 2009, 7, 155-158.
10. Kooti, M.; Jorfi, M. Mild and Efficient Oxidation of Aromatic Alcohols and Other Substrates Using NiO₂/CH₃COOH System *J. Chem.* 2008, 5, 365-369.
11. Kooti, M.; Tarassoli, A.; Javadi, H.; Jorfi, M. A Facile Conversion of Alcohols to Esters Mediated by Potassium Ferrate *J. Chem.* 2008, 5, 718-722.

Patent Applications

- P1. Weder, C.; Jorfi, M.; Foster, E.J. Physiologically Responsive Mechanically Adaptive Polymer Optical Fibers, Production and Methods of Use; US Provisional Patent Application 61/939,893, Patent Filed 2/14/2014.
- P2. Breuer-Thal, B.; Witt, R.; Weder, C.; Foster, E.J.; Jorfi, M.; Roberts, M.N. Medical Injection Device; European Patent Application 61/700,995, Patent Filed 9/14/2012.
- P3. Weder, C.; Foster, E.J.; Jorfi, M.; Roberts, M.N. Polymer Nanocomposites Having Switchable Mechanical Properties; European Patent Application 61/701,000, Patent Filed 9/14/2012.

Book Chapters

- B1. Jorfi, M.; Annamalai, P.K.; Weder, C. Preparation of Cellulose Nanocrystal/Polymer Nanocomposites via Sol-Gel Processes; In: *Handbook of Green Materials; Processing Technologies, Properties and Applications*; Oksman, K.; Mathew, A.P.; Bismarck, A.; Rojas, O.; Sain, M.; Eds.; World Scientific, 2014, Vol. 2, pp 23-34.

- B2. Jorfi, M.; Amiralian, N.; Biyani, M.V.; Annamalai, P.K. Biopolymer Nanocomposites Reinforced with Nanocrystalline Cellulose; In: *Biomass-based Biocomposites*; Thakur, V.K.; Singha, A.S.; Eds.; Smithers Rapra, 2013, pp 277-304.
- B3. Biyani, M.V.; Jorfi, M.; Weder, C.; Foster, E.J. Light-Responsive Cellulose-Based Materials; In: *Production and Applications of Cellulose Nanomaterials*; Postek, M.T.; Moon, R.J.; Rudie, A.; and Bilodeau, M.A.; Eds.; TAPPI Press, Georgia, 2013, pp 129-131.

PRESENTATIONS

1. Jorfi, M.; Potter, K.A.; Householder, K.T.; Foster, E.J.; Capadona, J.R.; Weder, C. Physiologically-Responsive Drug-Releasing Materials For Neural Interfaces; *MRS Fall Meeting*, 2013, Boston, USA (Oral).
2. Jorfi, M.; Foster, E.J.; Weder, C. Physiologically-Responsive Polymer Bio-Nanocomposites for Intracortical Implants; *European Polymer Congress*, 2013, Pisa, Italy (Oral).
3. Jorfi, M.; Robert, M.; Foster, E.J.; Weder, C. Mechanically adaptive Materials for Direct Neural Interfaces; *245th ACS National Meeting*, 2013, New Orleans, USA (Oral).
4. Householder, K.T.; Potter, K.A.; Jorfi, M.; Weder, C.; Capadona, J.R. Anti-Oxidant Releasing Mechanically adaptive Materials Improve Neural Device Tissue Integration; *Biomedical Engineering Society Annual Meeting*, 2012, Atlanta, USA (Oral).
5. Jorfi, M.; Foster, E.J.; Weder, C. Mechanically adaptive Polymer Bio-Nanocomposites for Biomedical Applications; *244th ACS National Meeting*, 2012, Philadelphia, USA (Oral).
6. Jorfi, M.; Foster, E.J.; Weder, C. Bio-Inspired Mechanically-Responsive Polymer Nanocomposites; *Smart Materials and Devices for Medical Applications*, 2012, Bern, Switzerland (Poster).
7. Jorfi, M.; Kooti, M. Nickel Oxide Nanoparticles: Synthesis and Characterization; *Iran-India Joint Conference on Nanotechnology*, 2008, Tehran, Iran (Poster).
8. Jorfi, M.; Kooti, M. Solid-Phase Synthesis of Novel Ferrate Compounds; *10th Iranian Inorganic Chemistry Conference*, 2008, Zahedan, Iran (Poster).

SCIENTIFIC AFFILIATIONS

American Chemical Society; ACS Polymeric Materials: Science and Engineering Division; Materials Research Society; Society for Biomaterials; IEEE Engineering in

Medicine and Biology Society; Biomedical Engineering Society; Society for Biological Engineering

TEACHING EXPERIENCE

Teaching Assistant Fall 2011
Adolphe Merkle Institute, University of Fribourg, Switzerland
Course: Physical Chemistry Laboratory, *Level:* Undergraduate

Teaching Assistant 2006 – 2007
Department of Chemistry, Shahid Chamran University of Ahvaz, Iran
Courses: General Chemistry Lab. & Inorganic Chemistry Lab., *Level:* Undergraduate

Instructor 2006 – 2008
Payame Noor University (PNU), Iran
Course: General Chemistry, *Level:* Undergraduate

Teaching Assistant 2004 – 2005
Department of Chemistry, University of Kashan, Iran
Courses: Instrumental Analytical Chemistry, *Level:* Undergraduate

DECLARATION OF ORIGINALITY

Last name, first name: Jorfi, Mehdi

Matriculation number: 10-215-937

Thesis Title: Physiologically Responsive Mechanically Adaptive
Polymeric Materials for Biomedical Applications

I hereby declare that this thesis represents my original work and that I have used no other sources except as noted by citations. All contents that were obtained from other sources are explicitly declared as such and acknowledged by citation.

Fribourg, 6/02/2014